Atomistic Simulation in Powder Technology - from Growth Control and Dispersion Stabilization to Segregation at Doped Interfaces

THÈSE N^{O} 4166 (2008)

PRÉSENTÉE LE 19 SEPTEMBRE 2008

À LA FACULTE SCIENCES ET TECHNIQUES DE L'INGÉNIEUR
LABORATOIRE DE TECHNOLOGIE DES POUDRES
PROGRAMME DOCTORAL EN SCIENCE ET GÉNIE DES MATÉRIAUX

ÉCOLE POLYTECHNIQUE FÉDÉRALE DE LAUSANNE

POUR L'OBTENTION DU GRADE DE DOCTEUR ÈS SCIENCES

PAR

Ulrich ASCHAUER

M.Sc en science et génie des matériaux EPF (ing. sc. mat. dipl. EPF)
et de nationalité allemande

acceptée sur proposition du jury:

Prof. M. Rappaz, président du jury
Dr P. Bowen, directeur de thèse
Dr P. Derlet, rapporteur
Prof. S. Parker, rapporteur
Prof. R. Schaller, rapporteur

ÉCOLE POLYTECHNIQUE
FÉDÉRALE DE LAUSANNE

Suisse
2008

Abstract

Despite many years of intensive research there still remain many unresolved questions in powder and ceramic technology. A majority of these issues are linked to interfacial phenomena of atomic scale origin, which makes their experimental investigation very difficult due to limitations in the spatial resolution of the available analysis techniques. Computer simulations at the atomic scale provide with the advent of more and more advanced methods and increasing computer power an ever more powerful tool for the investigation of these phenomena. The understanding of experimental systems gained at a fundamental theoretical level will help target key experiments in a knowledge based fashion for the rapid advance in top-performance materials development, saving time and resources with simulations showing the most promising routes and key parameters to be explored in experiments.

The present thesis investigates several key steps in the production cycle of a ceramic material using atomic scale computer simulation techniques, leading to advances in the understanding of the underlying atomic scale phenomena in each case. Instead of treating a single material throughout the ceramic production process, a series of different systems of experimental interest are looked at in order to show the generic nature of the approach.

Very often ceramic powders are produced by precipitation from solution, where many powders properties can be modified, amongst them the particle size, morphology and state of agglomeration, all of which have an important effect on the quality of the final ceramic. Growth can be modified by the reactive environment (temperature, pH) or extrinsic species such as ions or molecular additives. Growth modification of hematite (α-Fe_2O_3) by phosphonic acid molecules was simulated by energy minimization and experimentally validated, making the method useful as a predictive tool for other phosphonic acid molecules. Significant changes in morphology were predicted and experimentally observed, the main reason for preferential adsorption being the surface geometry and topology, major distortions of the molecule leading to unfavorably high adsorption energies on some faces.

Since experiments showed calcite ($CaCO_3$) particles grown in presence of polyaspartic acid (p-ASP) to have a higher specific surface area than with polyacrylic acid (PAA) despite the same functional groups on both additives, molecular dynamics simulations were used to investigate this difference. The presence of charged surface defects at steps was found to be the key requirement for adsorption, the molecules' approach being hindered by the highly coordinated water at the surface and the additive even desorbing without the attractive electrostatic force. PAA was found to form more complexes with counterions in solution and a more negative enthalpy of adsorption was found for p-ASP, both of which will lead to more marked growth suppression by binding of p-ASP to steps, which are expected to be the main growth sites. Further the adsorption conformation of p-ASP results in a better colloidal stabilization than PAA, preventing particle agglomeration. These three aspects can explain the higher specific surface area for powders precipitated in presence of p-ASP. These computational approaches can thus explain subtle differences between additives as well the same additive on different surfaces helping in the targeted use of additives and the design of new additives.

Dopants may be added to ceramics during powder synthesis or before sintering either as sintering agents or to add specific properties to the final material. Often dopant ions are oversized compared those replaced in the crystal lattice leading to segregation towards defects where their incorporation is facilitated. Interface segregation was studied for industrially relevant dopant ions in alumina and zinc oxide using energy minimization and microstructural models to help compare with experimental findings. The results show a strong tendency for surface and a slightly lesser tendency for grain boundary segregation in all cases, however with important differences between different interfaces. As a key result one possible reason for the microstructural homogenization effect of magnesium was found to be its capacity to narrow the grain boundary energy distribution resulting in more equiaxed grains due to isotropic grain growth.

The segregation of luminescent neodymium ions in YAG ceramics for laser applications was investigated and dopants were shown to accumulate at grain boundaries where their high concentration will make them inactive for lasing and result in light scattering due to slight local variations of the refractive index. Using microstructural models the proportion of inactive dopant ions was found to increase with decreasing grain size, making nanoceramic lasers less powerful. Optical models based on atomistic segregation results on the other hand show that light scattering is more severe for larger grains, nanoceramics thus being more transparent. There is therefore an optimal grain size where laser power and transparency will result in the best possible laser performance. Different microstructural models could be linked to the sintering procedure, predicting that the best laser performance should be obtained by slow conventional sintering rather than by novel rapid methods such as spark-plasma-sintering (SPS). These results are key in understanding the role of interfaces in this novel class of laser materials and will help improve their fabrication methods.

Experiment and simulation of oxygen self-diffusion in alumina so far showed large discrepancies, the simulations predicting diffusive jump activation energies by a factor five smaller than experiments. In this thesis a novel simulation approach based on Metadynamics allowed to determine activation free energies of individual jumps, then using these in kinetic Monte Carlo simulations to predict the macroscopic diffusion coefficient. The key result is that the activation energy for the diffusion dominating jumps is of the order of the experimentally determined one, the so far reported simulated jump energies not forming a continuous diffusion network. The calculated diffusion coefficient correlates relatively well with experimental results. The developed approach is generic and can be applied to investigate a variety of diffusive phenomena in solids providing answers to many more of the remaining questions.

While atomistic simulation approaches give very interesting results on local atomistic phenomena and allow understanding and elucidating which processes occur spontaneously in a system, for predictions on experimental length and time scales the use of larger scale models is immensely important to extrapolate atomistic results to these scales. The combination of techniques from the electronic structure through the atomistic and mesoscale to the continuum level in a multi-scale modeling approach seems very promising for material science applications, where the goal is to understand experimental observations and to target the next key experiment in a knowledge-based fashion.

Keywords: Atomistic simulation, powder technology, hematite, calcite, alumina, YAG

Resumé

Malgré la recherche intense pendant de longues années, il existent toujours beaucoup de questions non résolues en technologies des poudres et céramiques. Une majorité des ces problèmes sont liés aux phénomènes interfaciaux d'origine atomistique ce qui rend leur investigation expérimentale très difficile dû aux limites de résolution des techniques d'analyse. Des simulations numériques à l'échelle atomique se présentent avec le développement de méthodes de plus en plus avancées et une puissance augmentant des ordinateurs comme un outil performant à l'investigation de ces phénomènes. La compréhension de systèmes expérimentaux à un niveau fondamental va permettre de cibler des expériences clés basé sur ces connaissances permettant un avancement plus rapide dans le développement de matériaux de haute performance. Cette approche va économiser du temps et des ressources avec des simulations montrant les chemins les plus prometteurs à être explorés en expérience.

La présente thèse regarde plusieurs étapes clés dans le cycle de production des céramiques par des techniques de simulation à l'échelle atomique menant à des avances dans la compréhension des mécanismes atomiques dans tous les cas. Au lieu de suivre un matériau le long du cycle de production une série de matériaux est traitée afin de montrer la nature générique de cette approche.

Souvent des poudres céramiques sont produites par précipitation en solution où beaucoup des propriétés de la poudre peuvent être influencées, comme sa taille de particules, sa morphologie ou l'état d'agglomération, qui ont un effet important sur les propriétés de la céramique finale. La croissance peut être influencée par le milieu réactif (température et pH) ainsi que par des espèces extrinsèques comme les ions ou les molécules. La modification de la croissance de l'hématite (α-Fe_2O_3) par les molécules d'acides phosphoniques a été investiguée par minimisation d'énergie et validée expérimentalement. Cela rend cet approche utilisable comme outil de prédiction pour d'autres molécules d'acide phosphoniques. Des changement significatives de la morphologie ont été prédits et observés dans les expériences. Les raisons principales qui mènent à un attachement préférentiel sont la géométrie et topologie de la surface, des distorsions majeures des molécules resultants en énergies d'adsorption

très élevées sur certaines faces.

Dans les expériences des poudres de calcite ($CaCO_3$) sythéthisées en présence de l'acide polyaspartique (p-ASP) ont malgré les mêmes groupes fonctionnelles montrés une surface spécifique beaucoup plus grande que celles précipitées en présence de l'acide polyacrylique (PAA). Des simulations de type dynamique moléculaire ont été utilisés pour élucider cette différence. La présence de défauts chargés aux marches de surface a été trouvé d'être un facteur clé pour l'adsorption car l'approche des molécules est gênée par la présence d'une couche d'eau hautement coordonnée à la surface. Les molécules désorbent même sans cette force électrostatique attractive. Il a été trouvé que le PAA forme plus de complexes avec des contre ions en solution. D'autre part une enthalpie d'adsorption plus négative a été trouvée pour p-ASP. Ces deux effets vont mener à une modification de croissance plus marquée pour le p-ASP par liaison aux marches qui sont supposées être les lieux de croissance principaux. En plus, il a été montré que le p-ASP adsorbe dans une configuration menant à une stabilisation colloïdale plus élevée ce qui diminue plus l'agglomération des particules par rapport à PAA. Ces trois aspects peuvent expliquer la surface spécifique plus élevée observée en présence de p-ASP. Ces approches numériques peuvent ainsi donner des explications pour des différences subtiles entre des additives ou pour un même additive sur différentes surfaces permettant une utilisation plus ciblée ainsi que le développent spécifique de nouveaux additives.

Des dopants peuvent être ajoutés aux céramiques soit pendant la synthèse des poudres soit avant le frittage comme agent de frittage ou encore pour donner des propriétés spécifiques au matériau final. Souvent ces ions dopants sont plus grands que les ions lesquels ils remplacent dans la structure cristalline ce qui peut mener vers une ségrégation vers les défauts ou leur accommodation est plus aisée. La ségrégation aux interfaces a été investigué pour des dopant d'intérêt industriel dans l'alumine ainsi que l'oxyde de zinc et utilisant la minimisation d'énergie et les modèles microstructuraux pour aider la comparaison avec l'expérience. Les résultats montrent une tendance générale de ségrégation aux surfaces et moins forte aux joints de grains, malgré des différences marqués entre les différent interfaces. Un résultat clé est l'effet homogénéisateur du magnésium sur la microstructure par sa capacité de réduire la largeur de la distribution des énergies interfaciales, ce qui mène à des grains plus equiaxes dû à une croissance isotrope.

Des calculs de ségrégation des ions luminescents de néodyme dans les céramiques YAG pour des applications laser montrent une accumulation des dopants aux joints de grain ou ils ne contribuent plus à l'effet laser et diffractent la lumière par un petit changement local du coefficient de diffraction. En utilisant des modèles microstruc-

turaux il a été montré que la proportion de dopants aux joints de grains augmente quand la taille des grains diminue ce qui rend les céramiques de taille nanométrique moins performant pour les lasers. D'une autre part les modèles optiques basés sur les calculs atomistiques montrent que la diffraction de lumière est plus marquée pour les tailles de grains plus grands, prédisant une meilleure transparence des céramiques de taille nano. Pour ces raisons une taille de grain optimale existe où la puissance laser et la transparence vont mener à une performance du laser optimale. Différents modèles microstructuraux ont pu être liés à différent méthodes de frittage et une meilleure performance du laser est prédite pour le frittage conventionnel que pour des nouvelles méthodes rapides comme le “spark plasma sintering” (SPS). Ce sont des résultats clés pour la compréhension du rôle des interfaces dans cette nouvelle classe de matériaux lasers et pour améliorer leur méthode de fabrication.

Les expériences et la simulations de l'autodiffusion de l'oxygène dans l'alumine ont, à ce jour, montré une grande différence. Les simulations prédisent des énergies d'activation des sauts de diffusion plus petit d'un facteur 5 que ce qui est observé en expériences. Dans cette thèse une nouvelle méthode basé sur “Metadynamics” a permis de calculer l'énergie libre d'activation de sauts individuels qui ont été utilisés dans des simulations Monte Carlo cinétiques pour calculer le coefficient de diffusion macroscopique. Le résultat clé est que les énergies d'activation des saut dominant la diffusion sont de l'ordre de ceux déterminés expérimentalement, les sauts prédit par d'autres simulation ne formant pas un réseau de diffusion continu. Le coefficient de diffusion calculé correspond bien à l'expérience. La méthode est générique et peut être appliqué à l'investigation d'une variété d'autres phénomènes de diffusion donnant ainsi des réponses à d'autres questions non résolues.

Les simulations atomistiques donnent des informations très intéressantes sur les phénomènes atomistiques locales permettant de comprendre et élucider quels processus ont lieu spontanément dans un système. Néanmoins pour des prédictions à l'échelle de temps et de l'espace expérimentale des modèles pour l'extrapolation des résultats atomistiques sont très importantes. La combinaison de ces techniques partant de la structure électronique et passant par l'atomique et l'échelle méso vers le continu dans un approche “multi échelle” semble très prometteur pour des applications en sciences de matériaux ou le but est de comprendre des observations expérimentales et de cibler les prochaines expériences clés basé sur ces connaissances.

Mots clés: Simulation atomistique, technologie des poudres, hématite, calcite, alumine, YAG

Contents

Chapter 1

Introduction

> **We must not forget that when radium was discovered no one knew that it would prove useful in hospitals. The work was one of pure science. And this is a proof that scientific work must not be considered from the point of view of the direct usefulness of it. It must be done for itself, for the beauty of science, and then there is always the chance that a scientific discovery may become like the radium a benefit for humanity.** – Marie Curie

In this chapter the structure of the remainder of the thesis will be outlined and it's goals and the purpose for undertaking such studies will be presented. This is done by giving a quick overview of a ceramic production cycle then focusing on some remaining problems therein, which will be outlined in more detail and investigated later in separate chapters. The findings of this thesis will be summarized in a concluding chapter discussing how they can help in gaining fundamental understanding of ceramic synthesis with the aim of improving the experimental production and final properties of this important class of materials with a knowledge based predictive approach using computer simulations.

Technical ceramic materials are nowadays employed in diverse and ever widening fields of application ranging from artificial joints trough household appliances to aeroplane engines. Over the last century their elaboration procedure has been continuously refined leading to today's high-tech ceramics suitable for use in extreme conditions or having very specific properties. However progress has been made in many fields of ceramic processing in a quite empirical fashion, the fundamental understanding of the processes is often still missing. Over the whole production cycle of modern ceramics, from the precipitation of the precursor powders, through shaping to sintering many fundamental questions remain unsolved. However as many of the effects in experimental systems to be studied happen at an extremely small atomic-size length-scale, experimental analysis is tremendously difficult. Atomistic simulation of these processes is thus a means of having a close look and to gain insights in the mechanisms at the atomic scale. This thesis has the ambitious goal of looking at many stages of the production cycle of a ceramic material, using various state of the art atomistic simulation techniques and making efficient use of their combination, to help elucidate several steps in the production of a ceramic material and to provide a predictive tool to improve their final properties.

In order to set the stage for what is going to follow after a very brief history of ceramic production the typical production cycle of a ceramic will be outlined, putting emphasis on the processes which are going to be investigated in this thesis. In the next chapter the simulation techniques employed will be described, followed by a detailed chapter on each of the investigated production steps. Finally general conclusions will be drawn.

1.1 Ceramics history

Ceramics are amongst the most ancient materials known to man [1], having been discovered well before metals and other transformed materials. The first ceramics were produced by firing clay-rich soil, which results in formation of a vitreous mullite phase consolidating the grains to form a solid structure. Since then and up until the mid-twentieth century ceramics have largely evolved by using higher purity raw materials (pure kaolin instead of clay) and more advanced firing cycles, resulting in pieces of higher quality and better mechanical properties. After these traditional ceramics, refractory ceramics were discovered. These are defined as ceramics which can withstand temperatures of at least 1500°C and can be composed of many classes of materials, amongst them silicates, aluminates, zirconia, carbides and nitrides. Applications of these ceramics are found in many branches of industry however mainly (almost 60%) [2] in the metal producing industry. Since the 1950s a manifold of so called technical ceramics have been developed, which are most often based on oxides, borites, nitrides and carbides and posses very specific properties such as high mechanical strength or particular electrical behavior. A remarkable feature of these materials are their tunable properties by creation of defects in the crystal structure due to variations in stoechiometry or by small additions of extrinsic elements, the so called dopants.

1.2 Ceramic production cycle

Modern ceramics are normally produced from very reactive (high specific surface area) micron sized or smaller powders, which are cast or pressed into their final form either in dry or wet conditions. The quality of the powder is immensely important for the final properties of the ceramic material, as its chemistry (impurities), particle size distribution and state of agglomeration dictate the quality of the packing in the green body (the unfired piece) and consequently the properties of the final sintered ceramic.

In the following the important steps in the ceramic production will be outlined, starting with powder synthesis and passing via colloidal stability and doping to sintering. Shaping, which would be situated between colloidal stability/doping and sintering is only mentioned very briefly as the present work does not directly look at aspects related to this step. For the other production steps special emphasis is put on aspects being modeled during the remainder of this thesis. The state of the art will be given in the introduction of each separate chapter and here only a very general scheme of interest is presented.

1.2.1 Powder synthesis

The first step in the successful production of a ceramic is the controlled production of a powder having the required composition as well as a morphology, particle size and physical characteristics suitable for the chosen processing route. Powders can be produced by a variety of methods being either top-down such as milling of natural raw materials or bottom-up such as reactions between solid reactants or most commonly precipitation from solution.

Chapters 3 and 4 in this thesis are concerned with growth modifications molecular and macromolecular additives induce on ceramic powders grown from solution. An understanding of how these species can affect the growth and the resulting morphology of a powder is thus of great importance in this thesis. Therefore after outlining the first steps in precipitation, which are creation of a supersaturation and nucleation, the focus will be put first on growth and morphology development without additives followed by a description of how growth modifiers influence these processes.

Supersaturation

The supersaturation S is defined the ratio ($S = C/C_{SL}$) of the actual concentration (C) to the solubility limit (C_{SL}) of a species in solution [1, 2]. If the concentration of a species is beyond it's solubility limit, the supersaturation will be larger than one. Supersaturated solutions are in a metastable state since the amount of species in solution cannot be accommodated in a thermodynamically stable way and the system will tent to energetically more stable states, which happens most often by nucleation of solid phases due to aggregation of the species in solution.

From an atomistic point of view a solution can be seen as solvated species in their coordination shell of water molecules migrating under the action of temperature through the remaining water molecules. The contact rate of the solvated species will depend on their spatial separation, which depends on concentration as well as their speed, which depends on the temperature. By playing on these variables one can thus increase the number of collisions. At supersaturation the number of collisions is sufficiently high to give the solvated species the chance to aggregate in groups of two or more. The formation of these so called clusters is the first step towards nucleation and depends besides the collision rate also on the “sticking efficiency” or attachment kinetics, which are different for each species.

Nucleation

When solvated species collide they can aggregate and remain aggregated if the sum of interfacial and volume free energy (equation 1.1) of the resulting cluster is smaller than the one of the species alone [2], which means that the change in free energy with the cluster size $\Delta G(r)$ is negative.

$$\begin{aligned}\Delta G(r) &= \Delta G_{\text{volume}}(r) + \Delta G_{\text{surface}}(r) \\ &= -\frac{V(r)}{V_m} k_B T ln\left(S\right) + \gamma A(r) \\ &= -\frac{\beta_V r^3}{V_m} k_B T ln\left(S\right) + \gamma \beta_A r^2 \qquad (1.1)\end{aligned}$$

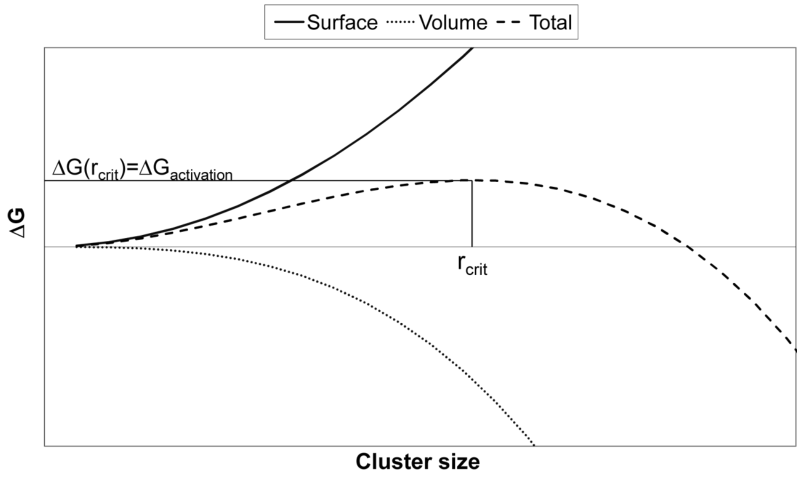

Figure 1.1: The interfacial and volume free energy variation as a function of the cluster size. The resulting total free energy change will present a maximum at the critical radius, which corresponds to the activation energy for nucleation.

Where V is the volume of the cluster, A it's surface, V_m the molecular volume of the growth unit (species in solution), k_B Boltzmann's constant, T the temperature and S the supersaturation. β_V and β_A are geometry factors for general particles, which for the special case of a sphere would be $\beta_V = \frac{4}{3}\pi$ and $\beta_A = 4\pi$. The surface free energy will follow a quadratic curve whereas the volume energy will follow a negative (since the formation of the solid phase frees energy) cubic law as shown in figure 1.1. By differentiating (equation 1.2), the maximum on the free energy variation curve can be found, which gives the critical radius r_{crit} (equation 1.3) from which onwards the cluster will reduce it's energy by attachment of further species.

$$\frac{d\Delta G(r)}{dr} = -\frac{3\beta_V r^2}{V_m} k_B T ln(S) + 2\gamma\beta_A r = 0 \tag{1.2}$$

$$\Rightarrow r_{\text{crit}} = \frac{2\gamma\beta_A V_m}{3\beta_V k_B T ln(S)} \tag{1.3}$$

The nucleation rate J can be written as a function of a system dependent rate constant J_{max}, and the activation energy for the formation of the critical nucleus $\Delta G(r_{\text{crit}})$ as given by the Arrhenius type relation in equation 1.4 [2].

$$J = J_{\text{max}} exp\left(-\frac{\Delta G\left(r_{\text{crit}}\right)}{k_B T}\right) \tag{1.4}$$

The nucleation theory presented so far is valid in solution without presence of any other solid and is commonly referred to as homogeneous nucleation. It can however be seen from equation 1.1 that the balance of free energies can be influenced by other means than the supersaturation. Since solid/solid interfaces are generally less energetic than solid/liquid interfaces, for species attaching to an existing solid, γ will be smaller and as a result the activation energy is reduced, making this event more likely. If the existing solid is different from the precipitating material (i.e. reactor walls, dust) one speaks about heterogeneous nucleation, whereas in the case of attachment to already precipitated particles the term secondary nucleation is used.

Heterogeneous nucleation is the predominant mechanism at low supersaturations since the activation energy associated with homogeneous nucleation is high. However once a certain degree of supersaturation is reached, homogeneous nucleation everywhere in solution will take place due to the high number of collisions. This sort of homogeneous nucleation will lead to a rapid decrease of supersaturation and thus many nuclei, whereas heterogeneous nucleation will result in relatively few nuclei.

Growth

Depending on the degree of supersaturation, different growth mechanisms may come into play [2]. At low supersaturation, growth units will attach the to surfaces of the relatively few and therefore isolated nuclei. This will result in unagglomerated single crystalline particles. At high supersaturation, a lot of nuclei form, growing rapidly accompanied by a sharp decrease in supersaturation. The result will be a lot of particles, which can agglomerate, resulting in polycrystalline particles. Here the first case is more interesting and will thus be further outlined.

The incorporation of a growth unit (ion, molecule) coming from the solution [1, 3] is usually assumed to take place by diffusion of the growth unit from the solution to the surface, followed by adsorption to the surface. The growth unit will loose it's hydration shell during this process and be in an energetically not very favorable position on a flat surface. It will thus migrate on the surface to a step, where it's energy is lowered due to the presence of additional bonds. Diffusion along the step to a kink site will allow the formation of more bonds and is thus energetically ever more favorable. This process is schematically shown in figure 1.2.

When there are no energetically favorable sites such as steps, the growth unit will have to remain on the flat surface and if it clusters together with other growth units also arriving on the flat surface, a stable island may form similarly to the nucleation theory outlined above. Such a surface nucleus can then serve to generate a new step on a surface. The same is true for kink creation along a step.

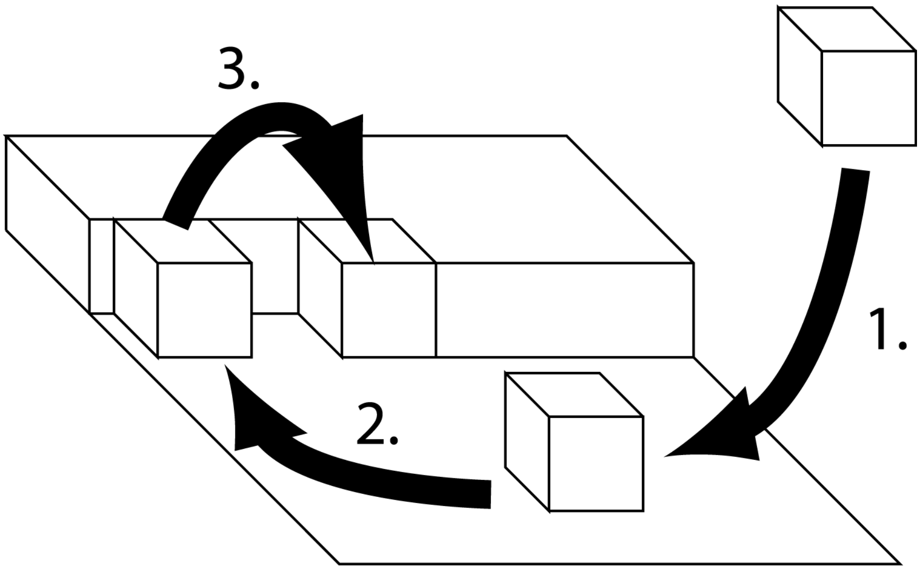

Figure 1.2: Schematic view of growth at a surface step. 1) the growth unit adsorbs on the surface, 2) migrates to a step and then 3) along that step to a kink site.

Morphology development

One generally differentiates between morphologies being dominated by thermodynamics or by kinetics [1, 3]. In the thermodynamically dominated case, which occurs only at very low supersaturations or during dissolution/reprecipitation experiments, the crystal shape is described by the classical Wulff construction [4]. This geometric/energetic construction will satisfy the minimum energy condition (equation 1.5) and is based on the fact that each crystallographic surface will have a certain normal vector as well a certain energy. If one plots for each normal direction a vector of length l as given by equation 1.6 then the inner envelope of all points is the Wulff shape. This is schematically shown for a two dimensional case in figure 1.3.

$$\sum_i \gamma_i A_i = min \tag{1.5}$$

$$\frac{\gamma_1}{l_1} = \frac{\gamma_2}{l_2} = \cdots = \frac{\gamma_i}{l_i} = const \tag{1.6}$$

For the case of crystals a theory by Donnay and Harker [5] predicts that surfaces with low Miller indices are likely to have low surface energies. It is therefore a common practice in atomistic simulation to calculate the surface energies of a certain number of low index surfaces and to create the Wulff construction based only on these surfaces and their symmetric equivalents. In the case where a morphologically important surface is missing in the set of surfaces, this will inevitably lead to incorrect results, the choice of surface directions thus being very important.

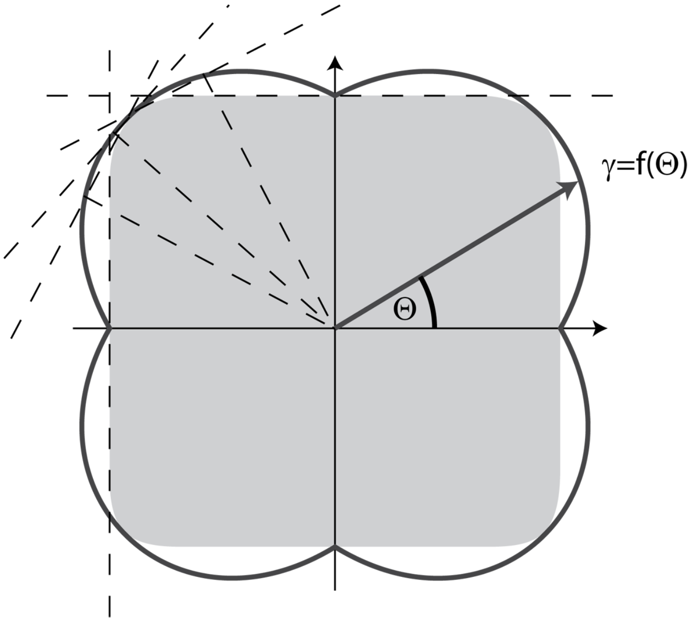

Figure 1.3: Schematic presentation of the Wulff construction in 2 dimensions. The thick black line represents a polar plot of the surface energy. On this plot are drawn in every point the normals to the line connecting it to the origin (thin dashed lines). The smallest area formed by this ensemble of lines is the equilibrium shape of the crystal, which is shown in gray.

When growth is dominated by kinetics, the morphology is best predicted by the so called growth morphology. This is usually the case for precipitated crystals especially when high supersaturations are used, which often produces nano-scale crystals. This model assumes the crystal to be composed of a set of faces, growing at different rates. The faster a face grows, the less it will be present in the morphology. This phenomenon known as outgrowth or overlapping [3] is illustrated in figure 1.4. It can be seen that faster growing faces will gradually disappear by reduction of their surface area due to the slower growth rate of the surrounding faces.

Computationally the growth rate of a surface is assumed to be proportional to it's attachment energy [6]. This energy is determined as the interaction energy of a stoichiometric monolayer of crystal at the surface with the rest of the crystal [7].

Action of growth modifiers

During the growth phase modification of many of the powders properties is possible. Such properties can be the morphology, the specific surface area (particle size) and the state of agglomeration all of which will be looked at in chapters 3 and 4 of this thesis. A manifold of growth modifying or growth inhibiting species are known for many industrially relevant or natural systems [8, 9, 10] as well as in medicine

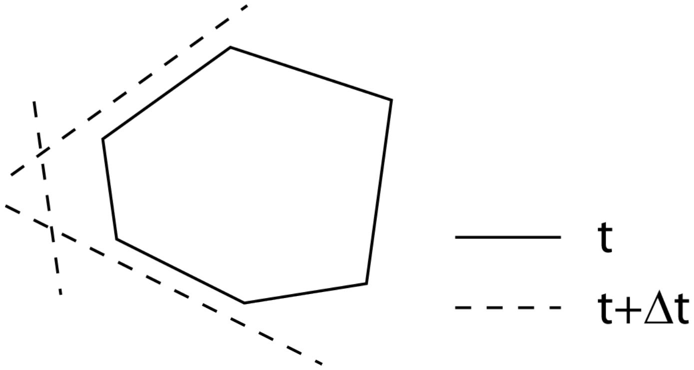

Figure 1.4: Schematic presentation of outgrowth. The particle surfaces at two instants t and $t + \Delta t$ are presented. It can be seen that one fast and two slow growing surfaces are present, the surface area of the fast one is getting smaller and will eventually disappear.

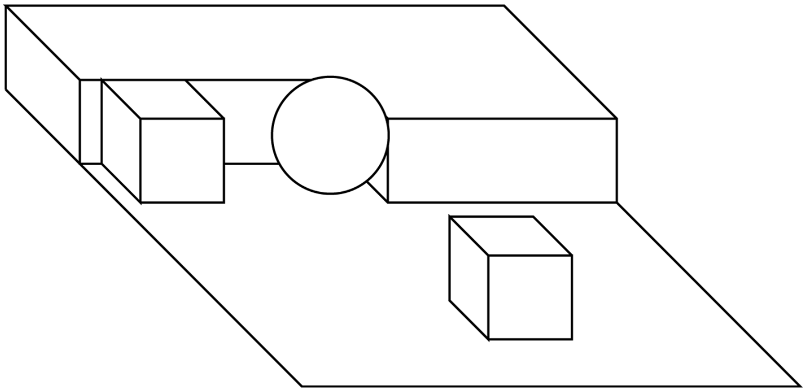

Figure 1.5: Blocking of a kink site by a growth modifier (sphere). The growth units can thus attach only to the step or the surface.

for the prevention of kidney stones [11, 12]. These species can be ionic [13, 14, 8], molecular [8, 15] and macromolecular [16, 17]. Depending on the growth mechanism and rate, growth modifiers can act in multiple ways. On one hand, for a growth morphology (kinetically dominated), it is possible that a growth modifier such as an ion or molecule can bind to growth sites (steps, kinks) on the particle surface (figure 1.5), thus forcing the system to form new nuclei on steps or the surface, which takes time due to the nucleation energy barrier involved. The affinity of the modifier for a certain site will depend on the precipitate crystallography and a selectivity may be observed, which will result in slowing growth on certain surfaces by blocking many of the growth sites thereon. Slower growing surfaces will then have a higher tendency to appear in growth morphologies as discussed above.

On the other hand for thermodynamically dominated equilibrium morphologies, the following reasoning can be applied. A surface represents an under-coordinated environment, where certain atoms are missing bonds as shown in figure 1.6a. A

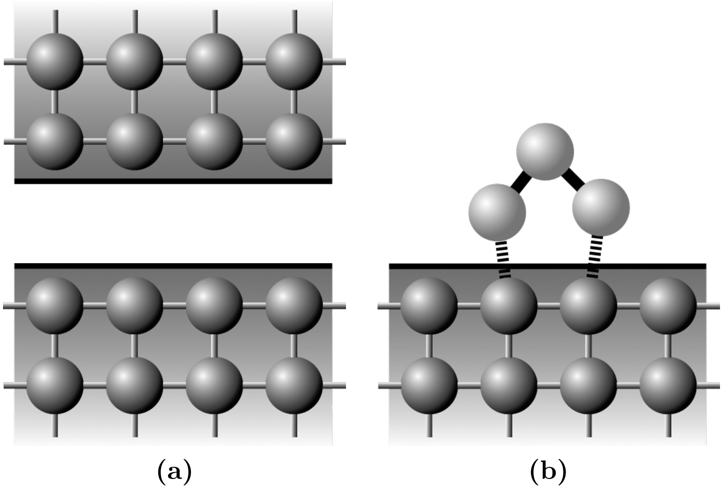

Figure 1.6: (a) Surface are undercoordinated environments, some atoms, missing bonds, which results in the surface energy; (b) additives may bind to surface atoms thus decreasing the surface energy;

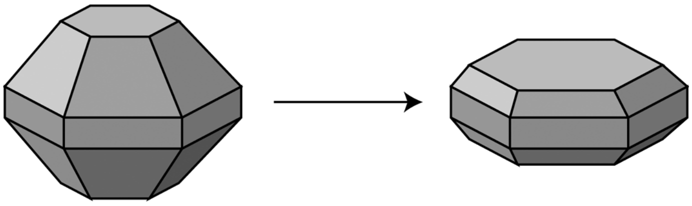

Figure 1.7: Estimated change in morphology when the hexagonal basal plane lowers it's surface energy, by the attachment of an additive.

growth-modifying additive may bind to a surface and form bonds with some of these atoms (figure 1.6b), which will as a result reduce the surface energy and make a surface appear more frequently in the morphology as shown schematically in figure 1.7. Again if an additive binds selectively to certain surfaces due to their atomic geometry and topology, these surfaces will appear in the morphology in higher proportions.

The presence of an additive will however not only have an influence on the particle morphology. If a sufficient number of growth sites is blocked, the particle size and as a result the specific surface area will be changed as well. The amount of additive can thus be used to tune the particle size and if agglomeration occurs also the nanostructuration of a powder. Different additives may show different affinities for a certain material, giving a higher modifying effect for one additive than for another.

Computational methods enable researchers to study the surface and attachment energies and thus the morphologies of powders. It is also possible to calculate the energetics associated with additive binding and thus to get an idea of the affinities of certain additives for certain crystal faces. This information will enable a knowledge based crystal design, due to the selective use of additives and even additive mixtures.

The shape of particles could be modified as wanted in order to obtain particles suitable for a certain application as will be shown in chapter 3. The adsorption energy of an additives can be used to sample promising growth modifiers for a certain crystal system, as done in chapter 4.

1.2.2 Colloidal stability

When powders are precipitated in presence of molecular additives, these may form a layer at the particle surface, which prevents particle agglomeration. This is the case for calcite in presence of polycarboxylates, a system which will be investigated in more detail in chapter 4. Therefore an overview of interparticle forces will be given to show the importance of these polymers in preventing agglomeration of particles. Since the measurement of these forces is very difficult, a theoretical assessment of their magnitude is of great help. In order to evaluate the interparticle potentials in colloidal suspensions the software Hamaker (available at http://ltp.epfl.ch/page65254.html) has been developed during this thesis. It was used to calculate all interaction potentials shown below.

Particles in suspension normally interact by a combination of attractive dispersion forces and repulsive forces. The repulsive forces can be both electrostatic (charged surfaces) or steric (adsorbed molecules or macromolecules). The amplitude of these forces as a function of distance will determine if particles in suspension agglomerate or not. The forces depend on the particle and the dispersion medium as will be seen from the parameters appearing in the equations below.

The dispersion force results from the interactions of oscillating dipoles and can be be described by different models, some of which take into account retardation, which is a phenomenon describing the fact that at large distances the interactions between dipoles decay faster than at short distances. This is related to the fact that the electromagnetic waves of interaction between two particles travel at the speed of light. If the distance is large enough that the thermal motion altered the dipole configuration of a first particle by the time the response of a second particle to the first particle's previous dipole state is received, the interaction between the two particle will experience a lag time. The classical non-retarded interaction potential $V_{\text{non retarded}}$ developed by Hamaker [18] is given by equation 1.7 for the general case

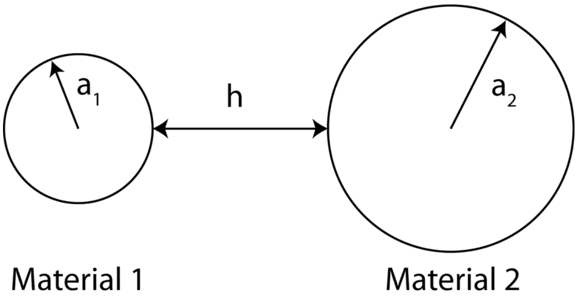

Figure 1.8: Schematic view of two spheres of radii a_1 and a_2 as well as material 1 and material 2 respectively, which are at a surface-surface distance h.

of particles of different size and material as shown in figure 1.8.

$$V_{\text{non retarded}}(h) = -\frac{\sqrt{A_{H1} \cdot A_{H2}}}{6} \cdot \left[\frac{2a_1a_2}{h^2 + 2a_1h + 2a_2h} + \frac{2a_1a_2}{h^2 + 2a_1h + 2a_2h + 4a_1a_2} + ln\left(\frac{h^2 + 2a_1h + 2a_2h}{h^2 + 2a_1h + 2a_2h + 4a_1a_2}\right)\right] \tag{1.7}$$

Here A_{H1} and A_{H2} are the Hamaker constants of particle 1 and particle 2 in the suspension medium respectively, h is the surface-surface distance of the particles and a_1 and a_2 are their radii. Hamaker constants are dependent on the powder material and the dispersion medium and can calculated from spectral measurements [19, 20]. For many materials/media combinations Hamaker constants can be found tabulated [21].

There are many models taking into account the effect of retardation. Here the approaches of Vincent [22] (equation 1.8) and Gregory [23] (equation 1.10) are given

Table 1.1: The validity of the different models as a function of particle size

Model	Size Range
Vincent	<10nm
Non Retarded	10-100nm
Gregory	>100nm

in their most general form for spheres of different radii and materials.

$$\begin{aligned} V_{\text{Vincent}}(h) = & -\frac{\sqrt{A_{H1}\cdot A_{H2}}}{12}\cdot\left\{a\left[\frac{y}{u}+\frac{y}{u+y}+2ln\left(\frac{u}{u+y}\right)\right]\right. \\ & \left.+\frac{8ba_1^2}{a_1+a_2+h}\cdot\left]2y+(2u+y)\cdot ln\left(\frac{u}{u+y}\right)\right]\right\} \end{aligned} \tag{1.8}$$

$$\begin{aligned} a = & 1.01 \\ \lambda = & 100\cdot 10^{-9} \\ b = & 0.14\frac{2\pi}{\lambda} \\ x = & \frac{h}{2a_1} \\ y = & \frac{a_1}{a_2} \\ u = & x^2+xy+x \end{aligned} \tag{1.9}$$

$$V_{\text{Gregory}}(h) = -\frac{\sqrt{A_{H1}\cdot A_{H2}}\cdot a_1a_2}{6h(a_1+a_2)}\cdot\left[1-\frac{bh}{\lambda}\cdot ln\left(1.0+\frac{\lambda}{bh}\right)\right] \tag{1.10}$$

$$\begin{aligned} b = & 5.32 \\ \lambda = & 100\cdot 10^{-9} \end{aligned}$$

Figure 1.9 gives a comparison of the three models for spherical alumina particles with an equal radius of 300nm (particle diameter 600nm). It can be seen that the fact of including retardation makes curves decay quicker. The validity of the different approaches has been evaluated by comparison with experiment [24] and table 1.1 gives the size ranges for which the equations best approximate experimental results.

As the particles will show the same average surface charge density there will be a repulsive electrostatic force between them. The potential giving rise to this force is usually described by the model of Hogg, Healy and Fuerstenau (HFF) [25], the

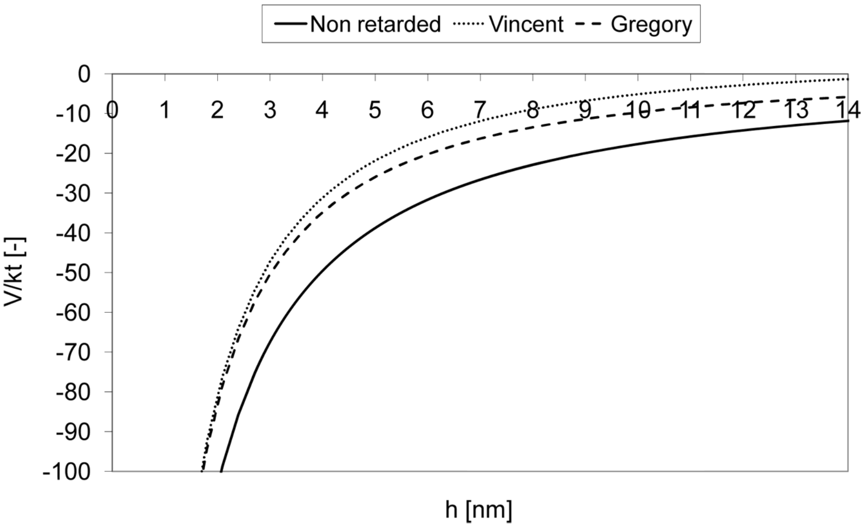

Figure 1.9: Comparison between different non-retarded and retarded dispersion interaction models. It can be seen that the interaction decays slowest with distance for the non retarded model, whereas for the two other models it decays quicker, the Vincent model being the fastest to decay to zero interaction.

formulation of which is given in equation 1.11.

$$\begin{aligned} V_{\mathrm{HFF}}(h) =& \pi\epsilon\epsilon_0 \frac{a_1 a_2}{a_1+a_2}\Big[(\Psi_1+\Psi_2)^2 ln\left(1+exp\left(-\kappa h\right)\right) \\ &+ (\Psi_1-\Psi_2)^2 ln\left(1-exp\left(-\kappa h\right)\right)\Big] \qquad (1.11)\\ \kappa^{-1} =& \sqrt{\frac{\epsilon\epsilon_0 kT}{2e^2 I_c N_A}} \qquad (1.12)\\ I_c =& \frac{1}{2}\sum_i c_i z_i^2 \qquad (1.13)\\ \Psi =& \zeta exp\left(\kappa d_s\right) \qquad (1.14) \end{aligned}$$

The parameters coming into play in these equations are the surface potentials Ψ which are obtained from the measurable ζ potential via the approximate equation 1.14. Also appearing is the inverse of the Debye length κ (equation 1.12), which in turn is based on the ionic strength (equation 1.13) of the suspending medium I_c. ϵ is the dielectric constant of the suspending medium, e the electron charge, z_i the valence of the ions in the dispersion medium and N_A Avogadro's constant. d_s is the distance from the surface where the zeta potential is measured, which is commonly fixed at 0.5nm.

The shape of a HHF potential for 600nm alumina particles in a 0.01M HNO_3 solution having a zeta potential of 30mv is shown in figure 1.10.

If macromolecular additives are used, they will if adsorbed onto the surface also

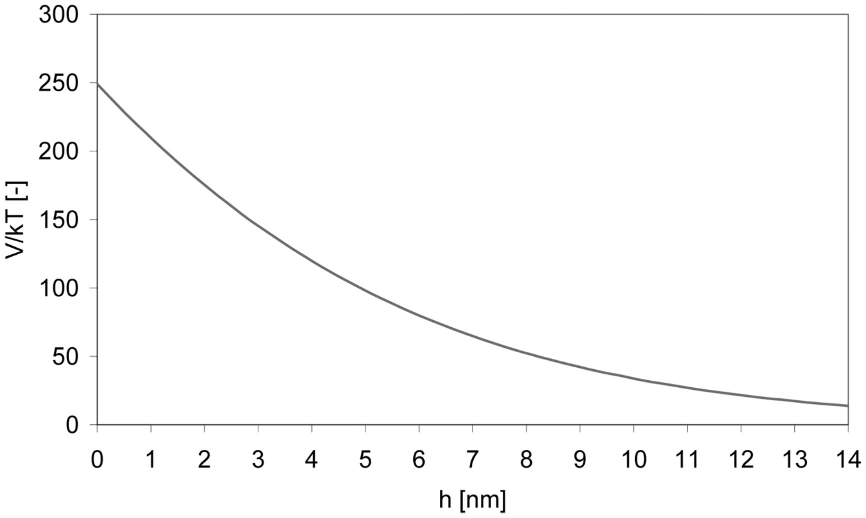

Figure 1.10: The electrostatic interaction potential as given the Hogg-Healy-Fuerstenau model.

influence the inter-particle interactions by forming a steric barrier, which prevents particles from approaching and forming agglomerates as is schematically shown in figure 1.11. The macromolecule can be a homopolymer, a block-copolymer or a polyelectrolyte with ionisable functional groups, often carboxylate groups.

The exact adsorption conformation of the additive depends on many factors such as the degree of dissociation of polyelectrolyte functional groups (dependent on pH), the arrangement of functional groups, the hydrophobicity/hydrophilicity of the backbone and specific interactions between atoms in the molecule and the powder surface. The conformation of the additive on the surface will result in short ranged (for a flat adsorption) or longer ranged (for an upright adsorption) steric repulsion forces [26]. The force functions (differentiated potentials) for some of the configurations given in figure 1.12 are given in equations 1.15 [27], 1.16 [28] and 1.17 [29]. It is assumed that for a brush the polymer chains are constrained by their neighbors due to a relatively close inter-chain spacing, whereas for the mushroom configuration, the chains are unconstrained.

$$F_{\text{pancake}}(h) = \frac{2\pi akT}{V_3}\Phi_2^2\left(0.5-\xi\right)\left(h-2\delta\right) \tag{1.15}$$

$$F_{\text{mushroom}}(h) = \frac{6\pi akT}{5s^2}\left[\left(\frac{2\delta}{h}\right)^{\frac{5}{3}}-1\right] \tag{1.16}$$

$$F_{\text{brush}}(h) = \frac{8\pi a\delta kT}{35s^3}\left[7\left(\frac{2\delta}{h}\right)+5\left(\frac{h}{2\delta}\right)^{\frac{7}{4}}-12\right] \tag{1.17}$$

Where δ is the thickness of the polymer layer, Φ_2 it's volume fraction of polymer

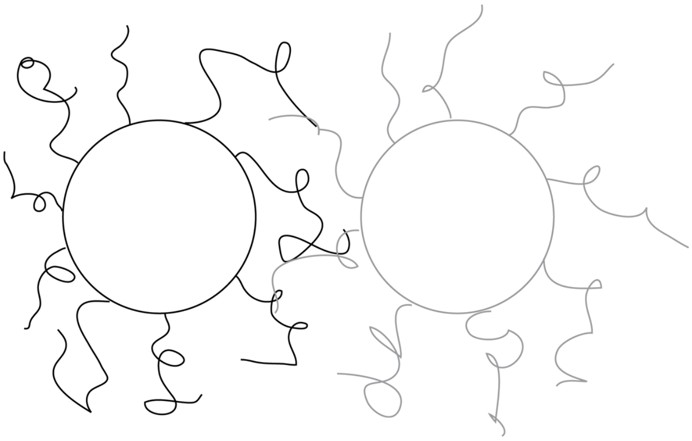

Figure 1.11: Schematic view of colloidal stabilization by means of a steric barrier formed by adsorbed polymers. The two particles can not approach further as the intervening polymer layer prevents approach.

which determines the stiffness. V_3 is the molar volume of the dispersion medium and ξ the solvent/polymer interaction parameter, which is usually fixed at 0.35 for carboxylates and s finally is the density of polymer anchoring points at the surface. Figure 1.13 shows the shape of this potential for the case of a 0.5nm pancake layer of volume fraction 0.5.

In order to observe the effect of each contribution and in particular the steric effect, which will be of interest in this thesis, the following example is illustrative. 100nm alumina particles are suspended in 0.01M HNO_3 (zeta potential 25mV), which results in the red curve shown in 1.14 being the superposition of the dispersion and electrostatic potentials. As it can be seen when two particles approach they have to overcome a potential barrier of about $9kT$ when their surface-surface distance is around 3nm. If this barrier is passed, a very deep attractive minimum is found, which will lead to agglomerate formation. An analysis of the particle kinetic energy and their contact probability as suggested by Israelachvili [30] (equations 1.18 to 1.22) can be used to estimate the required barrier for colloidal stability over a given

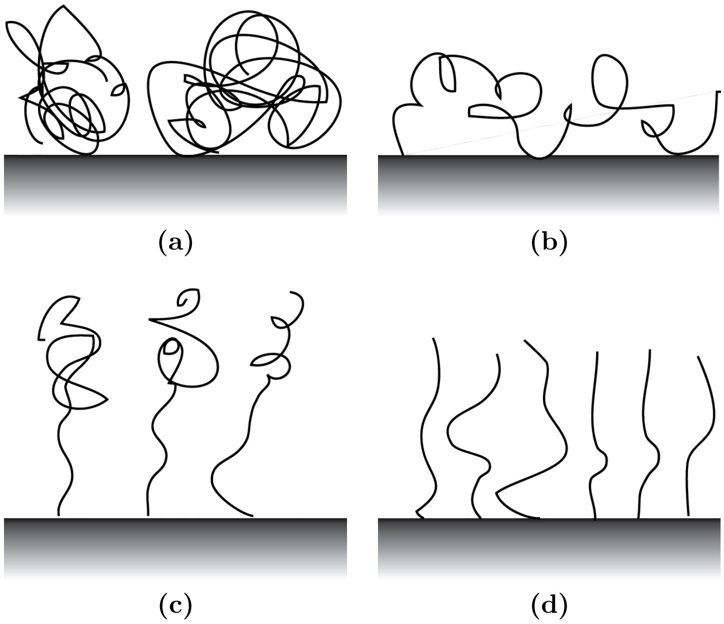

Figure 1.12: Polymer conformations according to de Gennes [26]: (a) coil; (b) pancake (train and loop); (c) mushroom; (d) brush;

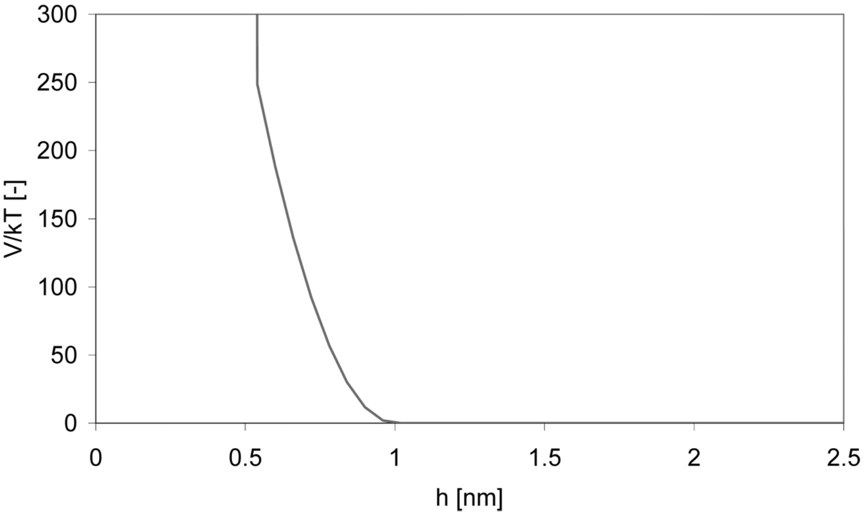

Figure 1.13: The steric repulsion potential for an adsorbed polymer layer of 0.5nm thickness, using the pancake adsorbed configuration model (equation 1.15).

time.

$$\begin{aligned}\frac{1}{2}mv^2 &= \frac{1}{2}\left(\frac{4}{3}\pi r^2 \rho_{\text{particle}}\right)v^2 \approx kT \\ \Rightarrow v &= \sqrt{\frac{kT}{\frac{2}{3}\pi r^3 \rho_{\text{particle}}}} \qquad (1.18)\end{aligned}$$

$$d_{\text{interparticle}} = \frac{1}{\sqrt[3]{N_{\text{particles}}}} \qquad (1.19)$$

$$N_{\text{particles}} = \frac{m_{\text{particles}} \cdot 0.01c_{\%\text{wt}} \cdot \rho_{\text{medium}}}{m_{\text{particles}} \cdot \frac{4}{3}\pi r^3 \cdot \rho_{\text{particle}}} = \frac{0.01c_{\%\text{wt}} \cdot \rho_{\text{medium}}}{\frac{4}{3}\pi r^3 \cdot \rho_{\text{particle}}} \qquad (1.20)$$

$$N_{\text{collisions}} = \frac{1}{\Delta t} = \frac{1}{\frac{d}{v}} = \frac{v}{d} \qquad (1.21)$$

$$\begin{aligned}\tau_{\text{collision}} &= \frac{1}{tN_{\text{collisions}}} = exp\left(-\frac{\Delta V}{kT}\right) \\ \Rightarrow \frac{\Delta V}{kT} &= -ln\left(\frac{1}{tN_{\text{collisions}}}\right) \qquad (1.22)\end{aligned}$$

Where ρ_{particle} and ρ_{medium} are the densities of the particle and the medium respectively, r is the particle radius and v the mean particle velocity. $d_{\text{interparticle}}$ is the mean interparticle distance of $N_{\text{particles}}$ particles arranged on a regular cubic lattice. The number of collisions $N_{\text{collisions}}$ is evaluated from the spacing and the velocity. The collision rate $\tau_{\text{collision}}$ finally gives access to the required potential barrier $\frac{\Delta V}{kT}$ normalized by kT. Numerically for the case of 10%wt. alumina ($\rho_{\text{particle}} = 3.998\text{gcm}^{-3}$) in HNO_3 ($\rho_{\text{medium}} = 1.000\text{gcm}^{-3}$) shows the required barrier for a 30 minutes of colloidal stability to be around $20kT$.

This shows that the energy barrier can easily be overcome and particles will agglomerate. In order to achieve colloidal stability an adsorbed polymer layer can be introduced. The green and blue curves in figure 1.14 show the effect of a 0.5nm and 1.5nm polymer layer respectively. The 0.5nm layer results in a partial elimination of the attractive potential well, reducing it to a finite depth, which can be escaped using an external energy source (e.g. ultrasonic treatment or shear force). The 1.5nm layer completely eliminates the potential well, the particles no longer have an attractive potential and the suspension will remain stable for as long as the polymer does not degrade.

This example shows the importance of polymer adsorption on the colloidal stability of suspensions of ceramic powders during either powder synthesis or the ceramic production cycle. Factors related to the dispersion and electrostatic interactions such as the surface potential can be evaluated from measured properties such as the zeta potential and other factors such as the ionic environment can be controlled. The

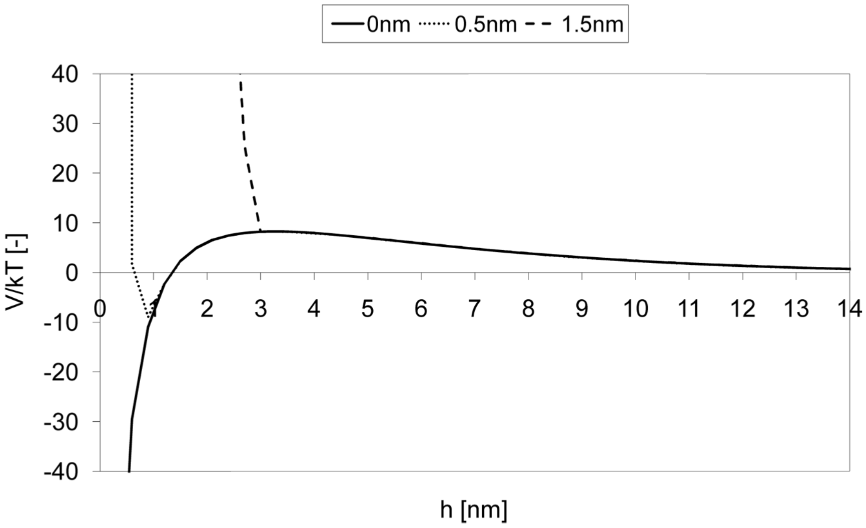

Figure 1.14: Example of the colloidal stabilization by polymer layers of 0.5 and 1.5nm thickness.

conformation of the polymer however is very hard to asses experimentally. AFM measurements are possible but very time consuming and only give data on the thickness of the polymer layer but not on the exact polymer conformation. Simulations can help to look at the adsorption of polymers and thus their conformation at the interface as will be shown for the case of polycarboxylic and polyamino acids on calcite surfaces in chapter 4. This data helps to predict the behavior of polymers at interfaces and will help in optimizing polymer admixtures on a systematic basis.

1.2.3 Doping

Ceramic materials are hardly ever sintered in their pure form as some degree of impurities or voluntarily added dopant species are inevitably present. Dopants can be added to ceramics either to help in the production (i.e. sintering agents) or to give the ceramic material specific properties (i.e. electric, mechanical). Doping is a key concept for top performance ceramics, which has to be mastered in order to fully exploit the properties ceramic materials offer. Even nowadays doping is normally optimized empirically using experimental plans with many variables, which may be feasible for simple single or double dopant systems, but gets more and more difficult with advanced multi-dopant systems. A systematic understanding of the role of dopants is a determinant factor for the targeted optimization of these systems.

In chapters 5 and 6 doping of alumina (α-Al_2O_3), zinc oxide (ZnO) and yttrium-aluminum-garnet (YAG, $Y_3Al_5O_{12}$) will be looked at. It is therefore important to know what energetic contributions affect the incorporation of dopant ions in crystal structures. In the following the concept of dopants segregation to low energy sites in ceramics will be outlined. This will allow to estimate the concentration of dopants at certain key locations in a ceramic microstructure.

Ceramics can be doped in different ways. The dopant ions can be introduced either during powder synthesis and will thus be located homogeneously within the powder particles. They can also be introduced either as solutions or solid particles prior to sintering and will then mainly be found at surfaces and thus grain boundaries, which will form during sintering. When the powder is subjected to high temperatures, be it during a calcination treatment or sintering, diffusive mechanisms in the material are activated and the dopants will start to migrate due to concentration or energy gradients. Concentration gradients will have the effect of homogenizing the dopant concentration, whereas energy gradients induced by favorable low energy dopant sites in the vicinity of vacancies, dislocations or interfaces will increase the inhomogeneity of the dopant concentration by favorable incorporation to these sites. This effect is known as dopant segregation. Inhomogeneity of dopants can have strong effects on many characteristics of the powder as well as the ceramic, amongst them the morphology [31, 32] and transport phenomena [33]. The segregation of dopant ions as well as any other species is controlled by the free energy of segregation, which is the difference in energy between two dopant incorporation sites as given by equation 1.23 for segregation from site 1 to site 2.

$$\Delta G_{\mathrm{seg}} = G_{\mathrm{site}\ 2} - G_{\mathrm{site}\ 1} \tag{1.23}$$

Where $G_{\mathrm{site}\ i}$ is the free energy of the system with a dopant on site i. If the free energy of segregation (ΔG_{seg}) is negative, dopants will accumulate on sites of type 2, depleting in course other regions of the material (site 1).

When dopants are inserted in the powder during synthesis and thus incorporated throughout the particles, their incorporation will lead to a certain variation of free energy $\Delta G_{\mathrm{bulk}}^{\mathrm{dopant}}$ when far from any interface or other defects such as a vacancy or dislocation. Sites near interfaces may be more favorable to dopant incorporation, for example if the dopant ion has a larger ionic radius than the host ion (e.g. Al substituted by Y), which will lead to a gain in energy (negative ΔG_{seg}) as given in equation 1.24.

$$\Delta G_{\mathrm{seg}} = G_{\mathrm{interface}} - G_{\mathrm{bulk}} < 0 \tag{1.24}$$

The dopant concentration resulting of this segregation is given by the statistical mechanics model of Mackrodt and Tasker [34] as shown in equation 1.25.

$$\frac{x_s}{x_b} = exp\left[-\frac{\Delta G_{\text{seg}} + x_s\left(x_s+1\right)\frac{dG_{\text{seg}}}{dx_s}}{kT}\right] \tag{1.25}$$

Where x_s and x_b are the cationic dopant fraction at the surface and in the bulk respectively. In this expression the term $x_s\left(x_s+1\right)\frac{dG_{\text{seg}}}{dx_s}$ takes into account the solute interaction at the interface. At low interfacial dopant concentrations when this interaction can be neglected $\left(\frac{dG_{\text{seg}}}{dx_s}=0\right)$ the equation can be simplified to equation 1.26.

$$\frac{x_s}{x_b} = exp\left[-\frac{\Delta G_{\text{seg}}}{kT}\right] \tag{1.26}$$

The fractions x_s and x_b are accessible to experiment by methods such as Auger electron spectroscopy (AES), X-ray photoelectron spectroscopy (XPS, ESCA) or energy-dispersive x-ray spectroscopy in scanning transmission electron microscopy (STEM-EDX). The measurement of these cationic ratios allows the calculation of the free energy of segregation [35].

Since the change in energy will only be sensed by ions in close proximity (1nm) to the surface, the gain in energy due to segregation ΔG_{seg} can be assumed to lower the energy of the surface and thus affect the surface energy according to equation 1.27.

$$\gamma_{\text{doped}} = \gamma_{\text{undoped}} + \frac{\Delta G_{\text{seg}}}{A} \tag{1.27}$$

Where A is the mean interface area per dopant ion (inverse of the interfacial concentration). This means that the presence of dopants can influence interfacial energies which will result in changes of the Wulff shape (section 1.2.1) for powders and the shape of grains in a ceramic. The presence of elongated grains [36] for some ceramic/dopant systems can be associated with this effect.

The free energy of segregation can be formulated for the case of multiple dopant ions as the concentration dependent free energy of segregation $\Delta G_{\text{seg}}(n)$ as given by equation 1.28.

$$\Delta G_{\text{seg}}(n) = G^{\text{doped}}_{\text{interface}}(n) - G^{\text{doped}}_{\text{interface}}(n-1) - \Delta G^{\text{dopant}}_{\text{bulk}} \tag{1.28}$$

Where n is the number of dopant ions, $G^{\text{doped}}_{\text{interface}}(n)$ the energy contained in the interface doped with n dopants and $\Delta G^{\text{dopant}}_{\text{bulk}}$ the energy for incorporation of the dopant ion in the infinite and otherwise perfect crystal. This difference in free energy gives the driving force for segregation of the nth dopant ion from the bulk to the interface.

When ceramics are doped by a solid state mixing route, the dopants are often inserted in form of minerals of the dopant ions and then ball milled in order to obtain a good mixture. However in that case there will still be particles of dopant oxides mixed with particles of the ceramic and not a solid solution at the atomic level. In this case an equilibrium between this second phase and the ceramic material is established and the exchange reaction (equation 1.29) taking place being the dissolution of a dopant ion coming from the dopant oxide into the ceramic material by substitution of a host ion.

$$\text{undoped} + \text{dopant} \Longrightarrow \text{doped} + \text{host ion} \tag{1.29}$$

The dopant will be coming from its stable mineral and the host ion can be considered to be found either in its stable mineral or to remain in the host phase. The change in free energy for this reaction is the free energy of solution which can be expressed as given by equation 1.30.

$$\Delta G_{\text{sol}}(n) = G^{\text{doped}}_{\text{interface}}(n) + nG_{\text{host ion/mineral}} - \left(G^{\text{undoped}}_{\text{interface}} - nG_{\text{dopant ion/mineral}}\right) \tag{1.30}$$

Where $G_{\text{host ion/mineral}}$ and $G_{\text{dopant ion/mineral}}$ are the energies per host ion and dopant ion in their stable minerals respectively and $G^{\text{undoped}}_{\text{interface}}$ the energy contained in the undoped structure. Similar to equation 1.27 the change in interfacial energy in this case can be written as given by equation 1.31.

$$\gamma_{\text{doped}} = \gamma_{\text{undoped}} + \frac{\Delta G_{\text{sol}}}{A} \tag{1.31}$$

While ΔG_{seg} gives a measure to what extent dopants are located at the interface rather than in the bulk, ΔG_{sol} expresses the probability of an ion to be found in a second phase or as a solid solution in a certain portion (i.e. interface in the present case) of the host material. Simulations can thus predict the location of dopants, be it in the bulk, second phase or at interfaces and predict the equilibria associated with the exchange reactions between these different sites. Since experimental atomic-scale resolution techniques are still very difficult to use, simulations can help in understanding the location and thus the role a dopant plays either during sintering or as a functional part of the ceramic. This knowledge can enable experimentalists to better design and use dopant systems in order to obtain the desired properties of the final ceramic piece.

1.2.4 Shaping and binder burn-out

In the ceramic production cycle shaping and binder burn-out are the next steps. As the present thesis does not deal with aspects related to these production phases, they will be treated only very briefly.

The main goal during this phase is to obtain a powder compact, the so called green body, as homogeneous and dense as possible and particle packing is thus a key aspect. Agglomerated powders have a poorer compaction behavior leading to less dense green bodies, the higher porosity of which is harder to close during sintering. The optimal packing density for monodisperse spheres is 64% of the theoretical density by random close packing [2]. Usually densities of about 60% are obtained for commercial ceramic powders [37]. One generally distinguishes between two main paths for ceramic shaping, either dry or wet. During wet shaping colloidal stability aspects as discussed above become important. Also important when in presence of a liquid is the drying of the green body, as differential and/or too rapid drying rates may lead to crack formation. The powder can then be brought into the desired shape by a multitude of methods based on casting and pressing [2].

For both the dry and wet path one can add a series of additives to reduce the interparticle friction as well as the one with the mold walls. For ceramic shaping by injection molding the ceramic powders are usually embedded at high volume fractions into a polymer matrix. These usually organic additives have however to be eliminated prior to sintering which is known as the binder burn-out. During this burn-out phase the green bodies are kept at moderate temperature (slightly above the decomposition temperature of the additives) and the gases resulting from their decomposition are evacuated by diffusion in the porous network in between the particles.

1.2.5 Sintering

Sintering is the step by which the green body is consolidated and densified. This is achieved by a thermal treatment at high temperature. Depending on the temperature with respect to the fusion temperature of the material one distinguishes between solid phase sintering ($T < T_f$) and liquid phase sintering ($T > T_f$) where T_f is the lowest fusion temperature in the system (i.e. eutectic if present). In liquid phase sintering transport phenomena are governed by diffusion in the liquid phase. This type of sintering will not be discussed further in the present context and the following discussions are related to solid phase sintering only.

The driving force for sintering is the reduction of the excess surface energy, which can take place either by a reduction of the relative surface area due to merging of particles (coalescence) or by the formation of solid/solid interfaces (grain boundaries) instead of the more energetic solid/gas interfaces (surfaces). This is followed by growth of the grains, which further reduces the excess interfacial energy. Surface curvatures induce a further driving force for sintering by compression of matter below convex parts of the surface as given by the Laplace law [2]. This compression will result in a reduction of the number of vacancies, whereas below a concave surface an excess in vacancies will be found due to stretching of the lattice. This concentration gradient $\left(\frac{dc}{dx}\right)$ of vacancies results in a flux of vacancies from the high to the low concentration regions as described by Fick's first law (equation 1.32).

$$J = -D\frac{dc}{dx} \tag{1.32}$$

Where J is the resulting flux, D is the diffusion coefficient, which depends on the diffusing species and the medium in which diffusion takes place. The diffusion coefficient is also a function of temperature as given by equation 1.33.

$$D = D_0 exp\left(-\frac{Q}{kT}\right) \tag{1.33}$$

Where Q is the activation energy which depends on the diffusion mechanism (vacancy or interstitial diffusion) as well as the diffusion path as discussed in the following paragraph.

Diffusion in a granular structure can take place by different paths (figure 1.15). All transport mechanisms shown will bring matter to the necks about to be formed, consolidating the ceramic. However for densification to occur, the matter has to come from inside the solid, be it from the bulk of the grains or from an already formed solid/solid interface (mechanisms 4, 5 and 6 in figure 1.15).

In general bulk diffusion has the highest activation energy, followed in decreasing order by grain boundary and surface diffusion. Vapor phase diffusion has the lowest activation energy and is thus activated at lower temperatures than the other processes.

Solid phase sintering is generally admitted to take place in three stages [2]. During the first stage neck formation between the powder particles is observed, which can lead to a slight densification if densifying transport mechanism are active. This stage is considered finished when the neck radii attain about half of the particle radii. During the intermediate state the porosity is still open and present in the

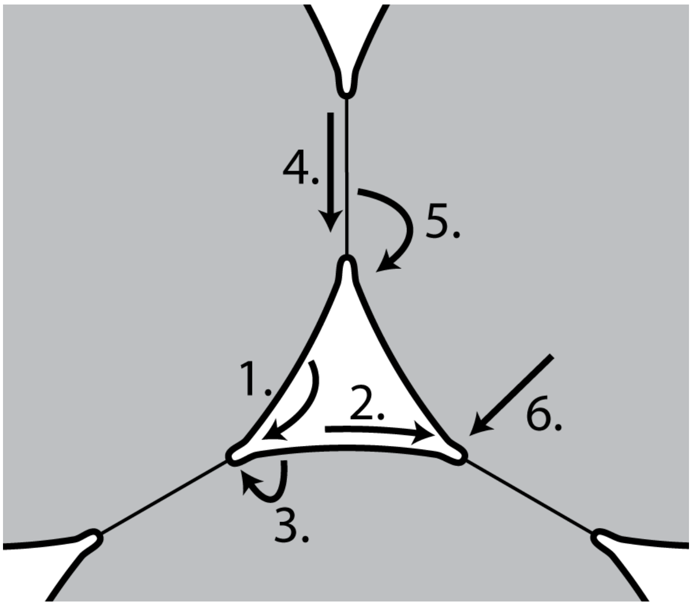

Figure 1.15: Schematic view of the different possible diffusion paths during sintering: 1. Vapor phase transport, 2. Surface diffusion, 3. Volume diffusion from surface, 4. Grain boundary diffusion, 5. Volume diffusion from grain boundary and 6. Volume diffusion. Redrawn based on [2].

form of channels along the edges of polyhedral grains. The main mechanism active during this stage is the diffusion of matter along the grain boundaries to the pores, leading to a densification of the piece. The intermediate stage is generally said to end when the porosity begins to be closed. During the final stage the porosity is closed and active transport mechanisms are thus grain boundary and volume diffusion. Pores will start to be isolated at triple points. However as the final sintering stage is usually accompanied by grain growth (grain boundary migration) the pores may dissociate from the boundaries and be found in the volume of the grains. This type of intragranular porosity is a lot harder to close than intergranular one as the necessary bulk diffusion is a lot slower than grain boundary diffusion.

Larger grains will grow to the detriment of smaller ones. This is due to the grain boundary curvature, which will results in a compression of matter in the smaller grain and an expansion in the larger grain. Under the influence of this pressure gradient atoms will migrate from the small to the large grain. Macroscopically these jumps will result in grain boundary migration and finally disappearance of the smaller grains. Dopants present in the ceramic will influence all these processes as will be discussed in the following section.

Role of dopants during sintering

As it has been seen above in the section dedicated to doping, the presence of dopant ions can affect interfacial energies. As was discussed the driving force for sintering is the reduction of the excess surface energy in the system. If dopants segregate, the interfacial energies may either homogenize or become accentuated, depending on the segregation behavior of a certain dopant. More homogeneous surface energies will result in surfaces having approximately the same excess surface energy and thus the same reactivity. If certain surfaces remain of very high energy, they will have a higher tendency to reduce this energy and thus be more reactive. Inhomogeneity of surface energies may lead to anisotropic grain growth and consequently elongated grains. It is thus important to know if a dopant will segregate homogeneously to all surfaces and result in a surface energy distribution with a small variance or if a dopant will preferentially lower the energy of certain surfaces only.

A next aspect linked to different dopants are the defects which are created accompanying their incorporation. If an isovalent dopant with a reasonably small size misfit is incorporated it is usually substituted for a host ion without creation of further defects. For the case of oxides the incorporation of an aliovalent dopants requires the creation of oxygen vacancies, cation interstitials or clustering with oppositely charged ions (impurity or other dopants) in the structure. One example is the case of magnesium in alumina, which is known to cluster with silicon impurity ions [38] or induce oxygen vacancies. Along the same line aluminum ions incorporated in zinc oxide are either accompanied by the creation of zinc vacancies or oxygen interstitials to compensate the difference in charge. When magnesium segregates to grain boundaries, the high local increase in the number of oxygen vacancies may result in an enhanced grain boundary diffusion [39, 40].

A final role of dopants is their interaction with grain boundary motion [2]. Since the dopants segregate to the grain boundary there is an attractive potential between the boundary and the dopant ions. At equilibrium the dopants will be located symmetrically on both sides of the boundary plane. As discussed above grain boundary migration is associated with diffusive jumps of atoms from one side of the boundary plane to the other or in other words a short displacement and the adoption of the crystal orientation of the new grain. If segregated dopants are associated to the boundary via the attractive potential a displacement of the boundary will produce an asymmetry of the dopant distribution around the boundary, which will have to be equilibrated by diffusion of the dopant ions. The transport mechanism associated with grain boundary motion will have a lower activation energy than the one for

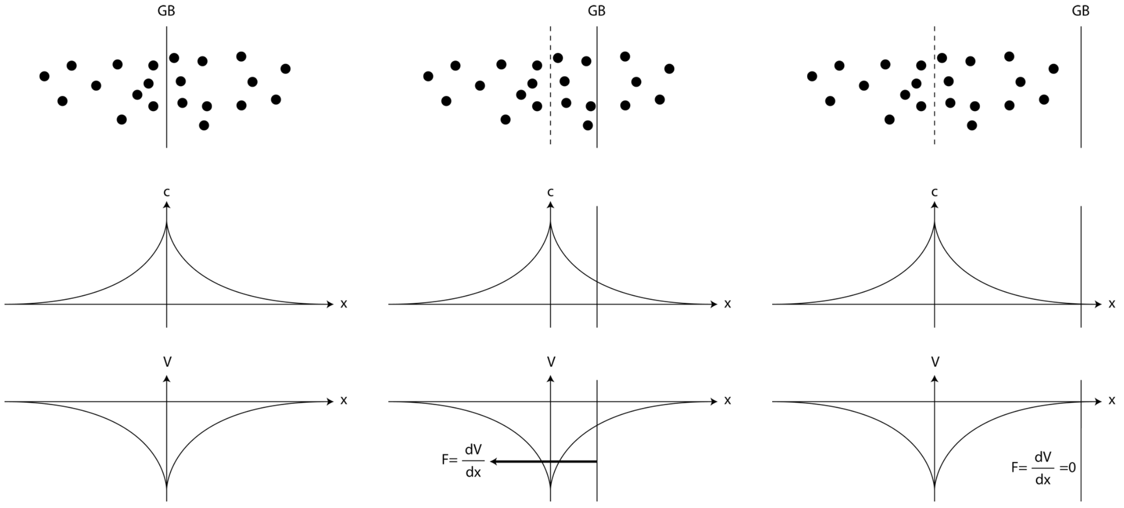

(a) (b) (c)

Figure 1.16: Illustration of the solute drag mechanism. (a) Equilibrium distribution of dopants around the grain boundary shown by the concentration profile as well as the resulting attractive potential. The grain boundary is located in the potential well. (b) The grain boundary migrates faster than the dopants can diffuse. The result is a shift in the potential, which will exert a dragging force on the grain boundary. (c) When grain boundary motion is fast enough the boundary may detach from the dopant cloud and the dragging force is lost.

diffusion of dopant ions, which will result in the dopant cloud lagging behind the grain boundary. The attractive potential will then exert a dragging force on the grain boundary, slowing it's motion, which is known as the solute drag mechanism. At slow grain boundary migration speeds the dopant ions can diffuse fast enough to stay within the range of the attractive potential. However at higher speeds it is possible that the grain boundary dissociates from the dopant cloud and the solute drag effect is lost. This process is illustrated in figure 1.16, where subfigure 1.16a shows the equilibrium case of the dopant distribution around the grain boundary, the concentration profile as well as the resulting attractive potential. Subfigure 1.16b shows the case where the grain boundary started moving and the attractive potential exerts a dragging force on the boundary. Subfigure 1.16c finally shows the case where the boundary escaped the attractive potential and no drag force is present.

Another aspect related to grain growth and dopants is that when grains grow, the relative grain boundary area will decrease with increasing grain size. If the dopant cloud moves along with the grain boundaries, which is the usual case for oxide ceramics during normal grain growth, this means a decrease of the number of favorable sites for dopants at the diminishing grain boundaries and dopants thus have to be accommodated elsewhere. The low solubility of most dopant species in common oxide ceramics determines the amount of dopants than can migrate to the bulk as the grain boundary area decreases. This will lead to a gradual increase in the grain boundary dopant concentration, which can eventually reach a supersaturation concentration and consequently result in precipitation of second phase along the grain boundary or at triple points. A critical grain size can be modeled [41] to follow a law of the type given in equation 1.34.

$$d_{\mathrm{crit}} = \frac{A \cdot L_{\mathrm{GB}}}{c_{\mathrm{bulk}} - L_{\mathrm{bulk}}} \tag{1.34}$$

Where c_{bulk} is nominal dopant concentration, L_{GB} and L_{bulk} are the solubility limits in the grain boundary and the bulk respectively and A is a constant dependent on the grain size. As a result there will be three domains with different behavior depending on whether the dopants can be accommodated in the bulk or at the grain boundary and in that case either as segregated dopants in solid solution or as a second phase if their concentration is over-critic. This behavior is illustrated in the microstructural map (figure 1.17), which gives for the case of magnesium and yttrium doped α-alumina the critical concentration as a function of grain size and dopant concentration.

Once this critical concentration is passed and precipitation occurs, the precipitates will also interact with the grain boundary motion and thus grain growth. This is due to the so called Zener pinning effect by which the precipitate will induce a local change in grain boundary curvature, which results in a drag force exerted on the grain boundary by the inclusion.

As shown in the above discussion dopants and their location in a microstructure play a critical role during sintering. The possibilities simulations offer for dopant segregation have been discussed above and results related to sintering will be shown for alumina and YAG in chapters 5 and 6 respectively. Also important during sintering are transport phenomena in order to understand grain growth and densification, which in turn will determine the microstructure evolution. Diffusion was for a long time difficult to investigate computationally as the time scales linked to these processes are well beyond those normally accessible to molecular dynamics. Recently so called time accelerated techniques allow the study of diffusion in solids, which will permit to better understand these processes as well as to extract diffusion coefficients (as shown in chapter 7), which are, along with surface energies, key parameters for larger scale simulations by methods such as discreet element modeling (DEM) or finite element modeling (FEM). The combination of the approaches will result in very powerful multi-scale simulations of sintering.

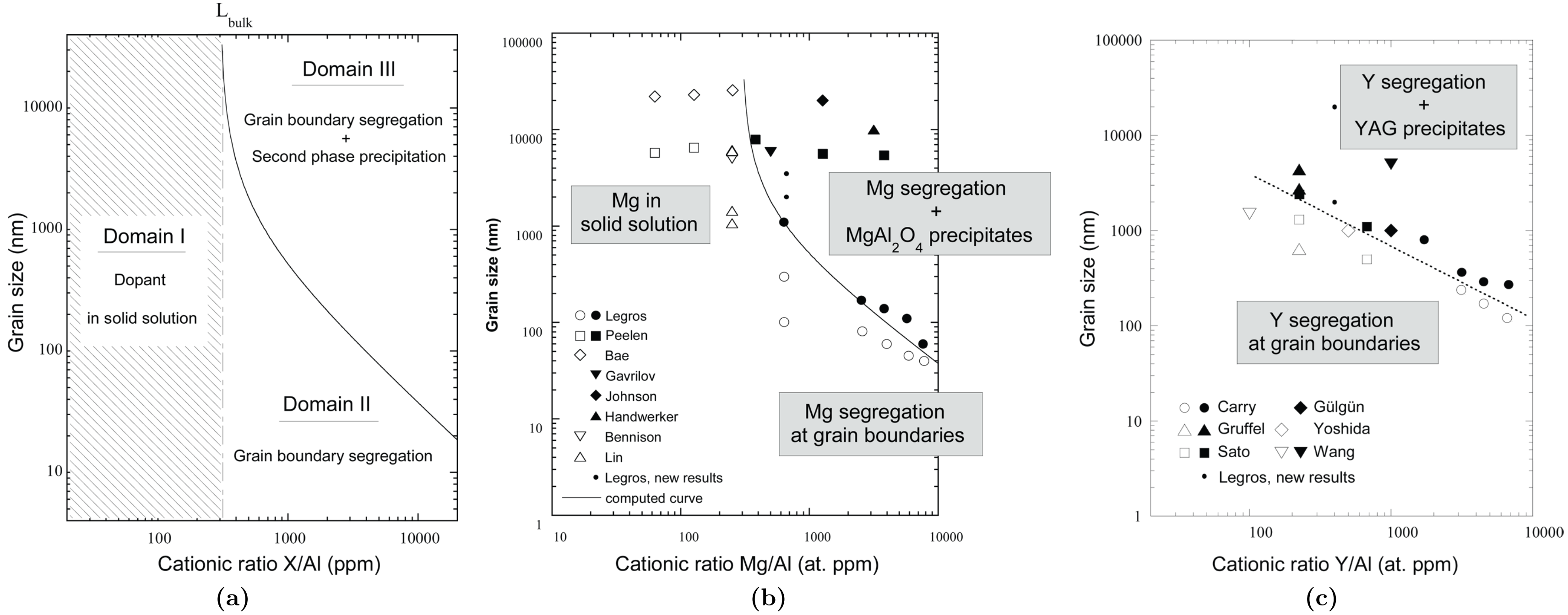

Figure 1.17: Microstructural map extracted from [41] (empty symbols represent data points without precipitation, whereas for filled ones precipitates were detected): (a) Generic example showing the three domains as a function of the bulk solubility limit (L_{bulk}), the grain size and dopant concentration. (b) Example for magnesium in α-alumina, where all three domains can be seen. The model reproduces experimental results very well. (c) Example for yttrium in α-alumina. Due to the low solubility only domains II and III are visible. The model again reproduces the experimental results very well. For references to the experimental data points please refer to [41]

1.3 Interest of simulation

As it can be seen from the above discussion many steps of the production of a ceramic material are linked to phenomena at surfaces and interfaces, which are the result of atomic scale mechanisms. Due to the atomic origin their investigation using experimental techniques is very difficult because of resolution limits of the available analysis methods.

However in order to optimize ceramic materials precise control over all production steps starting from powder production and ending with sintering has to be gained. In the past the understanding and finally control has been reached trough experimental optimization, which for todays complex nano-scale systems is often very difficult to carry out. For this reason optimization based on knowledge obtained from theoretical methods is an emerging novel way to accelerate material development.

In this thesis atomistic simulation techniques will be employed to investigate some of the key steps in a ceramic production, which are the modification of the morphology of powders grown from solution, the effect of different additives on the growth and steric stabilization as well as the segregation of dopants to powder surfaces and to interfaces in ceramics along with resulting morphology changes. Dopant segregation may also alter the functional properties of a ceramic material, which will be shown for the case of Nd:YAG ceramics. Finally transport mechanism in ceramics will be looked at in order to better understand the sintering behavior of these materials.

Bibliography

[1] T.A. Ring. *Fundamentals of Ceramic Powder Processing and Synthesis.* Academic Press, San Diego, 1996.

[2] J.-M. Haussonne, C. Carry, P. Bowen, and J. Barton. *Céramiques et Verres*, volume 16 of *Traité des Matériaux.* Presses Polytechniques et Universitaires Romandes, Lausanne, 2005.

[3] A.S. Myerson. *Molecular Modeling Applications in Crystallization.* Cambridge University Press, Cambridge, 1999.

[4] G. Wulff. On the question of speed of growth and dissolution of crystal surfaces. *Zeitschrift für Krystallographie und Mineralogie*, 34(5-6):449–530, 1901.

[5] J. D. H. Donnay and D. Harker. A new law of crystal morphology extending the law of bravais. *American Mineralogist*, 22(5):446–467, 1937.

[6] P. Hartman and P. Bennema. The attachment energy as a habit controlling factor: I. theoretical considerations. *Journal of Crystal Growth*, 49(1):145–156, 1980.

[7] J. D. Gale and A. L. Rohl. The general utility lattice program (GULP). *Molecular Simulation*, 29(5):291–341, 2003.

[8] W. J. Benton, I. R. Collins, I. M. Grimsey, G. M. Parkinson, and S. A. Rodger. Nucleation, growth and inhibition of barium sulfate-controlled modification with organic and inorganic additives. *Faraday Discussions*, 95:281–297, 1993.

[9] N. G. Harmandas, E. N. Fernandez, and P. G. Koutsoukos. Crystal growth of pyrite in aqueous solutions. inhibition by organophosphorus compounds. *Langmuir*, 14(5):1250–1255, 1998.

[10] L. M. Qi, H. Cölfen, and M. Antonietti. Control of barite morphology by double-hydrophilic block copolymers. *Chemistry of Materials*, 12(8):2392–2403, 2000.

[11] L. J. Wang, S. R. Qiu, W. Zachowicz, X. Y. Guan, J. J. DeYoreo, G. H. Nancollas, and J. R. Hoyer. Modulation of calcium oxalate crystallization by linear aspartic acid-rich peptides. *Langmuir*, 22(17):7279–7285, 2006.

[12] L. J. Wang, W. Zhang, S. R. Qiu, W. J. Zachowicz, X. Y. Guan, R. K. Tang, J. R. Hoyer, J. J. De Yoreo, and G. H. Nancollas. Inhibition of calcium oxalate monohydrate crystallization by the combination of citrate and osteopontin. *Journal of Crystal Growth*, 291(1):160–165, 2006.

[13] K. Zeppenfeld. Experimental study of the influence of some divalent and trivalent metal cations on nucleation and growth of $CaCO_3$. *Chemie Der Erde-Geochemistry*, 63(3):264–280, 2003.

[14] Y. Zhu, P. Demilie, P. Davoine, Th. Cartage, and M.-P. Delplancke-Ogletree. Influence of calcium ions on the crystallization of sodium bicarbonate. *Journal of Crystal Growth*, 275(1-2):e1333–e1339, 2005.

[15] F. Jones, M. Mocerino, M. I. Ogden, A. Oliveira, and G. M. Parkinson. Bio-inspired calix[4]arene additives for crystal growth modification of inorganic materials. *Crystal Growth & Design*, 5(6):2336–2343, 2005.

[16] J. J. De Yoreo and P. M. Dove. Shaping crystals with biomolecules. *Science*, 306(5700):1301–1302, 2004.

[17] J. Rieger, T. Frechen, G. Cox, W. Heckmann, C. Schmidt, and J. Thieme. Precursor structures in the crystallization/precipitation processes of $CaCO_3$ and control of particle formation by polyelectrolytes. *Faraday Discussions*, 136:265–277, 2007.

[18] H. C. Hamaker. The London - van der Waals attraction between spherical particles. *Physica*, 4(10):1058–1072, 1937.

[19] R. H. French, R. M. Cannon, L. K. Denoyer, and Y. M. Chiang. Full spectral calculation of nonretarded hamaker constants for ceramic systems from interband transition strengths. *Solid State Ionics*, 75:13–33, 1995.

[20] R. H. French. Origins and applications of London dispersion forces and Hamaker constants in ceramics. *Journal of the American Ceramic Society*, 83(9):2117–2146, 2000.

[21] L. Bergström. Hamaker constants of inorganic materials. *Advances in Colloid and Interface Science*, 70:125–169, 1997.

[22] B. Vincent. The van der Waals attraction between colloid particles having adsorbed layers: II. calculation of interaction curves. *Journal of Colloid and Interface Science*, 42(2):270–285, 1973.

[23] J. Gregory. Approximate expressions for retarded van der Waals interaction. *Journal of Colloid and Interface Science*, 83(1):138–145, 1981.

[24] W. R. Bowen and F. Jenner. The calculation of dispersion forces for engineering applications. *Advances in Colloid and Interface Science*, 56:201–243, 1995.

[25] R. Hogg, T. W. Healy, and D.W. Fuerstenau. Mutual coagulation of colloidal dispersions. *Transactions of the Faraday Society*, 62:1638–1651, 1966.

[26] P. G. de Gennes. Polymers at an interface: A simpified view. *Advances in Colloid and Interface Science*, 27(3-4):189–209, 1987.

[27] L. Bergström, C. H. Schilling, and I. A. Aksay. Consolidation behavior of flocculated alumina suspensions. *Journal of the American Ceramic Society*, 75(12):3305–3314, 1992.

[28] H. G. Pedersen and L. Bergström. Forces measured between zirconia surfaces in poly(acrylic acid) solutions. *Journal of the American Ceramic Society*, 82(5):1137–1145, 1999.

[29] W. M. Sigmund, N. S. Bell, and L. Bergström. Novel powder-processing methods for advanced ceramics. *Journal of the American Ceramic Society*, 83(7):1557–1574, 2000.

[30] J. N. Israelachvili. *Intermolecular and Surface Forces.* Academic Press, San Diego, 1991.

[31] M. Kitayama and A. M. Glaeser. The Wulff shape of alumina: III. undoped alumina. *Journal of the American Ceramic Society*, 85(3):611–622, 2002.

[32] M. Kitayama and A. M. Glaeser. The wulff shape of alumina: IV. Ti^{4+}-doped alumina. *Journal of the American Ceramic Society*, 88(12):3492–3500, 2005.

[33] D. Prot, M. Le Gall, B. Lesage, A. M. Huntz, and C. Monty. Self-diffusion in α-Al_2O_3: IV. oxygen grain-boundary self-diffusion in undoped and yttria-doped alumina polycrystals. *Philosophical Magazine A*, 73(4):935–949, 1996.

[34] W. C. Mackrodt and P. W. Tasker. Segregation isotherms at the surfaces of oxides. *Journal of the American Ceramic Society*, 72(9):1576–1583, 1989.

[35] S. Baik, D. E. Fowler, J. M. Blakely, and R. Raj. Segregation of Mg to the (0001) surface of doped sapphire. *Journal of the American Ceramic Society*, 68(5):281–286, 1985.

[36] G. D. West, J. M. Perkins, and M. H. Lewis. Characterisation of fine-grained oxide ceramics. *Journal of Materials Science*, 39(22):6687–6704, 2004.

[37] G. Bernard-Granger, C. Guizard, and L. San-Miguel. Sintering behavior and optical properties of yttria. *Journal of the American Ceramic Society*, 90(9):2698–2702, 2007.

[38] C. Elsässer and T. Elsässer. Codoping and grain-boundary cosegregation of substitutional cations in α-Al_2O_3: A density-functional-theory study. *Journal of the American Ceramic Society*, 88(1):1–14, 2005.

[39] K. A. Berry and M. P. Harmer. Effect of MgO solute on microstructure development in Al_2O_3. *Journal of the American Ceramic Society*, 69(2):143–149, 1986.

[40] S. J. Bennison and M. P. Harmer. Grain-growth kinetics for alumina in the absence of a liquid-phase. *Journal of the American Ceramic Society*, 68(1):C22–C24, 1985.

[41] C. Carry, C. Legros, and P. Bowen. Grain boundary segregation and precipitation maps: application to doped alpha and gamma aluminas. Unpublished work.

Chapter 2

Computational methods

> **Although simplification is a sheer mathematical necessity, for many-body problems, there is also a more positive reason for it. What is it we really want from a theory? In the most interesting cases, what we are seeking is enlightenment, a general understanding of what is going on, a physical picture, something essentially qualitative that could be explained in relatively few words... Simplification is an art rather like that of the cartoonist who captures the key features of a familiar face in a few deft strokes to make it instantly recognizable.** – Sir Alan Cottrell

This chapter will give a description of the computational methods used in the present thesis and point out their advantages and drawbacks, leading to their choice for the respective parts of this thesis.

After introduction of the two main descriptions of energies in atomistic simulation codes, the types of simulation cells and boundary conditions will be described. Finally it will be explained which methods can be used on the basis of this description of matter. The chapter will further describe the methods used to extend the time- and length-scale usually covered by atomistic simulation methods.

2.1 Classical description of the potential energy

Classical force field methods have been used in atomistic simulations for many years and represent a well-validated approach for the description of interatomic forces. In this method forces acting between atoms are approximated by empirically fitted analytical functions, the so-called potential functions. A collection of potential functions describing one or more materials is known as a potential set in the inorganic simulation community or as a forcefield in the organic simulation community.

The derivation of these interatomic potentials is a complicated and tedious process, during which the parameters of each potential function are fitted to a set of material data, either measured experimentally or calculated from first principle methods. The input data for fitting usually contains the atomic structure and a combination of properties such as elastic constants, surface energies, dielectric and magnetic properties. In the case of ab-initio derived potentials the potential energy hypersurface is calculated in as much detail as possible and the potential functions fitted to this data. When using a potential set it is always useful to know what properties it has been fitted to as for example a certain set can give excellent results for the bulk of a material but may completely fail for surfaces, as the surface energy was not used as a fitting parameter. Also the temperature at which the properties used to fit a potential were measured limits the validity of simulations carried out at very different temperatures.

An important number of different potential functions has been developed and published so far, as almost every class of materials requires a slightly different description. Metals for example require force fields describing the effect of the delocalized electrons, whereas ionic crystals have well localized electrons and can be treated with simple pair potentials. Materials of hybrid ionic-covalent character such as carbonates or phosphates may require additional functions for the correct description of covalent bond formation resulting in specifically arranged molecular orbitals such as within the carbonate tetrahedron.

As in the present work only pure ionic solids such as oxides and mixed ionic-covalent solids such as carbonates as well as purely covalent molecules are treated, the following presentation of potential functions is limited to those found in these classes of materials, omitting for example the embedded atom method (EAM) commonly used for metals. The interactions will be classed into electrostatic, non-bonded and bonded interactions, treating polarisability of atoms last.

2.1.1 Electrostatic interactions

As ions carry a non-zero charge, there will be an electrostatic interaction between them. It can be described as a coulombic interactions of point charges as given by equation 2.1, where q_i and q_j are the respective charges, r_{ij} is the distance between the ions and ϵ_0 is the permittivity of vacuum, which is $8.8542 \cdot 10^{-12}$ [AsV^{-1}m^{-1}].

$$V_{ij} = \frac{q_i q_j}{4\pi\epsilon_0 r_{ij}} \tag{2.1}$$

Electrostatic interactions are very complicated to treat as they decay with r^{-1}, the number of interacting ions is however a function of $4\pi r^2$. It can thus be seen that conceptually the energy of these interactions will never converge with increasing distance. There exists however an approach developed by Ewald [1], applicable at charge neutrality and zero dipole, where the electrostatic energy is split into two parts after application of a Laplace transformation, one part rapidly decaying in real space and the other rapidly decaying in reciprocal space. In order to correctly evaluate the energy, the self-interaction of an ion with itself has to be subtracted. The resulting relation is given equation 2.2 and its components are given in equations 2.3 to 2.5.

$$V_{\text{coulomb}} = V_{\text{real}} + V_{\text{reciprocal}} + V_{\text{self}} \tag{2.2}$$

$$V_{\text{real}} = \frac{1}{2}\sum_{i=1}^{N}\sum_{j=1}^{N} \frac{q_i q_j}{r_{ij}} erfc\left(\eta^{\frac{1}{2}} r_{ij}\right) \tag{2.3}$$

$$V_{\text{reciprocal}} = \frac{1}{2}\sum_{i=1}^{N}\sum_{j=1}^{N}\sum_{\vec{G}} \frac{4\pi}{V} q_i q_j exp\left(i\vec{G}r_{ij}\right) \frac{exp\left(-\frac{\vec{G}^2}{4\eta}\right)}{\vec{G}^2} \tag{2.4}$$

$$V_{\text{self}} = -\sum_{i=1}^{N} q_i^2 \left(\frac{\eta}{\pi}\right)^{\frac{1}{2}} \tag{2.5}$$

In these equations $\vec{G}$ is a reciprocal lattice vector ($\vec{G} = \vec{0}$ is excluded), V the volume of the cell and η is a parameter describing the proportion of interactions treated in each of the spaces. An optimal value for η is given by 2.6 where ω is a weight parameter describing the computational cost in real space compared to reciprocal space.

$$\eta_{\text{opt}} = \left(\frac{N\omega\pi^3}{V}\right)^{\frac{1}{3}} \tag{2.6}$$

As will be shown later in the section about boundary conditions, these equations will have to be modified when applied to systems with planar periodicity such as surfaces and grain boundaries.

2.1.2 Non-bonded interactions

These interatomic forces result from Van der Waals type interactions as well as short-range interactions of the electron clouds of the atoms. They are usually described by pair potentials using the Buckingham (equation 2.7) or Lennard-Jones (equation 2.8) type potential functions.

$$V_{ij}^{\text{buckingham}}(r_{ij}) = A_{ij} e^{-\frac{r_{ij}}{\rho_{ij}}} - \frac{C_{ij}}{r_{ij}^6} \tag{2.7}$$

$$V_{ij}^{\text{lennard-jones}}(r_{ij}) = \frac{A_{ij}}{r_{ij}^m} - \frac{C_{ij}}{r_{ij}^n} \tag{2.8}$$

For the Buckingham type potential the fitted parameters are A, C and ρ. The Buckingham potential can be parametrized in two ways. In the first C is zero, which results in a purely repulsive interaction (solid line in figure 2.1) used for example in conjunction with electrostatic forces for the description of cation-oxygen interaction in oxides. If C is non-zero, an attractive contribution exists as well (dashed line in figure 2.1) which can be used to model the slightly covalent character of oxygen-oxygen interactions in oxides.

The typical shape of a Lennard-Jones potential is given in figure 2.2. The relative contribution of attractive and repulsive parts depends on the values of A and B as well as the exponents m and n, which usually are integers. Commonly used values for m and n are 12 and 6 or 9 and 6 respectively, where one speaks about 12-6 or 9-6 Lennard-Jones potentials.

2.1.3 Bonded interactions

Bonded interaction potentials are used in order to describe the presence of a chemical covalent bonds. The geometry of a molecule depends on the spacial arrangement and type of the bonding orbitals. Molecules can often be described with three basic quantities: Distances, angles and torsions. Distance potentials (figure 2.3a) describe the energy as a function of the length of a bond. However without further restriction, the bond can be freely rotated around the atoms from which the bond originates as well as rotations around the bond axis are possible at no energetic cost. In order to describe these restrictions angle and dihedral potentials are used. An angle potential (figure 2.3c) describes a relative positioning of two bonds originating from

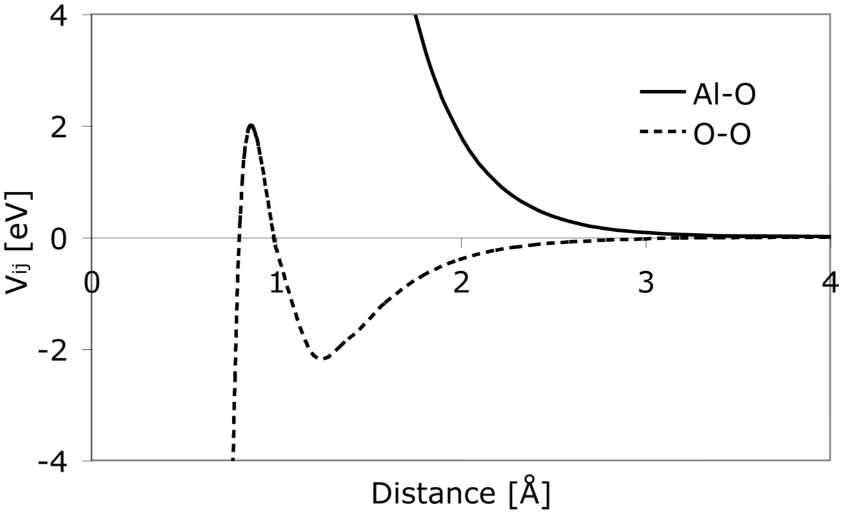

Figure 2.1: Buckingham potentials for the example α-Al_2O_3. The solid line represents the purely repulsive Al-O potential whereas the dashed line is the hybrid ionic-covalent O-O potential showing an optimal interatomic spacing.

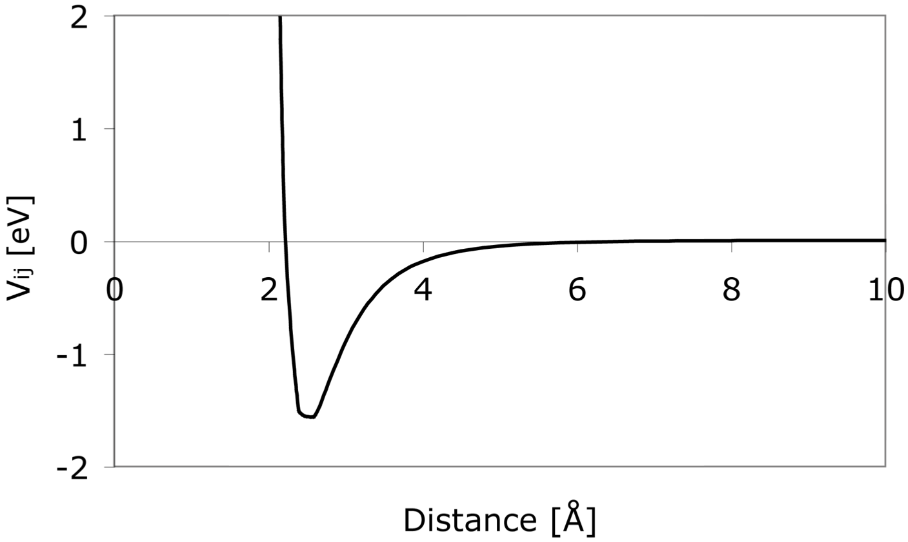

Figure 2.2: A typical shape of a Lennard-Jones type potential. One can see the repulsive and the attractive part of the function resulting in a slightly anharmonic energy well.

one atom, such as the dihedral angle in water. A torsion potential (figure 2.3e) finally describes the energetic cost of rotations around a bond axis where certain rotations are energetically more favorable than others.

The energetic increase associated with a deviation from the equilibrium value of these potentials can be described by a multitude of functions, the most common ones however being the Morse type potential (equation 2.9) for distances (figure 2.3b), a simple harmonic (equation 2.10) for the angles (figure 2.3d) as well as a periodic cosine (equation 2.11) for the torsion potentials (figure 2.3f).

$$V_{ij}^{\text{morse}}(r_{ij}) = D_{ij}[(1 - e^{-\alpha_{ij}(r_{ij} - r_{ij,0})})^2 - 1] \tag{2.9}$$

$$V_{ijk}^{\text{angle}}(\Theta_{ijk}) = \frac{1}{2}k_{ijk}(\Theta_{ijk} - \Theta_{ijk,0})^2 \tag{2.10}$$

$$V_{ijkl}^{\text{torsion}}(\Phi_{ijkl}) = k_{ijkl}(1 + cos(n_{ijkl}\Phi_{ijkl} - \Phi_{ijkl,0})) \tag{2.11}$$

The morse potential presents the big advantage of having parameters with a physical meaning. D_{ij} is the dissociation energy of the bond described by the potential, $r_{ij,0}$ is its equilibrium distance and α_{ij} describes the anharmonicity of the bond. The angle potential imposes an equilibrium angle $\Theta_{ijk,0}$ a deviation from which will penalized by a harmonic spring potential of constant k_{ijk}. The torsion potential finally is the most complicated. It describes the rotation around a bond as a function of the angle Φ_{ijkl} using the parameter n_{ijkl} in order to describe the number of oscillations within one complete revolution. The parameters m_{ijkl} and k_{ijkl} control the amount of energy required for a deviation from one of the minima, m_{ijkl} being a scaling parameter and k_{ijkl} the force constant.

2.1.4 Polarisability

Polarisability of ions is usually modeled with the core-shell model of Dick and Overhauser [2]. This model assumes an ion to be split into two parts, one known as the core, which is where the mass is located and one known as the shell, which is where the electrons are located. The sum of charges of core and shell will be the net charge of the ion. Potential interactions with other ions are applied on the shell only as they result from the electrons. In order to keep the core and shell attached to each other they are linked with a harmonic spring potential as given in equation 2.12.

$$V_{i}^{\text{spring}} = \frac{1}{2}k_{c-s,i}r_{c-s,i}^2 \tag{2.12}$$

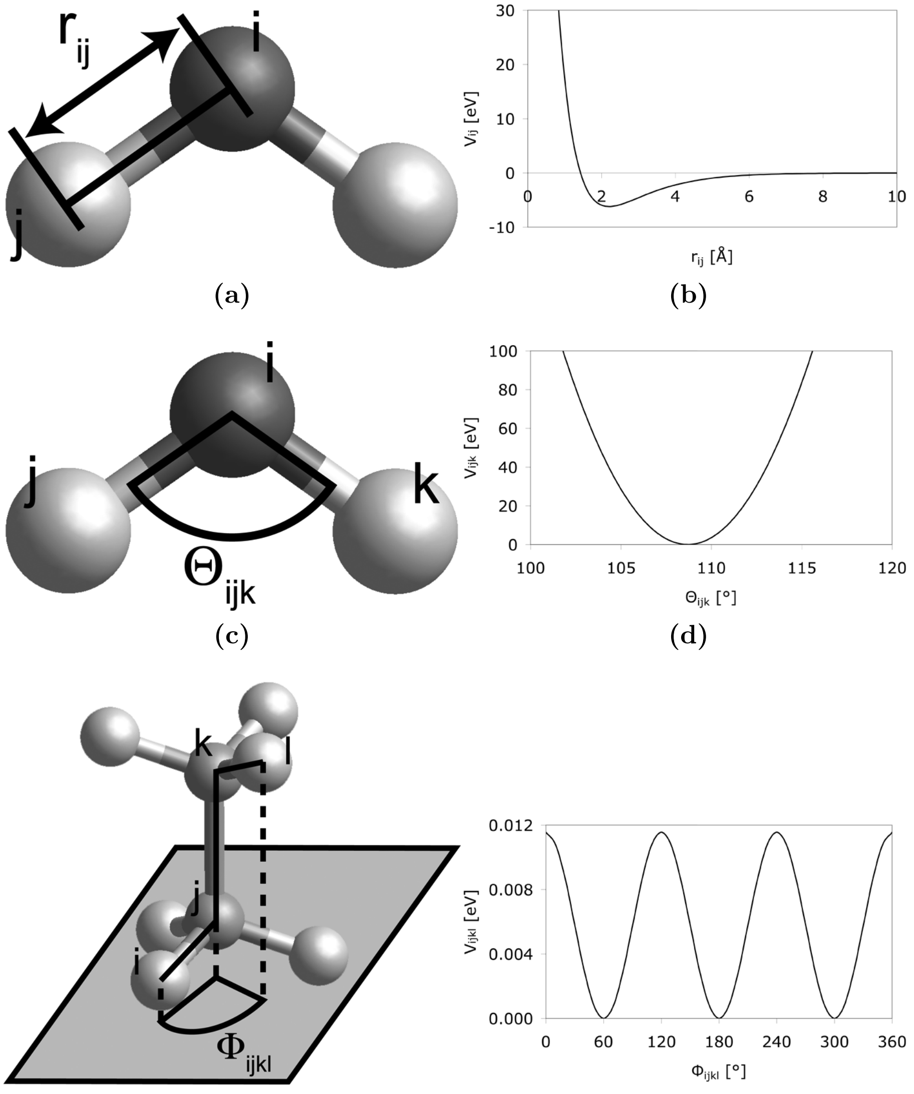

(a) (b)

(c) (d)

(e) (f)

Figure 2.3: Bonded Potentials: (a) Length defining the morse potential; (b) Shape of the morse potential; (c) Angle defining the angle potential; (d) Shape of the angle potential; (e) Angle defining the torsion potential; (f) Shape of the torsion potential;

The rigidity of the spring as given by the constant k_{c-s} determines how far the shell may move from the core (distance r_{c-s}) and thus how polarisable an ion is.

As it can be seen this model increases the computational cost significantly as the number of particles is doubled, when the core-shell model is applied to all ions in the system. In order to overcome this drawback, often only the most polarisable ions, such as oxygen, are treated with this model, considering only cores for the rest of the ions. In molecular dynamics atoms are propagated according to Newtons equation of motion as will be shown below. This approach will fail with massless particles, which is why for molecular dynamics, the shells usually carry a very small mass (usually about 0.2 a.m.u.) allowing them to follow the normal laws of motion [3]. An alternative approach [4] is to use massless shells with an energy minimization step of the shell positions performed after each molecular dynamics timestep.

A dipole moment as described by this model is only a low order ionic distortion and physically distortions of higher order appear, which may play important roles. Therefore efforts have been made do develop models, which include these contributions. In particular an extended compressible ion model (CIM) has been suggested by Wilson et al. [5, 6] which was shown to remove the ambiguity that shell models normally predict the Θ phase of alumina more stable than the α phase, leading to really transferable potential models. This is due to the fact that the negative polarization energy favors highly symmetric, charge-ordered structures, such as the α alumina phase. For cases of lesser symmetry such as low symmetry bulk phases as well as interfaces, where the symmetry is generally broken, this energetic stabilization is of lesser importance and can be considered negligible [7, 8].

2.2 Ab-initio description of the potential energy

As it has been seen in the previous section, the energy can be described using analytical potential functions with the big advantage of relatively fast calculations. The drawbacks, which are the inability to study chemical reactions directly and problems with the validity/transferability of these potential functions can be to some extent solved by using ab-initio quantum mechanical methods. The most popular amongst them being the density functional theory (DFT) method, which will be very briefly outlined in the following section.

2.2.1 Fully interacting system

The basis of this method is the solution of the time independent Schrödinger equation as given by equation 2.13 [9].

$$\hat{H}\Psi(\vec{r}^N, \vec{R}^K) = E\Psi(\vec{r}^N, \vec{R}^K) \tag{2.13}$$

Where $\hat{H}$ is the hamiltonian operator, Ψ the wave function of the N electron ($\vec{r}^N$) and K nucleus coordinates ($\vec{R}^K$). The Born-Oppenheimer approximation assumes the relatively heavy nuclei as stationary thus not having a kinetic energy and only appearing as parameters when calculating the energy of the electron system. The hamiltonian is composed of the kinetic energy ($\hat{T}$), the potential due to the nuclei ($\hat{V}_{ext}$), the electron-electron interaction ($\hat{V}_{int}$) as well as the classical interaction between nuclei (E_{II}) as given by equations 2.14 to 2.17 where lowercase indices i, j denote electrons and uppercase I nuclei.

$$\hat{H} = \hat{T} + \hat{V}_{\text{ext}} + \hat{V}_{\text{int}} + E_{II} \tag{2.14}$$

$$\hat{T} = \sum_i -\frac{\hbar}{2m_e}\nabla_i^2 \tag{2.15}$$

$$\hat{V}_{\text{ext}} = \sum_{i,I} V_I(|\vec{r}_i - \vec{R}_I|) \tag{2.16}$$

$$\hat{V}_{\text{int}} = \frac{1}{2}\sum_{i\neq j}\frac{e^2}{|\vec{r}_i - \vec{r}_j|} \tag{2.17}$$

The energy of the system is the expectation value of the hamiltonian as given in equation 2.18 where $n(\vec{r})$ is the electron density as defined by equation 2.19.

$$E = \frac{\langle\Psi|\hat{H}|\Psi\rangle}{\langle\Psi|\Psi\rangle} = \langle\hat{T}\rangle + \langle\hat{V}_{\text{int}}\rangle + \int d^3r V_{\text{ext}}(\vec{r})n(\vec{r}) + E_{II} \tag{2.18}$$

$$n(\vec{r}) = N\frac{\int d^3r_2 \dots d^3r_N |\Psi(\vec{r}, \vec{r}_2, \dots, \vec{r}_N)|^2}{\int d^3r_1 d^3r_2 \dots d^3r_N |\Psi(\vec{r}_1, \vec{r}_2, \dots, \vec{r}_N)|^2} \tag{2.19}$$

Here the electron-nucleus interaction is written as the interaction of the electron density with the external potential.

2.2.2 Density functional theory (DFT)

The formulation so far represents a very complicated many-body problem, which could not easily be solved for systems of scientific interest. The combination of two ground-breaking approaches usually referred to as the density functional theory

(DFT) however allows to transform the problem into one that can be solved. The Hohenberg-Kohn theorems [10] allows us to express the external potential as a functional of the ground state electron density. The energy can thus be written as a functional of the electron density n as given in equation 2.20

$$E = T[n] + E_{\text{int}}[n] + \int d^3r V_{\text{ext}}(\vec{r}) n(\vec{r}) + E_{II} \tag{2.20}$$

As it can be seen the kinetic energy and the electron-electron interaction are only a functional of the electron density. However this theorem alone would not allow calculations of the energy to be made unless the Kohn-Sham ansatz [11] is used, which replaces the interacting many-body system by an independent particle description of a system having the same ground state electron density. If the many-body terms can be grouped into an exchange-correlation functional of the density, the ground state density and energy of a system of interacting particles can be calculated by solving the simpler equations of the auxiliary system of non-interacting particles in an effective potential V_{eff}, the Schrödinger equation and hamiltonian of which is given equation 2.21 and 2.22 respectively.

$$\hat{H}_{\text{aux}} \Psi(\vec{r}, \vec{R}^K) = E \Psi(\vec{r}, \vec{R}^K) \tag{2.21}$$

$$\hat{H}_{\text{aux}} = T_s + \hat{V}_{\text{eff}} = -\frac{1}{2}\nabla^2 + \hat{V}_{\text{eff}} \tag{2.22}$$

The energy of such a system (equation 2.23) is defined by the kinetic energy T_s of the independent particles (equation 2.24), the interaction with the potential coming from the nuclei (V_{ext}), the classical interactions between the electrons (E_{Hartree}), the nuclei interactions (E_{II}) and the relativistic exchange-correlation energy (E_{xc}) all of which except the nuclei term are functionals of the electron density $n(\vec{r})$.

$$E = T_s[n] + \int d\vec{r} V_{\text{ext}}(\vec{r}) n(\vec{r}) + E_{\text{Hartree}}[n] + E_{II} + E_{xc}[n] \tag{2.23}$$

$$T_s = -\frac{1}{2} \sum_i < \Psi_i \left| \nabla^2 \right| \Psi_i >= \frac{1}{2} \int d^3r \left| \nabla \Psi_i (\vec{r}) \right|^2 \tag{2.24}$$

By comparing the previous total energy equations (equations 2.20 and 2.23) it can be shown that the exchange-correlation energy can be written as given by equation 2.25 showing that the exchange-correlation term includes the difference in kinetic energy between the many and single particle hamiltonians as well as the difference in electron-electron interaction between a correlated and an uncorrelated system.

$$E_{xc}[n] = \langle \hat{T} \rangle - T_s[n] + \langle \hat{V}_{\text{int}} \rangle - E_{\text{Hartree}}[n] \tag{2.25}$$

The exchange-correlation energy is defined by equation 2.26 where ϵ_{xc} is the energy of an electron at a point $\vec{r}$ which depends on the electron density $n(\vec{r})$ around that point.

$$E_{xc}[n] = \int d^3 r n(\vec{r}) \epsilon_{xc}([n], \vec{r}) \tag{2.26}$$

2.2.3 Density Functionals

The energy of a system of interacting and correlated electrons can now be calculated given an appropriate exchange and correlation functional is known. The most common functionals are the local density approximation (LDA) and the different types of generalized gradient approximations (GGA), which will be outlined briefly.

Local density approximation - LDA

The LDA is based on the assumption that solids can be approximated as being close to a homogeneous electron gas. The local exchange-correlation energy density is then the same as in a homogeneous electron gas of the same density. The total exchange-correlation energy is obtained by taking the integral over all space as given in equation 2.27;

$$E_{xc}^{\text{LDA}}[n] = \int d^3 r n(\vec{r}) \epsilon_{xc}^{\text{hom}}(n(\vec{r})) = \int d^3 r n(\vec{r}) (\epsilon_x^{\text{hom}}(n(\vec{r})) + \epsilon_c^{\text{hom}}(n(\vec{r})) \tag{2.27}$$

The actual exchange-correlation energy of the homogeneous gas is obtained by fitting to essentially correct quantum Monte Carlo (QMC) data published by Ceperley and Alder [12]. As an example of a functional the widely used Perdew-Zunger (PZ) [13] form is given in equation 2.28.

$$\epsilon_c^{\text{PZ}}(r_s) = \begin{cases} -0.0480 + 0.031 ln(r_s) - 0.0116 r_s + 0.0020 r_s ln(r_s) & r_s < 1 \\ -0.1423/(1 + 1.9529\sqrt{r_s} + 0.3334 r_s) & r_s > 1 \end{cases} \tag{2.28}$$

Where r_s is the radius of a sphere containing on average one electron which is directly dependent on the density as defined in equation 2.29.

$$r_s = \left(\frac{3}{4\pi n} \right)^{\frac{1}{3}} \tag{2.29}$$

Even if most solids are not very well described by a homogeneous electron gas, the LDA works remarkably well for many systems.

Generalized gradient approximation - GGA

The generalized gradient approximation (GGA) is based on the idea to not only including the density but also it's gradient $|\nabla n|$ in the functional, which leads to expressions for the exchange-correlation energy as given in equation 2.30.

$$E_{xc}^{\mathrm{GGA}}[n] = \int d^3 r n(\vec{r}) \epsilon_{xc}(n, |\nabla n|) = \int d^3 r n(\vec{r}) \epsilon_x^{\mathrm{hom}}(n) F_{xc}(n, |\nabla n|) \tag{2.30}$$

Where $F_{xc}(n, |\nabla n|)$ is a so called dimensionless exchange enhancement factor. There are many different forms of this exchange enhancement factor, which have been derived to satisfy different properties of exchange in electron systems. When applied to normal systems, the differences between the different GGA functionals are however very small and the exchange energy is in all cases lower than for LDA functionals. This corrects the overbinding, which is normally found in LDA calculations and generally makes results agree better with experiment.

2.2.4 Plane waves & Pseudopotentials

It was seen above that the square of the wave function is used to determine the electron density. In practice the wave function is very often expanded in plane waves as given by equation 2.31.

$$\Psi\left(\vec{r}, \vec{(R)}^K\right) = \sum_i c_i \varphi_i\left(\vec{r}\right) \tag{2.31}$$

Where φ_i is one plane wave defined by it's wave vector $\vec{G_i}$ as given in equation 2.32 and Ω is the volume of the simulation cell.

$$\varphi_i\left(\vec{r}\right) = \frac{1}{\sqrt{\Omega}} exp\left(i\vec{G_i}\vec{r}\right) \tag{2.32}$$

The number of plane waves in the expansion is determined by the maximum kinetic energy associated with the plane waves, which can be written as given by equation 2.33. One defines a cut-off value E_{cut} for the kinetic energy which then determines the wave vector up to which the plane waves will be included in the expansion (equation 2.34).

$$E_{\text{kin}} = -\frac{1}{2}\nabla^2\varphi_i\left(\vec{r}\right) = \frac{1}{2}\left|\vec{G}_i\right|\varphi_i\left(\vec{r}\right) \tag{2.33}$$

$$E_{\text{kin}} = \frac{1}{2}\left|\vec{G}_i\right| < E_{\text{cut}} \tag{2.34}$$

The number of plane waves in the expansion is of great importance as a too low number will not be able to correctly represent the wave function and thus lead to incorrect electron densities, whereas a too large number will require much more computational time and memory. The required number of plane waves is usually determined by studying the convergence of the total energy with increasing cutoff value.

Pseudopotentials are another aspect of the computational representation of the equations presented above. The idea is that since the strongly bound core electrons do not influence many properties one may replace their effect by including them in an effective potential added to the one of the core. The advantage of this approach is on one hand the reduction of the number of electrons, which will greatly accelerate calculations. However there are also advantages linked to the representation of the wave function. The atom is divided in a core and a valence region as shown in figure 2.4. The potential of the core on the core and valance electrons is shown as a red dashed line and the resulting wave function showing the tightly bound core states is drawn as a solid red line. It can be seen that the very localized core states show a lot of oscillations, which will require a large number of wave functions for a correct expansion. If the potential V is replaced by the effective potential V_{pseudo} (dashed green line), which is equivalent to the potential V in the valence region, the wave function Ψ can be replaced by the pseudo wave function Ψ_{pseudo} which is also equivalent to the normal wave function in the valence region. The pseudo wave function in the core region is a lot smoother since the discarded core states do not have be described anymore. The fact of using pseudo potentials to describe the effect of the tightly bound core electrons will thus lead to an important reduction in the number of plane waves and thus memory and computational time requirements.

2.2.5 Self-consistency

The Kohn-Sham equations are a cyclic dependent system of the density and the effective potential, which are not consistent except at the ground state. The way of solving the Kohn-Sham equations is thus to achieve self-consistency of the two quantities by an iterative solving method. This is done by an initial guess of the

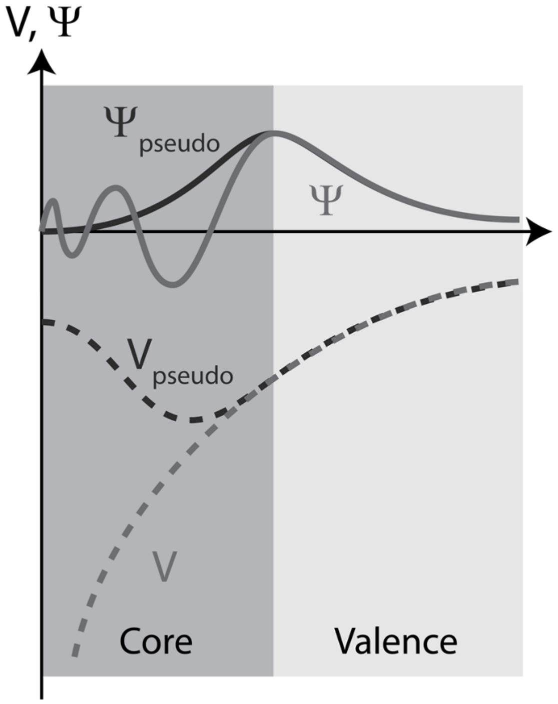

Figure 2.4: Pseudo potential and pseudo wave function

density, from which the effective potential is calculated. Next the Schrödinger like equations are solved and from the wave-function a new density can be obtained. The new density is then according to some mixing rule used for the calculation of a new effective potential and so on until convergence of the problem. The obtained potential and density at the end describe the ground state of the system.

2.3 Cell types & Boundary conditions

By considering a group of atoms without specifying any type of periodicity of the system, one would look at atoms situated in vacuum, without any interaction except with the other atoms of the group. This is often designated as an isolated cluster of atoms. However except maybe for gases this case is not realistic. For this reason, normally some sort of periodic boundary conditions are applied on the system. In the following these conditions will be presented, focusing on the ones used in this work.

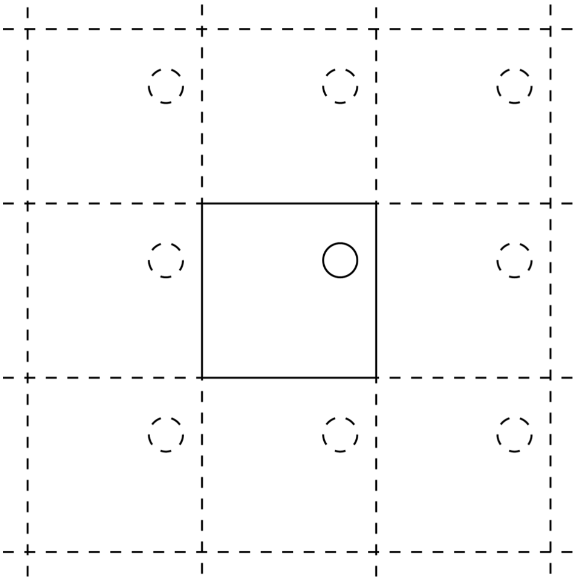

Figure 2.5: Periodic boundary conditions shown for a 2D case. The simulation box is surrounded by images of itself and atoms may interact with their own images.

2.3.1 Full 3D periodic boundary conditions

Crystals are usually described by means of a unit-cell, which is a set of three vectors, defining a volume in space, containing the atoms forming the crystal. The three vectors, also known as basis vectors, describe not only the volume and shape of unit-cell but also its periodicity in space. In a perfect crystal the same unit-cell will be found at every location in space, which is a linear combination of the basis vectors.

The simplest case is the cubic unit-cell, where all vectors are orthogonal to each other and of the same amplitude. A schematic 2D presentation of this cell type is given in figure 2.5. Other cells such as an orthorhombic box or trigonal cells are mathematically treated the same way, the choice depending on the crystal in question or for large biological systems to minimize interactions and the number of solvent molecules at the same time. For periodic boundary conditions, an atom leaving the simulation box on one side will thus reenter on the opposite side. This repetition in space also means that every atom will interact with the atoms of the periodically translated unit cells, known as images. For small cells, this can span quite a few unit-cells before interactions become negligible. For the case of electrostatic interactions, the Ewald method gives the possibility to correctly describe this energy component.

2.3.2 Unit cells and supercells

The crystallographic unit cell is good in order to describe a perfect and infinite crystal. When looking at defective crystals, with dopant or impurity contents or surfaces and interfaces the unit cell is no longer a valid description. This is due to the fact the when one would place a dopant ion in a small unit-cell and apply periodic boundary conditions, there would be a dopant in every unit cell, resulting in a very high dopant concentration and consequently dopant-dopant interactions. If one is interested in the properties of a single dopant there is the need to spatially separate the dopants far enough so as there is no interaction between them or any sort of perturbation created by them.

This can be achieved in two ways, either with supercells or by using an embedded cluster (section 2.3.6). A supercell is constructed from a basic cell by repetition of this cell l, m and n times along the 3 basis vectors of the cell. The volume of the supercell will thus be $l \cdot m \cdot n$ times the volume of the basic cell and number of atoms will be multiplied with $l \cdot m \cdot n$ as well.

2.3.3 Surface Slab

A surface slab is constructed by cutting the unit cell along the desired crystallographic plane (figure 2.6a). The atoms being cut away are reinserted in a periodic fashion, keeping the volume and the number of atoms constant as shown in figure 2.6b. The unit-cell can be cut at different depths. A different atomic surface structure will appear each time an atoms passes from one side of the cutting plane to the other. When the cutting plane passes trough a dense layer with N atoms theoretically all $2N$ permutations should be considered. However in practice this would often result in an unfeasibly large number of calculations, which is why random subsets or subsets selected based on the symmetry of the surface can be used. The surface slab is a block of matter with a thickness of d_{hkl}, which by itself does not present any physically meaningful object. It can however be used in the construction of other structures as will be seen in the following sections.

2.3.4 Vacuum Slab & Slab

A vacuum slab is one way of constructing surfaces in atomistic simulation, mainly used for the technique of molecular dynamics. It consists in repeating a simple slab n times in order to reach a thickness which allows for complete relaxation of

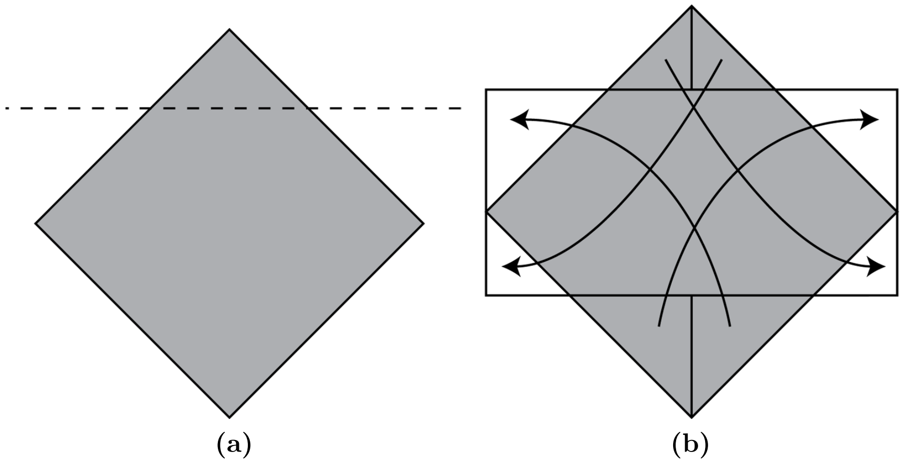

Figure 2.6: Schematic construction of a surface slab in 2D. (a) the unit cell and with cleaving plane; (b) slab-cell with the same volume. It can also be seen how matter is periodically reinserted in the cell.;

the surfaces and thus material with a bulk like characteristic in the center of the stack. A gap is then introduced in the direction perpendicular to the surface giving a separation large enough to exclude any image interactions along that direction. This setup (figure 2.7) describes a system of bulk matter exposing two surfaces in contact with a space filled with vacuum.

The same sort of setup can also be used in order to represent a system consisting of interfaces, which can be solid-solid, solid-liquid, solid-gas, or even liquid-gas by filling the gap previously created with the second material in question. In order to describe a system of a solid material in contact with a solvent like water the gap is filled to contain a number of water molecules, which will result in the correct density of water at the chosen simulation conditions.

2.3.5 Surface boundary conditions

The slab construction discussed previously has the drawback of containing two surfaces, properties calculated will thus be an average of the two surfaces and the number of atoms to be calculated is twice the number required for a single surface, which makes calculations slow. For these reasons another type of simulation cell has been invented. For this setup a slab is repeated m times in order to reach a depth where when the surface is relaxed the bottom-most atoms will see no displacement. The slab is then repeated another n times but the atom positions in this second series of slabs are held fixed. The number of slabs n is defined by the depth required to ensure negligible interaction between the atoms at the very top and the very bottom of the

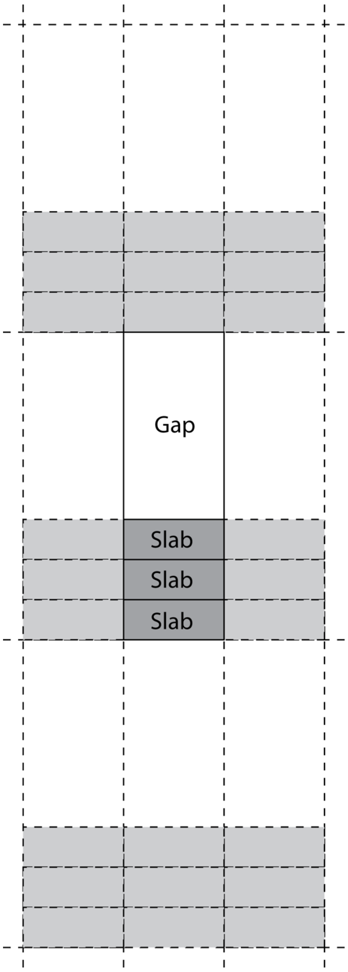

Figure 2.7: A schematic 2D presentation of a vacuum slab. 3 surface slabs have been stacked to make up the solid part and a gap has been introduced to prevent the solid surfaces from interacting. The gap could be filled with nothing (vacuum), a gas, a liquid or even another solid depending on the system of interest.

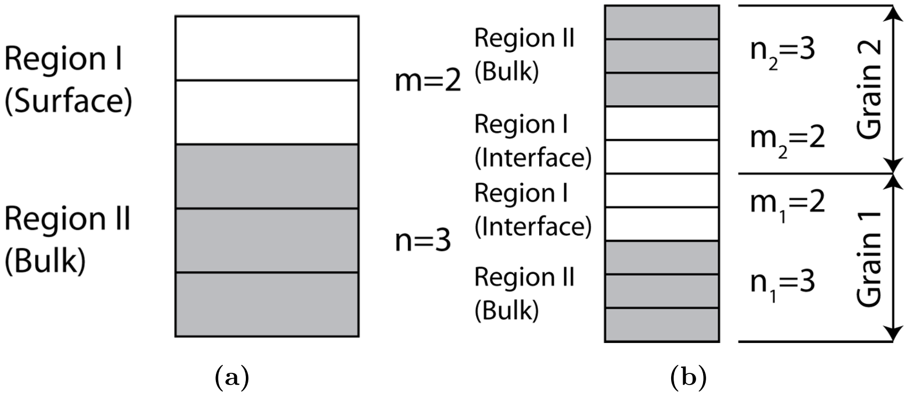

Figure 2.8: Schematic 2D view of the surface construction. (a) surface setup with m surface and n bulk cells; (b) grain boundary setup with m_1 and m_2 interface cells and n_1 and n_2 bulk cells.

n slabs. This setup (figure 2.8a) describes a region containing n slabs, which are held fixed at their perfect crystal structure having thus infinite bulk characteristics due to the negligible interaction of atoms at the top and the bottom on top of which is situated a surface region containing m slabs where the atoms can relax due to the missing interactions.

This setup can also be used to present a solid-solid interface (figure 2.8b) where two surfaces are put back to back resulting in two regions where relaxation is possible as well as two rigid bulk regions.

For this case periodic boundary conditions are applied only in the direction lying in the surface plane and therefore the standard Ewald summation method can not be applied anymore. A modification by Parry [14] exists however where Ewald type summations are made in planes perpendicular to the interface and finally these planes are summed up to give the electrostatic interaction of the surface slab.

The surface energy of an interface described in this fashion can be calculated according to equation 2.35. Where A is the surface area of the interface, $E_{\text{region 1}}$ the energy contained in region 1, $E_{\text{region 1 - region 2}}$ half of the total energy across the region 1-2 boundary and E_{bulk} the energy contained in a unit cell in the perfect bulk crystal. For a grain boundary m would be $m_1 + m_2$.

$$\gamma = \frac{E_{\text{region 1}} - E_{\text{region 1 - region 2}} - mE_{\text{bulk}}}{A} \tag{2.35}$$

This equation evaluates the change in energy in region 1 in presence of the interface compared to the energy in the perfect bulk crystal of the same size.

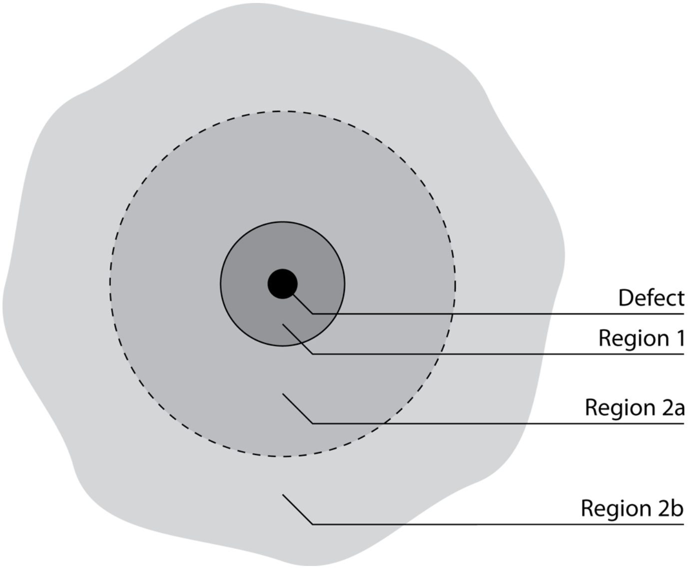

Figure 2.9: Schematic presentation of the Mott and Littleton method.

2.3.6 The Mott-Littleton Method

The method first formulated by Mott and Littleton [15] and also known as the embedded cluster method is a special way of treating defects at infinite dilution. As discussed in a review by Lidiard [16] the method has seen advances over the years, the implementation discussed here is the one found in the GULP [7] code.

The method is based on the setup wherein the defect (or it's barycenter) is located at the center of a sphere (region 1) of atoms with coordinates described by the 3n vector $\vec{x}$. Surrounding this sphere is another region called region 2, extending to infinity. Conceptually this second region is split in two parts, a and b, a being the finite inner part and b the infinite outer part. This setup is shown in figure 2.9. For region 2 only the displacements ($\vec{\xi}$) due to the presence of the defect are evaluated. The total energy can then be written as a function of the energies in region 1 and region 2 as well as the interaction of the two as given by equation 2.36.

$$E_{total}\left(\vec{(x)},\vec{\xi}\right) = E_{11}\left(\vec{x}\right) + E_{12}\left(\vec{x},\vec{\xi}\right) + E_{22}\left(\vec{\xi}\right) \tag{2.36}$$

By considering the displacements in region 2 to be small and thus harmonic, it can be shown [7] that the total energy can be calculated without having to know the self energy of region 2, which is due the infinite nature of this region not specified.

Thus in order to solve the problem the self energy in region 1 as well as the region 1-2 interaction has to be evaluated. For the finite region 1, the energy calculation is carried out by standard methods however for the infinite region 2 further conditions are required. It is imposed that the region sizes are larger than the short range cutoff. This means that short range forces originating from relaxations in region 1 due to the defect will not affect region 2b as the separation between the two is larger than the cutoff. The only remaining interaction component is thus electrostatic and it can be considered that the energy of region 2b due to its interaction with region 1 is the polarisation energy due to the net charge of the defect. The remaining interaction energy of region 1 with the finite region 2a can be explicitly calculated.

The Mott-Littleton method is useful in order to compare energetics of defect creation at an interface to the one in the infinite and otherwise perfect bulk crystal. This allows for example to evaluate energy differences which act as driving forces for defects to migrate from the bulk to an interface.

2.4 Energy Minimization

Energy minimization is the most basic technique in the family of atomistic simulation methods. It consists in changing the atomic coordinates (for a constant volume calculation) and in addition eventually the simulation box parameters (for a constant pressure calculation) of a given system in order to minimize the energy contained therein. This results in a description of the systems' energy as a function of $3n$ (the atomic coordinates - for constant volume) or $3n + 6$ (the atomic coordinates and cell lengths and angles - for constant pressure) variables. For a high number of atoms the minimum of such a function cannot be found analytically which is why numerical methods are used. The most common ones are the steepest decent, conjugate gradient and the Newton Raphson method, which will be briefly described in the following sections. All methods are however based on the same principle, which will be outlined first. The energy at a slight deviation $\vec{\delta x}$ from a position $\vec{x}$ in configurational space is given by an expansion in a Taylor series of the energy function as shown in (equation 2.37).

$$E(\vec{x} + \delta\vec{x}) = E(\vec{x}) + \frac{\partial E(\vec{x})}{\partial \vec{x}}\delta\vec{x} + \frac{1}{2!}\frac{\partial^2 E(\vec{x})}{\partial \vec{x}^2}(\delta\vec{x}^2) + \dots \tag{2.37}$$

Where $E(\vec{x})$ is the total interaction energy of the structure at a state described by the $3n$ (or $3n + 6$) vector $\vec{x}$. The Taylor series is usually truncated after the 3rd element. The first derivative term is known as the gradient vector (equation 2.38) and the second derivative term as the Hessian matrix (equation 2.39).

$$\frac{\partial E(\vec{x})}{\partial \vec{x}} = \vec{g}(\vec{x}) = \overrightarrow{grad}(E(\vec{x})) = \begin{pmatrix} \frac{\partial E(\vec{x})}{\partial x_1} \\ \frac{\partial E(\vec{x})}{\partial x_2} \\ \vdots \\ \frac{\partial E(\vec{x})}{\partial x_n} \end{pmatrix} \tag{2.38}$$

$$\frac{\partial^2 E(\vec{x})}{\partial \vec{x}^2} = H(\vec{x}) = \begin{pmatrix} \frac{\partial^2 E(\vec{x})}{\partial x_1 \partial x_1} & \cdots & \frac{\partial^2 E(\vec{x})}{\partial x_1 \partial x_n} \\ \vdots & \ddots & \vdots \\ \frac{\partial^2 E(\vec{x})}{\partial x_n \partial x_1} & \cdots & \frac{\partial^2 E(\vec{x})}{\partial x_n \partial x_n} \end{pmatrix} \tag{2.39}$$

The different methods all use these quantities in order to find the minimum in energy.

2.4.1 Determination of derivatives

As it can be seen from the above the first and second order derivatives are required for the determination of both the gradient vector and the hessian matrix. Numerically derivatives could be obtained by finite differences. This has however the disadvantage of being inefficient (requires the calculation of multiple points at small offsets on the function) as well as not very precise. Since all potential functions are analytical, they can also be differentiated. It is therefore a common practice in atomistic simulation codes to not only code the functional form of the potential but also it's first and second order derivatives, from which the above derivatives can be obtained by summation. In case free energy minimization is to be done even third order derivatives are required.

2.4.2 Steepest decent (or gradient decent)

The steepest decent [17] method is the most basic and intuitive of the order 1 methods (involving only the evaluation of the gradient vector). It is extremely robust even far from the minimum. One starts at a position $\vec{x}_0$ in configurational space where the direction with the steepest decent is $-\vec{g}(\vec{x}_0)$. In order to find the next point $\vec{x_1}$, the method will do a step in this direction, the length of the step being γ, which is usually determined by a line search procedure, where the energy along the chosen direction is monitored and γ determined so that the new position coincides with the closest minimum along the given direction i.e. where $-\vec{g}(\vec{x}_0)$ is tangent to a contour line of the energy hyper surface. This means that $-\vec{g}(\vec{x}_1)$ is orthogonal to

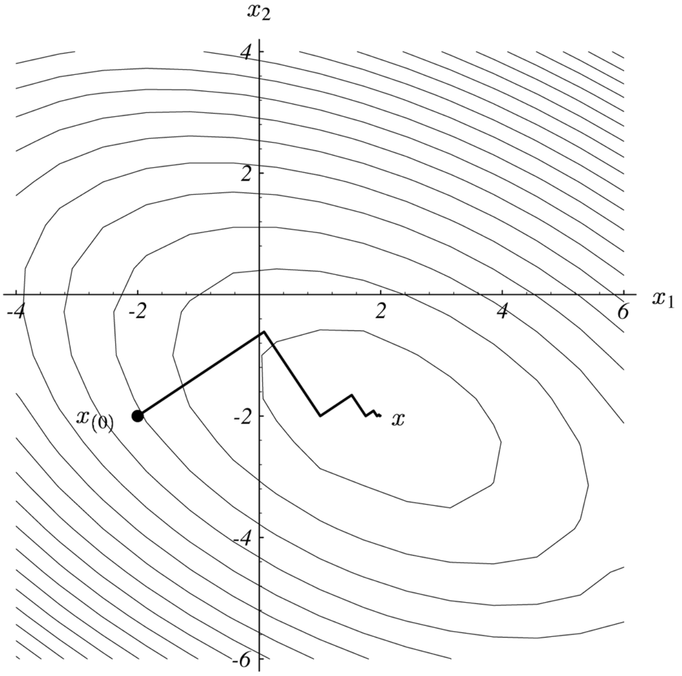

Figure 2.10: Representation of a minimization path using the steepest descent method in a system consisting of two variables x_1 and x_2. It can be seen that the segments continue until they are tangent to one of the contour lines and that the next segment is perpendicular. This leads to the zig-zag descent towards the minimum. Image extracted from [17].

$-\vec{g}(\vec{x}_0)$. At the new point $\vec{x}_1$ the same method as in $\vec{x}_0$ will be repeated leading due to the orthogonality to a zig-zag descent of segments of alternating directions towards the energy minimum. This iterative method is resumed in equation 2.40 and a representation of the minimization path on a simple 2D energy surface is shown in figure 2.10.

$$\vec{x}_{k+1} = \vec{x}_k - \gamma \cdot \vec{g}(\vec{x}_k) \tag{2.40}$$

2.4.3 Conjugate Gradient

The conjugate gradient method [17] starts out exactly as the the steepest descent method by taking a first step in direction $\vec{h}(\vec{x}_0) = \vec{h}_0 = \vec{g}_0 = \vec{g}(\vec{x}_0)$. The idea is then to make the search directions $\vec{h}_i$ form a set of mutually conjugate directions. The criterion for two vectors $\vec{h}_i$ and $\vec{h}_j$ to be conjugate is $\vec{h}_i \cdot H \cdot \vec{h}_j = 0$, where H is the Hessian matrix. Note however that the method is of order 1 and does not require the explicit evaluation of the Hessian matrix, the conjugate relationship between the

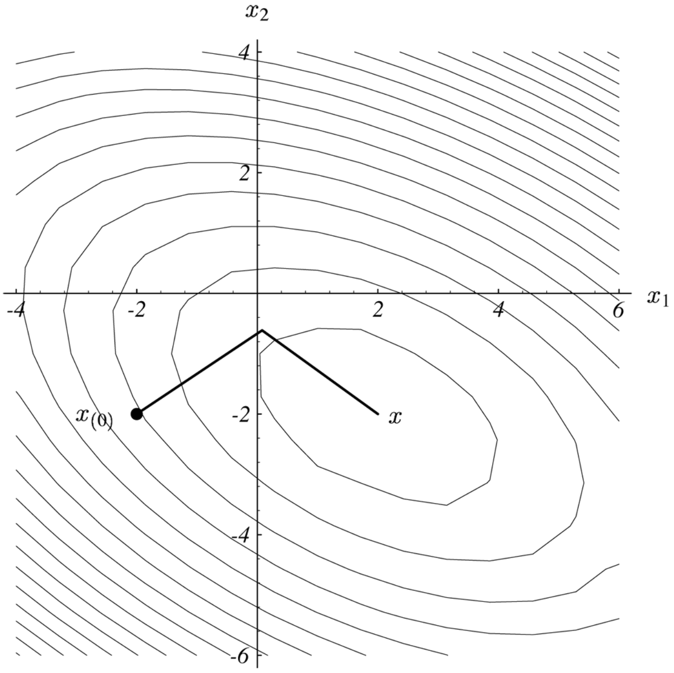

Figure 2.11: Representation of a minimization path using the conjugate gradient method in a system consisting of two variables x_1 and x_2. The first step is taken along the direction of steepest decent and the subsequent steps along directions being mutually conjugate. For harmonic systems, the method converges in a maximum number of steps equal to the number of variables. Image extracted from [17].

vectors coming from the iterative scheme, which is given in equations 2.41 to 2.43.

$$\vec{h}_k = \vec{g}_k + \alpha_{k-1} \cdot \vec{h}_{k-1} \tag{2.41}$$

$$\alpha_{k-1} = \frac{\vec{g}_k \cdot \vec{g}_k}{\vec{g}_{k-1} \cdot \vec{g}_{k-1}} \tag{2.42}$$

$$\vec{x}_{k+1} = \vec{x}_k - \gamma \cdot \vec{h}_k \tag{2.43}$$

Where γ is again the step length determined as for the steepest decent method using a line search. This method has the advantage over the steepest decent that it does not zig-zag towards the minimum. In fact since the search directions are conjugate for the case of a harmonic system (system with exactly one minimum) the minimum will be found in a maximum number of steps equal to the number of variables in the system. In a "real" system consisting of many non-harmonic minima, the number of iterations may be higher. The cost per iteration is slightly higher but the number of iterations will be significantly lower than for the steepest decent method. The convergence for the same system as before in only two steps is illustrated in figure 2.11.

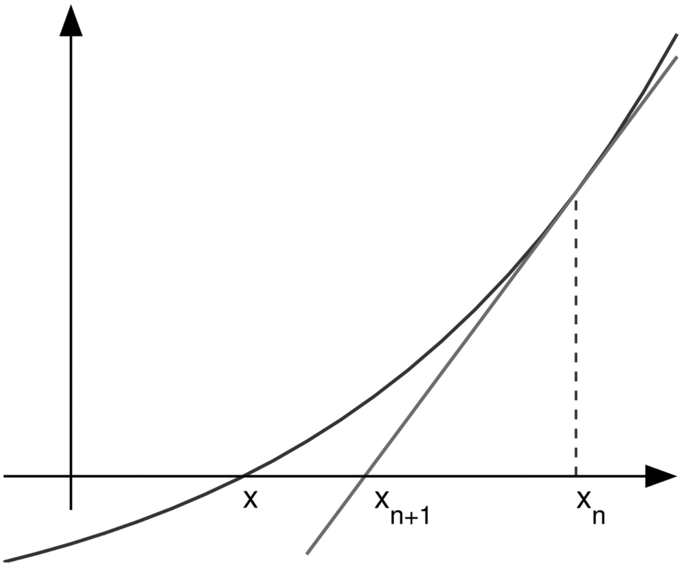

Figure 2.12: The Newton Raphson method for function minimization. Going from a point x_n the curvature is used to approximate where the root of the function will be. Iterative application of the method will lead to the root of the function.

2.4.4 Newton Raphson

The Newton Raphson method is an order 2 method, requiring the evaluation of the Hessian matrix. This step takes time, however convergence close to the minimum is extremely efficient since it also uses the curvature of the energy surface. The main drawback of the method is that far away from a minimum it tends to be unstable. The Newton Raphson method is basically a root finding algorithm, which is given in equation 2.44 and shown in figure 2.12, where $f'(x)$ denotes the first derivative of the function $f(x)$.

$$\vec{x}_{k+1} = \vec{x}_k - \frac{f(x_k)}{f'(x_k)} \tag{2.44}$$

In the case of a minimization the problem is to find a minimum in energy, i.e. $\frac{\partial E(\vec{x})}{\partial \vec{x}} = 0$. The root finding algorithm is thus applied to the first derivative and the useful form is as given in equation 2.45.

$$\vec{x}_{k+1} = \vec{x}_k - \frac{\frac{\partial E(\vec{x}_k)}{\partial \vec{x}}}{\frac{\partial^2 E(\vec{x}_k)}{\partial \vec{x}^2}} = \vec{x}_k - H^{-1}(\vec{x}_k) \cdot \vec{g}(\vec{x}_k) \tag{2.45}$$

It can be seen that the Hessian matrix not only has to be evaluated but also inverted, which for systems with many variables is a very expensive operation. Therefore so called Quasi-Newton methods [18] for approximating the Hessian matrix over time have been developed, explicitly calculating the matrix only at specific intervals or when changes in the energy are too large for the approximation to be valid. The most current of these methods is the Broyden-Fletcher-Goldfarb-Shanno (BFGS) algorithm, which is given in equations 2.46 and 2.47.

$$H_{i+1} = H_i + \frac{\Delta\vec{x} \times \Delta\vec{g}}{\Delta\vec{x} \cdot \Delta\vec{g}} - \frac{(H_i \cdot \Delta\vec{g}) \times (H_i \cdot \Delta\vec{g})}{\Delta\vec{g} \cdot H_i \cdot \Delta\vec{g}} + (\Delta\vec{g} \cdot H_i \cdot \Delta\vec{g}) \cdot (\vec{v} \times \vec{v}) \tag{2.46}$$

$$\vec{v} = \frac{\Delta\vec{x}}{\Delta\vec{x} \cdot \Delta\vec{g}} - \frac{H_i \cdot \Delta\vec{g}}{\Delta\vec{g} \cdot H_i \cdot \Delta\vec{g}} \tag{2.47}$$

2.4.5 Minimization Strategy

It has been mentioned in the above presentation of the methods that each of them has advantages and drawbacks. The steepest decent method is very robust far from the minimum, requires a very short time per iteration but converges slowly when close to minimum. The conjugate gradient method has a higher time per iteration and slightly higher memory requirements but converges faster than the steepest decent method. The Newton Raphson method finally has the best convergence close to the minimum, is however unstable far from it. Also it is relatively expensive due to evaluation and inversion of the Hessian matrix and requires a lot of memory to store this matrix. Due to these reasons none of the methods is perfectly adequate just by itself. Therefore one usually applies a combination, starting with a very crude method such as conjugate gradient or even steepest descent and switching to a finer one (Newton Raphson) once small changes in energy indicate the proximity of the minimum.

2.5 Molecular dynamics

Molecular dynamics [19] is a method for which the positions and velocities of the atoms are updated over time under the action of interatomic forces. The basis of the method is Newtons law of motion given in equation 2.48.

$$\vec{F} = m \cdot \vec{a} \tag{2.48}$$

The forces are the derivatives of the energy with respect to the coordinates as given in equation 2.49.

$$\vec{F} = \frac{\partial E(\vec{x}_k)}{\partial \vec{x}_k} \tag{2.49}$$

One could combine these equations directly by writing them as given in equation

2.50, however in practice the force calculation step is usually separated from the integration step.

$$\frac{\partial E(\vec{x}_k)}{\partial \vec{x}} = m \cdot \frac{\partial^2 \vec{x}_k}{\partial t^2} \tag{2.50}$$

There exist different ways of integrating the equation of motion, the most popular being the so called Verlet leapfrog (VLF) and velocity Verlet (VV) [20]. These algorithms have the advantage of increased numerical stability compared to a normal Euler integration since they use velocities at half-steps. For the VLF algorithm one takes the position and force at a time t and the velocities at a time $t - \frac{1}{2}\Delta t$. One then first advances the velocities to $t + \frac{1}{2}\Delta t$ as given in equation 2.51 followed by an update of the positions using these velocities as given by equation 2.52. The name of the algorithm comes from the fact that in time the velocity leaps the position, the two never being known at the same time t.

$$\vec{v}(t + \frac{1}{2}\Delta t) = \vec{v}(t - \frac{1}{2}\Delta t) + \Delta t \frac{\vec{f}(t)}{m} \tag{2.51}$$

$$\vec{r}(t + \Delta t) = \vec{r}(t) + \Delta t \cdot \vec{v}(t + \frac{1}{2}\Delta t) \tag{2.52}$$

In the VV algorithm the position and velocity are known at the same instant in time. However the velocity is updated in two steps of $\frac{1}{2}\Delta t$ (equations 2.53 and 2.55), the velocity after the first half step update being used to update the positions as given in equation 2.54 and the second half step update of the velocity being done with the forces obtained from updated positions.

$$\vec{v}(t + \frac{1}{2}\Delta t) = \vec{v}(t) + \frac{1}{2}\Delta t \frac{\vec{f}(t)}{m} \tag{2.53}$$

$$\vec{r}(t + \Delta t) = \vec{r}(t) + \Delta t \cdot \vec{v}(t + \frac{1}{2}\Delta t) \tag{2.54}$$

$$\vec{v}(t + \Delta t) = \vec{v}(t + \frac{1}{2}\Delta t) + \frac{1}{2}\Delta t \frac{\vec{f}(t + \Delta t)}{m} \tag{2.55}$$

The timestep Δt has to be chosen with care and as a function of the temperature and the atoms present. In fact one wants to sample the fastest vibrational motion in the system with a reasonable accuracy. The fastest vibrational motion is usually found for the lightest atom if the system is not far from equilibrium as the velocity will follow a Maxwell-Boltzmann distribution as given by equation 2.56.

$$\langle v^2 \rangle = \frac{3k_B T}{m} \tag{2.56}$$

A reasonable sampling can be assumed when an atom does not travel further than $\frac{1}{50}$ of an interatomic spacing per timestep. The limit for the timestep can thus be expressed as given by equation 2.57.

$$\Delta t = \frac{\Delta s}{v} = \frac{\frac{1}{50} d_{interatom}}{\sqrt{\frac{3k_B T}{m}}} \tag{2.57}$$

For the example of alumina where the lightest atom is oxygen with 16 a.m.u. at an interatomic spacing of 2.7Å the limiting timestep can be calculated as given in equation 2.58.

$$\Delta t_{oxygen} = \frac{\frac{1}{50} 2.7 \cdot 10^{-10}}{\sqrt{\frac{3 \cdot 1.3807 \cdot 10^{-23} \cdot 298}{16 \cdot 1.660 \cdot 10^{-27}}}} = 8 \cdot 10^{-15} s = 8 fs \tag{2.58}$$

As this equation considers the average velocity in practice 1fs is used in order to sample the fast end of the velocity distribution correctly. As mentioned above a core-shell model can be applied in order to model the polarisability of atoms, the shell carrying a very small mass of 0.2 a.m.u. only. This has a severe effect on the timestep which will have to be divided by a factor $\sqrt{\frac{16}{0.2}} = 8.94$ to accommodate the light shells. The timestep to be used for core-shell dynamics (0.1 fs) thus has to be 10 times smaller than for core-only dynamics.

2.6 Metadynamics

It was seen in the previous section that timesteps in molecular dynamics have to be quite small in order to achieve an accurate sampling of the vibrational motion. This limits the timescales accessible to MD simulations to a few nanoseconds on current computer clusters. Rare events such as chemical reactions or solid state diffusive phenomena however happen at timescales beyond the nanosecond, which makes their investigation using molecular dynamics very unpractical. A manifold of methods have been developed in order to overcome this limitation [21, 22]. Amongst these methods, metadynamics (MTD) [23, 24, 25] is a particularly interesting method as it allows to determine the free energy of the underlying processes while sampling configurational space with a high efficiency.

The metadynamics method is based on the idea of defining certain reaction coordinates, the so called collective variables (CVs), in the system. This can be interatomic distances, angles, coordination numbers or any other property definable from atomic coordinates. The motion of the system in the space defined by these collective variables (the CV space) is monitored. In a normal MD, the system would visit only a small portion of this space due to high energy barriers surrounding the current state. In metadynamics these barriers are overcome by inserting every n_h molecular dynamics timesteps little “gaussian” hills of energy into the CV space at the point where the system currently is. This illustrated in figure 2.13 where the accumulation of hills is shown on the underlying free energy landscape. The resulting bias potential at a certain point $\vec{r}$ in CV space is the sum of all hills inserted up to that point of time as given by equation 2.59.

$$V_{\text{hills}}(\vec{r}, t) = \mathrm{h}_h \sum_{i=1 \ldots n(t)} exp\left(-\frac{(\vec{r}-\vec{r_i})^2}{2\,(\mathrm{h}_w)^2}\right) \tag{2.59}$$

Where $\vec{r_i}$ is the position of the hill i in CV space, h_h the height of the hill (in units of energy) and h_w the width of the hill. This bias potential is then applied to all atoms making up a certain CV, resulting in an additional force making them move away from the current point in CV space. This additional energy will allow the system to visit a larger portion of the CV space by overcoming energy barriers. The energy landscape formed by the hills is an unbiased estimator [25] of the free energy surface due to the fact that “gaussians” are injected where the system spends most of its time and thus where the free energy is lowest. The property that the system will eventually flatten out the energy surface when all wells are filled makes it possible to determine the free energy change associated with processes occurring in the system from this sort of simulation.

The drawback is that the trajectories obtained from MTD runs are no longer on a physical timescale and diffusion can not directly be accessed as it would be possible for other methods such as hyperdynamics [21]. However metadynamics allows precise sampling of the energy changes associated with single processes in the system, making it well suited for energy studies.

2.7 Kinetic Monte Carlo

The original Monte Carlo method is founded on the Metropolis algorithm [26] which considers that a system being in a state A can go to a state B anywhere in it’s configurational space by a probability determined by the difference in energy ΔE between the two states as given by equation 2.60 where k is Boltzmann’s constant

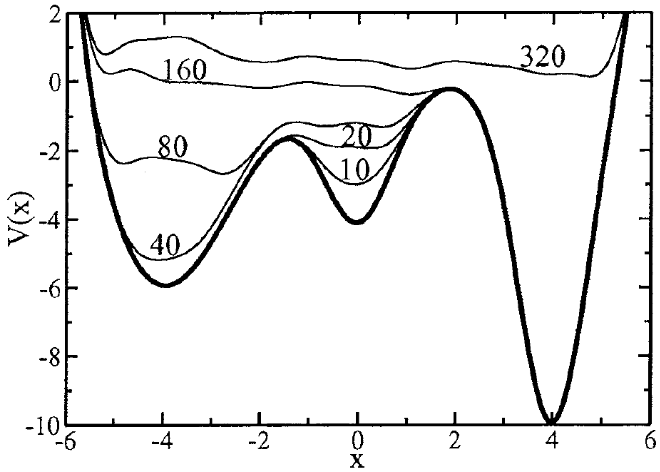

Figure 2.13: View of the hill evolution on top of the free energy surface (bold line). The system will start it the central minimum, which it will escape after the 20th timestep. The left well will be filled (timestep 80) and the system can then freely evolve in the basin defined by the two left minima. At step 160 the rightmost basin will become accessible, which is filled at step 320 and the system can now freely evolve across all three basins. The free energy barriers between basins can be estimated since the added hills will tend to present a flat surface. Figure extracted from [23]

.

and T the temperature.

$$p = exp\left(\frac{-\Delta E}{kT}\right) \tag{2.60}$$

The algorithm is to choose a random transition, calculate it's probability and then carry it out if a random number uniformly distributed between 0 and 1 is smaller than the probability. This method will thus result in a randomly selected sequence of transitions which are carried out or not at a random rate. This method is thus well suited for simulations of a system tending to an equilibrium state.

The kinetic Monte Carlo method (kMC) [27] also known as n-fold Monte-Carlo method is a variation of the Metropolis algorithm. Here the system is considered at a state A, from where it can move to a finite collection of n states B_i. Each transition from A to a B_i is associated with a reaction rate r_i. One calculates the cumulative function R_i which is defined as given in equation 2.61.

$$R_i = \sum_{j=1}^{i} r_j \tag{2.61}$$

This function is evaluated for all $i = 1, \ldots, n$ and a random number u uniformly distributed between 0 and 1 is selected. One then finds the transition i for which

$R_{i-1} < uR_n \leq R_i$, which is carried out. In order to advance the simulation time a new random number v uniformly distributed between 0 and 1 is selected and the timestep defined as given in equation 2.62.

$$\Delta t = -\frac{logv}{R_n} \tag{2.62}$$

This method will thus result in a system evolving trough a series of known to be connected states, controlled by the reaction rate of the individual transitions. The cumulative function will ensure that transitions with a faster rate will be selected more often and that the time will be advanced less if one of these high probability transitions is carried out.

The kMC method is very interesting in order to extrapolate results obtained from atomistic simulations to much higher time- and length scales usually referred to as the meso-scale. This can be achieved since in molecular dynamics be it classic or ab-initio transitions can be directly observed and reaction rates measured by averaging over a sufficient number of events. On the other hand all atomistic simulation methods also allow the determination of energies. If a transition state energy can be calculated and compared to the ground states which it separates, the energy barrier associated with a certain event can be determined. As seen above, special methods such as metadynamics can also determine energy barriers. From an energy barrier the associated reaction rate can be calculated as given by equation 2.63.

$$r_i = \frac{kT}{h} exp\left(-\frac{\Delta G_i}{kT}\right) \tag{2.63}$$

Where h is Planck's constant and ΔG_i is the free energy barrier associated with the transition in question.

Bibliography

[1] P. P. Ewald. The calculation of optical and electrostatic grid potential. *Annalen Der Physik*, 64(3):253–287, 1921.

[2] B. G. Dick and A. W. Overhauser. Theory of the dielectric constants of alkali halide crystals. *Physical Review*, 112(1):90–103, 1958.

[3] P. J. Mitchell and D. Fincham. Shell-model simulations by adiabatic dynamics. *Journal of Physics-Condensed Matter*, 5(8):1031–1038, 1993.

[4] P. J. D. Lindan and M. J. Gillan. Shell-model molecular-dynamics simulation of superionic conduction in caf$_2$. *Journal of Physics-Condensed Matter*, 5(8):1019–1030, 1993.

[5] M. Wilson, P. A. Madden, and B. J. Costa-Cabral. Quadrupole polarization in simulations of ionic systems: Application to AgCl. *Journal of Physical Chemistry*, 100(4):1227–1237, 1996.

[6] M. Wilson, M. Exner, Y. M. Huang, and M. W. Finnis. Transferable model for the atomistic simulation of Al_2O_3. *Physical Review B*, 54(22):15683–15689, 1996.

[7] J. D. Gale and A. L. Rohl. The general utility lattice program (GULP). *Molecular Simulation*, 29(5):291–341, 2003.

[8] M. Blanchard, K. Wright, and J. D. Gale. Atomistic simulation of Mg_2SiO_4 and Mg_2GeO_4 spinels: a new model. *Physics and Chemistry of Minerals*, 32(5-6):332–338, 2005.

[9] R. Martin. *Electronic structure: basic theory and practical methods.* Cambridge University Press, Cambridge, UK, 2004.

[10] P. Hohenberg and W. Kohn. Inhomogeneous electron gas. *Physical Review B*, 136(3):B864–B871, 1964.

[11] W. Kohn and L. J. Sham. Self-consistent equations including exchange and correlation effects. *Physical Review*, 140(4A):1133–, 1965.

[12] D. M. Ceperley and B. J. Alder. Ground-state of the electron-gas by a stochastic method. *Physical Review Letters*, 45(7):566–569, 1980.

[13] J. P. Perdew and A. Zunger. Self-interaction correction to density-functional approximations for many-electron systems. *Physical Review B*, 23(10):5048–5079, 1981.

[14] D. E. Parry. Electrostatic potential in surface region of an ionic-crystal. *Surface Science*, 49(2):433–440, 1975.

[15] M. F. Mott and M. J. Littleton. Conduction in polar crystals: I. electrolytic conduction in solid salts. *Transactions of the Faraday Society*, 34(1):485–499, 1938.

[16] A. B. Lidiard. The mott littleton method - an introductory survey. *Journal of the Chemical Society-Faraday Transactions II*, 85(5):341–349, 1989.

[17] J. R. Shewchuk. An introduction to the conjugate gradient method without the agonizing pain. Technical report, Carnegie Mellon University, 1994.

[18] D. F. Shanno. Conditioning of quasi-newton methods for function minimization. *Mathematics of Computation*, 24(111):647–656, 1970.

[19] B. J. Alder and T. E. Wainwright. Studies in molecular dynamics: I. general method. *Journal of Chemical Physics*, 31(2):459–466, 1959.

[20] W. Smith and T. R. Forester. DL_POLY 2.0: A general-purpose parallel molecular dynamics simulation package. *Journal of Molecular Graphics*, 14(3):136–141, 1996.

[21] A. F. Voter. Hyperdynamics: Accelerated molecular dynamics of infrequent events. *Physical Review Letters*, 78(20):3908–3911, 1997.

[22] M. R. Sorensen and A. F. Voter. Temperature-accelerated dynamics for simulation of infrequent events. *Journal of Chemical Physics*, 112(21):9599–9606, 2000.

[23] A. Laio and M. Parrinello. Escaping free-energy minima. *Proceedings of the National Academy of Sciences of the United States of America*, 99(20):12562–12566, 2002.

[24] M. Iannuzzi, A. Laio, and M. Parrinello. Efficient exploration of reactive potential energy surfaces using Car-Parrinello molecular dynamics. *Physical Review Letters*, 90(23):238302, 2003.

[25] A. Laio, A. Rodriguez-Fortea, F. L. Gervasio, M. Ceccarelli, and M. Parrinello. Assessing the accuracy of metadynamics. *Journal of Physical Chemistry B*, 109(14):6714–6721, 2005.

[26] N. Metropolis, A. W. Rosenbluth, M. N. Rosenbluth, A. H. Teller, and E. Teller. Equation of state calculations by fast computing machines. *Journal of Chemical Physics*, 21(6):1087–1092, 1953.

[27] W. M. Young and E. W. Elcock. Monte carlo studies of vacancy migration in binary ordered alloys: I. *Proceedings of the Physical Society of London*, 89:735, 1966.

Chapter 3

Growth modification by small organic molecules

In this chapter the growth modification by organic molecules will be investigated. This is done for the case of hematite (α-Fe_2O_3) modified by phosphonate additives. Seven hydroxylated surfaces of hematite have been calculated and the replacement energy for the condensation reaction of the additives with surface hydroxyl groups calculated. This energy is then used in order to predict the changes in morphology. Two different additives were tested and both were found to result in the development of a less elongated morphology. One of the additives showed an affinity for a surface not originally in the morphology resulting in its appearance in the Wulff shape. These results were validated by experiment and can thus be used as a predictive tool for the calculation of the growth modification with other phosphonate additives.

3.1 Introduction

The interaction of organic molecules with the surfaces of inorganic particles is an important field of research for the knowledge-based synthesis of nanocrystals. In order to control the synthesis with organic molecules one has to understand the interactions between the particle surface and the additives. This level of insight is difficult to achieve experimentally, but with increasing computer power and development of sophisticated methods, atomistic simulations are becoming a more and more powerful tool for the determination of such interactions. Additives can show an affinity for a specific crystalline surface, which gives the possibility to tailor-shape nanoparticles as a docked additive will slow growth of that specific face. It would be desirable to know the interaction of a specific molecule on the morphologically most important surfaces in order to have a basis for experimental design. If systematic docking behavior exists, one would be able to screen for prospective candidate molecules, when trying to find an additive, or even additive-mixture, which will result in a given morphology. Furthermore if the additive molecule has a chemically active group, which can be functionalised, applications far beyond the scope of morphology-modification become possible. One could think of applying a certain function to a specific family of faces only by means of specific attachment of functional molecules. Another possibility could be to functionalise the additive with molecules having specific interactions amongst each other as would be the case for example for short strands of a specifically binding molecule such as DNA as illustrated in figure 3.1, which would make auto-assembly operations possible.

In this schematic view a crystal is grown in presence of two additives M1 and M2 (figure 3.1a), which specifically attach to face 1 and face 2 respectively (figure 3.1b). When additives specifically interact with each other as shown with the triangle and cone functional groups, which could be base-pairs of DNA. When two particles being thus covered with the additives meet, their interaction will be governed by the additives, joining always a type 1 and type 2 faces (figure 3.1c) resulting in a periodic arrangement as shown in (figure 3.1d).

Hematite has been chosen as the system to be studied in the present work since it is a technologically important system for which a lot of experimental data exists. An outline of applications and properties as well as previous studies on hematite will be given in the following paragraphs.

Hematite is one of the most common iron ores and is also commonly found in soils. Cornell and Schwertmann [1] give an overview on applications of hematite, which can be found in bright red pigments for chemically and physically high resistant paints,

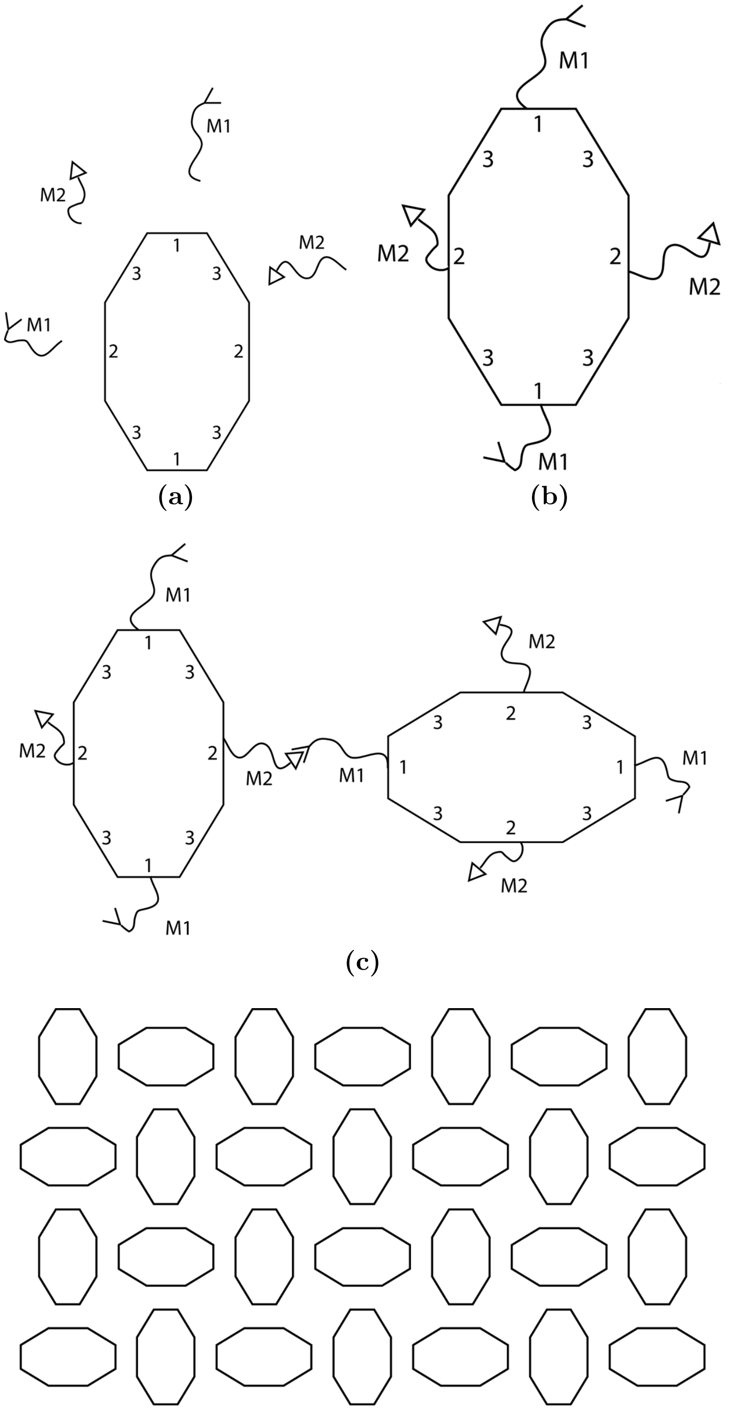

(a) (b)

(c)

(d)

Figure 3.1: Schematic view of an autoassembly process in presence of specifically interacting additives: (a) Particle and additives in solution, (b) M1 and M2 bin selectively to type 1 and 2 faces respectively, (c) specific interaction between M1 and M2 additives and (d) final assembled structure.

for coloring of food and pharmaceuticals, where a relatively small and narrow particle size distribution is required for good optical properties. Another welcome property in these applications is that all iron oxides strongly absorb UV-light thus protecting the paint or pharmaceutical from degradation. A very important application of hematite can be found as a catalyst in the production of hydrocarbons and styrene as well as aldehyde and ketones. As for all catalysts the most important property is a high specific surface area, which is achieved with extremely small particle sizes at the nano-scale. Auto-assembly operations could be used in order to transform these nano-powders into porous solid catalysts with a much higher specific surface than currently used catalysts.

As Cornell and Schwertmann [1] mention, most experimental studies have not identified the occurring crystal faces for hematite but as they further state, computational studies of the surfaces of hematite in vacuum exist by Mackrodt [2, 3, 4] and Reeves and Mann [5]. However these results are inconsistent showing a very large dispersion in surface energies and agreeing only on the fact that the rhombohedral (102) plane should frequently appear. These computational studies also attribute quite a low surface energy to the hexagonal (0001) basal plane. Later computational studies looking at a range of surfaces have been done by Rohl and Gay [6], Wasserman et al. [7], Jones et al. [8], Cooke et al. [9, 10] as well as de Leeuw and Cooper [11]. The surface energies given by these authors are given in table 3.1. As it can be seen, all authors except Jones and de Leeuw attribute the lowest surface energy to the rhombohedral surface (110). However the dispersion of values is very large and even the sequence of faces of increasing surface energy is not conserved from one author to another. This may be due to the fact the authors used different interatomic potentials as well as different computational tools.

In addition to the above mentioned publications, the basal plane has been studied by many authors, both by experimental and computational means. The stable termination has been shown to vary as a function of oxygen partial pressure. Wang et al. [12] and Shaikhutdinov and Weiss [13] have shown computationally and experimentally a gradual change from oxygen terminated surfaces at high oxygen partial pressure towards domains of either oxygen or iron termination and finally to a pure iron terminated surface at low oxygen partial pressure. The oxygen termination at high oxygen partial pressure is confirmed by Bergermayer et al. [14]. Atomistic calculations [15, 16, 17], considering the surface in vacuum, show the iron termination as stable. Eggleston et al. [18] have shown the coexistence of both terminations in aqueous media using scanning tunneling microscopy (STM). STM has also been applied on the iron terminated surface to show special conformations of iron as adatoms

Table 3.1: Miller indices of the calculated surfaces, given in the rhombohedral and hexagonal system as well as their interplanar spacing. The surfaces energies reported by different authors are given as well.

Rhombohedral	(110)	(112)	$(10\bar{1})$	(222)	(102)	(411)
Hexagonal	$(00\bar{1}2)$	$(1\bar{1}04)$	$(11\bar{2}0)$	(0001)	$(1\bar{2}12)$	$(10\bar{1}2)$
$\mathbf{D_{hkl}}$	4.0378	2.8071	2.5164	2.2546	2.1974	1.2212
Dry surface energies [$\mathbf{Jm^{-2}}$]						
Mackrodt [2]	1.47		2.03	1.53		
Rohl [6]	0.55	1.03	0.81	0.76	1.58	
Wasserman [7]				1.65	2.78	
Jones [8]	1.15			0.75	1.02	
Cooke [9]				2.5		2.8
Cooke [10]	2.10			2.41		
de Leeuw [11]	1.88		2.03	1.78		2.36
Hydroxylated surface energies [$\mathbf{Jm^{-2}}$]						
de Leeuw [11]	0.97		0.81	1.21		0.97

[19] or bound as ferryl (Fe=O) groups [20].

Hematite surfaces will almost always be hydroxylated when in contact with aqueous solutions. Infrared characterization of the surface hydroxyl groups on hematite powders was first reported by Rochester and Topham [21] however without determination of the different faces present. Busca and Lorenzelli [22] prepared hematite by a method where the (0001) basal plane should be dominant and performed IR spectroscopy of the surface hydroxyl groups present. They found OH stretch absorptions, which they attribute to monocoordinated and bridged free surface hydroxyl groups. Henderson et al. [23] showed dissociative water adsorption on the (012) surface. They found terminal hydroxyl groups as well as bridging hydroxyls which seem to participate in hydrogen bonding. This was confirmed by Trainor et al. [24] who used crystal truncation rod diffraction on the (0001) surface to show hydroxyl groups singly and doubly coordinated to iron atoms which lowers the surface energies significantly. A later publication [25] using the same method shows the existence of Fe-OH_2, Fe-OH and Fe-O groups at the surface which has been confirmed with density function calculations [26].

Barrón and Torrent [27] have studied geometrically possible surface hydroxyl configurations on unrelaxed hematite surfaces, however no energetic contributions were considered in their approach resulting in qualitative results only. Several hematite surfaces have been studied using an atomistic simulation approach by Jones et al. [8], where they looked at their hydroxylation state. They found that the O-terminated basal plane is the most stabilized by reaction with water whereas the Fe-terminated basal plane gets unstable in presence of water, hydroxylation below 67% coverage is however possible. They found that the (210) plane does not get stabilized by hydroxylation whereas the (011) plane does. Rustad et al. [28] studied water adsorption on the hematite (012) surface using atomistic simulation techniques. They found that 75% of the water adsorbed at this surface is dissociated forming surface hydroxyl groups. Hartmann [29] showed that specific water adsorption is likely on the basal plane due to the atomic surface structure, stabilizing it and explaining its dominance in experimental morphologies. Cooke et al. [9] found dissociative water adsorption on the basal plane with adsorption energies of up to -270kJmol^{-1} as well as -80kJmol^{-1} for the $(10\bar{1}2)$. The enthalpies of adsorption have recently been measured by Mazeina and Navrotsky [30] and range from -67.1kJmol^{-1} to -25.5kJmol^{-1} depending on the configuration. More recently de Leeuw and Cooper [11] have calculated the associative as well as dissociative adsorption of water on a number of iron oxides and hydroxides. They found energies for dissociative adsorption in the range of -75.8kJmol^{-1} to -189.0kJmol^{-1} depending on the surface. Further they evaluated the surface energies in their hydroxylated state.

Growth modifying organic additives have been experimentally studied by Reeves and Mann [5] looking at amongst other molecules, the influence of phosphonates on the morphology of hematite. They determined the presence of $(10\bar{1}4)$ faces in unmodified hematite grown at pH 2. However no indexation of crystallographic faces has been done on their diphosphonate-modified sample. Formation of hematite at pH 1.1 has been studied by Jones et al. [31] looking at the influence of different phosphonate-based additives. They found uniform rhombic crystals when synthesizing without the additive, which became hexagonal in shape in presence of the additive, explained as being due to growth inhibition of the $(2\bar{1}\bar{1}\bar{4})$ face.

This raises the question of how phosphonate molecules bind to hematite surfaces. The functional part of the system which are phosphonate-iron complexes has been studied by Barja et al. [32] using a variety of analytical techniques. They found that the phosphonates bind in every case very strongly to the iron ion. Interaction of phosphonates with hematite surfaces has so far not been studied in detail, however there exists XPS work on the isostructural compound Al_2O_3 formed on aluminum surfaces by Hoque et al. [33], which shows that the phosphonate binds to the surface by a condensation reaction with surface hydroxyl groups, forming water as a byproduct, thus replacing the surface hydroxyl group.

From the above discussion we see that the energetics associated with docking reactions of specific additives with specific surfaces is of a great practical importance. Therefore the present study looks at the binding of two organic phosphonate molecules (methyl nitrilo dimethylenephosphonic acid - MNDP, ethylenediamine tetraphosphonic acid - EDTP) onto the surfaces of hematite (α-Fe_2O_3), using atomistic simulation techniques, putting the focus on the changes in morphology as well as selective docking. We have considered a pH of 9, where the additives should be deprotonated. Experimental work using the MNDP and EDTP additives was carried out for comparison with the calculations, as no such data has been published so far for the pH considered in this work.

3.2 Approach

Six crystalline surfaces of hematite with the lowest interplanar spacing, resumed in table 3.1, have been determined and their non-dipolar surface terminations created with the GDIS [34] computer program. Surface terminations have to be non-dipolar as the periodic boundary conditions would otherwise result in an infinite dipole. The surfaces were described by a two region model as described in section 2.3.5.

The surface was then hydroxylated by adding OH^- groups to the not fully coordinated iron atoms and an equal number of H^+ ions to the not fully coordinated oxygen atoms, in order to achieve full coordination. The structures were relaxed using the GULP [35] program with interatomic potentials described as given by equation 3.1.

$$V_{ij}^{\text{coulomb+buckingham}}(r_{ij}) = \frac{q_i q_j}{4\pi\epsilon_0 r_{ij}^2} + A_{ij} exp\left(\frac{-r_{ij}}{\rho_{ij}}\right) - C_{ij} r_{ij}^{-6} \tag{3.1}$$

In this equation q_i and q_j are the charges of atoms i and j respectively, r_{ij} is the distance between the atoms i and j and A_{ij}, ρ_{ij} and C_{ij} are empirically fitted potential parameters for the pair-wise interaction of atoms i and j. The first term describes the coulombic interaction (section 2.1.1), which is evaluated by an Ewald sum and the two remaining terms are a Buckingham interaction potential (section 2.1.2) describing the short range forces resulting from the electronic cloud overlap. In addition to these a Morse potential (section 2.1.3) was used in order to describe the covalent character of the O-H bond of the hydroxyl group.

Polarization of all ions was described by the core-shell model of Dick and Overhauser [36] as presented in section 2.1.4.

The potential parameters used in this work for the crystal and hydroxyl interactions were taken from Jones et al.[8]. About 20 starting configurations per surface with hydroxyl groups in different coordinations and positions were sampled and the one with the lowest energy considered for the remainder of this study. The resulting surface structures were used to build supercells big enough to ensure no image-image interactions of the additive, which was assumed to be the case when the surface cell dimensions were about twice the size of the biggest molecule dimension.

Docking is assumed to take place by the condensation reaction experimentally observed for Al_2O_3 by Hoque et al. [33], which involves a surface hydroxyl group and a proton coming from the additive to form one water molecule. In forcefield based simulations, where speciation changes are not possible as they would be for first principle methods, this process has to be assumed and certain constraints applied in our model. Therefore the protons have been removed from the additive and the required number of hydroxyl groups manually removed from the surface. This was done by sampling the hydroxylated surface for all possible combinations of OH^- groups matching the geometry of the deprotonated phosphonate groups of the additive. Two OH^- groups for each phosphonate group on the molecule were removed from the surface, creating possible sites for docking. The additive was then placed at a distance of about 2Å above the surface and the structure was allowed to relax. Potentials for the intra-additive and the additive-surface interactions were taken from the ESFF forcefield [37] obtained from MSI [38]. The complete forcefield is given in annex A. In order to sample configurational space, around 30 configurations per surface and additive with different arrangements of the removed surface hydroxyl groups as well as different starting positions of the additive were run, only the one with the lowest energy being taken into account for the remainder of this study.

The surface and attachment energy of the hydroxylated surfaces were calculated, the surface energy being corrected for the presence of the hydroxyl groups by the method developed by de Leeuw et al. [39] and successfully applied to hematite by Jones et al. [8]. The correction considers the energy required to dissociate a water molecule to form an OH^- group and an H^+ ion, however as this dissociation is highly material dependent, one has to use an enthalpy cycle, which takes into account the material in question. The reactions considered in this work are given in table 3.2. One has to consider the difference in formation energies observed experimentally (letter F in table 3.2) and the ones calculated from lattice energies (letter G in table 3.2). The approach used here is slightly different from Jones [8] in the respect that the correction value of 2.475eV used there is obtained from the difference of the enthalpy cycle of -1122.667kJmol^{-1} only after addition of twice the dissociative energy of the O-H Morse potential in order to correct for the self energy of the hydroxyl group, which is however not mentioned. In the present approach this O-H Morse potential is included in the calculated lattice energy of goethite and this correction is thus no longer necessary. The surface energy can then be corrected as given in equation 3.2.

Table 3.2: Enthalpy cycle and resulting correction for water dissociation in presence of hematite

	Reaction	**ΔH [kJ/mol]**
A	$2Fe^{3+} + 2O^{2-} \rightarrow Fe_2O_3$	-14516.085
B	$Fe_2O_3 \rightarrow 2Fe + \frac{3}{2}O_2$	823.411
C	$2FeOOH \rightarrow 2Fe^{3+} + 2O^{2-} + 2OH^-$	14432.098
D	$2Fe + 2O_2 + H_2 \rightarrow 2FeOOH$	-1116.290
E	$H_2O \rightarrow H_2 + \frac{1}{2}O_2$	285.830
Expt: F=D+E+B	$Fe_2O_3 + H_2O \rightarrow 2FeOOH$	-7.049
Calc: G=-C-A	$Fe_2O_3 + 2OH^- \rightarrow 2FeOOH$	83.988
Corr: F-G	$H_2O + O^{2-} \rightarrow 2OH^-$	-91.037 = -15.116 J

E_{corr} being the calculated correction energy (letter H in table 3.2), A the area of the surface cell and $\frac{1}{2}n_{\text{hydroxyl}}$ being the number of water molecules that have to be dissociated in order to get the number of hydroxyl groups observed on the surface.

$$\gamma_{\text{corr}} = \gamma_{\text{raw}} + \frac{\frac{1}{2}n_{\text{hydroxyl}}E_{\text{corr}}}{A} \tag{3.2}$$

The attachment energy describes how much energy is consumed when a formula unit of crystal is added onto the surface. The more negative this energy is, the faster the face will grow and the likelier it is that it will be eliminated by overlapping from the slower growing faces. A morphology calculated based on the surface energy will give the equilibrium shape whereas the attachment energy based morphology will best describe a morphology dominated by growth.

For each of the docking simulations, the replacement energy as defined by Rohl et al. [40] given by equation 3.3 was calculated.

$$E_{\text{repl}} = (E_{\text{latt+add}} + nE_{\text{OH}} + nE_{\text{OH}}^{\text{solv}} - (E_{\text{latt}} + E_{\text{add}} + E_{\text{add}}^{\text{solv}}) \tag{3.3}$$

In this equation, $E_{\text{latt+add}}$ is the energy of the docked configuration, E_{latt} is the energy of the hydroxylated surface without additive. E_{OH} is the energy of the isolated hydroxyl group and E_{add} that of the isolated additive molecule. The solvation energies ($E_{\text{OH}}^{\text{solv}}$ and $E_{\text{add}}^{\text{solv}}$) were calculated using the COSMO model [41].

Finally in order to get an idea of the morphology change the surface energy in presence of the additive has been approximated by equation 3.4 which calculates the change in surfaces energy weighted by replacement energies, the magnitude of which is controlled by the maximum change in surface energy ($\Delta\gamma_{\mathrm{max}}$).

$$\gamma_{\text{surf, additive, } i} = \gamma_i + \Delta\gamma_{\mathrm{max}} \frac{E_{\text{repl, } i}}{E_{\mathrm{repl}}^{\mathrm{max}}} \tag{3.4}$$

3.3 Experimental validation

Synthesis of the hematite was carried out by mixing 100ml of a 2M $FeCl_3$ (Sigma) solution with 100ml of a 6M NaOH (Univar) solution, which resulted in the immediate precipitation of the metastable precursor ferrihydrite. A screening of the iron supersaturation was performed by placing the ferrihydrite in pyrex bottles adjusting the iron concentration by adding water. The pH was adjusted to 9 by adding concentrated HCl. The bottle was then placed in an oven at 98 °C for 7 days in order for the transformation into the more stable hematite to take place. Samples were washed by centrifugation, twice in water and twice in ethanol. For synthesis using the additive, an aqueous solution of the additive was added in the desired amount before pH adjustment. X-ray diffraction (XRD) spectra were recorded in order to verify that the phase produced was hematite. Samples for microscopy were prepared from very dilute dispersions of the powders in methanol, a small amount of which was placed on the sample holder after disagglomeration in an ultrasonic bath. The samples were gold coated in order to avoid charging effects in the microscope.

3.4 Results & Discussion

The morphology of the hematite particles without the additive was determined computationally. Table 3.3 gives the surface and attachment energies for the investigated surfaces.

In the following, a brief description of the structural features of the surfaces will be given. The (110) surface is oxygen terminated and presents a rather low surface energy of 0.75Jm^{-2}. The surface energies found in literature range from 0.55Jm^{-2} [6] to 2.41Jm^{-2} [9] which places the present result within this range. The hydroxyl groups are formed in non-bridging configurations with the surface oxygen atoms found to relax slightly back into the surface. The (112) surface is iron terminated, the surface energy 1.68Jm^{-2} being again situated within the values reported in literature which range from 1.03Jm^{-2} [6] to 2.36Jm^{-2} [2]. The hydroxyl groups are formed in non-bridging configurations. The oxygen terminated $(10\bar{1})$ surface shows a surface energy of 0.79Jm^{-2} which lies again in the range of 0.81Jm^{-2} [6] and 2.03Jm^{-2} [2]

Table 3.3: Surface and attachment energies of the investigated surfaces. For the (102) surface, two terminations have been investigated the results of which are given separated by slashes.

	Surf Energy [Jm^{-2}]		**Attach Energy [eV/unit]**	
Surface	**Unhydrox**	**Hydrox**	**Unhydrox**	**Hydrox**
(100)	1.15	0.75	-6.58	-6.54
(112)	1.68	1.01	-22.89	-19.37
($10\bar{1}$)	0.98	0.82	-8.26	-2.59
(222)	0.79	1.28	-15.05	-0.18
(102)	1.24 / 1.02	0.54 / 0.90	-24.16 / -26.50	-27.15 / -1.44
(411)	1.46	0.75	-79.75	-11.64

reported in literature. The (222) basal plane is the surface which has been by far the most investigated in the past. Surface energies reported range from $0.55Jm^{-2}$ [6] to $2.41Jm^{-2}$ [10] for the iron terminated structure, which is investigated here, placing the $0.79Jm^{-2}$ found in the present work within this range. The terminal iron atom is fully coordinated by accepting 3 hydroxyl groups and due to their presence relaxes out of the surface by about 0.75Å. For the (102) surface, the iron terminated surface (second termination, $1.02Jm^{-2}$) is found to be more stable than the oxygen terminated surface ($1.24Jm^{-2}$). However the surface energy is lower than the $1.58Jm^{-2}$ to be found in literature [6]. Hydroxyl groups on the iron terminated surface are found in non bridging configurations presenting again hydrogen bonds. For the oxygen terminated surface, bridging hydroxyl groups seem to be the most stable showing again the hydrogen bonds. The (411) was reported to have a surface energy of $2.8Jm^{-2}$ [9] which does not correspond very well to the $1.46Jm^{-2}$ found in the present study. A reason for this may be a significantly different potential model. The surface considered in this work is iron terminated with hydroxyl groups in a combination of bridging and non-bridging configurations. For all surfaces stabilization by formation of hydrogen bonds within the hydroxyl oxygen atoms and the hydrogen atoms adsorbed to surface oxygen atoms was observed.

It can be seen that the (222) surface does not lower its surface energy after being hydroxylated, which is consistent with experimental observations by Kurtz and Henrich [42] and Jones et al. [8] but also contradicts the fact that the basal plane is generally assumed to be highly reactive as discussed by Hartmann [29]. Also de Leeuw and Cooper [11] suggest that the fully hydroxylated basal plane considered here may be unfavorable when compared to only a partial hydroxylation. The slight difference in surface energy of the (222) surface compared to Jones [8] may be due to the use of different software including an improved minimiser able to find more favorable configurations. Therefore the (222) surface was considered to

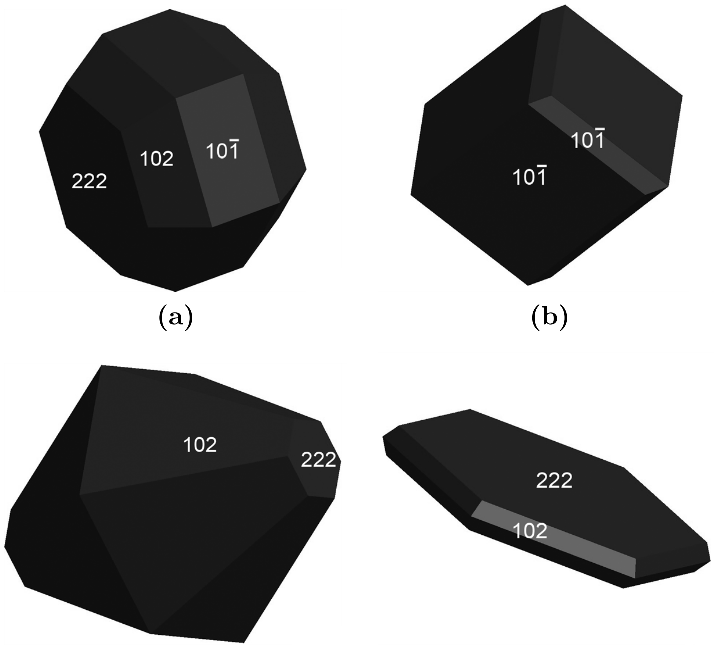

(a) (b)

(c) (d)

Figure 3.2: The morphologies calculated from the energies given in table I: (a) Unhydroxylated equilibrium morphology, (b) unhydroxylated growth morphology, (c) hydroxylated equilibrium morphology and (d) hydroxylated growth morphology.

remain unhydroxylated and the morphology calculations were performed with the unhydroxylated surface energy only. All the other surfaces can lower their surface energy to some extent by accepting a certain number of dissociated water molecules at the surface as has also been observed by de Leeuw and Cooper. The use of these energies results in the calculated morphologies given in figure 3.2.

As can be seen the four predicted equilibrium or growth morphologies, hydroxylated or not, are very different. The unhydroxylated equilibrium morphology shows a hexagonal habit with the appearance of (10$\bar{1}$) facets. Once the hydroxyl groups are attached to the surface, these facets disappear and the basal plane gets less dominant in the morphology. The growth morphology is predicted to be cubic with trimmed edges without hydroxyls present at the surface. When hydroxyls are taken into account, the morphology is predicted to be a platelet like hexagonal habit. For our synthesis method which is a hydrothermal route at 98°C for 1 week, an equilibrium morphology (figure 3.2c) rather than a growth morphology (figure 3.2d) would be expected. As it has been mentioned before the unhydroxylated (222) surface is more stable than the hydroxylated one, which is why all the morphologies in this work are calculated with the surface in the unhydroxylated state. However if the hydroxylated (222) surface is considered for morphology calculations, the (222) faces disappear from the morphology in figure 3.2c, which then consists solely of (102)

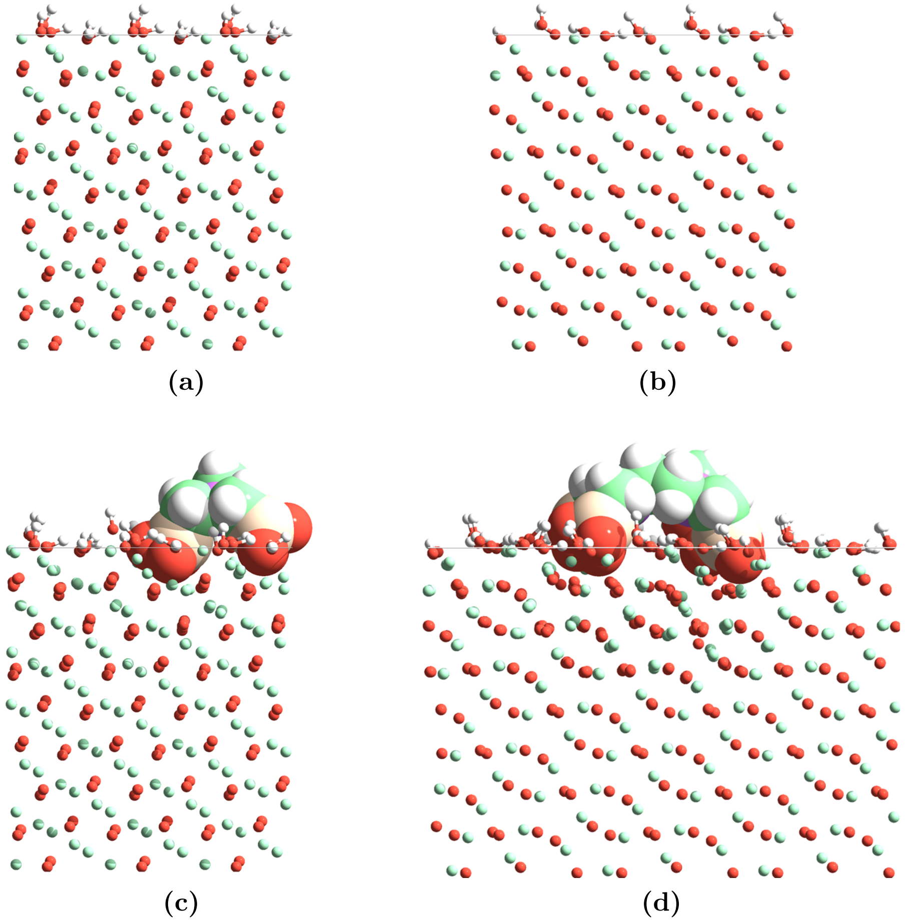

Figure 3.3: Structures of the surface layer of the hydroxylated (102) surface viewed along (a) the b vector of the surface lattice, (b) the a vector of the surface lattice, (c) with the additive MNDP along the b vector and (d) with the EDTP additive along the a vector. Color code: green=iron&carbon, red=oxygen, white=hydrogen, purple=nitrogen and ocher=phosphorus

faces. The particles prepared at pH 9 during this work (figure 3.7) show a morphology that corresponds well to the one predicted in figure 3.2c from our calculations. The morphology appears to consist of a hexagonal bipyramid of (102) faces capped with (222) basal planes at both ends, although further TEM studies in diffraction mode would be required in order to confirm the crystallographic faces. The hematite morphologies determined by Reeves and Mann [5] and Jones et al. [31] contain hexagonal (10$\bar{1}$4 surfaces which correspond to (211) surfaces in the rhombohedral system. The morphologies calculated in this work do not exhibit this particular face which is probably due to the strongly acidic ionic environment (pH 2) used during their synthesis.

In the next step, the affinity of the different surfaces for the two additives was determined. Figure 3.3 gives the structures of the surface layer of the (102) surface

Table 3.4: Replacement energies of the investigated surfaces

	Replacement Energy [eV]	
Surface	**MNDP**	**EDTP**
(100)	-10.47	-18.91
(112)	-9.22	-14.11
(10$\bar{1}$)	-6.81	-20.47
(222)	-14.67	-24.18
(102)	-6.70 / -7.53	-11.36 / -15.05
(411)	-8.25	-15.05

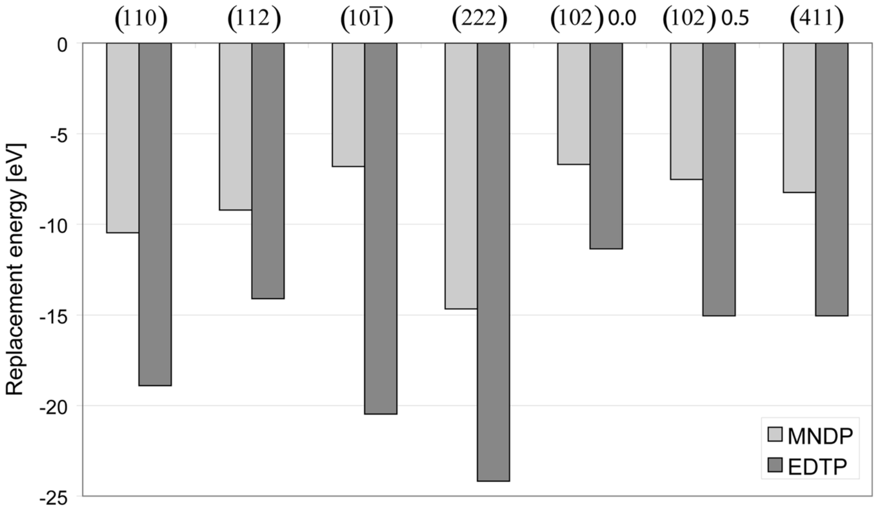

Figure 3.4: Replacement energies of MNDP and EDTP on the surfaces investigated. For the (102) surface both of the investigated surface terminations are given.

viewed along the two vectors of the surface lattice and with the MNDP and EDTP additives docked in the most favorable configuration.

The affinity is given by the replacement energies given in table 3.4 and represented graphically in figure 3.4. The replacement energies may seem high, but are comparable to simulations of the same additives on barium sulphate surfaces [43]. In that work, it was demonstrated that the absolute magnitude of the replacement energies is strongly dependent on the potential used, however the relative magnitude is retained for different potential sets. Another point to keep in mind is that the solvation model is not completely adequate. In fact the additive is considered to be either in gas phase (on the surface) or completely solvated (when away from the surface) whereas in reality it would still be partly solvated when in contact with the surface. The solvation energy could be better evaluated using molecular dynamics simulations, however at a much higher computational cost. A third point is that the replacement energy as given in equation 5 considers the hydroxyl groups to be removed to infinite separation both from the surface as well as each other. There will be an energy gain due to the spatial separation of these charged groups, which will make the left term is equation 3.3 more negative for an increasing number of phosphonate groups. The right term does not undergo this same change as the charged groups on the molecule are confined in space by the bonding structure of the molecule. With these limitations in mind, the present approach serves as a good first approximation giving an idea of the general trend, as the results should only be shifted by an additive constant. The basal plane has a significant affinity for both additives. The major difference between the two additives is the affinity of the EDTP for the $(10\bar{1})$ surface, which has one of the lowest affinities for the MNDP additive. The morphological dominant (102) faces do not exhibit a high affinity for neither of the additives. This data suggests the basal plane will get more dominant in the morphology due to the presence of either additive. Stabilization of the (110) and (411) faces but not of the (102) face would eventually lead to a partial replacement of the (102) surfaces by (110) or (411) surfaces having a similar orientation relative to the basal plane. The surface energy morphology model shows however that a relatively high stabilization of about $-0.2\mathrm{Jm}^{-2}$ is needed in order to make this replacement likely. A slight change in angle between the basal plane and the pyramidal faces would be expected due to this replacement. Due to the spatial arrangement of the crystal planes, appearance of the (110) and (411) faces would be on every second of the pyramidal edges, the (411) faces quickly leading to the appearance of a triangular basal plane. The affinity of the EDTP for the $(10\bar{1})$ faces leads to the formation of a mid level band of $(10\bar{1})$ faces perpendicular to the basal plane around the particles. A more rigorous evaluation of the morphological changes is however not possible as the surface energy would have to be corrected for the presence of hydroxyl groups and the additive but the material dependent dissociation of the additive is unknown. However, an idea of the modified morphologies has been obtained by slightly modifying the surface energies proportional to their respective replacement energy. It must be clearly stated that these morphologies, which are shown in figure 3.5.

An analysis of the surface structures and the resulting attachment energies revealed that the main reason for the affinity of an additive for a specific face is a close match in geometry between the hydroxyl groups of the surface and the functional groups of the additive. Surface structures which lead to a large distortion of the molecule are not favored. This means that a purely geometric analysis of the surface structure and the additive can give a first indication of the degree of affinity of a certain additive. The same analysis also showed that the zone between the docking

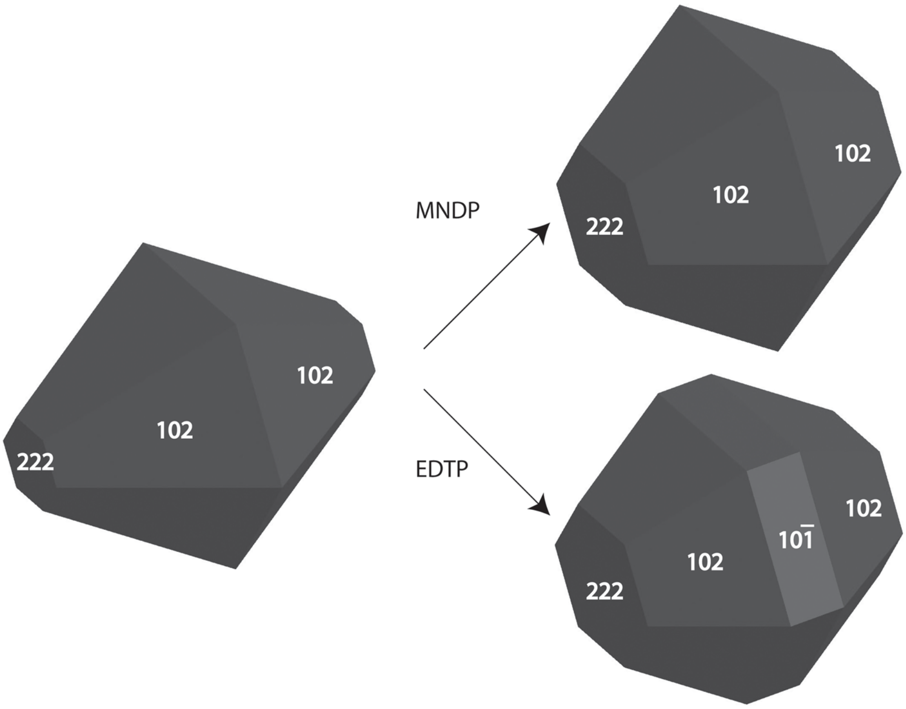

Figure 3.5: Changes of the equilibrium morphology due to the presence of the two additives as it can be estimated from the respective replacement energies.

sites plays an important role due to the steric effects between surface groups and the additive. Surfaces which have a certain roughness at the length-scale of the additive inhibit the docking of shorter molecules by repulsion between the backbone part of the additive and the surface atoms. This effect was observed to be more severe for the quite small MNDP, whereas the EDTP has a longer and thus more flexible backbone enabling it to dock on atomically rougher i.e. micro-faceted surfaces.

The XRD data shown in figure 3.6 clearly show that hematite is formed under all of the conditions explored in this work. The theoretical data used for comparison has been calculated from the crystal structure used for the modeling part of this work.

We have recorded scanning electron microscope (SEM) as well as transmission electron microscopy (TEM) micrographs of the powders synthesized in the laboratory. SEM imaging of the powders synthesized without additive proved to be extremely difficult due to their high degree of agglomeration as can be seen in figure 3.7a. Few particles with facets can be distinguished - however it was decided to record TEM images shown in figure 3.7b of the same sample in order to get a better idea of the morphology. Figure 3.7b) clearly shows a faceted morphology with parallel faces terminating the particles at two sides. However the overall morphology seems to be rather ill-defined, which indicates that the surface energies may be quite

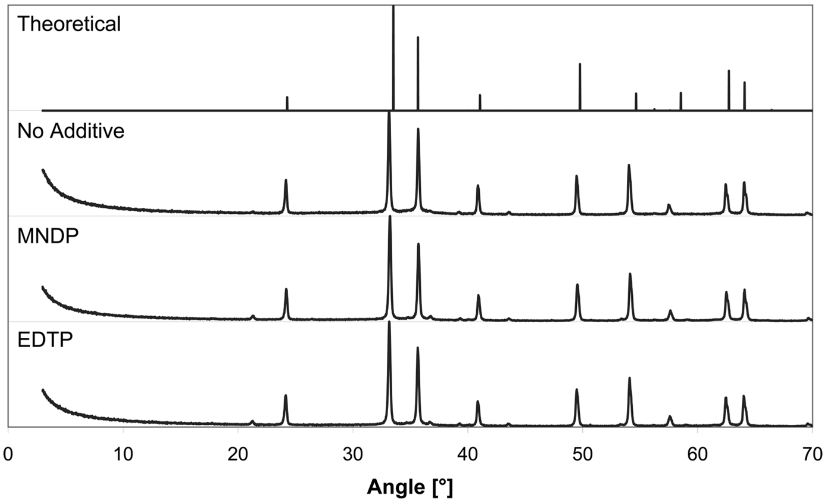

Figure 3.6: XRD spectra of the synthesized powders. It can be seen that hematite is formed under all conditions.

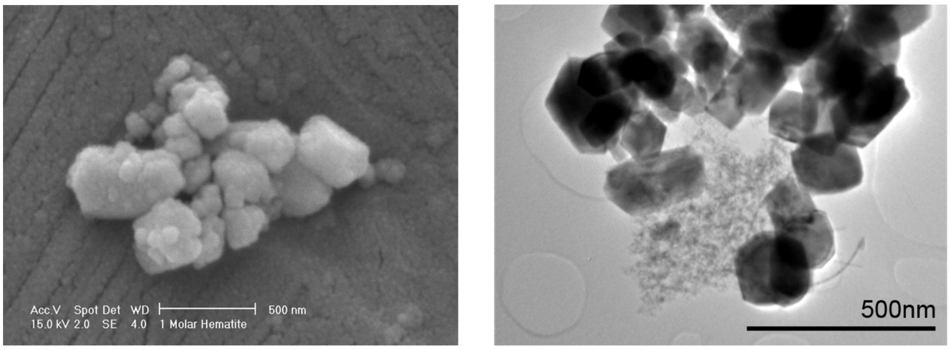

(a) **(b)**

Figure 3.7: Morphology of the unmodified hematite, recorded by (a) SEM and (b) TEM.

similar, not resulting in the development of a clearly defined morphology.

In presence of additives the morphologies are well defined faceted shapes as can be seen in figure 3.8 for the MNDP and figure 3.9 for the EDTP. This suggests an accentuation of the difference in surface energies by selective stabilization of one or more of the faces. The morphologies developed in presence of the two additives are similar except for the appearance of small facets perpendicular to the basal plane along the sides of the particles in the presence of EDTP. Both experimental morphologies shown in figures 3.8 and 3.9 closely match the predicted morphologies shown in figure 3.5, are not based on real calculated surface energies and have to be understood as an estimation only.

In order to get an idea of the faces involved, angular measurements have been performed, where the particles could be assumed to be projected close to perpen-

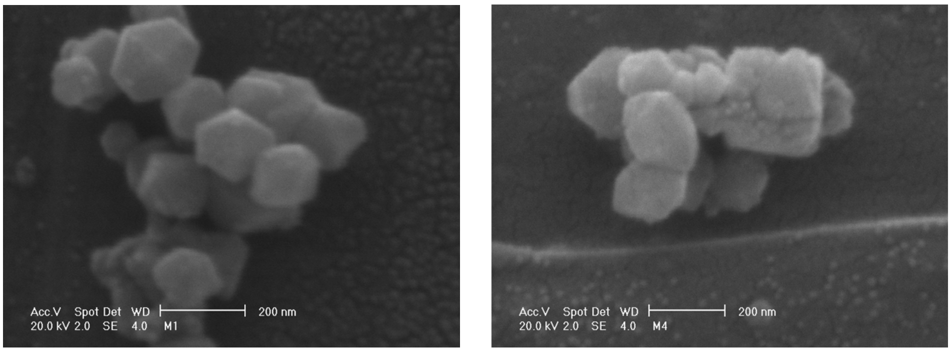

(a) **(b)**

Figure 3.8: Morphology of MNDP modified hematite recorded by SEM

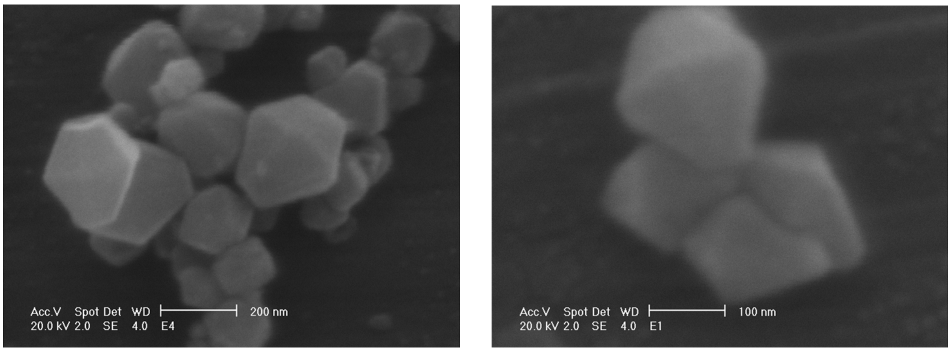

(a) **(b)**

Figure 3.9: Morphology of EDTP modified hematite recorded by SEM

Table 3.5: Interplanar angles of the calculated hematite surfaces calculated from the crystal structure.

	(110)	(112)	$(10\bar{1})$	(222)	(102)	(411)
(110)	-	-	-	-	-	-
(112)	95.01	-	-	-	-	-
$(10\bar{1})$	43.28	112.02	-	-	-	-
(222)	57.20	37.81	90.00	-	-	-
(102)	111.82	31.94	115.89	60.84	-	-
(411)	49.71	80.20	43.28	57.20	74.70	-

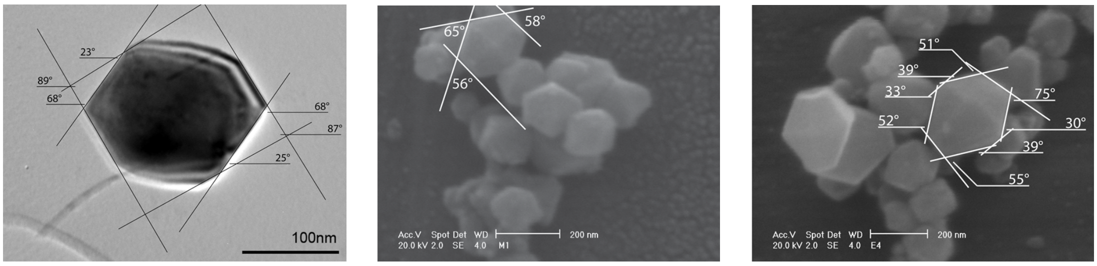

(a) **(b)** **(c)**

Figure 3.10: Angular measurements between faces of ideally oriented hematite nanoparticles (a) in their unmodified state, (b) modified with MNDP and (c) modified with EDTP.

dicular. This technique can be used to get a first validation only and indexing in TEM diffraction mode should give more insights. When compared to the theoretical angles given in table 3.5, measurements on the unmodified particles (figure 3.10a) suggest the presence of (222), (102) and maybe (411) faces. It is however difficult to be certain on the particle orientation in this TEM image. When modified with the additives no additional pyramidal faces seem to appear only (222) and (102) faces appearing in the morphology. This suggests that the stabilization by the additive is not high enough to lead to replacement of the (102) faces by either (110) or (411) faces. The small faces appearing on the sides in presence of the EDTP (figure 3.10c) are perpendicular to the (222) faces and are thus attributed to $(10\bar{1})$ faces.

The agreement between experimental data and the computational model is excellent as the appearance of the $(10\bar{1})$ faces are predicted for the EDTP additive but not the MNDP additive.

3.5 Conclusions

Atomistic simulations have been performed on seven surfaces likely to appear in experimental hematite morphologies, looking at their hydroxylated surface structure and surface energy. From this the equilibrium morphology in the hydroxylated state was predicted. Experimental synthesis without the additive did not show a clear morphology, however angular measurements on some of the more faceted particles seem to validate the morphologies calculated. When additives were used during the synthesis the morphology became more well defined however no additional pyramidal faces appear in the morphology, which suggests that stabilization is not high enough to favor the formation of either (110) or (411) faces. However the development of a mid-level band of $(10\bar{1})$ faces can be observed experimentally in the presence of the EDTP additive, but not for the MNDP additive. The computational model predicts a three times higher affinity of the EDTP for this particular face, indicating a much higher probability of formation of $(10\bar{1})$ faces in presence of EDTP than MNDP. The main reason for the selective docking behavior is the surface geometry. Large distortions of the additives to allow adsorption on some surfaces are not energetically favorable. Surfaces with a rough atomic structure can make the docking of the additive more difficult, which is especially marked for the smaller MNDP additive, the EDTP being bigger and more flexible is able to span rougher surfaces.

The current approach presents a way to rapidly calculate the interaction of additives with mineral surfaces. However the effect of water is only implicitly taken into account and chemical reactions are anticipated. This together with the fact that during energy minimization the rotational and translational degrees of freedom of the additive are limited leads to limitations in the variety of configurations which can be visited by the system, thus requiring a high number of calculations in order to ensure finding the global energy minimum.

The agreement between calculations and experiment is excellent, validating the use of this technique as a predictive tool for the synthesis of tailor shapes nanocrystals. By extending the number of additives calculated in a systematic way, one could build a database with the ambitious goal of creating a tool for the determination of additives or even additive mixtures which will result in a given desired morphology. The application of the insights gained by the present work to the synthesis of a technologically important material such as hematite could lead to the control of growth of nanoparticles as well as the development of auto-assembly operations due to specific interactions and the development of novel high performance materials such as extremely high specific surface area solid catalysts.

Bibliography

[1] R. M. Cornell and U. Schwertmann. *The Iron Oxides*. VCH Verlagsgesellschaft mbH, Weinheim, Germany, 2003.

[2] W. C. Mackrodt, R. J. Davey, S. N. Black, and R. Docherty. The morphology of α-Al_2O_3 and α-Fe_2O_3 - the importance of surface relaxation. *Journal of Crystal Growth*, 80(2):441–446, 1987.

[3] W. C. Mackrodt. Atomistic simulation of oxide surfaces. *Physics and Chemistry of Minerals*, 15(3):228–237, 1988.

[4] W. C. Mackrodt. Atomistic simulation of the surfaces of oxides. *Journal of the Chemical Society-Faraday Transactions II*, 85(5):541–554, 1989.

[5] N. J. Reeves and S. Mann. Influence of inorganic and organic additives on the tailored synthesis of iron-oxides. *Journal of the Chemical Society-Faraday Transactions*, 87(24):3875–3880, 1991.

[6] A. L. Rohl and D. H. Gay. Calculating the effects of surface relaxation on morphology. *Journal of Crystal Growth*, 166(1-4):84–90, 1996.

[7] E. Wasserman, J. R. Rustad, A. R. Felmy, B. P. Hay, and J. W. Halley. Ewald methods for polarizable surfaces with application to hydroxylation and hydrogen bonding on the (012) and (001)surfaces of α-Fe_2O_3. *Surface Science*, 385(2-3):217–239, 1997.

[8] F. Jones, A. L. Rohl, J. B. Farrow, and W. van Bronswijk. Molecular modeling of water adsorption on hematite. *Physical Chemistry Chemical Physics*, 2(14):3209–3216, 2000.

[9] D. J. Cooke, S. E. Refern, D. J. Osguthorpe, and S. C. Parker. Structure and stability of iron oxide surfaces and their reactivity with water. *Radiation Effects and Defects in Solids*, 156(1-4):75–79, 2001.

[10] D. J. Cooke, S. E. Redfern, and S. C. Parker. Atomistic simulation of the structure and segregation to the (0001) and ($01\bar{1}2$) surfaces of Fe_2O_3. *Physics and Chemistry of Minerals*, 31(8):507–517, 2004.

[11] N. H. de Leeuw and T. G. Cooper. Surface simulation studies of the hydration of white rust $Fe(OH)_2$, goethite α-FeO(OH) and hematite α-Fe_2O_3. *Geochimica Et Cosmochimica Acta*, 71(7):1655–1673, 2007.

[12] X. G. Wang, W. Weiss, S. K. Shaikhutdinov, M. Ritter, M. Petersen, F. Wagner, R. Schlögl, and M. Scheffler. The hematite (α-Fe_2O_3) (0001) surface: Evidence for domains of distinct chemistry. *Physical Review Letters*, 81(5):1038–1041, 1998.

[13] S. K. Shaikhutdinov and W. Weiss. Oxygen pressure dependence of the α-Fe_2O_3(0001) surface structure. *Surface Science*, 432(3):L627–L634, 1999.

[14] W. Bergermayer, H. Schweiger, and E. Wimmer. Ab initio thermodynamics of oxide surfaces: O_2 on $Fe_2O_3(0001)$. *Physical Review B*, 69(19):195409, 2004.

[15] O. Warschkow, D. E. Ellis, J. H. Hwang, N. Mansourian-Hadavi, and T. O. Mason. Defects and charge transport near the hematite (0001) surface: An atomistic study of oxygen vacancies. *Journal of the American Ceramic Society*, 85(1):213–220, 2002.

[16] F. Alvarez-Ramirez, J. M. Martinez-Magadan, J. R. B. Gomes, and F. Illas. On the geometric structure of the (0001) hematite surface. *Surface Science*, 558(1-3):4–14, 2004.

[17] A. Rohrbach, J. Hafner, and G. Kresse. Ab initio study of the (0001) surfaces of hematite and chromia: Influence of strong electronic correlations. *Physical Review B*, 70(12):125426, 2004.

[18] C. M. Eggleston, A. G. Stack, K. M. Rosso, S. R. Higgins, A. M. Bice, S. W. Boese, R. D. Pribyl, and J. J. Nichols. The structure of hematite (α-Fe_2O_3) (001) surfaces in aqueous media: Scanning tunneling microscopy and resonant tunneling calculations of coexisting O and Fe terminations. *Geochimica Et Cosmochimica Acta*, 67(5):985–1000, 2003.

[19] C. M. Eggleston, A. G. Stack, K. M. Rosso, and A. M. Bice. Adatom Fe(III) on the hematite surface: Observation of a key reactive surface species. *Geochemical Transactions*, 5(2):33–40, 2004.

[20] C. Lemire, S. Bertarione, A. Zecchina, D. Scarano, A. Chaka, S. Shaikhutdinov, and H. J. Freund. Ferryl (Fe=O) termination of the hematite α-$Fe_2O_3(0001)$ surface. *Physical Review Letters*, 94(16):166101, 2005.

[21] C. H. Rochester and S. A. Topham. Infrared study of surface hydroxyl-groups on hematite. *Journal of the Chemical Society-Faraday Transactions I*, 75:1073–1088, 1979.

[22] G. Busca and V. Lorenzelli. IR characterization of surface hydroxy-groups on hematite. *Reaction Kinetics and Catalysis Letters*, 15(2):273–278, 1980.

[23] M. A. Henderson, S. A. Joyce, and J. R. Rustad. Interaction of water with the (1x1) and (2x1) surfaces of α-$Fe_2O_3(012)$. *Surface Science*, 417(1):66–81, 1998.

[24] T. P. Trainor, A. M. Chaka, P. J. Eng, M. Newville, G. A. Waychunas, J. G. Catalano, and G. E. Brown. Structure and reactivity of the hydrated hematite (0001) surface. *Surface Science*, 573(2):204–224, 2004.

[25] K. S. Tanwar, C. S. Lo, P. J. Eng, J. G. Catalano, D. A. Walko, G. E. Brown, G. A. Waychunas, A. M. Chaka, and T. P. Trainor. Surface diffraction study of the hydrated hematite $(1\bar{1}02)$ surface. *Surface Science*, 601(2):460–474, 2007.

[26] C. S. Lo, K. S. Tanwar, A. M. Chaka, and T. P. Trainor. Density functional theory study of the clean and hydrated hematite $(1\bar{1}02)$ surfaces. *Physical Review B*, 75(7):075424, 2007.

[27] V. Barron and J. Torrent. Surface hydroxyl configuration of various crystal faces of hematite and goethite. *Journal of Colloid and Interface Science*, 177(2):407–410, 1996.

[28] J. R. Rustad, E. Wasserman, and A. R. Felmy. Molecular modeling of the surface charging of hematite: II. optimal proton distribution and simulation of surface charge versus pH relationships. *Surface Science*, 424(1):28–35, 1999.

[29] P. Hartman. The effect of surface relaxation on crystal habit - cases of corundum (α-Al_2O_3) and hematite (α-Fe_2O_3). *Journal of Crystal Growth*, 96(3):667–672, 1989.

[30] L. Mazeina and A. Navrotsky. Enthalpy of water adsorption and surface enthalpy of goethite (α-FeOOH) and hematite (α-Fe_2O_3). *Chemistry of Materials*, 19(4):825–833, 2007.

[31] F. Jones, M. I. Ogden, A. Oliveira, G. M. Parkinson, and W. R. Richmond. The effect of phosphonate-based growth modifiers on the morphology of hematite nanoparticles formed via acid hydrolysis of ferric chloride solutions. *CrystEngComm*, 5(30):159–163, 2003.

[32] B. C. Barja, J. Herszage, and M. D. Alfonso. Iron(III)-phosphonate complexes. *Polyhedron*, 20(15-16):1821–1830, 2001.

[33] E. Hoque, J. A. DeRose, P. Hoffmann, H. J. Mathieu, B. Bhushan, and M. Cichomski. Phosphonate self-assembled monolayers on aluminum surfaces. *Journal of Chemical Physics*, 124(17):174710, 2006.

[34] S. Fleming and A. Rohl. GDIS: a visualization program for molecular and periodic systems. *Zeitschrift für Kristallographie*, 220(5-6):580–584, 2005.

[35] J. D. Gale and A. L. Rohl. The general utility lattice program (GULP). *Molecular Simulation*, 29(5):291–341, 2003.

[36] B. G. Dick and A. W. Overhauser. Theory of the dielectric constants of alkali halide crystals. *Physical Review*, 112(1):90–103, 1958.

[37] S. H. Shi, L. Yan, Y. Yang, J. Fisher-Shaulsky, and T. Thacher. An extensible and systematic force field, ESFF, for molecular modeling of organic, inorganic, and organometallic systems. *Journal of Computational Chemistry*, 24(9):1059–1076, 2003.

[38] MSI. Insight II, 2003.

[39] N. H. de Leeuw, G. W. Watson, and S. C. Parker. Atomistic simulation of the effect of dissociative adsorption of water on the surface-structure and stability of calcium and magnesium-oxide. *Journal of Physical Chemistry*, 99(47):17219–17225, 1995.

[40] A. L. Rohl, D. H. Gay, R. J. Davey, and C. R. A. Catlow. Interactions at the organic/inorganic interface: Molecular modeling of the interaction between diphosphonates and the surfaces of barite crystals. *Journal of the American Chemical Society*, 118(3):642–648, 1996.

[41] A. Klamt and G. Schüürmann. Cosmo - a new approach to dielectric screening in solvents with explicit expressions for the screening energy and its gradient. *Journal of the Chemical Society-Perkin Transactions II*, (5):799–805, 1993.

[42] R. L. Kurtz and V. E. Henrich. Surface electronic-structure and chemisorption on corundum transition-metal oxides - α-Fe_2O_3. *Physical Review B*, 36(6):3413–3421, 1987.

[43] F. Jones, W. R. Richmond, and A. L. Rohl. Molecular modeling of phosphonate molecules onto barium sulfate terraced surfaces. *Journal of Physical Chemistry B*, 110(14):7414–7424, 2006.

Chapter 4

Growth modification and steric stabilization by macromolecules

> **Everything that living things do can be understood in terms of the jiggling and wiggling of atoms.** – Richard Feynman

In this chapter the growth modification by macromolecules will be investigated. As these larger molecules can also have an effect on the steric repulsion between particles, this aspect will be looked at as well as other growth related aspects already seen in the previous chapter.

The system to be studied here is calcite and the growth modifiers are a polycarboxylic acid and a polyamino acid. In experiments significant but so far unexplainable differences between two additives of these classes were found. The present chapter has the goal of investigating the interaction of these two additives with calcite surfaces by computational means in order to gain insights into the mechanism by which they affect calcite growth and to finally understand sources for the experimentally observed differences. These insights can hopefully be used in order to design specific additives, which modify growth even stronger.

4.1 Introduction

Calcium carbonate (calcite, $CaCO_3$) is a material used in many industrial application ranging from fillers in polymers [1] trough paint pigments to catalysts [2], with changing requirements towards the phases (aragonite, vaterite, calcite), the particle size and the morphology. Calcite also occurs in many living organisms, where very specific morphologies are observed [3, 4, 5, 6]. A large number of publications has been devoted to research trying to control these aspects in many reactive environments, be it industrial or biological. For biomimetic synthesis many attempts have been made to understand and reproduce structures found in carapaces of a manifold of animals.

Based on observations of living organisms it is known that organic molecules or macromolecules can have marked effects on calcite morphology development by affecting growth in very specific ways. Experimental work has looked at the influence of small polyanions (tartaric acid, $C_4H_6O_6$) and it was reported that these species can influence the nucleation but not the growth phase [7]. Contradicting results exist [8], showing that for seven small carboxylic acids no modification of nucleation but only of growth was observed. Larger molecules such as double-hydrophilic block copolymers [9, 10, 11], polyamino acids [12, 13, 14, 15, 16, 17] and polycarboxylic acids [18, 8, 19, 20, 21, 22, 23, 24, 25] were shown to be able to influence growth of calcium carbonate. The effect of these additives depends on the hydrophilic/hydrophobic structure of the polymer and it's molecular structure in general [9, 11], the ratio of polymer to calcium carbonate and the pH, which controls the state of dissociation of the polyelectrolytes [9, 18]. Phosphonate additives were also found to modify growth [26] and AFM measurements [27] showed that phosphonate additives with a different number of functional groups result in different shapes and density of steps at the surface.

Amongst the molecules cited above carboxylic acids were shown to be very effective at modifying growth of many minerals [23, 28, 29, 30, 31, 32] amongst them the calcite phase. The surface complexation of mono-, di- and tri-carboxylic acids has been studied by measuring the concentration of additive remaining in solution [19]. The results reported show that a single carboxylic group does not bind to the surface of calcite, whereas molecules with two or three carboxylic groups can bind to surface cations. This was interpreted as a surface complexation during which the carboxylic group acts a an electron donor for the surface metal cations.

Polyacrylic acid (PAA) is a polycarboxylic acid, found to have a marked effect on calcite growth and it has therefore been used extensively as a growth modifier and inhibitor [33]. This macromolecule was found to completely inhibit nucleation when present in high concentrations, which is not the case for smaller molecules such as glutamic acid [24]. The effect of PAA varies as a function of temperature, resulting in cubic morphologies at 80°C, whereas rounded particles are formed at room temperature [18]. The effect of pH was also investigates and found to be most marked for pH values around 10-11, lower values leading to insufficient dissociation of the carboxy groups and thus a low density of groups able to attach to the surface whereas higher pH values lead to uncontrolled morphologies [18]. The growth mechanism in presence of PAA is suggested to be rapid formation of many nuclei either homogeneously [20] or heterogeneously on added calcite seeds [34]. These nuclei remain small due to the rapid decrease in supersaturation and will aggregate to form larger particles. Cementation can take place, giving them the appearance of macroscopic single crystal particles, the underlying nanostructure being visible by crystallite size determination using X-ray diffraction (XRD) line broadening [34]. It was suggested that the additive can be incorporated in the substructure of the aggregated particles [34]. The amount of additive may change the type of particles formed [34] and it was suggested that different chain lengths and concentrations can favor the formation of the (104) or (001) face respectively [35]. Complex formation of PAA and calcium ions in solution was studied by looking at the gelation and deriving phase diagrams [36], by activity measurement [37] and by calorimetry [38] where the formation energy was found to be strongly endothermic even if the process occurs. The authors concluded that the driving force for complex formation must be entropic in nature. This is confirmed for surface complexation of calcite by small carboxylic polyanions where endothermic adsorption behavior was found by calorimetric measurements [39].

Polyamino acids are another group of macromolecules, which were shown to have a marked effect on the morphology of calcite and they are present during many biomineralization processes in living organisms. Polyaspartic acid (p-ASP) was found to influence growth [14, 15, 16, 17, 40] and dissolution [12, 13, 41, 42] of calcite, leading to the appearance of steps of well defined orientation. It was therefore suggested that p-ASP binds to step edges [14, 40], short chains preferring acute steps, whereas long chains bind to obtuse steps due to the equilibrium in energies required for the dehydration of the step and the one released during binding of the additive. The adsorption of a compound of similar chemistry (EDTA, $C_{10}H_{16}N_2O_8$) was found to result in strong growth inhibiting effects [43].

Experimental student work co-supervised during this PhD thesis [44, 45] compared the effect of the two additives discussed above (PAA and p-ASP) having the same number of functional groups in equivalent experimental conditions. Since the

Table 4.1: Key results obtained for calcite powders precipitated in presence of PAA and p-ASP.

Additive	R	$\mathbf{d_{v50}}$ [μm]	SSA [$\mathbf{m^2g^{-1}}$]	$\mathbf{F_{ag}}$	Yield [%]
PAA	0.027	0.43	30.3	5.3	85.9
PAA	0.037	0.52	36.2	6.5	79.3
PAA	0.110	0.41	45.3	7.7	63.1
p-ASP	0.075	0.59	70.3	18.7	-

difficulty to interpret the results obtained in these projects was the motivation to undertake the simulation work in the present chapter, the method and main results will be resumed here. Precipitation experiments were carried out at high supersaturations (S=50) in 20ml mini-batches by rapid mixing of solutions of calcium nitrate and potassium carbonate in a double syringe injection system. Calcite seed particles (<20nm) [34], which ensured the formation of the calcite phase by secondary nucleation, and the additive were added to the potassium carbonate solution. The ratio between the concentration of dissociated carboxylic acid groups and calcite ions in solution R has been used to compare the effect of the two additives. Properties measured were the median volume diameter ($\mathrm{d_{v50}}$) by laser diffraction, the specific surface area (SSA, $\mathrm{S_{BET}}$) using monolayer nitrogen adsorption within the Brunauer-Emmett-Teller (BET) model [46] and the yield of the precipitation from the amount of ions in solution and the amount of solid formed. The agglomeration factor (F_{ag}) was calculated as given in equation 4.1.

$$F_{\mathrm{ag}} = \frac{d_{\mathrm{v50}}}{d_{\mathrm{BET}}} = \frac{d_{\mathrm{v50}} S_{\mathrm{BET}} \rho}{6} \tag{4.1}$$

This factor describes the degree of agglomeration, being 1 for unagglomerated powders and larger than one if agglomeration occurred. The key results obtained by the two students are shown in table 4.1 and will be briefly discussed before continuing to the state of the art in the simulation of calcite interfaces.

An increasing PAA concentration has the effect of increasing the specific surface area. The median volume diameter does not seem to be affected in a systematic way, which suggests that the additive does not play a significant role in changing the agglomeration of the particles. This means that the primary particles have to be smaller for higher PAA concentrations, suggesting a growth suppression due to the presence of the additive. As it can be seen, with increasing PAA concentration (increasing R) the yield is reduced. This suggests that less ions can take part in the precipitation reaction and thus have to be trapped in other parts of the system. p-ASP gives a higher specific surface area than PAA, the reason for this difference not being obvi-

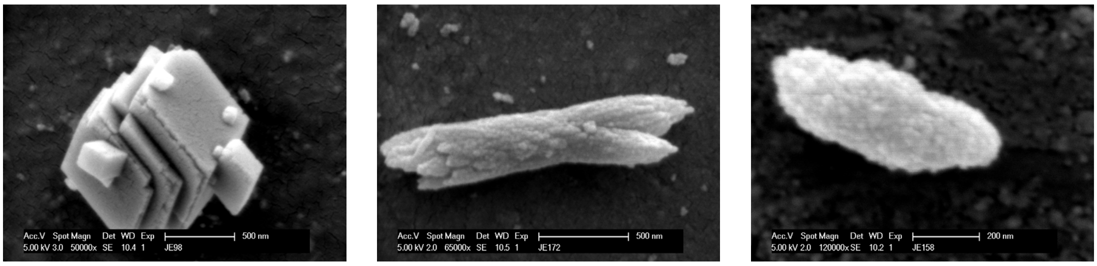

(a) (b) (c)

Figure 4.1: Powders obtained in presence of: (a) No additive, (b) polyacrylic acid (PAA) and (c) polyaspartic acid (p-ASP).

ous since both polymers will bind to the surface with the same carboxylic functional groups. One could imagine p-ASP to prevent particle agglomeration, thus conserving the nanostructure better than PAA. Figure 4.1 shows particles obtained in presence of no additive and PAA and p-ASP respectively. It can be seen that the particle morphology changes completely from a well defined faceted rhombic morphology of seemingly monocrystalline particles to particles agglomerated from smaller subunits. XRD line broadening showed the powder precipitated without additive to also have nano-sized crystallites [34], which means that cementation and surface ripening takes place. This suggests that the additives can prevent this cementation and ripening, conserving the apparent nanostructure up to the final state.

Previous atomistic simulation work on calcite looked at the equilibrium morphology in vacuum [47] and showed the morphological dominance of the (10.4) surface in absence of ionic or molecular additives. The interaction of water and certain ions was studied [48, 49], where water was found to adopt a strongly layered structure up to about 7Å above the surface. Metal ions amongst them calcium were found to be located in low water density regions between these layers, the layered structure presenting considerable free energy barriers to the approach of ions to the surface. The interaction of PAA and calcium ions in water was studied using molecular dynamics simulations [50] and partially dehydrated ions were found to interact with the additive by bridging over neighboring carboxylic acid groups. Complex formation of some alkali metals (Li, Na and K) with aspartic acid was studied using DFT [51] and it was found that lithium forms the most stable complexes in a triple coordinated fashion, whereas sodium and potassium form doubly coordinated complexes, which are slightly less stable. The adsorption of phosphonate additives was studied in vacuum on flat (10.4) and stepped surfaces, both monophosphonate [52] and diphosphonate [53] additives preferentially binding to steps, the driving force being electrostatic. Binding to steps, which are growth sites (section 1.2.1) could be an explanation for the growth modifying effect of these molecules. This is supported by calculations of the changes in step free energy upon binding of amino acids [40], which determines crystal growth together with stereochemical effects present with this class of additives. Adsorption of hydroxyl, carbonyl and amine functional group additives was studied on the flat (10.4) as well as stepped surfaces [54], showing a strong binding of hydroxyl and carbonyl groups to step edges, whereas the amine group by itself binds weaker. The authors conclude that carboxylic acids should be good growth inhibitors by binding from a step to the terrace below thus effectively blocking the growth site for further attachment of calcium and carbonate ions. The interaction of stearic acid, which belongs to the carboxylic acid group, with calcite surfaces was calculated [55] and the degree of dissociation of the polymer was found to be determinant for the strength of adsorption on different surfaces. This suggests that the pH dependent dissociation can be used to control the morphology of calcite. The adsorption of PAA on calcite (11.0) and (10.4) surfaces was previously simulated by Zhang [56] however in vacuum which is a serious limitation as will be seen below. They found that PAA adsorbs stronger than comparable additives (acrylic acid-methyl acrylate copolymer - AA-MA and polymethylacrylic acid - PMMA) and that adsorption was stronger on the (11.0) face than on the (10.4) face. As mentioned above the adsorption of polyaspartic acid on step edges was calculated [14] and longer molecules were found to prefer binding to obtuse steps, whereas shorter ones bind to acute ones. The reason being the energy required to dehydrate the step compared to the binding energy. This means that different length polyaspartic acid molecules can be used as so called stereochemical switches which control the morphology due to selective blocking of either acute or obtuse steps.

It should be noted that all these simulations were carried out on bare calcite surfaces, some however in presence of water. The surface chemistry of calcite was shown to be governed by hydrolysis [57, 58], where the resulting H^+ and OH^- species chemisorb to the surface by binding with the dangling bonds created by the cleavage. CO_2 is also known to react with hydroxyl groups at the surface prior incorporation into the crystal as CO_3^{2-} [59]. It would therefore be important to include these effects in simulations, which are however often neglected in classical forcefield based simulations, so also in the present work.

From the existing simulation data it is not possible to see the difference between PAA and p-ASP and thus in order to better understand the PAA/p-ASP - calcite system and to be able to take advantage of the difference between the two additives to further increase the specific surface area with specifically designed additives, molecular dynamics simulations have been undertaken. As outlined above, key aspects to be investigated are the attachment of the additives to the surface of calcite,

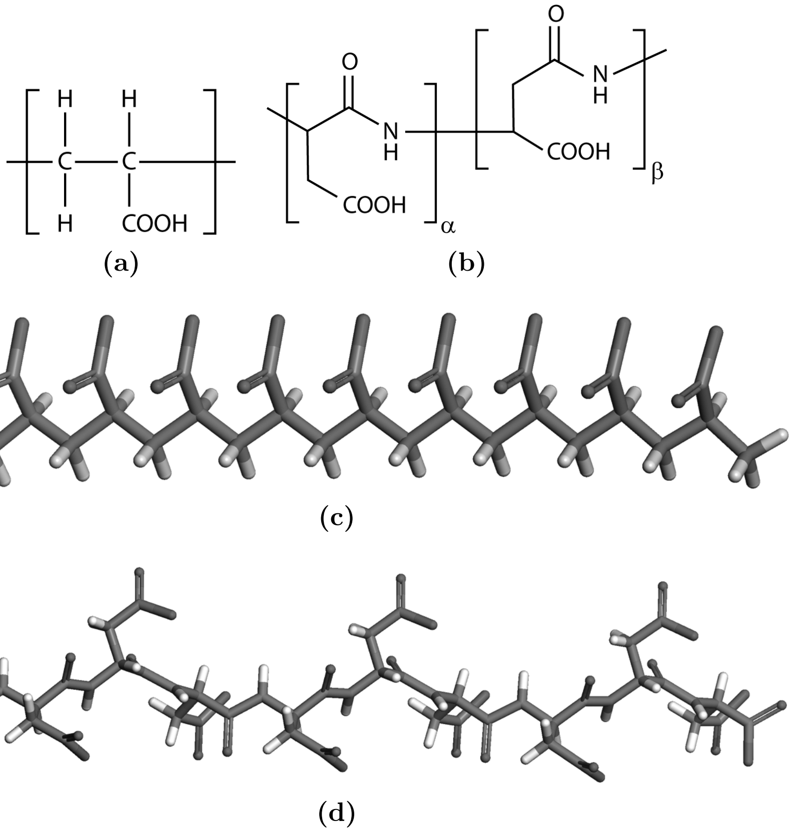

Figure 4.2: The additives looked at: (a) PAA repeat unit, (b) α and β p-ASP repeat units, (c) PAA 10 repeat unit oligomere and (d) p-ASP 10 repeat unit oligomere.

the interaction of ions and additives in solution and the effect of steric repulsion due to the polymers.

4.2 Approach

The molecular structure of the PAA repeat unit is shown in figure 4.2a. p-ASP occurs in two forms α and β, which differ in the polymerization point along the backbone (figure 4.2b). Experimentally both forms are observed concurrently, the α form being observed for about 30% of the repeat units and the β form making up the remaining 70% [60]. For the reason of its higher abundance β-p-ASP has been chosen for the calculations carried out here. The additives looked at in this work were both 10-meres of PAA (figure 4.2c) and β-p-ASP (figure 4.2d). Calcite surfaces studied were the flat (10.4) surface (figure 4.3a) as well as the same surface presenting an acute step (figure 4.3b).

The forcefield used in the present simulations has been assembled from multiple sources since at the time of starting this work no complete forcefield was published.

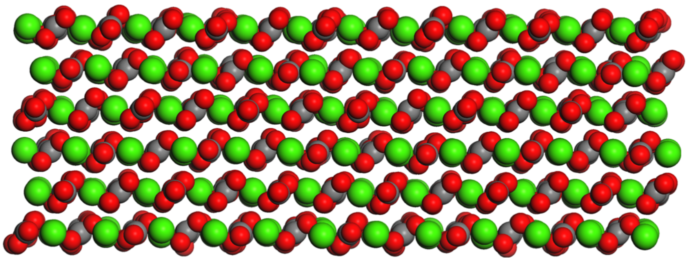

(a)

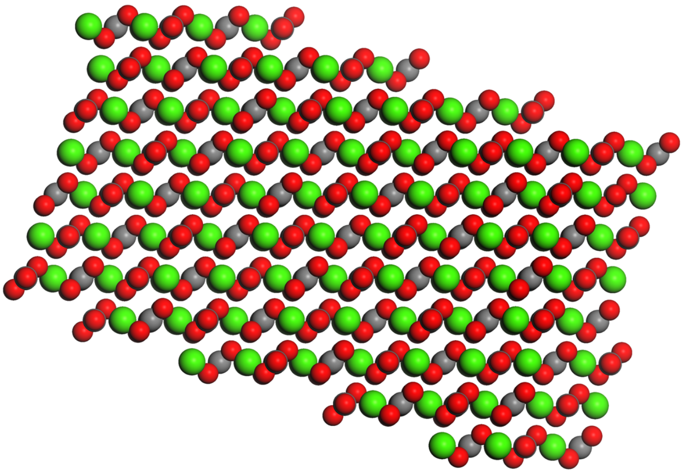

(b)

Figure 4.3: Calcite surfaces: (a) Flat (10.4) surface and (b) acute step (10.4) surface. Please note the flat surface shown is equilibrated at 300K whereas the stepped surface is a 0K structure prior to equilibration, hence the difference in order. Color code: green=calcium, red=oxygen, gray=carbon

In the meantime a forcefield containing all necessary types has been published [61] but the authors assured us that the results should not be very different since the same starting potentials were used for their fitting procedure. The potentials are composed of a combination of long range coulomb (section 2.1.1) and short range forces (section 2.1.2) within the Born model for solids [62]. The geometry of the carbonate ion has been ensured by dihedral angles (section 2.1.3). The carbonate oxygen is treated as polarizable using the core-shell approach (section 2.1.4). The additive is described using a complicated combination of many-body potentials, which are tabulated in organic forcefields. The non-bond potentials finally are based on a combination of Buckingham and Lennard-Jones type potentials (section 2.1.2). The calcite crystal potential parameters, which are known to reproduce the calcite phase very well [63, 64, 65, 66, 67, 68], have been taken from Pavese [69, 70] and the calcite-water interface was modeled using the parameters published by Kerisit [68, 48]. For the additive and additive-water interactions the well validated organic DREIDING forcefield [71] has been used. Finally the interaction of the additive and the surface is modeled by the ab-initio derived potential parameters for stearic acid published by Duffy and Harding [55]. The additives were considered completely deprotonated and the mass and charge of the remaining hydrogen atoms was merged with the atoms which they are bound to in order to save computational time (this approach is commonly referred to as coarse-graining). The charge repartition within the 10-mere additives was calculated using the GAUSSIAN code [72] and the Mulliken charges [73] with hydrogen charges summed into heavy atoms have been used for the additives.

The calcite surfaces were constructed using the METADISE [74] code, the structures being solvated by inserting the required number of water molecules out of a water box equilibrated at the target temperature using the in-house code “polyview” developed at the University of Bath.

The molecular dynamics simulations have been performed with the DL_POLY2 code [75] using the verlet leap frog integrator with a timestep of 0.2fs for shell masses of 0.2amu. The NPT (variable volume) ensemble was used for equilibration of the configurations whereas the NVT (constant volume) ensemble was used for production runs. Barostats and thermostats used were Hoover and Nose-Hoover types respectively with a relaxation time of 0.5ps. The short range cutoff was fixed at 8Å and the electrostatic interactions were treated using the smooth particle mesh Ewald (SPME) method using the same real space cutoff. The additives were tethered (attached to a fixed point in space by a strong harmonic potential) during equilibration in order to prevent the system from exploring adsorbed states during this phase. Radial distribution functions were calculated throughout production runs (at least 1ns) whereas configurational energy averages were taken over the last 300ps only.

Since the exact simulation setup varies from case to case a more thorough description will be given along with the results.

4.3 Results & Discussion

4.3.1 Flat (10.4) surface

At first an attempt was made to study adsorption of the molecules on the flat (10.4) surface. The completely dissociated (charge -10) additives (pK values supporting this state at experimental pH conditions can be found for PAA [50] and p-ASP [76, 77]) were placed with the corresponding number of charge balancing counter ions (Ca^{2+} and Na^{+}) in a water layer of about 40 Å thickness separating the two surfaces of the 15 Å thick calcite slab in the periodic setup (section 2.3.4). The distance to the nearer of the two slabs was about 10 Å at simulation start. During the equilibration (0.5ns) of the system, the additives were tethered in 3 points, one at each extremity and one in the center. The additives were then untethered and production carried out for 1ns.

During the 1ns of simulation time the additives did not show any tendency to bind to the surface, instead floating at a distance of about 4 Å from the surface (figure 4.4). Kerisit and Parker [48] found that water above calcite surfaces shows a very particular layered structure with pronounced minima and maximima in density. They concluded that even if the water does not behave like ice it is best described as "viscous" water. The water density relative to bulk water as a function of distance from the surface which they published is shown in figure 4.5.

By comparing the distance from the surface at which the additive was found to remain (4Å) with this water structure and knowing that the backbone is hydrophobic it is intriguing to see that the additive resides in the most pronounced minimum in density situated slightly below 4 Å from the surface as seen on the red curve in figure 4.5. One can even see the water structure in figure 4.4, where at both surfaces three regions of alternating high and low density can be seen. It could be argued that the water structure around the additive will be disrupted and the layering is not present, however this would still mean that the highly coordinated water has to be displaced during the approach of the additive. Even if the additive did not bind during this simulation it does not mean that it will never bind, however the time required to

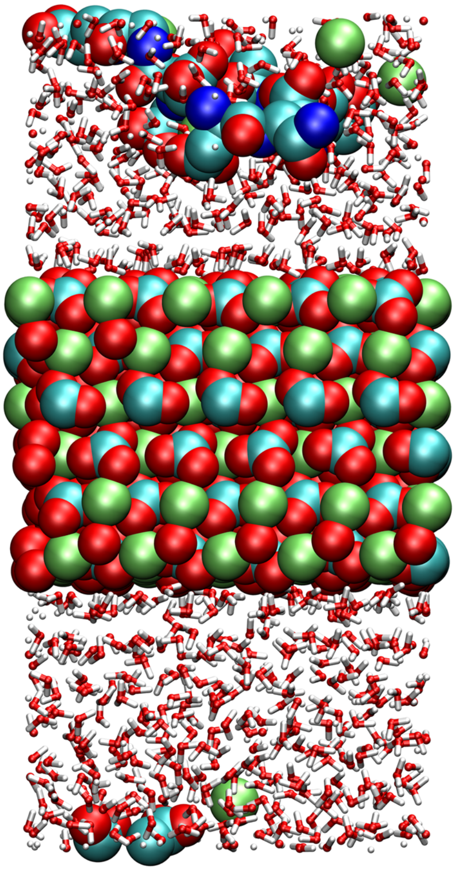

Figure 4.4: p-ASP additive at the end of the 1ns simulation floating at about 4 Å above the flat (10.4) calcite surface. Color code: lime=calcium, red=oxygen, light blue=carbon, dark blue=nitrogen, white=hydrogen

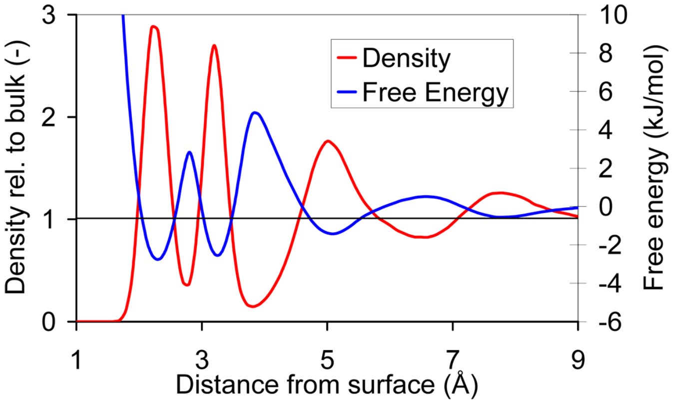

Figure 4.5: The water density relative to the bulk as well as the free energy of a water molecule as a function of distance from the surface. Redrawn using data obtained from the authors of [48].

overcome the energy barrier resulting from the layered water structure could be much larger than timescales accessible to current molecular dynamics simulations.

Another aspect may be that, as can be seen from figure 4.4, the additive has a tendency to form strong complexes with the counterions in solution. Polycarboxylic acids are known to strongly complex with Ca^{2+} and to a lesser extent with Na^{+} ions [50, 38]. As the Ca^{2+} concentration in the simulation cell is about 0.4M compared to the 0.01M in experimental conditions, the number of complexes formed in these simulations will be much larger than in experiment. An over-complexation will make the additive less likely to bind to the surface as it's functional groups have already bound to solvated ions.

These two aspects were further investigated by running appropriate simulations, the results of which will be discussed in the next sections.

4.3.2 Forced adsorption

In order to investigate the behavior once the energy barrier is passed, the additive was put in close contact with the surface and the calculation run. Figure 4.6 shows a number of snapshots at key instants of the simulation. As it can be seen the additive desorbs very rapidly (figures 4.6a and 4.6b) from the surface into the first low density water layer. From there further desorption is slower with a single carboxy group remaining in the first low density water layer, a large portion of the molecule extending into the diffuse part of the solution (figure 4.6e).

By looking at the enthalpy (configuration energy) evolution of the system (figure 4.7) it can be seen that the desorption step into the first low water density layer seems to enthalpy driven (most likely due to favorable hydration of the surface) whereas the further steps do not show clear barriers. This may be due to the fact that the additive passes trough energetically favorable layers continuously or to the fact that the desorption out of the first layer is entropy driven. In any case it can be stated from this result that adsorption to the flat surface itself is not favorable and that the additive adsorbs if at all to the highly coordinated water rather than surface atoms of the flat (104) surface.

4.3.3 Complexation behavior

Simulations of both additives solvated with either 5 Ca^{2+} or 10 Na^{+} ions in water were carried out in order to investigate the complexation of counterions in solution. Simulations were run for 0.5ns, which is sufficient for the counterions to form

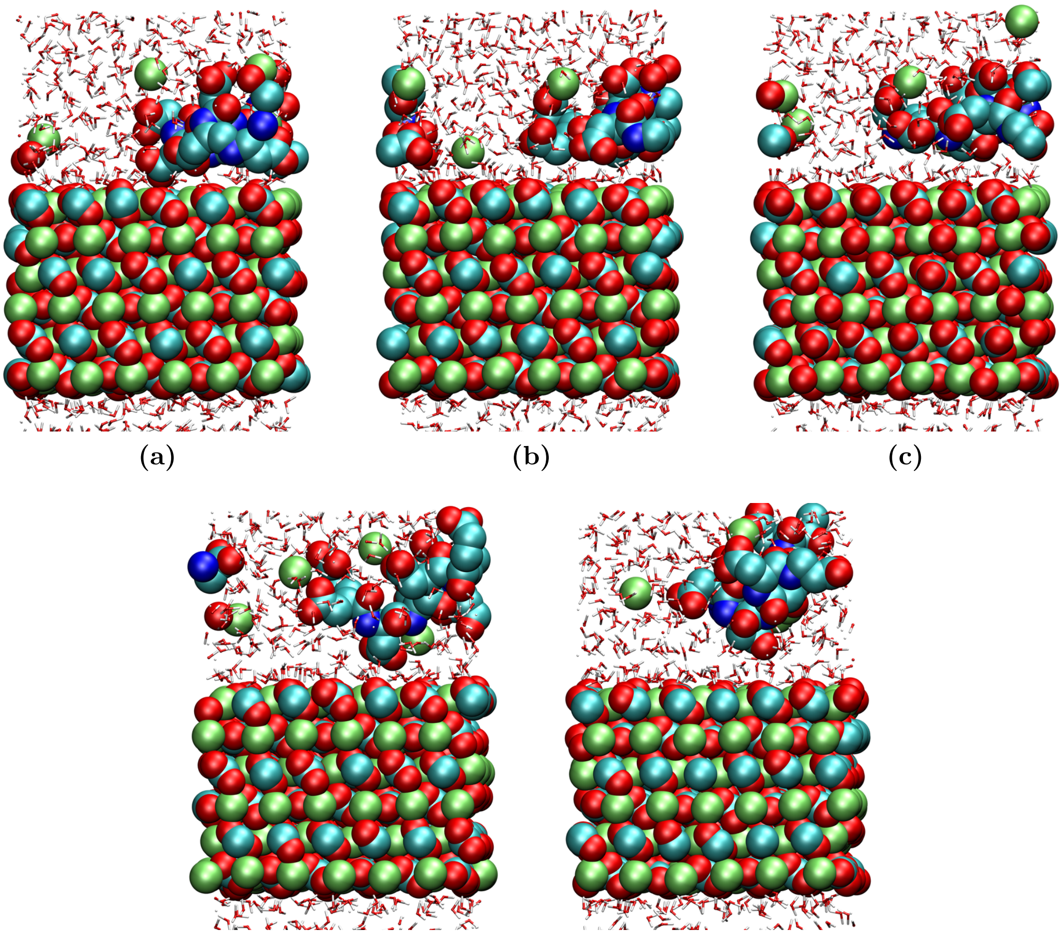
(a) (b) (c)

(d) (e)

Figure 4.6: p-ASP additive starting at the interface at different times: (a) Simulation start, (b) 10ps, (c) 30ps, (d) 120ps and (e) 200ps. Color code: lime=calcium, red=oxygen, light blue=carbon, dark blue=nitrogen, white=hydrogen

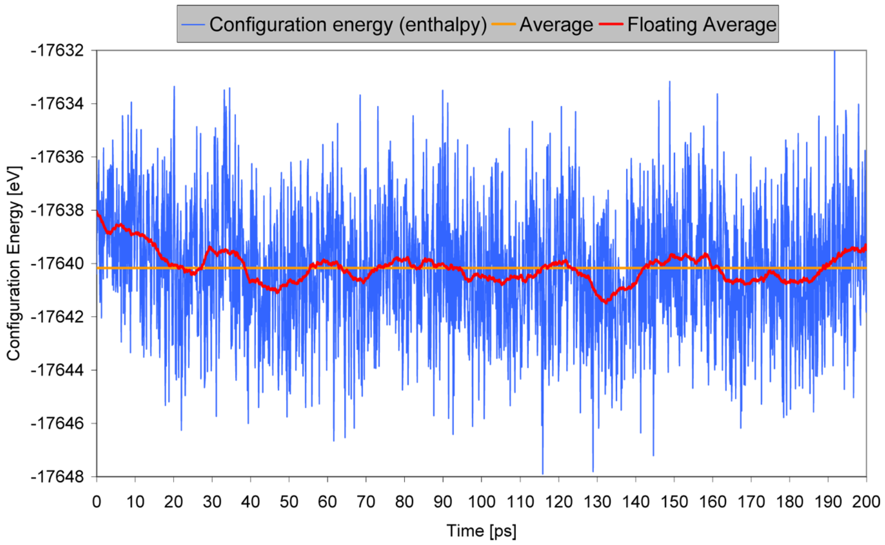

Figure 4.7: Enthalpy (configuration energy) evolution of p-ASP desorption.

and dissociate different complex conformations. The complexation behavior was studied by looking at the radial distribution functions (RDF) of the different additive/counterion pairs as shown in figure 4.8. By first looking at the structure of the coordination shell of water around the ions (red and orange lines) it can be seen that there is a first shell at 2.3 Å for Na and 2.4 Å for Ca ions, followed by a second more diffuse shell at 4 Å for both ions, the water adopting the bulk structure further away. This behavior is reproduced no matter which additive is present, showing that ion solvation is not influenced by the presence of the additives.

The RDFs for the distance between the ions and carboxylic acid oxygen atoms (dark and light blue lines) are very different for the different additives and counterions. For PAA and Na it can be seen that a very strong peak exists at a distance collocated with the first water coordination shell. A second smaller peak collocated with the second coordination shell exists as well. For p-ASP, the first peak is smaller than the second one and more importantly the magnitude of the peaks is much smaller than for PAA. These results suggest that PAA forms primarily very strong inner sphere complexes, the outer sphere ones probably being transitory. p-ASP also forms inner sphere complexes with Na, however the number seems to be less important compared to the outer sphere ones. Looking at the RDFs for Ca it can be seen that PAA again forms a lot of inner sphere complexes, the magnitude of the outer sphere peak being even smaller than for sodium. However the most interesting fact is that p-ASP only forms outer sphere complexes with calcium, the first peak being non-existent.

This complexation behavior can also be seen by looking at atomic structures of the additives and counterions shown in figure 4.9 where the water molecules have been hidden. It can be seen that PAA for both counterion types folds into two sheet-like halves, which are linked by complexing the same sodium or calcium ions. p-ASP remains elongated in presence of many sodium ions but seems to form a more compact structure when complexing with a smaller number of calcium ions. Due to the lesser flexibility of the additive (p-ASP has a peptide backbone with a high double bond character) inner sphere complex formation is not possible as no two carboxy groups can complex the ion at the same time. In general the number of non-complexed ions is higher for p-ASP than for PAA, which confirms the lower complexation strength of this additive as already seen in the amplitude of the peaks in the RDFs. These results shown that PAA will trap a higher number of calcium ions than p-ASP and retain them for a longer time, thus reducing the supersaturation of the solution, which explains the marked decrease in reaction yield observed for PAA as well as the capacity of this additive to inhibit nucleation when present at

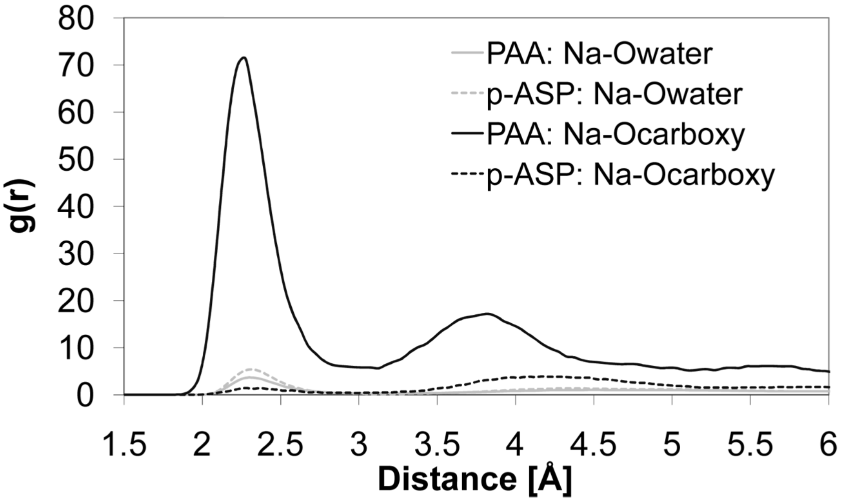

(a)

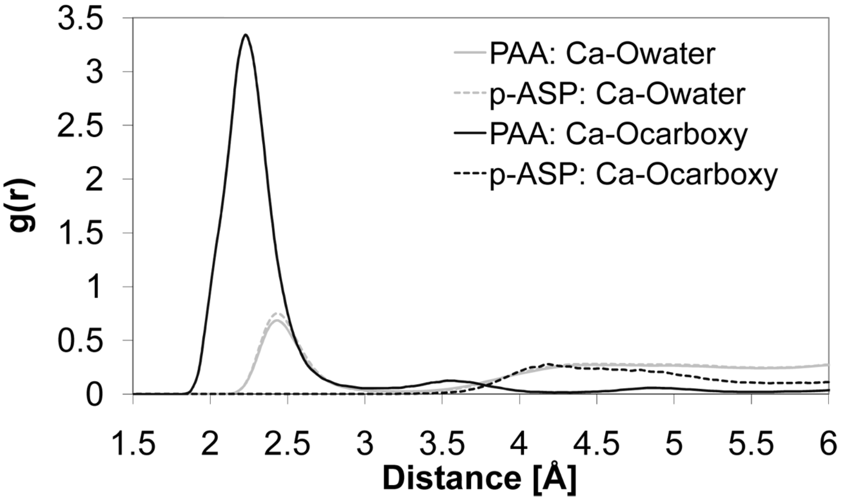

(b)

Figure 4.8: Radial distribution functions of the distances between counterions and the oxygen atoms in their coordination shell as well as the ones of the carboxylic acid groups for: (a) Sodium ions and (b) calcium ions.

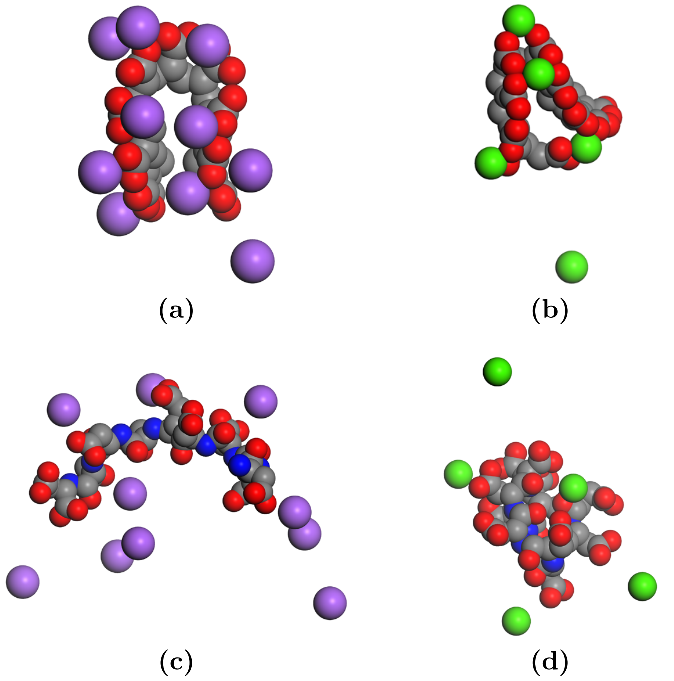

Figure 4.9: Complex configurations for the following combinations: (a) Sodium + PAA, (b) calcium + PAA, (c) sodium + p-ASP, (d) calcium + p-ASP. Color code: purple=sodium, green=calcium, red=oxygen, gray=carbon, blue=nitrogen

high concentrations.

4.3.4 Removal of counterions & Electrostatic driving force

As it was seen above, the counterion concentration with 5 Ca^{2+} or 10 Na^{+} is much higher than experimental concentrations. It would thus be desirable to remove these counterions from the simulation. It was also seen that the driving force for adsorption on the flat (10.4) calcite surface is not high enough to overcome the energy barrier associated with the displacement of the water within the timescale of the simulations. It would therefore further be desirable to create an additional driving force for adsorption.

These two objectives can be attained by removing carbonate species from the surface. Carbonate ions are the more soluble species in calcite due to the possible formation of the bicarbonate ion in water. The situation with missing carbonates would correspond to a low CO_2 partial pressure experiment, where the bicarbonate concentration is lower than equilibrium, thus resulting in a shift of the carbonate dissolution equilibrium. The most likely sites from where carbonate groups can be removed are steps, which are commonly seen in experiment [41]. From thermodynamic calculations of the zeta potential (ζ) at low CO_2 partial pressure in the early

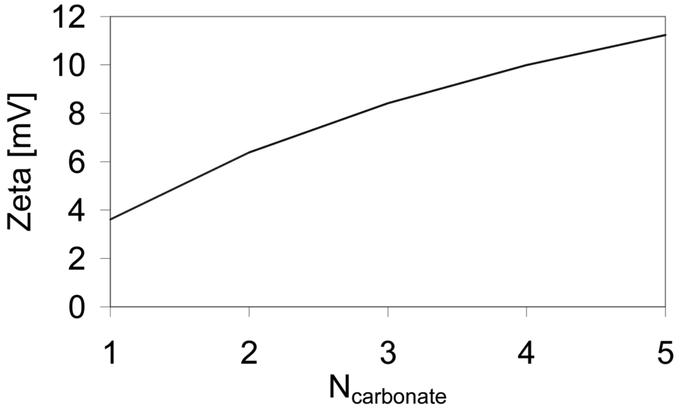

Figure 4.10: The zeta potential as a function of the number of removed carbonate groups.

stages of the reaction (13mV) [78, 79] it is possible to calculate the number of carbonate groups to be removed ($N_{CO_3^{2-}}$) per simulation cell of surface area A. This development is shown in equations 4.2 to 4.5 and is based on the calculation of the surface potential (Ψ) from the measurable zeta potential, from where the surface charge density (φ) can be calculated [80], taking κ and d=0.5nm as defined in the introduction (section 1.12).

$$\Psi = \zeta exp\left(kd\right) \tag{4.2}$$

$$\Psi = \frac{2kT \cdot asinh\left(\frac{\phi}{\sqrt{2kTc_0^*\epsilon_0\epsilon}}\right)}{ze} \tag{4.3}$$

$$\Rightarrow \varphi = sinh\left(\frac{\Psi ze}{2kT}\right)\sqrt{8kTc_0^*\epsilon_0\epsilon} \tag{4.4}$$

$$N_{CO_3^{2-}} = \frac{\varphi A}{z_{CO_3^{2-}}} \tag{4.5}$$

If the zeta potential is plotted as a function of the number of carbonate vacancies at the surface while assuming an electrolyte of calcium and carbonate (z=2) at experimental concentrations ($c_0^*=2.4\cdot10^{26}\mathrm{m}^{-3}$) at 300K one obtains for a surface cell of 25Å x 27Å the plot shown in figure 4.10. It can be seen that for the thermodynamically predicted zeta potential slightly more than 5 carbonate groups would have to be removed per simulation cell.

For practical reasons since the creation of 5 carbonate vacancies exactly counterbalances the charge of the polymer, it was decided to remove 5 groups from the surface. This was done by removing them one after another from the step edge, while equilibrating the system at each step for 0.5ns. This resulted in calcium atoms "popping" out of the step to be located as adatoms on the surface as can be seen in

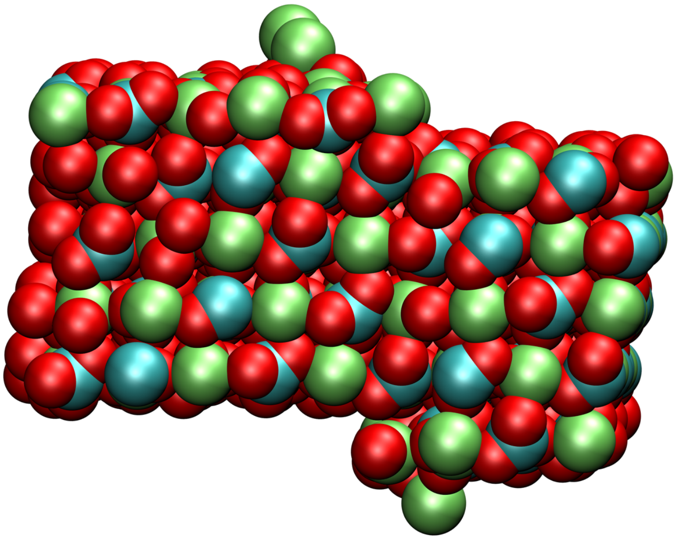

Figure 4.11: The step with 5 carbonate groups removed from the step edge. The intervening calcium ions transformed to adatoms upon equilibration. Color code: lime=calcium, red=oxygen, light blue=carbon

figure 4.11. This situation can be seen as a snapshot during particle growth, where ions are migrating on the surface in order to be incorporated in favorable sites.

All subsequent adsorption calculations were run on this defective stepped surface and the adsorption behavior of the two additives will be shown in the following two sections, followed by the adsorption energies of the two additives and conclusions on possible sources for the differences between them.

PAA adsorption

The PAA molecule was placed about 10 Å above the surface and tethered in 3 points in order to keep it in this position during equilibration. Equilibration was carried out for 0.5ns followed by untethering and a production run of 1.0ns. The molecule was found to adopt a helix like conformation (figure 4.12a) while at a certain distance from the surface and without counterions around to form complexes with. This helix structure got lost as the additive started approaching the surface and interaction of the carboxy groups with the calcium adatoms got stronger (figure 4.12b) Finally the additive approaches in a very quick transition and binds to the adatoms with 4 functional groups (figure 4.12c).

The enthalpy evolution of the process is shown in figure 4.13 where it can be seen that an energy barrier exists at about 400ps, which corresponds to the final

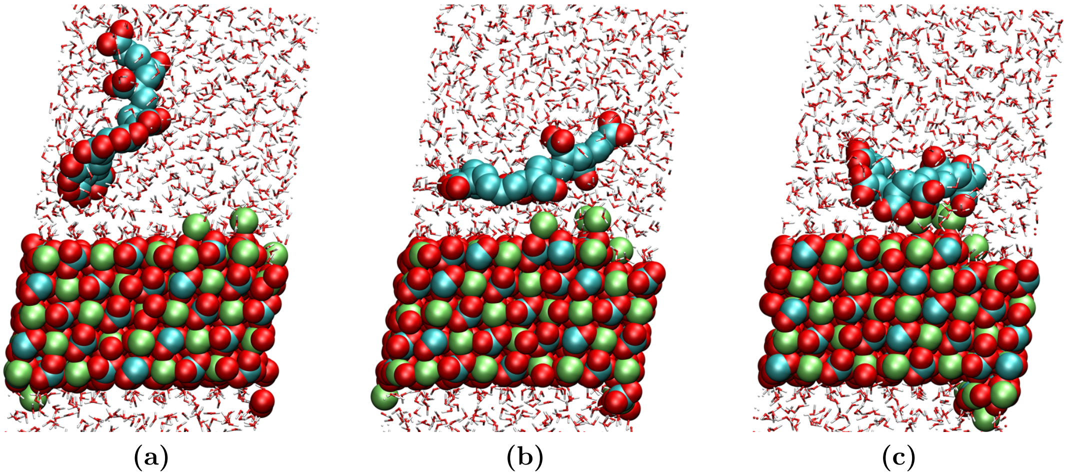
(a) (b) (c)

Figure 4.12: Adsorption of PAA, snapshots taken at: (a) 150ps, (b) 400ps and (c) 500ps. Color code: lime=calcium, red=oxygen, light blue=carbon, white=hydrogen

binding transition. This energy barrier can be associated with the displacement of the hydration shell of the adatoms.

The final adsorption conformation (figure 4.12c) is flat (∼0.5nm thick) and probably best described by the "loop and train model" 1.12. This conformation is known to give raise to a rather short range steric repulsion force which in cases of deep attractive minima of the interparticle interaction potential cannot prevent particle agglomeration.

p-ASP adsorption

p-ASP adsorption was carried out in exactly the same way as described for PAA above. It can be seen from the simulation snapshots in figure 4.14 that one calcium ion is found in solution. This atom is one of the surface adatoms, which was dissolved from the surface. These dissolution reactions were thought to be events happening at a lot longer timescale than accessible to simulations. In order to test if this dissolution was a random event the simulation was restarted with a different starting configuration but the dissolution event occurred again thus being attributed to the presence of the additive. It is interesting to note that while with PAA this dissolution was never observed it occurred in both of the two simulations carried out in the same fashion for p-ASP. This suggests that the dissolution event did not occur at random but rather is a normal transition of the system. This would suggest that p-ASP has a higher attractive force towards calcium ions than PAA. From the forcefield definition (see appendix B) the van der Waals interactions between both molecules are treated in the same way except for the nitrogen interactions, which are not present for

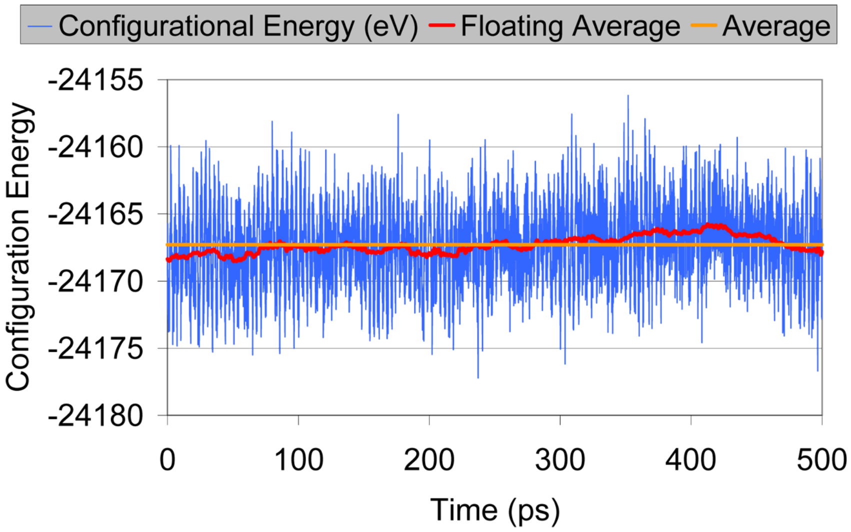

Figure 4.13: Enthalpy (configuration energy) evolution of PAA adsorption to the defective calcite step. Only a 500ps portion of the production run is shown.

PAA and of which the Ca-N interactions is a purely repulsive buckingham potential, whereas the $O_{\mathrm{carbonate}}$-N interaction contains an attractive part in the Lennard-Jones potential. This would suggest that the improved attraction between p-ASP and Ca can not be due to van der Waals interactions but must come from the electrostatic interactions of the slightly negative nitrogen ions, the remaining ions either carrying the same charge as in PAA or being positively charged.

In figure 4.14 the molecule can be seen to approach the surface with one of its terminal ends and to bind with the carboxylic groups, while the upper carboxylic groups form complexes of changing configurations with the calcium ion in solution. Initially being placed at the same distance from the surface than PAA, the p-ASP molecule bound to the surface with the first carboxy group after 170ps, whereas for PAA this happened only at about 400ps. This suggest that p-ASP either has a higher diffusion coefficient in water due to its more elongated shape and thus smaller hydrodynamic radius or due to a stronger attractive force with the surface. As discussed before, the stronger attraction does exist due to electrostatic forces between Ca and N as well as van der Waals forces between the $O_{\mathrm{carbonate}}$ and nitrogen atoms. The hydrodynamic radius will however play a role as well and a superposition of both effects is likely.

In its final configuration p-ASP binds with 3 carboxylic acid groups to the surface adatoms, the molecule remaining in an upright position while complexing the calcium ion in solution. From the energy evolution shown in figure 4.15 it can be seen that there are no clear energy barriers. The adsorption process may however be masked by

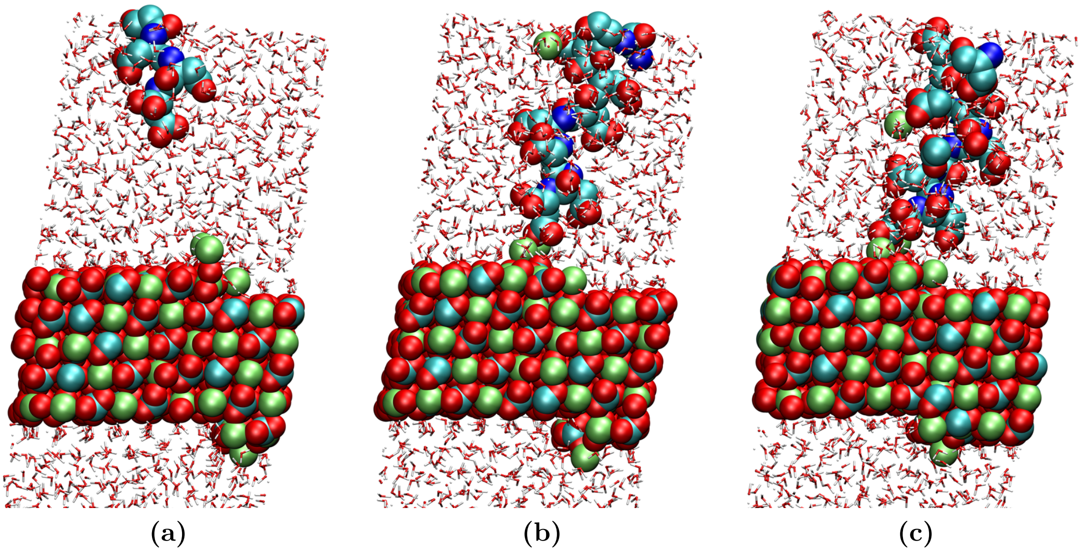
(a) (b) (c)

Figure 4.14: Adsorption of p-ASP, snapshots taken at: (a) 150ps, (b) 400ps and (c) 500ps. Color code: lime=calcium, red=oxygen, light blue=carbon, dark blue=nitrogen, white=hydrogen

the energetics of complex formation with the ion in solution. The upright position of the adsorbed polymer may be best described by the mushroom conformation (∼2nm thick) which gives a relatively long range steric barrier able to close attractive minima of the interparticle interaction potential and thus prevent particle agglomeration.

This shows that the calcium ion in solution could have a effect on the adsorption conformation due to complex formation. As it was not possible to run simulations where p-ASP did not dissolve a calcium ion from the surface, the same ion was artificially dissolved from the surface in a PAA simulation, the results of which are shown in the next section.

PAA with counterion

As it was seen above the presence of ions dissolved from the surface and found in solution may have an influence on the adsorption conformation. This was further tested by removing a calcium ion from the surface in presence of PAA. Figure 4.16 shows the resulting adsorption conformations. It can be seen that the additive also adsorbs upright (∼2nm thick layer) at 405ps, the carboxy groups further away from the surface complexing the ion in solution. The number of binding carboxy groups is 3 as for p-ASP. At 460ps the calcium ion PAA binds to is transformed from the former outer sphere complex to an inner sphere complex and it it dissolved from the surface. For the remaining simulation time it remains however in the first low density layer and the additive is bound upright to this ion in solution. The complex

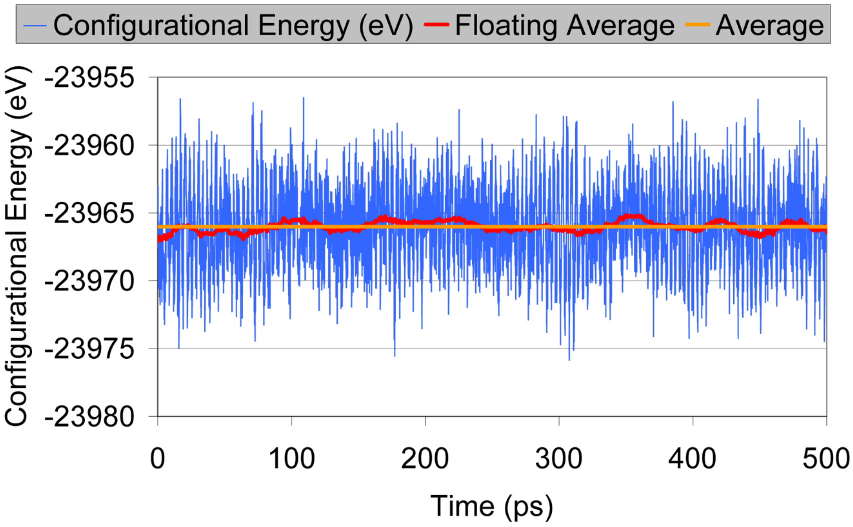

Figure 4.15: Enthalpy (configuration energy) evolution of p-ASP adsorption to the defective calcite step. Only a 500ps portion of the whole production run is shown.

formed with the first ion is an inner sphere complex, which does not break up and reform in different conformations at it was seen for p-ASP above.

This shows that the presence of counterions in solution can strongly affect the adsorption conformation, resulting in mushroom or loop and train like adsorption, which in turn has a strong influence on the steric stabilization due to the additive. However in these upright conformations the number of anchoring points is reduced and as a result the polymer may desorb more easily. It was further found for the PAA simulation that the adatoms to which the additive binds can be taken out of the surface and into the first low water density layer, the additive binding to this ion. Of course in this way the adsorption strength is even further reduced as it depends on the interaction of the calcium ion with the surface.

Adsorption energies

In order to compare the strength of adsorption, the enthalpies of adsorption of the two additives were calculated. This was done by considering the transition E1 to E2 in the system shown in figure 4.17, where the system transforms from an unbound state to the bound state. As it is difficult to ensure no long-range interaction between the surface and the additive in state E1, this state is usually represented by a combination of the states E3 to E5. The total energy of state E1 can be represented by their energies as given by equation 4.6.

$$\Delta E_{\text{binding}} = E2 - E1 = E2 - (E3 + E4 - E5) \tag{4.6}$$

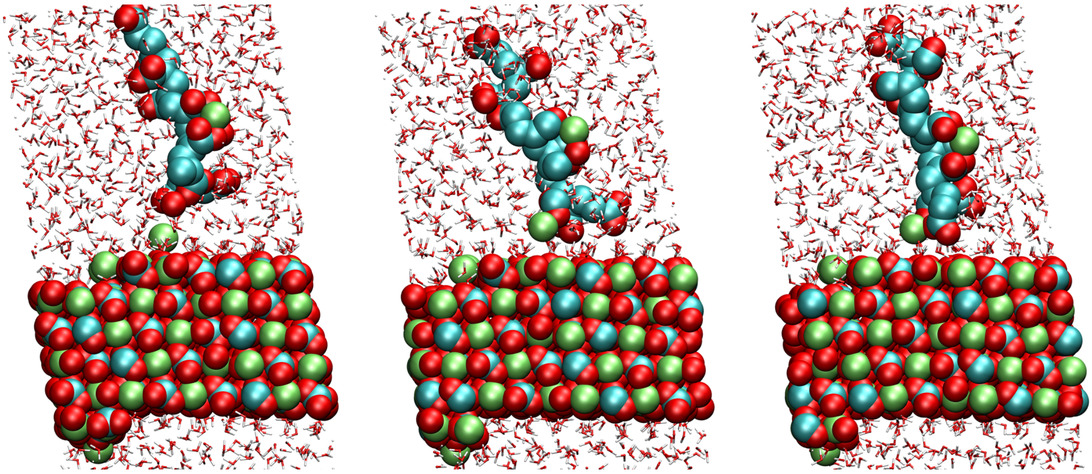
(a) (b) (c)

Figure 4.16: Adsorption of PAA in presence of a calcium ion dissolved from the surface, snapshots taken at: (a) 405ps, (b) 460ps and (c) 800ps. Color code: lime=calcium, red=oxygen, light blue=carbon, white=hydrogen

This equation approximates the state E1 by the summing the energy of a system only containing the water-surface interaction (E3) and one only containing the water-polymer interaction (E4). This will lead to a double counting of the water-water interaction, which as a result has to subtracted (E5) for the result to be correct.

This approach works well for uncharged additives but presents problems when charges are introduced since it can be seen that the charge is + or - Z (Z=10 for the present case) depending on the surface defect and the dissociation of the additive. The cells are charged and the Ewald summation will result in the interaction of the cell with all of it's images. The cell charge can be neutralized by inserting "virtual" particles, carrying the required charge but not interacting with anything in the system. In order to achieve this a new potential has been created in DL_POLY which exactly counterbalances the electrostatic interaction within the short range cutoff. This means that an atom which interacts via this potential with all other atoms will not interact electrostatically with its surrounding within the short-range cutoff. Since the interaction outside the cutoff is considered small this will result in a reasonable canceling of electrostatic energies as well as the charged cell problem. The "virtual" particle was tethered far away from the surface and additive for these simulations. In that way the main part of the small interaction outside the short range cutoff should be with water only and thus the same for both additives, adding as a result only a small and systematic error.

The interaction energies calculated according to this scheme for the two additives are presented in table 4.2. Please note that since the same number of water molecules

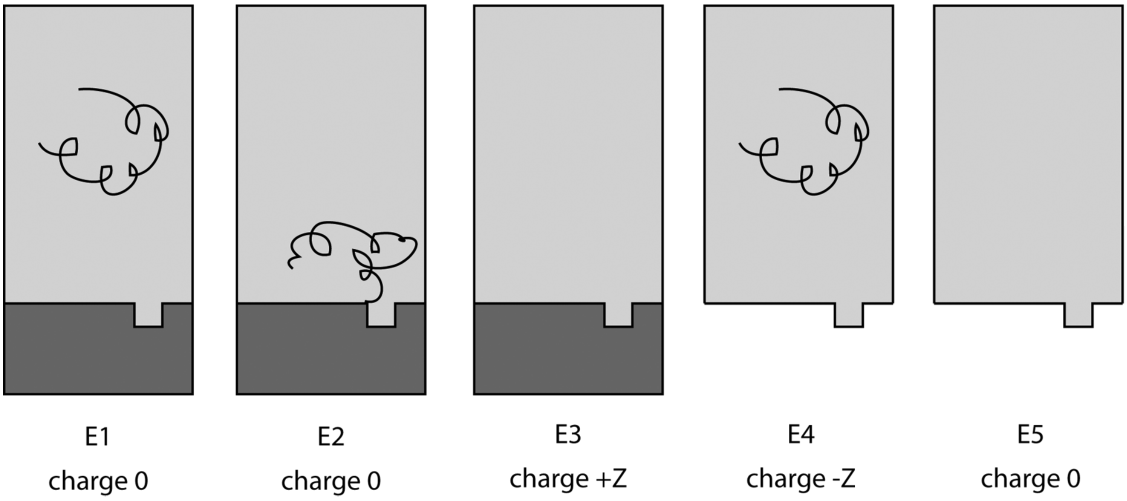

Figure 4.17: States of the system during binding. E1 unbound state, E2 bound state. The states E3 to E5 are used to abstract the state E1 for the actual calculations.

Table 4.2: Interaction energies for PAA and p-ASP with the defective stepped surface.

Energy component	**PAA**		**p-ASP**	
E2	-24166.73	eV	-23966.04	eV
E3	-24082.01	eV	-23885.89	eV
E4	-13508.26	eV	-13338.98	eV
E5	-13462.34	eV	-13271.87	eV
$\mathbf{\Delta E_{binding}}$	4.09	eV	-13.04	eV

has to be used for all calculations of the same additive in order to cancel the double contribution of the water, not only the bound energy E2 varies but also the energies E3, E4 and E5.

It is very interesting to see that p-ASP has a negative enthalpy of adsorption and PAA a positive one. As it was seen above both additives adsorb to the surface, showing that the free energy of adsorption has to be negative in both cases. This means that for PAA the entropy component of the free energy has to be more negative than -4.09eV as otherwise adsorption would not occur. This entropy driven surface complexation is not unexpected as it has been experimentally observed for carboxylic acids on calcite surfaces [39] as well as for calcium ions in solution [38]. As discussed above the enhanced enthalpic interaction of p-ASP compared to PAA has to come from an electrostatic driving force due to the relatively highly charged nitrogen atoms as well as the interaction of the nitrogen atoms with carbonate oxygen atoms, since all other components of the van der Waals interactions in the forcefield are either repulsive or equivalent for the two additives.

These results show a higher strength of adsorption for p-ASP which should result in a more rapid binding of the additive and a longer residence time at the surface, the combination of both giving a more marked growth modification.

4.4 Conclusions

The present simulations show the high importance to include water in simulation in order to get a correct adsorption behavior. It was found that charged surface defects such as defective step edges, which are growth sites, dominate the adsorption processes. This explains the high growth modifying effect of these additives by blocking of growth sites. The difference between the two additives polyacrylic acid (PAA) and polyaspartic acid (p-ASP) was found to be twofold.

On one hand the complexation behavior in solution plays a key role where PAA was found to form stronger inner sphere complexes with calcium, whereas p-ASP only forms weaker outer sphere complexes. For PAA the complexes did not redissociate during the simulation time whereas for p-ASP a continuous dissociation/reformation was observed. This stronger complexation behavior of PAA suggests that this additive traps a higher number of calcium ions, which can thus not be incorporated in the crystal. This is confirmed by the reduced reaction yield with increasing PAA concentration and by the fact that at high concentrations, PAA can completely inhibit calcite nucleation. Furthermore since the complexes do not redissociate easily, many of the functional groups of PAA can as a result not interact with surface calcium ions and thus not take part in a growth modifying process. For p-ASP where this strong complexation is not observed, a higher precipitation yield and a higher reactivity with the surface is to be expected.

On the other hand the interaction with the surface is a lot stronger for p-ASP. This should result in a faster adsorption at the surface as well as a stronger binding and thus a longer residence time and for these two reasons a higher growth modifying effect. It was further found that PAA adsorbs in a loop and train conformation, whereas p-ASP remains in a mushroom conformation. This could be explained by the stiffer peptide backbone of p-ASP, which has around 70% double bond character. These two conformations would result in a higher steric stabilization by p-ASP thus preventing particle agglomeration and conserving the nanostructure of the particles, explaining the higher specific surface area observed in presence of p-ASP. However since the conformation of PAA was shown to also tranform to mushroom when counterions are present, this has to be investigated further.

The enhanced specific surface area observed with p-ASP can thus be related to a higher reactivity of the additive with the surface due to lesser complex formation and a more negative binding energy. Further it is possible that p-ASP more effectively prevents particle agglomeration, thus conserving the nanostructure throughout growth.

Bibliography

[1] M. A. Osman, A. Atallah, and U. W. Suter. Influence of excessive filler coating on the tensile properties of LDPE-calcium carbonate composites. *Polymer*, 45(4):1177–1183, 2004.

[2] S. Wada and H. Suzuki. Calcite and fluorite as catalyst for the Knovenagel condensation of malononitrile and methyl cyanoacetate under solvent-free conditions. *Tetrahedron Letters*, 44(2):399–401, 2003.

[3] A. M. Belcher, X. H. Wu, R. J. Christensen, P. K. Hansma, G. D. Stucky, and D. E. Morse. Control of crystal phase switching and orientation by soluble mollusc-shell proteins. *Nature*, 381(6577):56–58, 1996.

[4] M. F. Butler, N. Glaser, A. C. Weaver, M. Kirkland, and M. Heppenstall-Butler. Calcium carbonate crystallization in the presence of biopolymers. *Crystal Growth & Design*, 6(3):781–794, 2006.

[5] A. W. Xu, Y. R. Ma, and H. Cölfen. Biomimetic mineralization. *Journal of Materials Chemistry*, 17(5):415–449, 2007.

[6] B. Wucher, W. B. Yue, A. N. Kulak, and F. C. Meldrum. Designer crystals: Single crystals with complex morphologies. *Chemistry of Materials*, 19(5):1111–1119, 2007.

[7] A. Prevost, M. F. Butler, and M. Heppenstall-Butler. Controllable modification of calcium carbonate crystal morphology through the use of organic and inorganic additives. In *16th International Symposium on Industrial Crystallization*, volume 1901 of *VDI Berichte*, pages 739–744, Dresden, 2005. VDI.

[8] N. Wada, K. Kanamura, and T. Umegaki. Effects of carboxylic acids on the crystallization of calcium carbonate. *Journal of Colloid and Interface Science*, 233(1):65–72, 2001.

[9] H. Cölfen and L. M. Qi. A systematic examination of the morphogenesis of calcium carbonate in the presence of a double-hydrophilic block copolymer. *Chemistry - A European Journal*, 7(1):106–116, 2001.

[10] K. Kaluzynski, J. Pretula, and S. Penczek. Poly(ethylene glycol)-b-phosphorylated polyglycidols as $CaCO_3$ crystal growth modifiers: II. macromolecular architecture versus the crystal size and shape and crystallization inhibition. *Journal of Polymer Science Part A - Polymer Chemistry*, 45(1):90–98, 2007.

[11] J. Rudloff, M. Antonietti, H. Cölfen, J. Pretula, K. Kaluzynski, and S. Penczek. Double-hydrophilic block copolymers with monophosphate ester moieties as crystal growth modifiers of $CaCO_3$. *Macromolecular Chemistry and Physics*, 203(4):627–635, 2002.

[12] K. Burns, Y. T. Wu, and C. S. Grant. Mechanisms of calcite dissolution using environmentally benign polyaspartic acid: A rotating disk study. *Langmuir*, 19(14):5669–5679, 2003.

[13] Y. T. Wu and C. Grant. Effect of chelation chemistry of sodium polyaspartate on the dissolution of calcite. *Langmuir*, 18(18):6813–6820, 2002.

[14] S. Elhadj, E. A. Salter, A. Wierzbicki, J. J. De Yoreo, N. Han, and P. M. Dove. Peptide controls on calcite mineralization: Polyaspartate chain length affects growth kinetics and acts as a stereochemical switch on morphology. *Crystal Growth & Design*, 6(1):197–201, 2006.

[15] D. Volkmer, M. Fricke, T. Huber, and N. Sewald. Acidic peptides acting as growth modifiers of calcite crystals. *Chemical Communications*, (16):1872–1873, 2004.

[16] H. H. Teng, P. M. Dove, C. A. Orme, and J. J. De Yoreo. Thermodynamics of calcite growth: Baseline for understanding biomineral formation. *Science*, 282(5389):724–727, 1998.

[17] J. M. Didymus, S. Mann, W. J. Benton, and I. R. Collins. Interaction of poly(α,β-aspartate) with octadecylamine monolayers - adsorption behavior and effects on $CaCO_3$ crystallization. *Langmuir*, 11(8):3130–3136, 1995.

[18] J. G. Yu, M. Lei, B. Cheng, and X. J. Zhao. Effects of PAA additive and temperature on morphology of calcium carbonate particles. *Journal of Solid State Chemistry*, 177(3):681–689, 2004.

[19] C. Geffroy, A. Foissy, J. Persello, and B. Cabane. Surface complexation of calcite by carboxylates in water. *Journal of Colloid and Interface Science*, 211(1):45–53, 1999.

[20] J. Rieger, T. Frechen, G. Cox, W. Heckmann, C. Schmidt, and J. Thieme. Precursor structures in the crystallization/precipitation processes of $CaCO_3$ and control of particle formation by polyelectrolytes. *Faraday Discussions*, 136:265–277, 2007.

[21] K. Westin and A. C. Rasmuson. Crystal growth of aragonite and calcite in presence of citric acid, DTPA, EDTA and pyromellitic acid. *Journal of Colloid and Interface Science*, 282(2):359–369, 2005.

[22] K. J. Westin and A. C. Rasmuson. Nucleation of calcium carbonate in presence of citric acid, DTPA, EDTA and pyromellitic acid. *Journal of Colloid and Interface Science*, 282(2):370–379, 2005.

[23] M. M. Reddy and A. R. Hoch. Calcite crystal growth rate inhibition by polycarboxylic acids. *Journal of Colloid and Interface Science*, 235(2):365–370, 2001.

[24] T. Kato, T. Suzuki, T. Amamiya, T. Irie, and N. Komiyama. Effects of macromolecules on the crystallization of $CaCO_3$ the formation of organic/inorganic composites. *Supramolecular Science*, 5(3-4):411–415, 1998.

[25] S. Mann, B. R. Heywood, S. Rajam, and J. D. Birchall. Controlled crystallization of $CaCO_3$ under stearic-acid monolayers. *Nature*, 334(6184):692–695, 1988.

[26] R. G. Jonasson, K. Rispler, B. Wiwchar, and W. D. Gunter. Effect of phosphonate inhibitors on calcite nucleation kinetics as a function of temperature using light scattering in an autoclave. *Chemical Geology*, 132(1-4):215–225, 1996.

[27] M. M. Reyhani, A. Oliveira, G. M. Parkinson, F. Jones, A. L. Rohl, and M. I. Ogden. In situ characterisation of calcite growth and inhibition using atomic force microscopy. *International Journal of Modern Physics B*, 16(1-2):25–33, 2002.

[28] Z. Amjad. The influence of polyphosphates, phosphonates, and poly(carboxylic acids) on the crystal-growth of hydroxyapatite. *Langmuir*, 3(6):1063–1069, 1987.

[29] F. Grases, A. Garciaraso, J. Palou, A. Costabauza, and J. G. March. A study of the relationship between the chemical-structure of some carboxylic-acids and their capacity to inhibit the crystal-growth of calcium-fluoride. *Colloids and Surfaces*, 54(3-4):313–319, 1991.

[30] J. M. Ouyang, L. Duan, and B. Tieke. Effects of carboxylic acids on the crystal growth of calcium oxalate nanoparticles in lecithin-water liposome systems. *Langmuir*, 19(21):8980–8985, 2003.

[31] J. M. Ouyang, N. Zhou, L. Duan, and B. Tieke. Ability of multifunctional sodium carboxylates to favor crystal growth of calcium oxalate dihydrate and trihydrate in lecithin-water liposome systems. *Colloids and Surfaces a-Physicochemical and Engineering Aspects*, 245(1-3):153–162, 2004.

[32] B. M. Borah, B. J. Bhuyan, and G. Das. Low-molecular-weight poly-carboxylate as crystal growth modifier in biomineralization. *Journal of Chemical Sciences*, 118(6):519–524, 2006.

[33] S. Moulay, M. Boukherissa, F. Abdoune, and F. Z. Benabdelmoumene. Low molecular weight poly(acrylic acid) as a salt scaling inhibitor in oilfield operations. *Journal of the Iranian Chemical Society*, 2(3):212–219, 2005.

[34] M. Donnet, P. Bowen, N. Jongen, J. Lemaitre, and H. Hofmann. Use of seeds to control precipitation of calcium carbonate and determination of seed nature. *Langmuir*, 21(1):100–108, 2005.

[35] A. Kotachi, T. Miura, and H. Imai. Morphological evaluation and film formation with iso-oriented calcite crystals using binary poly(acrylic acid). *Chemistry of Materials*, 16(16):3191–3196, 2004.

[36] M. A. V. Axelos, M. M. Mestdagh, and J. Francois. Phase-diagrams of aqueous-solutions of polycarboxylates in the presence of divalent-cations. *Macromolecules*, 27(22):6594–6602, 1994.

[37] S. Iida. Interaction of calcium ions and polyelectrolytes. *Biophysical Chemistry*, 57(2-3):133–142, 1996.

[38] C. G. Sinn, R. Dimova, and M. Antonietti. Isothermal titration calorimetry of the polyelectrolyte/water interaction and binding of Ca^{2+}: Effects determining the quality of polymeric scale inhibitors. *Macromolecules*, 37(9):3444–3450, 2004.

[39] J. Plank and G. Bassioni. Adsorption of carboxylate anions on a $CaCO_3$ surface. *Zeitschrift für Naturforschung Section B - A Journal of Chemical Sciences*, 62(10):1277–1284, 2007.

[40] C. A. Orme, A. Noy, A. Wierzbicki, M. T. McBride, M. Grantham, H. H. Teng, P. M. Dove, and J. J. DeYoreo. Formation of chiral morphologies through selective binding of amino acids to calcite surface steps. *Nature*, 411(6839):775–779, 2001.

[41] H. H. Teng. Controls by saturation state on etch pit formation during calcite dissolution. *Geochimica Et Cosmochimica Acta*, 68(2):253–262, 2004.

[42] H. H. Teng and P. M. Dove. Surface site-specific interactions of aspartate with calcite during dissolution: Implications for biomineralization. *American Mineralogist*, 82(9-10):878–887, 1997.

[43] L. Xiang, Y. Xiang, Z. G. Wang, and Y. Jin. Influence of chemical additives on the formation of super-fine calcium carbonate. *Powder Technology*, 126(2):129–133, 2002.

[44] J. Ebert. Precipitation of nanostructured calcium carbonate - effects of additives. Technical report, EPFL, 2006.

[45] S. Pedrazzini. Précipitation et caractérisation de particules de calcite nanostructurés - effet d'additifs. Technical report, EPFL, 2006.

[46] J.-M. Haussonne, C. Carry, P. Bowen, and J. Barton. *Céramiques et Verres*, volume 16 of *Traité des Matériaux*. Presses Polytechniques et Universitaires Romandes, Lausanne, 2005.

[47] J. O. Titiloye, S. C. Parker, and S. Mann. Atomistic simulation of calcite surfaces and the influence of growth additives on their morphology. *Journal of Crystal Growth*, 131(3-4):533–545, 1993.

[48] S. Kerisit and S. C. Parker. Free energy of adsorption of water and metal ions on the {1014} calcite surface. *Journal of the American Chemical Society*, 126(32):10152–10161, 2004.

[49] D. Spagnoli, D. J. Cooke, S. Kerisit, and S. C. Parker. Molecular dynamics simulations of the interaction between the surfaces of polar solids and aqueous solutions. *Journal of Materials Chemistry*, 16(20):1997–2006, 2006.

[50] F. Molnar and J. Rieger. "Like-charge attraction" between anionic polyelectrolytes: Molecular dynamics simulations. *Langmuir*, 21(2):786–789, 2005.

[51] W. Sang-Aroon and V. Ruangpornvisuti. Conformational analysis of alkali metal complexes of anionic species of aspartic acid, their interconversion and deprotonation: A DFT investigation. *Journal of Molecular Graphics & Modelling*, 26(6):982–990, 2008.

[52] S. A. Ojo, B. Slater, and C. R. A. Catlow. Computer simulation of calcite growth inhibition: A study of monophosphonate interaction with calcite. *Molecular Simulation*, 28(6-7):591–606, 2002.

[53] M. A. Nygren, D. H. Gay, C. R. A. Catlow, M. P. Wilson, and A. L. Rohl. Incorporation of growth-inhibiting diphosphates into steps on the calcite cleavage plane surface. *Journal of the Chemical Society-Faraday Transactions*, 94(24):3685–3693, 1998.

[54] N. H. de Leeuw and T. G. Cooper. A computer modeling study of the inhibiting effect of organic adsorbates on calcite crystal growth. *Crystal Growth & Design*, 4(1):123–133, 2004.

[55] D. M. Duffy and J. H. Harding. Simulation of organic monolayers as templates for the nucleation of calcite crystals. *Langmuir*, 20(18):7630–7636, 2004.

[56] S. G. Zhang, W. Y. Shi, W. Lei, M. Z. Xia, and F. Y. Wang. Molecular dynamics simulation of interaction between calcite crystal and water-soluble polymers. *Acta Physico-Chimica Sinica*, 21(11):1198–1204, 2005.

[57] P. Van Cappellen, L. Charlet, W. Stumm, and P. Wersin. A surface complexation model of the carbonate mineral-aqueous solution interface. *Geochimica Et Cosmochimica Acta*, 57(15):3505–3518, 1993.

[58] S. L. S. Stipp. Toward a conceptual model of the calcite surface: Hydration, hydrolysis, and surface potential. *Geochimica Et Cosmochimica Acta*, 63(19-20):3121–3131, 1999.

[59] C. Santschi and M. J. Rossi. Uptake of CO_2, SO_2, HNO_3 and HCl on calcite ($CaCO_3$) at 300K: Mechanism and the role of adsorbed water. *Journal of Physical Chemistry A*, 110(21):6789–6802, 2006.

[60] G. D. Bennett. A green polymerization of aspartic acid for the undergraduate organic laboratory. *Journal of Chemical Education*, 82(9):1380–1381, 2005.

[61] C. L. Freeman, J. H. Harding, D. J. Cooke, J. A. Elliott, J. S. Lardge, and D. M. Duffy. New forcefields for modeling biomineralization processes. *Journal of Physical Chemistry C*, 111(32):11943–11951, 2007.

[62] M. Born and K. Huang. *Dynamical Theory of Crystal Lattices*. Oxford University Press, Oxford, U.K., 1954.

[63] N. H. de Leeuw and S. C. Parker. Surface structure and morphology of calcium carbonate polymorphs calcite, aragonite, and vaterite: An atomistic approach. *Journal of Physical Chemistry B*, 102(16):2914–2922, 1998.

[64] N. H. de Leeuw and S. C. Parker. Modeling absorption and segregation of magnesium and cadmium ions to calcite surfaces: Introducing $MgCO_3$ and $CdCO_3$ potential models. *Journal of Chemical Physics*, 112(9):4326–4333, 2000.

[65] N. H. de Leeuw and S. C. Parker. Surface-water interactions in the dolomite problem. *Physical Chemistry Chemical Physics*, 3(15):3217–3221, 2001.

[66] D. M. Duffy and J. H. Harding. Modelling the interfaces between calcite crystals and langmuir monolayers. *Journal of Materials Chemistry*, 12(12):3419–3425, 2002.

[67] N. H. de Leeuw. Molecular dynamics simulations of the growth inhibiting effect of Fe^{2+}, Mg^{2+}, Cd^{2+}, and Sr^{2+} on calcite crystal growth. *Journal of Physical Chemistry B*, 106(20):5241–5249, 2002.

[68] S. Kerisit, S. C. Parker, and J. H. Harding. Atomistic simulation of the dissociative adsorption of water on calcite surfaces. *Journal of Physical Chemistry B*, 107(31):7676–7682, 2003.

[69] A. Pavese, M. Catti, G. D. Price, and R. A. Jackson. Interatomic potentials for $CaCO_3$ polymorphs (calcite and aragonite), fitted to elastic and vibrational data. *Physics and Chemistry of Minerals*, 19(2):80–87, 1992.

[70] A. Pavese, M. Catti, S. C. Parker, and A. Wall. Modelling of the thermal dependence of structural and elastic properties of calcite, $CaCO_3$. *Physics and Chemistry of Minerals*, 23(2):89–93, 1996.

[71] S. L. Mayo, B. D. Olafson, and W. A. Goddard. Dreiding - a generic force-field for molecular simulations. *Journal of Physical Chemistry*, 94(26):8897–8909, 1990.

[72] M. J. Frisch, G. W. Trucks, H. B. Schlegel, G. E. Scuseria, M. A. Robb, J. R. Cheeseman, J. A. Montgomery, Jr., T. Vreven, K. N. Kudin, J. C. Burant, J. M. Millam, S. S. Iyengar, J. Tomasi, V. Barone, B. Mennucci, M. Cossi, G. Scalmani, N. Rega, G. A. Petersson, H. Nakatsuji, M. Hada, M. Ehara, K. Toyota, R. Fukuda, J. Hasegawa, M. Ishida, T. Nakajima, Y. Honda, O. Kitao, H. Nakai, M. Klene, X. Li, J. E. Knox, H. P. Hratchian, J. B. Cross, V. Bakken, C. Adamo, J. Jaramillo, R. Gomperts, R. E. Stratmann, O. Yazyev, A. J. Austin, R. Cammi, C. Pomelli, J. W. Ochterski, P. Y. Ayala, K. Morokuma, G. A. Voth,

P. Salvador, J. J. Dannenberg, V. G. Zakrzewski, S. Dapprich, A. D. Daniels, M. C. Strain, O. Farkas, D. K. Malick, A. D. Rabuck, K. Raghavachari, J. B. Foresman, J. V. Ortiz, Q. Cui, A. G. Baboul, S. Clifford, J. Cioslowski, B. B. Stefanov, G. Liu, A. Liashenko, P. Piskorz, I. Komaromi, R. L. Martin, D. J. Fox, T. Keith, M. A. Al-Laham, C. Y. Peng, A. Nanayakkara, M. Challacombe, P. M. W. Gill, B. Johnson, W. Chen, M. W. Wong, C. Gonzalez, and J. A Pople. Gaussian 03, 2004.

[73] R. S. Mulliken. Electronic population analysis on LACO-MO molecular wave functions I. *Journal of Chemical Physics*, 23(10):1833–1840, 1955.

[74] G. W. Watson, E. T. Kelsey, N. H. de Leeuw, D. J. Harris, and S. C. Parker. Atomistic simulation of dislocations, surfaces and interfaces in MgO. *Journal of the Chemical Society-Faraday Transactions*, 92(3):433–438, 1996.

[75] W. Smith and T. R. Forester. DL_POLY 2.0: A general-purpose parallel molecular dynamics simulation package. *Journal of Molecular Graphics*, 14(3):136–141, 1996.

[76] Z. L. Zhu, X. M. Liang, and R. H. Zhang. Determination of the dissociation constants of polyaspartic acid. *Chinese Journal of Analytical Chemistry*, 33(12):1722–1724, 2005.

[77] W. Sang-Aroon and V. Ruangpornvisuti. Determination of aqueous acid-dissociation constants of aspartic acid using PCM/DFT method. *International Journal of Quantum Chemistry*, 108(6):1181–1188, 2008.

[78] M. Magnin. Caractérisation des particules de calcite nanostructurées - potentiel de surface. Technical report, EPFL, 2007.

[79] J. Lemaitre. Thermodynamic calculations. Personal communication, 2008.

[80] D.F. Evans and H. Wennerström. *The Colloidal Domain.* Wiley-VCH, New York, 1999.

Chapter 5

Segregation of dopants in powders and sintered ceramics

Segregation never brought anyone anything except trouble.[1]
– Paul Harris

The location of dopants in a ceramic microstructure has an important influence on the morphology and the effect of these dopants on densification as well the mechanical, electrical and optical properties of the final ceramic material. In this chapter simulation results on two different industrially relevant ceramics (Al_2O_3 and ZnO) and some of their most common dopants are presented. The results help understanding the way dopants act on processing and properties of ceramic materials and can serve as baseline data to experimentally improve dopant systems to obtain optimum ceramic microstructures for specific applications, based on knowledge rather than trial and error, thus saving time and resources.

---

[1] Although related to a somewhat different type of segregation, this can also be true for ceramics.

5.1 Introduction

As discussed in the introduction, doping is a key concept in ceramics technology, be it to influence and optimize the microstructure as is the case for sintering agents or to obtain a ceramic with very specific properties such as mechanical, electrical or optical. In order to optimize the way ceramics are doped, it would be desirable to understand the role of each dopant ion as well as interactions and synergic effects between dopants on a fundamental level. This is especially required for industrially relevant systems composed of many dopants, which are experimentally very difficult to optimize. The way dopant ions can act depends on their location, concentration and atomic neighborhood. Atomistic simulations can give access to this information, which is experimentally very difficult to obtain as will be discussed in the next paragraph.

Oversized dopant ions are known [1, 2, 3, 4, 5, 6, 7] to strongly segregate to defects in the ceramic microstructure, which can be point defects such as vacancies or substitutional ions, linear defects like dislocations or planar defects such as surfaces and grain boundaries. However the extent of this segregation and the energetic driving force are difficult to measure experimentally as analysis techniques allowing the required sub-nanometer spacial resolution (i.e. scanning transmission electron microscopy - STEM, electron energy loss spectroscopy - EELS or high-resolution imaging secondary ion mass spectrometry - HRI-SIMS) are sparse and often difficult to implement. Lower resolution techniques such as X-ray photoelectron spectroscopy (XPS, ESCA) will only measure averages over many surfaces or grain boundaries thus masking the required information on a single interface. Simulations allow us to take a bottom-up approach if segregation towards a high number of interface types, including special as well as more general ones, can be calculated. This information can be used to approach a microstructure composed of many interfaces thereby predicting a macroscopic behavior. This approach will give a fundamental understanding of the dopant location in ceramics, which will allow to use the dopants in a more knowledge based fashion, fully exploiting the capacities of the material. In this chapter atomistic simulation results on Al_2O_3 and the segregation of Mg and Y dopants therein will be used as input data for a microstructural model, thus predicting the effect of segregation of these dopants in a microstructure. Further atomistic simulation results on segregation of lanthanide (La, Gd, Yb) dopants in alumina as well as Mn, Co and Al dopants in ZnO ceramics will be presented. The results allow us to understand some of the effect these dopants have on sintering as well as the functionality of the ceramic.

5.1.1 Alumina

α-alumina is together with titania and zirconia one of the most common technical ceramic and therefore a large number of studies have been devoted to this material. Alumina ceramics are very often doped with magnesium, usually at proportions around 500 cationic ppm, which seems to improve densification and limit grain growth [8, 9]. The exact mechanisms are still debated but are thought to be related to enhancement of the interfacial diffusion [10, 8], changes of the interface structure and energy [11, 12] and decrease of the grain boundary mobility [8, 10, 13]. As presented in the introduction (section 1.17) a too high dopant concentration for a given grain size can lead to precipitation of $MgAl_2O_4$ particles at grain boundaries and triple points since the solubility of magnesium in Al_2O_3 is limited to around 130 cationic ppm [14]. Surface segregation of magnesium has been studied by Baik an coworkers [15] and it was found that annealing in air resulted in a measurable enrichment of surfaces whereas in vacuum Mg tends to evaporate once at the surface. The effective heat of segregation was evaluated as -1.4eV based on the surface concentrations measured by Auger electron spectroscopy.

Rate earth (lanthanide) elements are another common class of dopants for alumina ceramics, yttrium being the most common element, followed by lanthanum and less frequently lutetium, ytterbium and others elements within this period. Yttrium is added to alumina mainly in order to improve the mechanical properties, especially the high temperature creep resistance. The exact mechanism is still speculated upon but may be related to diffusion suppression by site blocking in the grain boundary due to the larger yttrium ions [16] or the fact the the Y-O bond is stronger than the Al-O bond [17]. Yttrium was shown to strongly segregate and as a result to be located in the grain boundary core until saturation is reached. At higher concentrations a near boundary layer of yttrium ions can form [18, 19]. Bicrystal studies have shown that yttrium concentrations vary between different mirror twin grain boundaries [20, 5]. A fair number of studies [21, 22, 23, 24, 25, 26, 27] looked at grain boundaries and yttrium segregation in alumina by means of computational methods based either on empirical potentials or first principles. Segregation energies for yttrium were found to range from -0.71eV to -3.00eV. It was found that yttrium dopants can be accommodated in pairs, which lowers the energy by about 0.3eV [26] compared to an incorporation of single dopant ions, suggesting an interaction between yttrium ions. Lanthanum is also added to alumina in order to enhance it's creep performance [28] but also to improve the optical transparency of the material [29]. La, Gd and Yb ions are known to strongly segregate, forming a grain boundary layer thinner than 1nm [6]. The presence of these oversized ions may prevent grain boundary diffusion

[30] and thus creep [28, 16]. Simulations of the segregation behavior of these dopants do to our knowledge not exits. Other aliovalent dopants such as titanium can be used to create charged defects, which are of interest for electrotechnical applications.

A very important result of the previous computational studies is that the empirical potential methods give qualitatively the same results even if the energies and geometries show slight variations [31]. This shows that pair potential methods can be used to calculate interface structures and segregation therein, the advantage compared to first-principle methods being that more and larger structures can be looked at with only a slight loss in precision. This is desirable since as mentioned above experimental studies showed important variations between different interfaces. As in a ceramic a large population of different interfaces exists the more interfaces are calculated, the better they can represent the interface population found in a ceramic microstructure.

5.1.2 Zinc oxide

Zinc oxide is a ceramic first used for electro technical applications in varistors by Matsuoka in 1969 [32, 33]. Varistors are electro technical elements, which protect an electrical circuit from over-voltage due to their property of being isolators below a certain voltage but to become conductive once this threshold voltage is reached. This is shown in figure 5.1 where a linear region like in a normal ohmic material exists at low field, letting only a small current leak, whereas once the “switch field” is attained, the current increases dramatically up to a value dictated by the presence of a second linear region at higher field coming from the intrinsic resistivity of the grains. A normal ohmic material would show a linear behavior throughout the whole field range without the presence of the plateau.

This behavior known as nonlinearity permits in the event of a surge or voltage transient the current to pass trough the varistor to the ground and the remaining circuit is protected. A relatively recent article [34] reviews the functioning mechanism of varistor ceramics at a microstructural and atomic level as well as the role dopants play. The particular current-voltage (I-V) behavior is achieved by selective doping of the microstructure in a way that the grain bulk is conductive but the grain boundaries are isolators. A varistor grain boundary can thus be seen as given in figure 5.2a where two grains are joined by means of a grain boundary material. This grain boundary material is essentially the same as the grains, but contains defects, which change it’s Fermi level (make it less conductive) by creating new states in the former band gap (circles in figure 5.2b). When the three components are joined together an

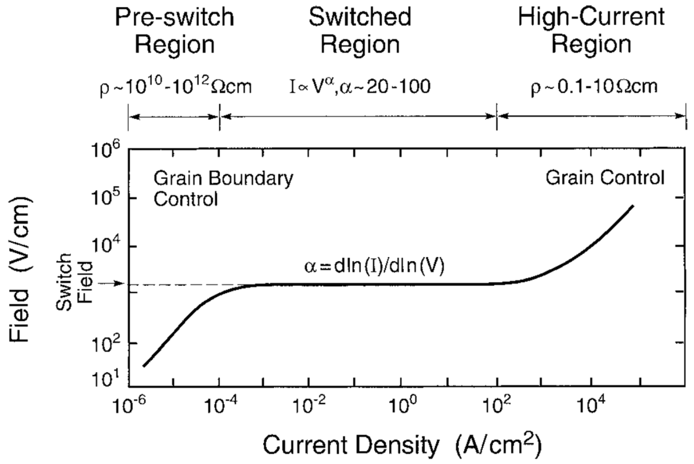

Figure 5.1: Nonlinear current-voltage behavior of a varistor ceramic. Extracted from [34].

equilibrium will establish by drawing electrons away from the bulk and towards the grain boundary where they are trapped by the defect states in the former band gap. This process continues until the Fermi level is constant throughout the material. The accumulation of electrons will result in an electrostatic barrier at the grain boundary, preventing electrons to pass trough the boundary. A voltage applied to this boundary will result in a change in the band structure as shown in figure 5.2c. The lowering of the Fermi level on the right side will allow electrons to flow from left to right through the boundary, the required voltage depending on the barrier height (Φ_B) and width (d).

In practice the barrier is obtained by the presence of bismuth and excess oxygen at the grain boundary, with cobalt and manganese controlling the degree of nonlinearity. Mn and Co are normally assumed to be in solid solution in the bulk acting as electron donors. The bulk conductivity of ZnO is controlled by the presence of oxygen vacancies and zinc interstitials and the presence of aliovalent dopants such as aluminum.

The threshold voltage is a linear function of the number of grain boundaries the current has to pass. Since today one of the big goals in electrotechnics is the downscaling of components to produce smaller chips, the size of the varistor elements decreases as well. If the grain size is to remain constant, this would mean lesser grain boundaries for the current to pass and thus a lower threshold voltage. Miniaturisation thus has to go along with a decrease in grain size if the same electrical properties are to be retained. This reduction in grain size towards the nano-scale however could result in problems with dopant segregation due to the increased fraction in grain boundary volume. Segregation effects will thus be accentuated and it has to

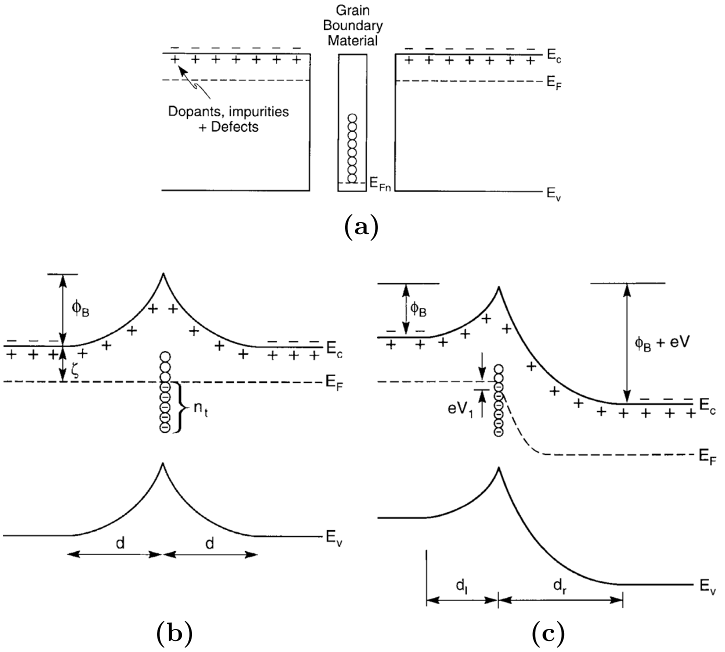

Figure 5.2: (a) Construction of a model varistor grain boundary and its band structure evolution (b) without and (c) with an applied voltage. Extracted from [34].

be made sure that the dopants responsible for bulk properties will not segregate to grain boundaries and modify the insulating properties.

Dopants in zinc oxide have been simulated in the past [35, 36] with recent calculations looking at grain boundary structures [37] and segregation by empirical methods [38]. First principle calculations looked at the effect of bismuth [39, 40, 41, 42] and antimony [43, 44, 45] doping on the electronic structure of ZnO grain boundaries. Segregation energies were evaluated between -0.8eV for a twist boundary and -1.5eV for a tilt boundary for bismuth and in between -1.0eV and -1.4eV for antimony. The segregation energies were found to change considerably if defect clustering is taken into account and strongly depend on the defect state of the boundary before addition of a further defect [42]. These theoretical studies seem however to overestimate the segregation energies as the experimentally determined value is -0.67eV for bismuth [46].

Industrially relevant dopants are the isovalent ions Mn^{2+} and Co^{2+} as well as the aliovalent ions Bi^{3+} and Al^{3+}. Following the above discussion it will be interesting to simulate the segregation behavior of these dopants in zinc oxide in order to ascertain their still somewhat disputed role in the creation of the varistor behavior.

Table 5.1: The miller indices of the calculates interfaces, their slab thickness and surface area

(hk.m)	(00.1)	(01.2)	(11.3)	(11.0)	(10.0)	(10.1)	(22.3)	(11.1)
D_{hkl}[**Å**]	12.43	3.41	2.05	2.36	4.09	3.88	1.13	2.32
A[**Å**^{2}]	19.28	70.20	116.91	101.60	58.60	61.75	211.27	103.41

5.2 Approach

In the following the approach used to create and calculate the interfaces as well as the segregation calculation technique will be outlined. As the techniques for alumina and zinc oxide are very similar, the alumina approach will be described firstly, followed by the differences encountered in the calculations of zinc oxide.

5.2.1 Alumina

Before segregation could be studied, the undoped interface structures were constructed. This was done using the METADISE [47] code applying the two region scheme [48] as described in section 2.3.5. For all structures the potential model by Lewis and Catlow [49] was used, which is particularly good at describing undercoordinated environments such as surfaces and grain boundaries. This potential model takes into account only dipole polarization of oxygen ions, neglecting higher order distortions such as quadrupoles, which is a limitation in the case of bulk alumina [50] but is considered negligible [51, 52] in the case of low symmetry environments such as grain boundaries and surfaces. Surfaces were constructed by cleaving the crystallographic unit-cell [53] (figure 5.3) along a chosen set of directions, for which the characteristics of the resulting slabs are shown in table 5.1.

The slabs were stacked up to a depth of at least 15 Å for region 1 and at least an additional 75 Å for region 2. Relaxation until convergence of the energy was carried out using the energy minimization module in METADISE, first applying 10 steps of conjugate gradient optimization followed by the Newton-Raphson method until convergence. Of all possible surface terminations only the one with the lowest energy was considered for the remainder of this study.

Grain boundaries were constructed by placing a mirror image of the surface above itself, using the surface plane as the mirror plane. As there is a degree of freedom associated with the rigid body displacement of the two half crystals, the two surfaces were displaced one above another by shifting the top crystal in steps of 0.5 Å with respect to the lower one, first along one direction of the surface plane, then along

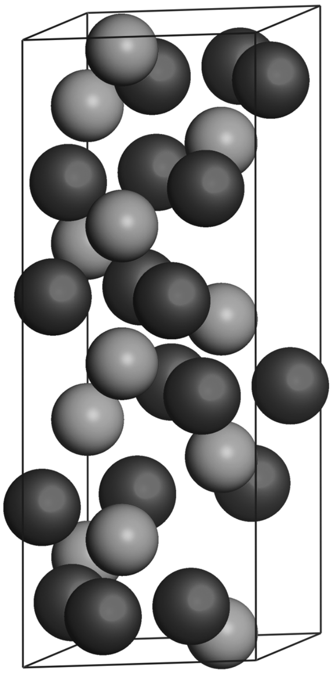

Figure 5.3: The hexagonal unit cell of α-alumina. Aluminum = light, oxygen = dark

the other one doing a line by line scan as shown on the left side in figure 5.4. An additional degree of freedom is associated with the spacing of the two half crystals. This was treated by introducing a 2Å gap between the half crystals, which was allowed to close during the relaxation procedure by rigid body displacement of the upper half crystal in the direction normal to the interface plane. The gap will open if unfavorable like-charge repulsion dominates or close if attraction between ions is present. The scanning of the two surfaces results in an energy surface (figure 5.4 right side), the minimum on which was considered to give the relative position of the two half crystals of the equilibrium undoped grain boundary. For all surfaces and grain boundaries, the interfacial energy was calculated as described in section 2.3.5.

Y doping

Yttrium is incorporated in the alumina crystal structure by substitution for an isovalent aluminum ion (ionic radii Al=0.535Å, Y=0.9Å) as given by the defect creation reaction 5.1.

$$Y_2O_3 \overset{Al_2O_3}{\Longrightarrow} 2Y_{Al}^{X} + 3O_{O}^{X} \tag{5.1}$$

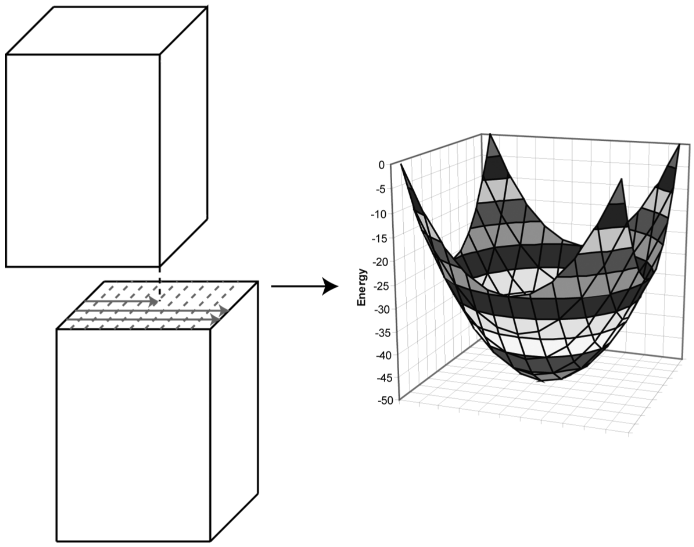

Figure 5.4: Scanning method to obtain the grain boundary configuration.

Yttrium doping was carried out in two steps, first a single dopant ion was placed on all sites in the simulation cell within a certain distance of the interface. This allows to calculate the enthalpy of segregation when the energy of incorporation in the infinite and otherwise perfect bulk crystal is compared to the one at the interface as described in section 1.2.3. It should be noted that as usual in energy minimization calculations ΔH was used instead of ΔG. The cost of incorporation in the infinite and otherwise perfect bulk crystal is calculated from the interatomic potentials using the Mott and Littleton [54] method implemented in the GULP [51] code.

The second step carried out was doping with multiple dopant ions in the same simulation cell. As the number of permutations when putting multiple dopant ions on multiple sites is very high (2^n permutations when placing 0 to n dopant ions on n sites), in a first step the following simple strategy has been adopted. It was considered that the sequence of dopant incorporation on the sites follows the sequence of increasing $\Delta H_{\mathrm{seg,\ i}}$, which considers that sites do not interact. In order to keep the number of permutations at a reasonable level, a maximum of nine dopant ions have been inserted into the structure, resulting in a maximum of $2^9 = 512$ permutations per structure. For smaller simulation cells this number was decreased to a minimum of four dopant ions for the very small (00.1) surface, which however results in comparable interfacial concentrations as for the larger cells with nine dopant ions.

Of these permutations for each number of dopants, the one with the lowest energy ($H_n^{\mathrm{interface}}$) was selected and the enthalpy of segregation, the surface energy and the enthalpy of solution in contact with the thermodynamically stable YAG ($Y_3Al_5O_{12}$) precipitates was calculated as described in section 1.2.3.

The statistical mechanics model by Mackrodt and Tasker [55] was used to predict the interface enrichment. The equation given in section 1.2.3 can be slightly rewritten as given in equation 5.2.

$$\frac{x_s}{x_b} = exp\left(-\frac{\Delta H_{seg} + \frac{dH_{seg}}{dx_s} x_s\left(x_s+1\right)}{RT}\right) = C\left(x_s, T\right) exp\left(-\frac{\Delta H_{seg}}{RT}\right) \tag{5.2}$$

The C factor can be obtained by fitting to experimental data and incorporates entropic contributions as well as the variation of the heat of segregation with the surface concentration. For the C factor used here, Sandra Galmarini used experimental data by McCune [56] for the fitting procedure carried out during her master project [57]. The C factor obtained was $1.004 \cdot 10^{-}5$ and has been used to calculate all surface concentrations for yttrium doped alumina.

It has to be noted that the interfacial energy change as a function of temperature is only related to the dopant coverage at this temperature. Achutaramayya and Scott [58] measured the changes in interfacial energy and fitted the change in interfacial energy by means of the factor $\Delta\gamma$ in equation 5.3.

$$\gamma(T) = \gamma(0) + \Delta\gamma T \tag{5.3}$$

They found values of $-0.232 \cdot 10^{-3} \mathrm{Jm}^{-2}\mathrm{K}^{-1}$ and $0.169 \cdot 10^{-3} \mathrm{Jm}^{-2}\mathrm{K}^{-1}$ for $\Delta\gamma$ in the case of surfaces and grain boundaries respectively. This correction is however not taken into account in the present approach due to it's empirical nature and lack of validation.

Mg doping

Magnesium doping is similar to yttrium doping with the exception that since the dopant is aliovalent the charge has to be compensated. This done by creating an oxygen vacancy for each pair or Mg ions as given in equation 5.4.

$$\mathrm{2MgO} \overset{\mathrm{Al_2O_3}}{\Longrightarrow} \mathrm{2Mg}_{\mathrm{Al}}^{'} + \mathrm{V}_{\mathrm{O}}^{\cdot\cdot} + \mathrm{3O}_{\mathrm{O}}^{\mathrm{X}} \tag{5.4}$$

This defect has a lot more degrees of freedom than a simple substitutional defect as the positions of 3 defect elements has to be defined. In order to get an idea of the defect geometry a preliminary defect cluster study in the bulk was performed. For this study all permutations of the bulk defect for which the Mg ions where maximally at a distance of 6Å from the oxygen vacancy have been calculated in the

Table 5.2: Fitted contribution values for the Mg-Mg-O$_{\text{vac}}$ defect cluster in the bulk.

E_0	$E_1 = E_2$	E_3	$E_{11} = E_{22} = E_{12}$	E_{33}	$E_{13} = E_{23}$
81.0028	0.5556	-0.2247	-0.0435	0.0115	0.0099

Mott-Littleton approach using region radii of 10Å and 25Å respectively which gives a converged energy for the defect cluster with the biggest extent. The energies have then been analyzed according to the quadratic model given by equations 5.5 to 5.8 where the vectors $\vec{r_i}$ denote the positions of the defect elements before relaxation (for the vacancy position the location of the oxygen ion prior to removal is taken) and the E_i are fitting factors describing the energy contributions coming from the interaction of the three defect elements. Since the two Mg ions interact with the oxygen vacancy in the same way it is assumed that $E_1 = E_2$, $E_{11} = E_{22} = E_{12}$ and $E_{13} = E_{23}$.

$$d_1 = |\vec{r}_{Mg_1} - \vec{r}_{O_{vac}}| \tag{5.5}$$

$$d_2 = |\vec{r}_{Mg_2} - \vec{r}_{O_{vac}}| \tag{5.6}$$

$$d_3 = |\vec{r}_{Mg_1} - \vec{r}_{Mg_2}| \tag{5.7}$$

$$\begin{aligned} E_{model} &= E_0 + d_1E_1 + d_2E_1 + d_3E_3 + d_1^2E_{11} + d_2^2E_{11} + d_3^2E_{33} \\ &+ d_1d_2E_{11} + d_1d_3E_{13} + d_2d_3E_{13} \end{aligned} \tag{5.8}$$

A least squares fit resulted in the parameters for the energy contributions given in table 5.2.

A graphical presentation (figure 5.5) can be obtained when the number of variables in the system is reduced two 2 by assuming the two magnesium ions to be at the same distance from the oxygen vacancy.

As it can be seen from figure 5.5 the Mg ions have a tendency to separate as far as possible due to the electrostatic repulsion between them as well as a better relaxation of structural distortions induced by the ions (ionic radii Al=0.535Å, Mg=0.72Å) at larger separation. The separation between the oxygen vacancy and the magnesium is best as small as possible due to the easier incorporation of the magnesium close to the vacancy. A maximum value is reached at 4.5Å which suggests that there is an energy barrier associated with the dissociation of the defect cluster.

This is certainly a simple description of the defect nevertheless these findings suggest that in fact the magnesium ions will stay as close as possible to the oxygen vacancy, while ensuring a maximum separation between them. This is valid in the bulk, but should as a general trend also be valid at interfaces, these rules can thus

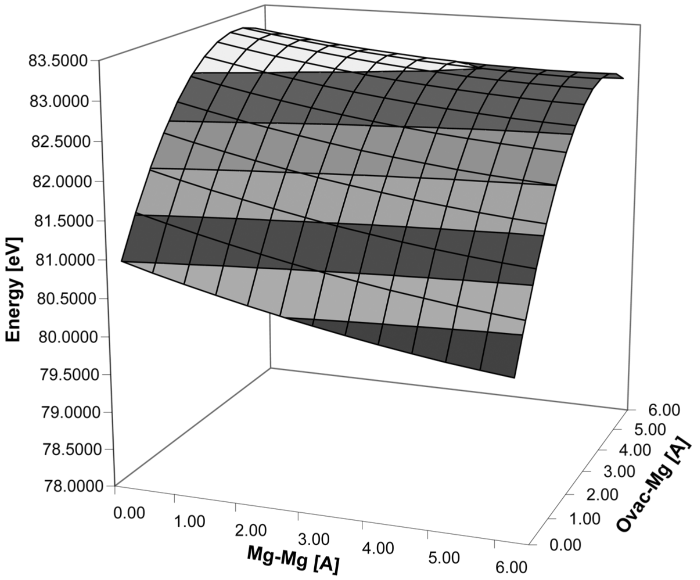

Figure 5.5: The defect energy as a function of $O_{vac} - Mg$ and $Mg - Mg$ distance in the defect cluster.

serve to restrict the number of permutations to be looked at. The defect has thus been restricted in a way that the Mg ions were at a maximum 4Å from the oxygen vacancy, which reduced the number of permutations to be looked at dramatically.

Fitting to experimental data by Baik [1] gave the same C factor as used for yttrium. This factor seems to be reasonably independent of the segregant.

La, Gd, Yb doping

The isovalent dopants lanthanum, gadolinium and ytterbium have been treated in a slightly different manner than yttrium doping in alumina, the two methods were however verified to give the same results. The defect creation reaction for a rare earth ion RE is given in equation 5.9.

$$\mathrm{RE_2O_3} \overset{\mathrm{Al_2O_3}}{\Longrightarrow} \mathrm{2RE_{Al}^{X}} + \mathrm{3O_{O}^{X}} \tag{5.9}$$

In order to calculate the segregation of these dopant ions, a driver code (ProbSeg) for METADISE [47] based on probability estimation of the different configurations has been developed. In a first step this code works in the same way as the previous approach by calculating the energy for incorporation on all sites up to a certain depth using METADISE for the energy minimization. The current implementation is limited to 32 dopant sites, which determines the maximum accessible depth as a function of the number of host sites. For these 32 sites each permutation of zero to

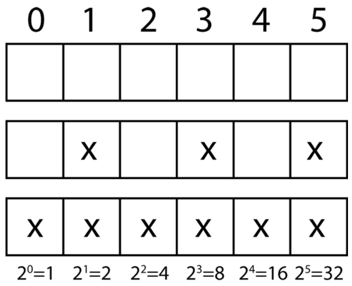

Figure 5.6: Permutation presentation in ProbSeg for an example of n=6 sites. The sites are numbered from 0 to n-1. The first line shows the undoped conformation, the second line a permutation with 3 dopants on sites 1, 3 and 5 and the last line a permutation, where all sites are occupied by dopant ions.

32 dopants can be described by a 32 digit number, each digit being either 0 for 'not occupied' or 1 for 'occupied'. In a computer it is easiest to store this information in a 32 bit number such as an integer variable and to use bitwise operations to access the data. The dopant sites are numbered from 0 to 31 or for the example shown in figure 5.6, which contains only 6 sites numbered 0 to 5.

As there is no distinction between the dopants, repetitions do not have to be taken into account. In the bit field defined by the 32 sites each permutation corresponds to a unique number when converting the binary code into a decimal number. The undoped configuration in figure 5.6 would correspond to 0, the second configuration to $2^1+2^3+2^5 = 2+8+32 = 42$ whereas in an equivalent fashion the last permutation carries the number 63. Each permutation is thus uniquely identified by a number between 0 and $2^n - 1$. ProgSeg's approach is then to loop over these permutations and to estimate the probability of each one according to equation 5.10.

$$p = \prod_{\text{i } \epsilon \text{ occupied sites}} \frac{exp\left(-\Delta H_{\text{seg}}\right)}{1 + exp\left(-\Delta H_{\text{seg}}\right)} \tag{5.10}$$

This equation is derived from a standard expression for transition probabilities in Monte Carlo simulations, however the usual factor of kT (or RT) is omitted, giving the probability on an arbitrary scale. This estimation does not take interaction between the sites into account. This ambiguity was resolved by calculating the 15 most probable permutations as it was shown for a test set of surfaces that the real energy minimum was always found amongst the 10 most likely permutations. During the probability calculation a bubble sort retaining the 15 most likely configurations is carried out, which are then be passed on to METADISE for structural relaxation by energy minimization. This approach has the advantage of reducing the computational cost from 2^n to $15n$ which gets advantageous starting from 7 dopant sites

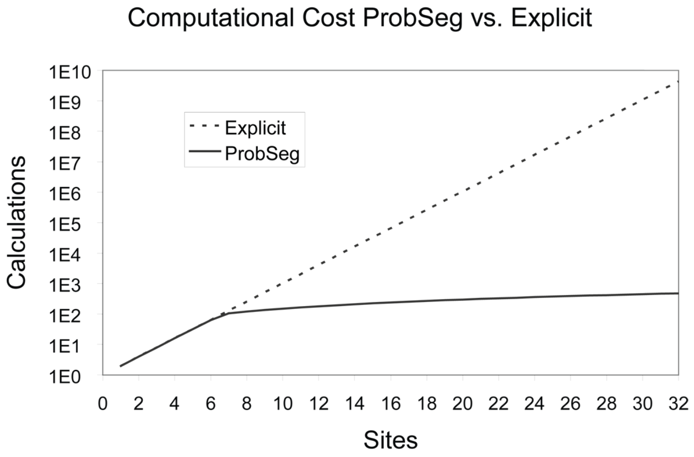

Figure 5.7: The computational cost with ProbSeg compared to an explicit calculation of all permutations. It can be seen that for 7 and more sites, this approach becomes advantageous.

as can be seen in figure 5.7. Properties such as the coverage dependent enthalpy of segregation, the enthalpy of dissolution from the stable mineral as well as the interfacial energy for the doped interface as given in section 1.2.3 were calculated for the lowest energy permutation of each number of dopants (H_n).

5.2.2 Zinc Oxide

Calculations with existing potentials

Zinc oxide presents the particularity of exposing a large number of highly polar surfaces when cleaved. In nature these surfaces will be reconstructed to remove these dipoles. Mirror twin boundaries built from polar surfaces are physically not stable and would need to include defects in the grain boundary to be stable as will be discussed in the results. In the zinc oxide lattice only cuts perpendicular to the c axis of the hexagonal unit cell (figure 5.8) [59] do not show a dipole perpendicular to the interface.

The mirror twin boundary planes used in this work are given in table 5.3. The surface and interface construction has been carried out in exactly the same fashion as for alumina, with the only exception that supercells were constructed in order to have cells of at least 10Å along all crystallographic axes. As pointed out above, the (00.1) boundary will be unstable, but is given here as an example to point out the effect of the dipole. For all calculations the potential model by Lewis and Catlow [49] has been used.

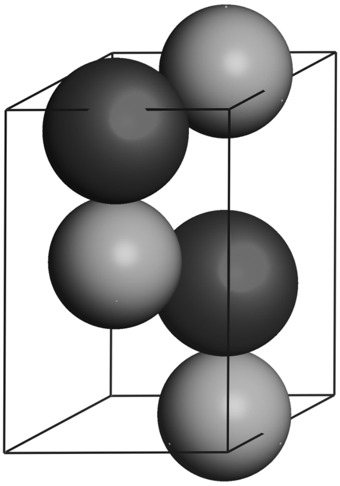

Figure 5.8: The hexagonal wurzite type unit cell of ZnO. Zn = light, O = dark

Table 5.3: The miller indices of the calculated ZnO grain boundaries. The parameters are given for the supercells calculated.

Boundary Plane (hk.m)	D_{hkl}	**A (Å^2)**	**Dopants**
(10.0)	2.798	65.598	Co^{2+}, Mn^{2+}, Al^{3+}
(11.0)	1.615	113.619	Co^{2+}, Mn^{2+}
(32.0)	0.642	142.968	Co^{2+}, Mn^{2+}, Al^{3+}
(00.1)	5.077	81.336	Co^{2+}, Mn^{2+}

Segregation of isovalent dopants (Mn^{2+} and Co^{2+}) (defect reactions given in equations 5.11 and 5.12) was studied using the ProbSeg method outlined above (section 5.2.1). For aliovalent dopants (Al^{3+}), additional charge compensating defect have to be created. Charge neutrality can be achieved by either creating a Al-Al-Zn$_{\mathrm{vac}}$ or Al-Al-O$_{\mathrm{int}}$ cluster according to the following Kröger-Fink reactions (equations 5.13 and 5.14).

$$\mathrm{MnO} \overset{\mathrm{ZnO}}{\Longrightarrow} \mathrm{Mn}_{\mathrm{Zn}}^{\mathrm{X}} + \mathrm{O}_{\mathrm{O}}^{\mathrm{X}} \tag{5.11}$$

$$\mathrm{CoO} \overset{\mathrm{ZnO}}{\Longrightarrow} \mathrm{Co}_{\mathrm{Zn}}^{\mathrm{X}} + \mathrm{O}_{\mathrm{O}}^{\mathrm{X}} \tag{5.12}$$

$$\mathrm{Al_2O_3} \overset{\mathrm{ZnO}}{\Longrightarrow} 2\mathrm{Al}_{\mathrm{Zn}}^{\cdot} + 3\mathrm{O}_{\mathrm{O}}^{\mathrm{X}} + \mathrm{V}_{\mathrm{Zn}}^{“} \tag{5.13}$$

$$\mathrm{Al_2O_3} \overset{\mathrm{ZnO}}{\Longrightarrow} 2\mathrm{Al}_{\mathrm{Zn}}^{\cdot} + 2\mathrm{O}_{\mathrm{O}}^{\mathrm{X}} + \mathrm{O}_{\mathrm{i}}^{“} \tag{5.14}$$

In order to model all permutations of the first reaction an approach as for Mg in alumina (section 5.2.1) was chosen: the two aluminum ions were placed in the structure, defining a maximum permissible distance (4Å) between them and a maximum permissible distance from the grain boundary plane (5Å). Then within a given distance of these two aluminum ions (4Å of either one) zinc ions were looked for and

Table 5.4: Comparison of the properties predicted by the two ZnO potential models with experimentally measured values.

	Experiment [62]	Lewis	Whitmore
a (Å)	3.2496	3.2304	3.2518
c (Å)	5.2042	5.0769	5.1969
z_O (fract)	0.3819	0.3892	0.3806
ϵ_{11}^{0}	9.26	7.8557	9.3666
ϵ_{33}^{0}	11.00	11.0849	10.5917
ϵ_{11}^{∞}	4.117	4.1077	3.8958
ϵ_{33}^{∞}	4.048	4.6047	4.0008
C_{11} (GPa)	209.7	237.5	200.0
C_{33} (GPa)	210.9	214.7	216.7

removed in order to create the vacancy.

The second reaction is more difficult to model as this time not ions, which can be removed to create vacancies are looked for but the most likely interstitial sites have to be found, which corresponds to finding the location in space where the interstitial will be most easily accommodated. For this problem a code called InterStitcher was developed by Christian Monachon during his semester project [60]. This software creates METADISE input files for all permutations by investigating the "overlap density" of the structure. This density function is obtained by summing over the density contributions of all atoms in the structure as given in equation 5.15.

$$D(\vec{r}) = \sum_{i}^{\text{atoms}} max\left(0, 1 - \frac{|\vec{r} - \vec{r_i}|^2}{s_{\text{interstitial}} + s_i}\right) \tag{5.15}$$

Where $\vec{r}$ is a location in space for which the density is to be evaluated, $\vec{r_i}$ is the location of a certain atom i in the structure and $s_{\text{interstitial}}$ and s_i are the ionic radii of the interstitial atom and the atom i respectively. In order to account for periodicity the 8 surrounding cells in the interface plane are included in the set of sites in the structure. InterStitcher calculates this density on a regular 3D grid of spacing 0.3Å and places the interstitial on the 5 points with lowest density in the grid.

Fitting and test of ZnO defect potentials

The defect energies found are not always the same as in other studies [35, 61] which is most likely due to the potential employed. Another more recent potential set by Whitmore [62] reproduces the ZnO lattice and properties a lot better than the Lewis and Catlow [49] potential as shown in table 5.4.

This new potential is rather complicated, consisting of 3 Buckingham potentials for distinctive coordination shells, which are splined together by polynomial potentials. The interaction within the first coordination shell is modeled using a combination of a Lennard-Jones and Buckingham potential. This model has been validated for surfaces [62] and will thus also be well suited for the study of ZnO grain boundaries. However this potential set does not include any dopant ions, which makes it impossible to be applied for segregation studies. It would therefore be desirable to augment the Whitmore potential to include dopant ions of interest.

This work has been started by carrying out DFT calculations with the Perdew-Burke-Ernzerhof GGA functional for exchange and correlation and Fritz-Haber-Institute Trouiller-Martins-type pseudopotentials using the ABINIT [63, 64] code. The total energy calculations were carried out in the bulk, using a 3x3x2 supercell to minimize dopant-dopant interactions and performing reciprocal space integration only at the gamma point. The energy was determined to be converged with a plane wave cutoff of 30 Hartree. The resulting cell contained 72 atoms one of which (in the center of the cell) was replaced with the dopant in question. Then the wave function was optimized until self-consistency was achieved.

In order to sample the potential energy surface of the dopant location around the substitutional position, small shifts of 0.1, 0.05 and 0.025Å were applied to the dopant along the negative and positive direction of all three crystallographic axes. The atomic conformations and associated energies were then collected and input into the GULP [51] code for fitting. Three Buckingham potentials were fitted for the same coordination shells as in the Whitmore potential for cobalt and manganese dopants. The ranges of the respective shells have been determined from the radial distribution functions calculated using the VMD [65] code. The initial potential parameters were taken the same as for the Zn-O interactions. The simultaneous fitting of A and ρ parameters in Buckingham potentials can be problematic as the parameters are interdependent, therefore the following fitting strategy was adopted. First the sequence A_1, A_2, A_3, C_1, C_2, C_3, ρ_1, ρ_2, ρ_3 was fitted until each variable converged within a small number of cycles (<5). Then the sets (A_1, A_2, A_3), (C_1, C_2, C_3), (ρ_1, ρ_2, ρ_3) were fitted also until convergence within less than 5 cycles was reached. A final cycle fitting all variables together was done and convergence reached within 20 or less cycles for both manganese and cobalt, all energies being reproduced within 10% or less.

5.3 Results and Discussion

5.3.1 α-Al_2O_3 surfaces and grain boundaries

Figures 5.9a and 5.9b show the structures of the undoped surfaces and grain boundaries respectively, which were calculated by Sandra Galmarini [57] and Yann Aman [66] during their master projects. It can be seen that certain surfaces like the (00.1), (11.0), (10.0) or (01.2) are highly symmetric, whereas larger ones like the (11.1), (11.2) or (22.3) surfaces show important relaxations and faceting. The same can be observed for the grain boundaries, where certain like the (10.0) and (01.2) adopt an almost bulk like structure, others like the (11.2) (11.1) or (22.3) showing a very open structured grain boundary core. One would expect dopant incorporation as well as diffusion to be facilitated in these open structures. The surface and grain boundary energies will be reported in the next section together with the doped interfacial energies to make comparison easier.

5.3.2 Y and Mg segregation in α-Al_2O_3

In this section data from Sandra Galmarini [57] is used to compare the segregation behavior of these two dopants using a microstructural model, developed during this thesis (section 6.3.1). Table 5.5 gives the calculated surface energies (γ) for the undoped and the 10ppm Y and 6ppm Mg doped case at 1600°C. The surface energies are in the range of those reported by other computational studies [67, 68, 69] and the relative ranking and magnitude is in agreement with experimental findings [70, 71]. It can be seen that except for the very regular (00.1) surface all other surfaces can lower their surface energy by accommodating Y dopants and that every surface can lower it's surface energy by accommodating Mg dopant ions. The magnitude of this decrease varies a lot, however it seems that for Mg the reduction is in general higher. This is also reflected by the mean values of the surface energy decreases. It is interesting to note that yttrium has a tendency to increase the standard deviation of the surface energies more than Mg. This hints towards the fact that magnesium keeps interfacial energies homogeneous whereas yttrium has a higher tendency to accentuate differences. It is further interesting to note that higher energy surfaces show a trend to accommodate more dopants than lower energy ones.

The morphologies calculated based on the surface energies are given in figure 5.10. It can be seen that the undoped morphology (figure 5.10a) is equiaxed and reproduces the experimental morphology by Kitayama and Glaeser [70] as well as the

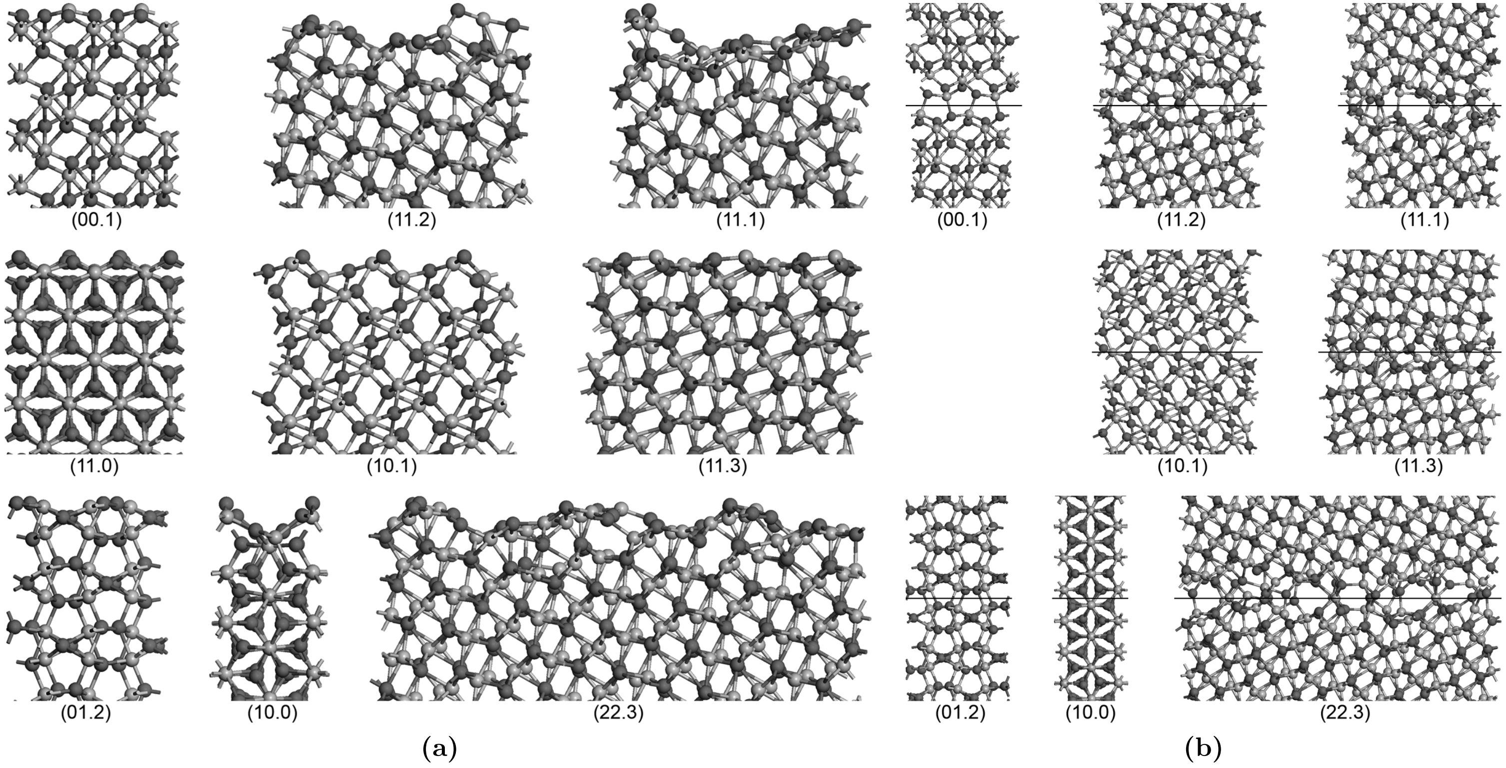

Figure 5.9: Undoped alumina structures: (a) surfaces and (b) grain boundaries. Oxygen=dark, aluminum=light

Table 5.5: Surface energies (γ) for undoped, 10ppm Y and 6ppm Mg doped alumina surfaces. The change in surface energy during doping ($\Delta\gamma$) as well as the coverage (Γ) are given for the doped cases at 1600°C.

Orientation	**Undoped**	**10 ppm Y 1600°C**			**6 ppm Mg 1600°C**		
h k m	γ [Jm^{-2}]	γ [Jm^{-2}]	$\Delta\gamma$ [Jm^{-2}]	Γ_Y [nm^{-2}]	γ [Jm^{-2}]	$\Delta\gamma$ [Jm^{-2}]	Γ_Y [nm^{-2}]
0 0 1	2.99	2.99	0.00	0.01	2.98	-0.01	7.78
1 0 0	2.88	2.80	-0.08	0.41	2.87	-0.01	1.70
1 0 1	3.67	2.68	-0.99	3.69	2.27	-1.40	4.81
0 1 2	2.62	2.58	-0.04	0.20	2.60	-0.02	1.42
1 1 0	3.02	2.01	-1.01	3.65	2.18	-0.84	3.00
1 1 1	3.48	2.04	-1.44	5.12	1.99	-1.49	5.07
1 1 3	3.20	2.98	-0.22	0.99	2.16	-1.04	3.71
2 2 3	3.18	2.32	-0.86	3.22	2.41	-0.77	2.79
Mean	3.13	2.55	-0.58		2.43	-0.70	
Std. Dev.	0.31	0.36	0.55		0.33	0.61	

one calculated by ab-inito method by Marmier [69] reasonably well. It can further be seen that both Mg and Y dopants have the effect of elongating the morphology even at the rather low concentrations of 10ppm and 6ppm respectively. For both dopants the number of surfaces appearing in the equilibrium morphology is reduced, which is due to the fact seen above that both dopants accentuate differences in surface energies. For yttrium this effect is more marked, which will lead to the quite faceted morphology shown in figure 5.10b. Magnesium on the other hand leads to a more rounded elliptical morphology which is due to the homogenizing effect magnesium has on the surface energies compared to yttrium.

Table 5.6 list the interfacial energies for undoped as well as 10ppm Y and 6ppm Mg doped alumina grain boundaries. It can be seen that the range of boundaries spans highly special $\Sigma 3$ boundaries as well as boundaries which are considered general such as the $\Sigma 93$ boundary. The variation in undoped grain boundary energies is rather large but the energies lie in the range of previously reported grain boundary energies [72, 73]. It is interesting to note that only three boundaries can lower their energy by accommodating Y dopants, whereas magnesium is accommodated at all but one interface but does not lower the interfacial energy significantly when at low concentrations. The interfacial energy homogenization due to dopant ions at the interface gets even more marked than for surfaces. It can be seen that both dopants have a tendency to lower the interfacial energies significantly, magnesium about twice as much as yttrium. Magnesium also shows an important microstructural homogenization effect by decreasing the interfacial energy standard deviation

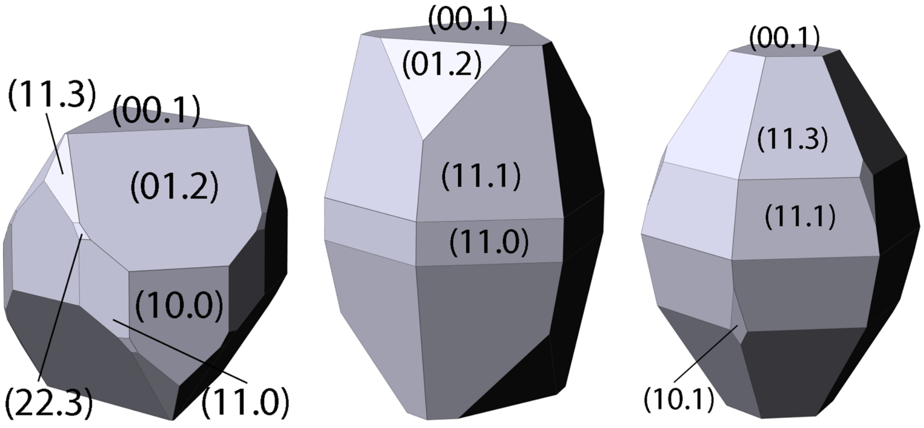

(a) (b) (c)

Figure 5.10: Morphologies calculated based on the surface energies reported in table 5.5: (a) The undoped morphology is rather equiaxed and close to the one reported by Kitayama and Glaeser [70], (b) the yttrium doped morphology is more elongated and is composed of lesser faces and (c) the magnesium doped morphology is also elongated but of a more regular rounded shape than the yttrium morphology

significantly. This will lead to a more equiaxed growth and thus more homogeneous microstructures, which can also be experimentally observed (figure 5.11). Again as already for the surfaces it is the two highest energy interfaces, which accommodate the most dopants. It will be interesting to see later if other dopants such as lanthanides (section 5.3.3) also follow this behavior and if it is even transferable to other crystalline systems such as YAG (chapter 6).

Segregation in powders and ceramics has been calculated using a microstructural model based on dodecahedral grains (for more details on the full model - only a

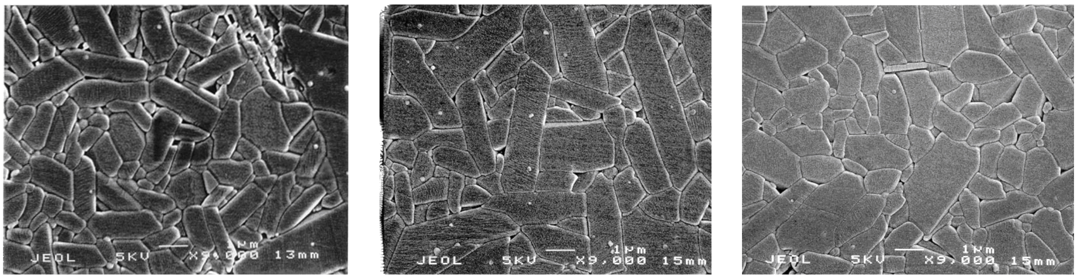

(a) (b) (c)

Figure 5.11: Experimental morphologies of: (a) undoped alumina (b) yttrium doped alumina and (c) magnesium doped alumina. It can be seen that the grains are on average most equiaxed for the magnesium doped case. Figures extracted from [74]

Table 5.6: Grain boundary energies (γ) for undoped, 10ppm Y and 6ppm Mg doped alumina grain boundaries. The change in interfacial energy during doping ($\Delta\gamma$) as well as the coverage (Γ) are given for the doped case at 1600°C. The (110) boundary is not listed as it is a mirror plane in the corundum structure and the boundary adopts thus the bulk structure. The (223) boundary could not yet be calculated due to restrictions in the number of atoms.

Plane				**Undoped**	**10 ppm Y 1600°C**			**6 ppm Mg 1600°C**		
h	k	m	Σ	γ	γ	$\Delta\gamma$	Γ_Y	γ	$\Delta\gamma$	Γ_Y
				[Jm^{-2}]	[Jm^{-2}]	[Jm^{-2}]	[nm^{-2}]	[Jm^{-2}]	[Jm^{-2}]	[nm^{-2}]
0	0	1	3	2.66	2.32	-0.34	0.45	1.17	-1.49	21.23
1	0	0	3	0.50	0.50	0.00	0.00	0.50	0.00	0.01
1	0	1	11	1.88	1.88	0.00	0.00	1.88	0.00	0.03
0	1	2	7	0.27	0.27	0.00	0.00	0.27	0.00	0.00
1	1	1	93	2.87	2.10	-0.77	3.23	2.01	-0.86	3.23
1	1	3	13	2.42	2.22	-0.20	0.96	2.42	0.00	0.02
Mean				1.77	1.55	-0.22		1.38	-0.39	
Std. Dev.				1.12	0.91	0.30		0.87	0.64	

simplified version is used here - please refer to section 6.3.1). Based on the present data the construction of an equilibrium and non-equilibrium powder model is possible, the former one based on the Wulff shape and the latter one on the assumption that all surfaces will appear according to the inverse of their interfacial energy. The equilibrium model may best describe a powder produced by a slow method such hydrothermal precipitation whereas the non-equilibrium case can describe a powder produced by a flame method. For grain boundaries only this second type of model is possible as a single grain boundary per interface plane has been calculated. The model used here is thus a simplification of the one applied to YAG in the next chapter since the microstructure is always considered at equilibrium as would be the case approached during slow conventional sintering. This does not allow an estimation of effects as they would appear for rapid sintering techniques such as the emerging spark plasma sintering (SPS) [75].

The resulting proportions of segregated dopants are reported graphically in figure 5.12. It can be seen that for both dopants the equilibrium powder can accommodate most dopant ions at the interface (the red curves being the highest ones for both series of solid and dashed lines). The non-equilibrium powder accommodates slightly less dopants than the equilibrium one but in every case more than the grain boundaries in a ceramic. It can be seen that for magnesium a larger amount of dopants will be found at the interfaces than for yttrium.

Two interesting conclusions can be drawn from the data presented in figure 5.12.

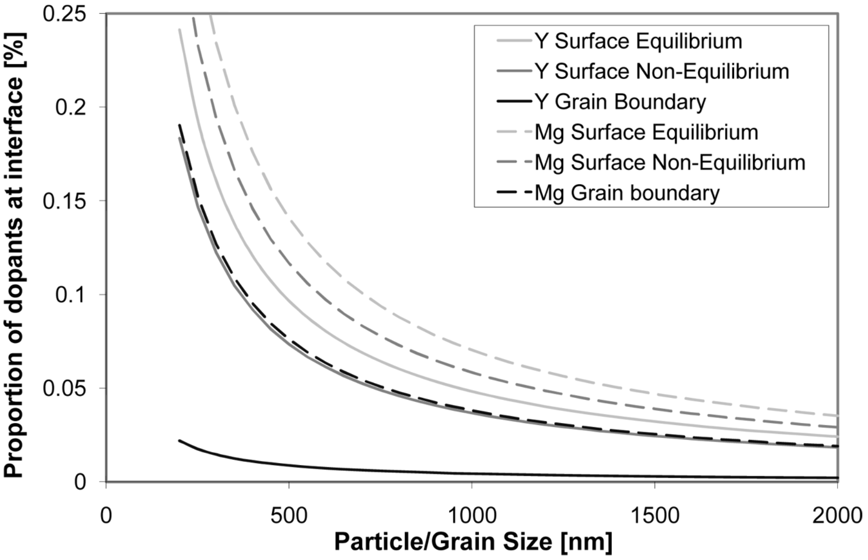

Figure 5.12: Proportion of segregated dopants as a function of particle/grain size for yttrium (solid lines) and magnesium (dashed lines) dopant alumina. For powder surfaces two different models are considered one with a powder having it's equilibrium shape and one where the equilibrium is not attained. For grain boundaries only one model, which is close to equilibrium is considered.

Firstly it can be seen that when two surfaces join to form a grain boundary a dopant rejection towards the bulk is required since the proportion of dopants, which can be in the boundary is in every case less than for the separate surfaces. This effect will be more marked when equilibrium powders are used as they will contain a higher proportion of dopants at the surface. This diffusional process takes time, which means that fast sintering methods will have a higher risk of precipitate formation than slower ones. Secondly it can be seen that for smaller particles and grains a higher proportion of dopants is found at the interfaces than for larger ones. When during sintering grain growth occurs there will also have to be a dopant reject towards the bulk. The simultaneous appearance of these two effects during sintering accentuates the problematic of dopant evacuation from the grain boundary. However it has to be said that equilibrium powders are likely to have a lower reactivity than non equilibrium powders. This means that grain growth will be reduced in this case and the fact that for equilibrium powders more dopants have to be rejected towards the bulk will become less severe.

5.3.3 La, Gd and Yb segregation in α-Al_2O_3

In this section the segregation behavior of lanthanide dopants (La, Gd and Yb) to surfaces and grain boundaries in alumina will be predicted. Some preliminary results from [66] have been used and are included for completeness. In this series of results it will be interesting to compare the segregation and dissolution behavior of the isovalent dopants with slightly different ionic radii (La=1.032Å, Gd=0.938Å and Yb=0.868Å).

Figure 5.13 shows the enthalpy of dissolution behavior of lanthanum, ytterbium and gadolinium coming from the respective stable phases La_2O_3, Yb_2O_3 and Gd_2O_3 in selected surfaces and grain boundaries of alumina. The interfaces have been chosen to be a good representation of the different types calculated, including very large ones such as the (111) and (223) surface but also highly symmetric ones such as (001), (012) and (100).

It can be seen that generally the curves follow an increasing trend with increasing interfacial concentration. There are secondary minima on some of the curves, which hints that dopants can adopt favorable configurations at certain higher concentrations. For the (001) surface the incorporation of Gd and Yb is not favorable at all. It is however interesting to see that at higher concentrations there is a favorable incorporation at surfaces for the larger La ions. This is most likely related to formation of a second phase like structure. This is further supported by a dip in the enthalpy of solution curve for Gd at the same concentration. The difference in whether incorporation is favorable or not is then determined by the relative stability of the dopant oxide mineral. It can be seen that for the (012) surface La can be incorporated up to around 7nm^{-2} whereas for Gd the limit is around 3nm^{-2}, incorporation being completely unfavorable for ytterbium. All other surfaces are able to accommodate a certain amount of all three dopants. The maximum possible concentration being always the highest for lanthanum, followed by gadolinium and ytterbium. This behavior is inversely proportional to the bulk dopant incorporation energies of La=22.91eV, Gd=17.48eV and Yb=14.36eV, which would rather hint at the inverse behavior. The dissolution behavior of these dopants seems thus to be governed rather by the energy of the dopant in it's mineral than in the alumina surface.

For the grain boundaries only the (111) and (223) mirror twins are capable of accommodating dopant ions. For all the others the energy of dissolution is positive however it is interesting to note that it gradually decreases with increasing dopant concentration. This means that at higher concentrations energetically more favor-

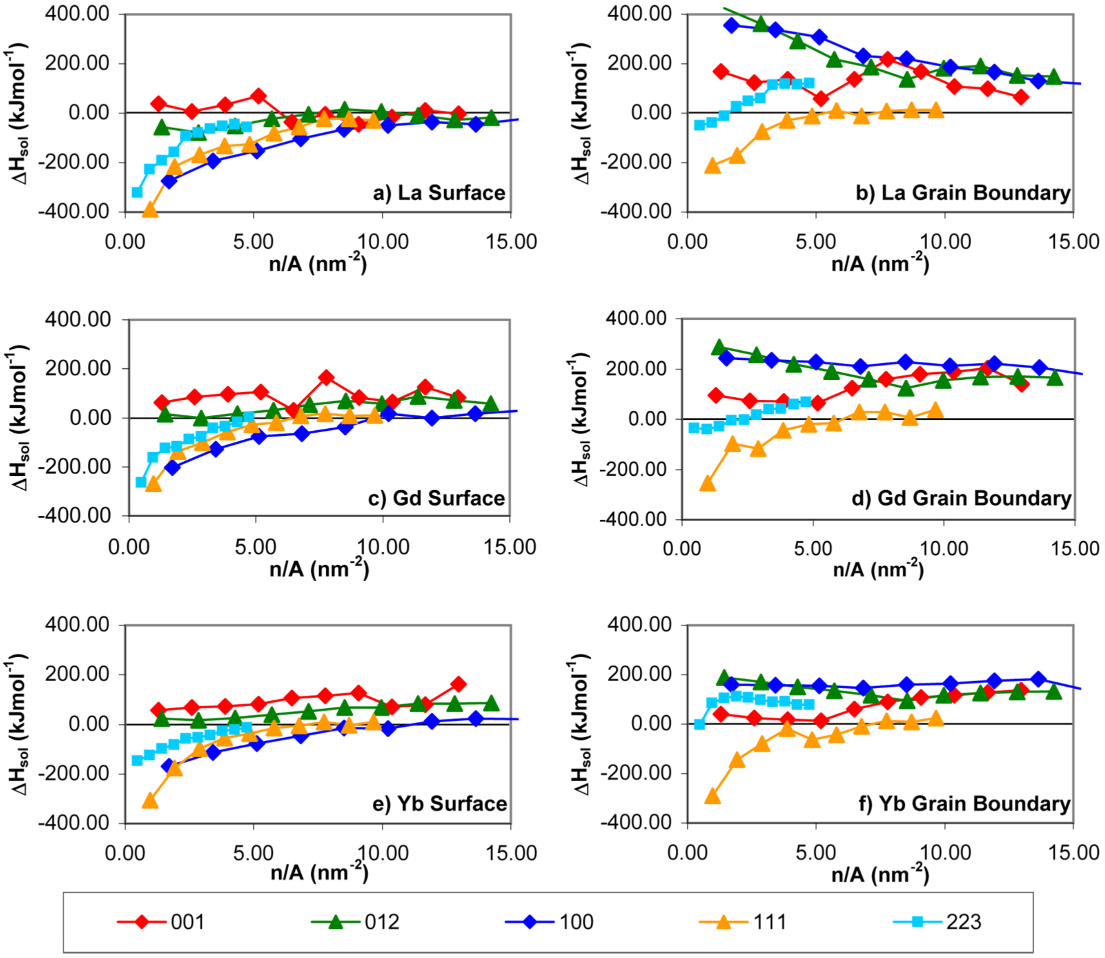

Figure 5.13: Enthalpy of dissolution in contact with La_2O_3, Yb_2O_3 and Gd_2O_3 (solid state doping) for selected alumina surfaces and grain boundaries.

able configurations probably close to second phase structures can be adopted. The dissolution behavior for the three dopants at the two accepting grain boundaries does not seem to be as distinct as for surfaces, the maximum concentrations being all in the same range. The only exception is ytterbium which is not accommodated at the (223) mirror twin.

The segregation behavior of the same dopants is shown in figure 5.14. Contrary to the the enthalpy of dissolution, the segregation behavior follows the sequence of bulk incorporation as well as ionic radius. Lanthanum shows the largest segregation energies followed by gadolinium and ytterbium. For surfaces as for grain boundaries the (111) plane seems to give the highest trend for segregation. This may be related to it's very faceted surface structure and the very open boundary core, which makes it easier to accommodate misfit strains. The (001) and (012) surfaces and grain boundaries show comparatively low trends for segregation, which seems to confirm the hypothesis emitted in the previous section that low energy interfaces generally

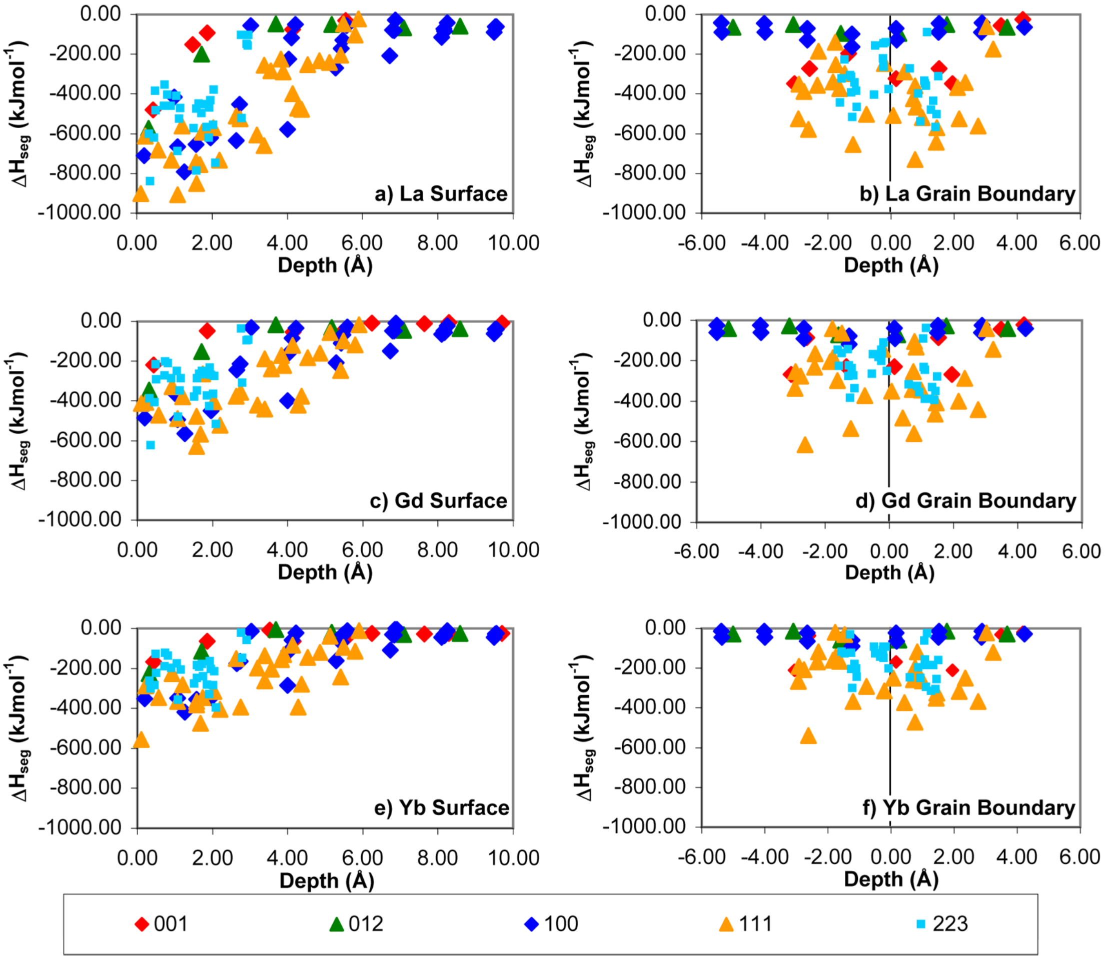

Figure 5.14: Segregation behavior La, Gd and Yb at surfaces and grain boundaries in alumina.

accommodate less dopants. It can also be seen from these graphics that the depth up to which dopant incorporation is favorable is around 7Å for surfaces and 4Å at each side of the boundary plane for the mirror twins.

Compared to magnesium-magnesium-oxygen clusters (-600kJmol^{-1}) and yttrium (-300kJmol^{-1}) [57] the enthalpies of segregation are almost twice as high. This shows that lanthanides cannot be accommodated in the bulk very well and that there will be a high driving force for segregation towards interfaces. It was however seen above that the dissolution of these dopant ions into grain boundaries and to a lesser extent also surfaces is highly unfavorable, which means that the dopants would prefer to adopt the mineral structure once segregated to the grain boundary. In order to get an idea of the interfacial energy of such a Al_2O_3/Gd_2O_3 a setup of a cubic Gd_2O_3 (100) and an Al_2O_3 (012) surface, where the misfit for 1x3 and 1x5 supercells respectively was small enough to be adjusted by slightly stretching one lattice and compressing the other one. The interfacial energy for this setup shown in figure 5.15a was evaluated

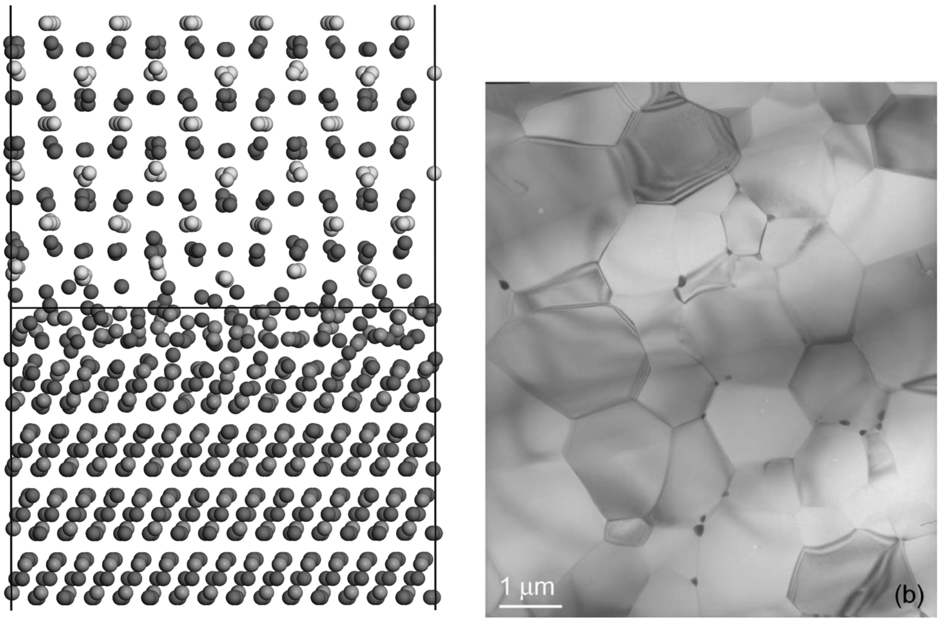

(a) (b)

Figure 5.15: (a) Structure of an Al_2O_3 (012)/Gd_2O_3 (100) interface (dark grey=oxygen, medium gray=aluminum, light gray=gadolinium) and (b) Microstructure of Gd doped alumina showing precipitated on triple points and grain boundaries. Image extracted from [6].

as 2.96Jm^{-2}. This energy is not significantly higher than grain boundary energies, which indicates that precipitation of secondary phases would not be hindered by large interfacial energies of the precipitates with the host crystal. It was also shown above that Gd doped interfaces adopt energetically more favorable structures at higher coverages (i.e. (111) and (012) mirror twins around 9nm^{-2} in figure 5.13) most likely due to adoption of a second phase like structure. This shows that precipitate nucleus formation is possible and that precipitate formation at grain boundaries is from a energetic point of view likely even at very low interfacial concentrations ($<1\text{nm}^{-1}$). The present data does however not allow the estimation of kinetic aspects related to precipitate formation. The likeliness of precipitate formation in Gd doped alumina is supported by experimentally observed microstructures published by West [6] as shown in figure 5.15b.

5.3.4 ZnO grain boundaries

This section looks at Mn and Co dopant segregation in zinc oxide ceramics. Some preliminary results have been taken from [60] and are included here for completeness. Table 5.7 gives the interfacial energies obtained for ZnO grain boundaries. The zero value for the (11.0) boundary is not unexpected as this is a mirror plane in

Table 5.7: Interfacial energies of the calculated ZnO grain boundaries. All energies were calculated by Christian Monachon during his semester project [60].

Boundary Plane (hk.m)	γ **(Jm^{-2})**
(10.0)	0.812
(11.0)	0.000
(32.0)	1.216
(00.1)	2.065

the wurzite structure and the resulting interface adopts the bulk structure. This “non-boundary” is not interesting to study but it validates that the grain boundary construction approach yields correct structures and energies. The remaining grain boundary energies except for the (00.1) case lie in a range which is reasonable for these quite special grain boundaries. The energy of the (00.1) boundary on the other hand is quite high, which is related to the presence of a dipole moment perpendicular to the interface. In the following the effect of this dipole on the grain boundary structure of the (00.1) boundary will be demonstrated, followed by a discussion of the segregation to the two remaining valid grain boundaries (10.0) and (32.0).

In his pioneering work Tasker [48] shows that surfaces in ionic crystals having a dipole moment perpendicular to the surface plane are physically unstable. In order to systematize the treatment of ionic crystal surfaces, Tasker classed surfaces in three groups. Type I surfaces consist of a stacking of charge neutral planes perpendicular to the surface direction (figure 5.16a). The repeat unit in this case can be seen as the single plane and due to the charge neutrality there will be no dipole in the structure. Type II surfaces consist of planes of alternating charge of different magnitude as shown in figure 5.16b, the repeat unit being defined as the neutral union of three planes. As a result this type of surface will also show no dipole and will be physically stable. Type III surfaces (figure 5.16c) finally consist of alternating planes of the same charge, the repeat unit being the, from a charge point of view, asymmetric union of two planes. Within the repeat unit as well as the crystal there will be a dipole moment, which will not cancel with increasing distance from the surface. Tasker further discusses that these surface directions can be observed in experiment however severe reconstruction by faceting, addition of surface vacancies or adatoms is necessary. This will result in a charge balancing across the crystal as shown in figure 5.16d, resulting in a removal of the dipole and thus stability of this type of surface.

For the case of polar ZnO thin films [76], a charge transfers from the valence band of the O terminated surface of a slab to the conduction band of the opposite Zn terminated surface was observed. This shows the importance to use first principle

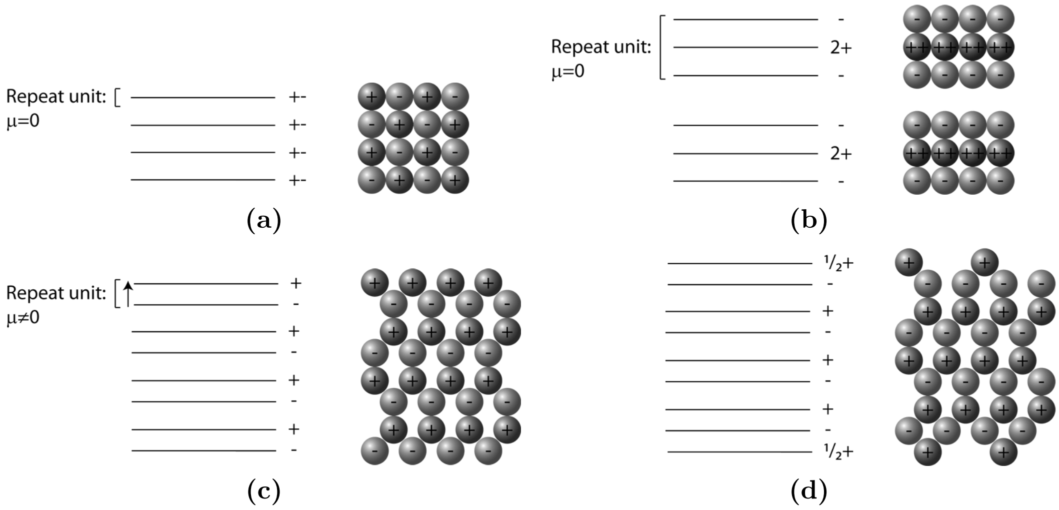

(a) (b) (c) (d)

Figure 5.16: Surface type models redrawn after Tasker [48]: (a) Unpolar type I surface as in a rocksalt (100) surface, (b) unpolar type II surface as found for fluorite (111) surfaces, (c) polar type III surface as found for (100) surfaces in the zincblende structures and (d) a possible reconstruction to remove the dipole from a zincblende (100) surface.

methods to correctly treat charge transfers in polar thin films. For the case of infinite surfaces reconstruction is required as charge transfers cannot take place for one slab surface to the other [77]. For the case of twist grain boundaries of the polar (001) surface Sato [37] used one oxygen and one zinc terminated half-crystal to eliminate the dipole. This effectively results in a twist boundary in created the bulk structure.

The relaxation of ions in an unpolar (10.0) an a polar (00.1) boundary are plotted in figure 5.17. As it can be seen for the case of the (10.0) boundary the relaxation along x is very small and the relaxations along y and z converge towards zero with increasing distance from the surface. This means that at the region 1-2 boundary a bulk like structure is to be found. On the other hand for the (00.1) boundary where a dipole exists, the amplitude of the displacements is a lot higher and more importantly it does not converge with increasing distance from the interface and it is not the same for ions in one plane parallel to the interface. This means that the the two region setup is invalid as it will result in large strains at the region 1-2 boundary, which adds additional unphysical energy terms.

Grain boundary energies (0.2-1.1 Jm^{-2}) reported by Domingos [38] for (001) twist boundaries of Zn and O terminated half-crystals respectively lie in the range of the ones found for the tilt boundaries calculated in the present work.

Figure 5.18 shows the atomic structures of the two grain boundaries. It can be seen that the (320) boundary (figure 5.18b) adopts a very open boundary core struc-

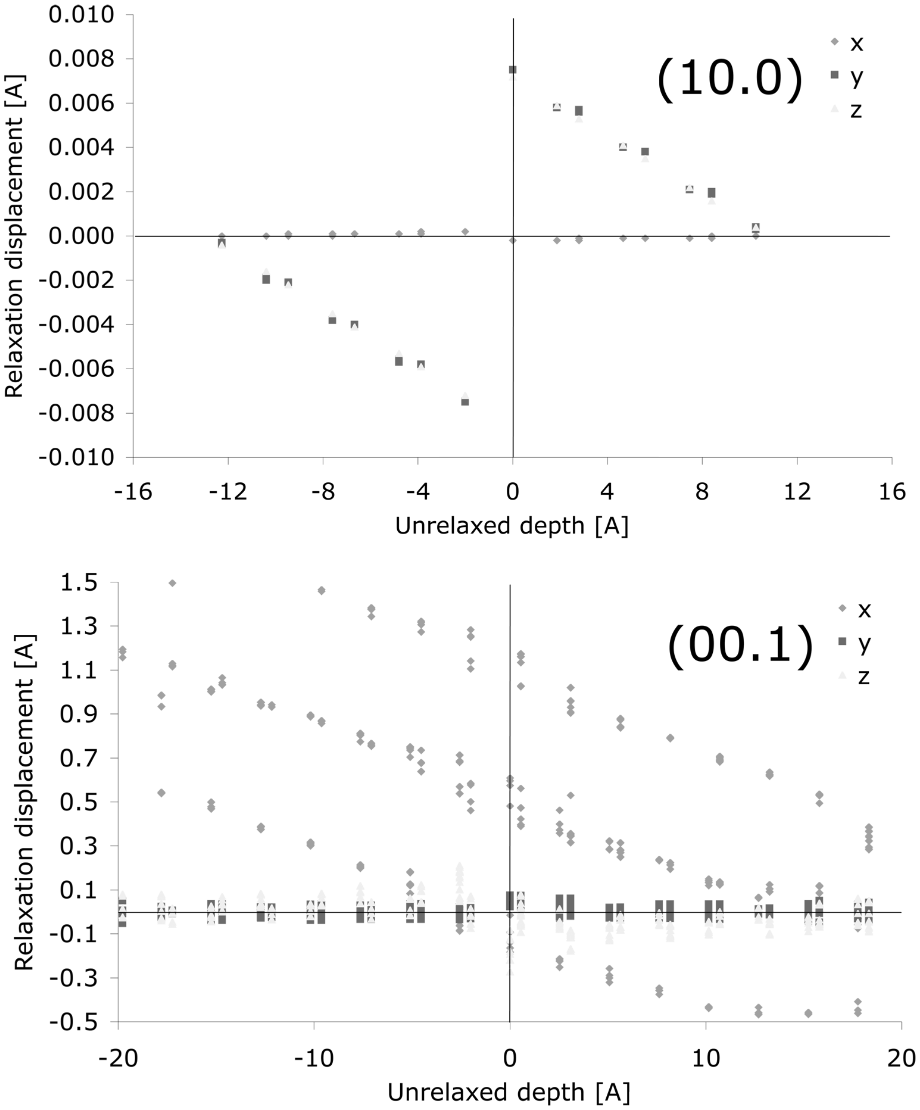

Figure 5.17: The relaxation in x, y and z direction as a function of the depth from the grain boundary.

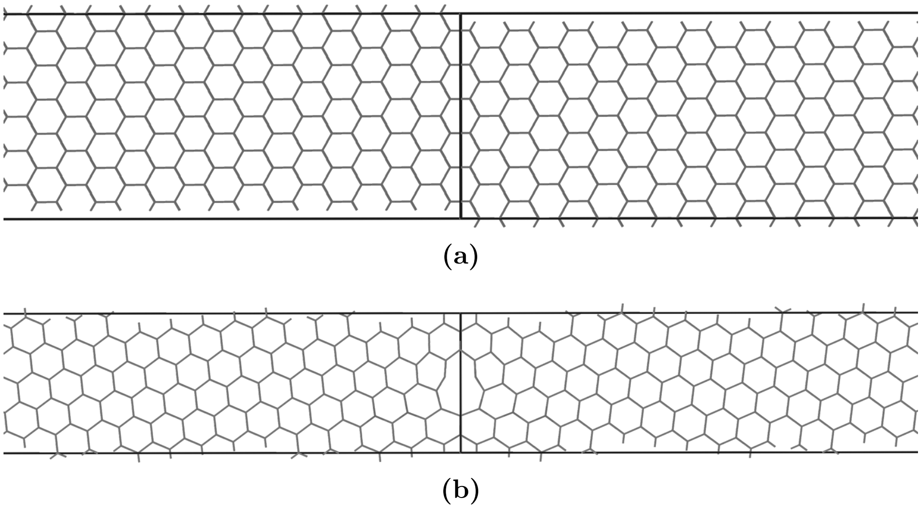

Figure 5.18: ZnO grain boundary structures: (a) the bulk-like (100) boundary and (b) the very open (320) boundary structure.

Table 5.8: Dopant defect energies and ionic radii of the defect ions in bulk ZnO.

Defect	Energy (eV)	Ionic radius (Å)
Zn		0.74
Co	-1.68	0.745
Mn	1.25	0.46
Al	-26.14	0.535
O_{int}	-15.18	
Zn_{vac}	22.84	
Al-Al-O_{int}	-81.83	
Al-Al-Zn_{vac}	-43.39	

ture, whereas the (100) boundary (figure 5.18a) has a very dense bulk-like structure.

5.3.5 Mn, Co and Al segregation in ZnO

As it has been seen above, only two valid grain boundaries ((10.0) and (32.0)) were constructed. The segregation of Mn, Co and Al to these two boundaries was looked at.

The first step was to determine the bulk dopant incorporation energies for the three dopants using the Mott-Littleton approach (section 2.3.6). For the substitutional Mn and Co ions a single calculation has been performed, whereas for the Al ion a multitude of structural permutations with either oxygen interstitial or zinc vacancy creation were looked at. From these permutations the minimal value is used. Table 5.8 gives the bulk dopant energies found.

It can be seen that the substitution with Co is energetically favorable whereas the one with manganese is slightly endothermic. The incorporation of an aluminum ion is very exothermic, however since charge compensating defects are necessary, either an oxygen vacancy or a zinc interstitial have to be created for every pair of aluminum ions. It is seen that an oxygen interstitial creation is energetically favorable (the octahedral site [78] being favored) whereas the zinc vacancy leads to an increase in energy. The energy of the Al-Al-$\mathrm{O_{int}}$ and Al-Al-$\mathrm{Zn_{vac}}$ defect clusters is lower than the sum of their constituents (which is -67.46eV and -29.44eV respectively) showing that defect aggregation occurs. Figure 5.19 shows the atomic configuration of these defects in ZnO.

It was shown using first principle calculations [61] that due to charge transfer the zinc ions may convert to uncharged metallic atoms. This sort of defect is not taken into account in the present work, as empirical potential models do not easily allow the coupling of metallic and ionic parts of the system.

Figure 5.20 shows the segregation behavior for Co and Mn in a highly symmetric (100) and the more open (320) boundary. It can be seen that cobalt does not segregate to the (100) boundary ($\Delta\mathrm{H_{seg}}$ is positive). This is in opposition with the results by Domingos [38] where cobalt showed a very slight trend for segregation ($\Delta\mathrm{H_{seg}}$ = -0.15eV = -14.47kJmol^{-1}). This difference may be related to the different bulk defect energy found in the present study (-1.68eV versus -0.5eV for Domingos). The type of grain boundary may also play a role. Domingos looked at a $\Sigma 7$ twist boundary, whereas in the present study the more symmetric (100) mirror twin is looked at. This is supported by the fact that for the much more open structured (320) boundary segregation energies of the order of -20kJmol^{-1} were found, which compares well with the findings by Domingos. Manganese shows much the same behavior with no segregation to the (100) boundary - the segregation energy being even more positive than for cobalt. For the (320) boundary a slightly higher trend for segregation ($\Delta\mathrm{H_{seg}}$ = -35kJmol^{-1}) is observed than for cobalt. These results indicate that cobalt which is easily accommodated in the bulk shows a lesser trend for segregation than manganese. It can also be seen that for these substitutional dopants open structured grain boundaries show more dopants segregation than highly symmetric ones.

Figure 5.21 shows the segregation behavior of the Al-Al-$\mathrm{O_{int}}$ and Al-Al-$\mathrm{Zn_{vac}}$ dopant clusters to the symmetric (100) and the more open structured (320) grain boundary. The two possible defect clusters show completely different segregation behaviors. It can be seen that for one given defect mean position ($x = \frac{1}{3}(x_1 + x_2 + x_3), y = \frac{1}{3}(y_1 + y_2 + y_3), z = \frac{1}{3}(z_1 + z_2 + z_3)$, where 1, 2 and 3 denote the different defect elements) a multitude of configurations exist, some more and some less ener-

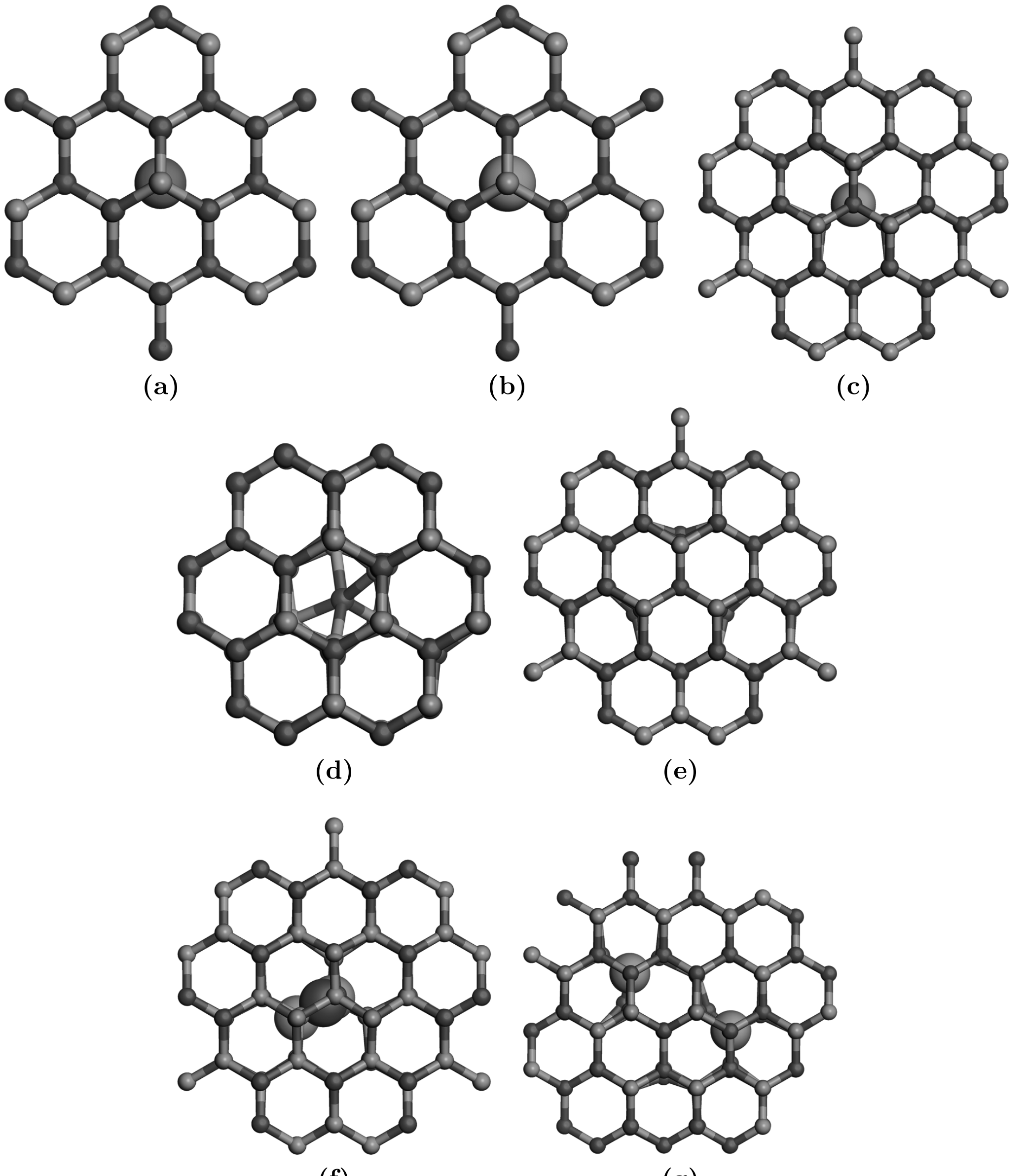

(a) **(b)** **(c)**

(d) **(e)**

(f) **(g)**

Figure 5.19: Defects in the ZnO structure: (a) For the cobalt defect the very similar ionic radius leads to almost no distortion, (b) for the manganese defect the oxygen ions relax slightly outwards, (c) the attractive force leads to an inwards relaxation of the oxygen ions for the Al defect, (d) the oxygen interstitial in one of the ZnO hexagonal channels, (e) repulsive forces between negatively charged vacancy and oxygen leads to an outwards relaxation when a zinc vacancy is created, (f) upon creation of an Al-Al-O_{int} cluster attraction between the interstitial and the aluminum leads to an oxygen position in the channel wall, also the oxygen ions around the defect relax inwards towards the aluminum ions and the zinc inwards as well towards the oxygen interstitial, (g) for the Al-Al-Zn_{vac} defect cluster relaxation of oxygen ions away from the vacancy but towards the aluminum ions is observed. Color code: light=zinc, dark=oxygen, dopants and interstitials oversized.

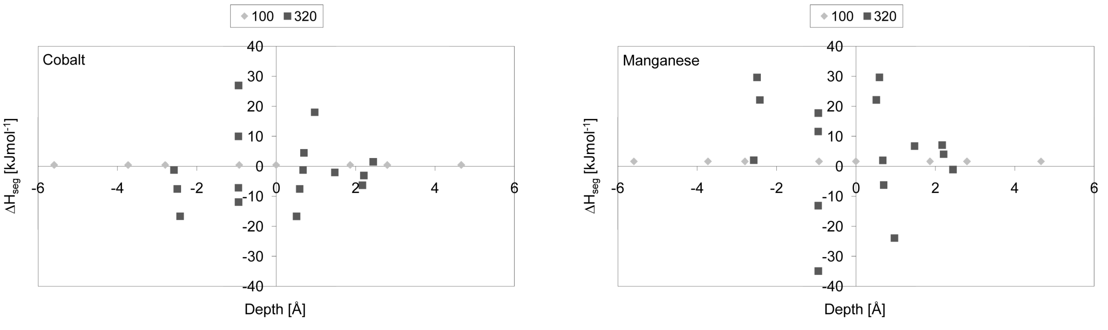

(a) (b)

Figure 5.20: Segregation behavior of cobalt and manganese dopants at the (100) and (320) grain boundaries in ZnO: (a) Cobalt segregation is slightly unfavorable for the highly symmetric 100 boundary, whereas for the more open (320) boundary favorable and unfavorable sites exist and (b) manganese does also not segregate to the (100) boundary but even stronger but to lesser sites at (320) boundaries than cobalt.

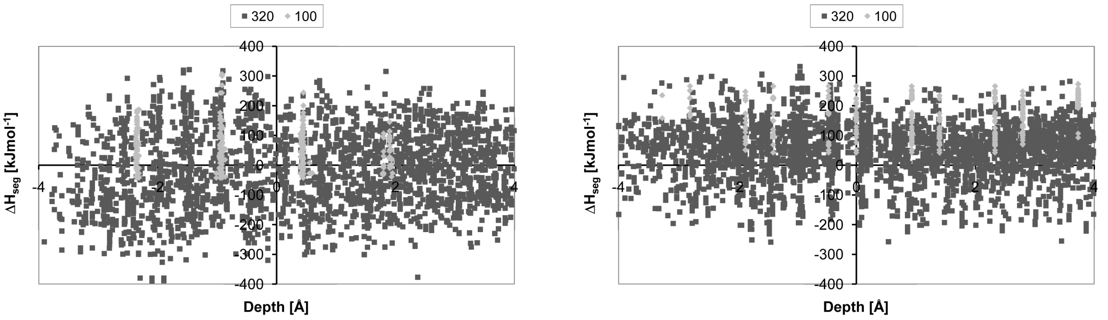

(a) (b)

Figure 5.21: Segregation behavior of aluminum dopants at the (100) and (320) grain boundaries in ZnO: (a) In the case of the oxygen interstitial creation segregation to both boundaries is favorable. The (320) boundary however showing more negative enthalpies of segregation. (b) for charge compensation by zinc vacancy creation only segregation to the (320) boundary is favorable.

getically advantageous. For the less structured (320) boundary a configuration cloud exists including negative segregation energies as well as positive ones. Segregation to the negative ones will be favorable whereas the positive configurations will not accommodate dopants. The (100) interface shows defects the centers of which are arranged in more structured bands.

In general the configuration with the oxygen interstitial shows a higher trend to segregation (more negative ΔH_{seg}) than the zinc interstitial configuration. For the (100) boundary only the oxygen interstitial cluster shows a trend to segregate whereas the zinc vacancy configurations would remain in the bulk. From the above bulk defect calculations it can be seen that the oxygen vacancy configuration is energetically a lot more favorable and will appear more frequently than the zinc vacancy one. This suggests that aluminum ions will show a slight trend to segregate since they are predominantly found in the oxygen interstitial configuration. Segregation will depend on the grain boundary as for the two cases calculated here quite different enthalpies of segregation were found. As for manganese and cobalt the dopant concentration at the (100) boundary is expected to be small or zero, whereas the (320) boundary accommodates a lot more segregated dopants. Large differences in dopant concentration may thus be expected for the different interfaces. In order to confirm this behavior more interfaces some also based on reconstructed dipolar surfaces should be undertaken.

Based on the current findings Mn and Co seem to have a low trend for segregation (ΔH_{seg} = -30kJmol^{-1}) to certain boundaries, whereas others do not seem to accommodate dopants. This suggests that for micron sized ceramics most Mn and Co dopants will be found in solid solution in the bulk, where they act as electron donors as mentioned above. Aluminum is also supposed to be in solid solution in the bulk. The present data shows that certain boundaries may show a large (ΔH_{seg} = -300kJmol^{-1}) trend for segregation. The main segregating species is however the Al-Al-O$_{int}$ cluster. This means that segregation will lead to an oxygen excess at the grain boundaries, which is also thought to be a reason for the varistor behavior of these ceramics. The presence of aluminum at the grain boundaries has however not been reported and a possible dissociation of the defect cluster should be looked at. It would further be interesting to model segregation behavior of bismuth as this ion is supposed to segregate strongly and be responsible for the varistor effect of the grain boundary.

5.3.6 Fitting and test of ZnO defect potentials

Tables 5.9 and 5.10 give the potential parameters obtained for manganese and cobalt respectively together with the potential parameters for ZnO published by Whitmore [62]. It can be seen that the fitting of the repulsive Lennard-Jones potential for the first coordination shell was omitted as it was found to fit to zero indicating a negligible contribution for the defect ions.

The defect energies calculated with these potentials are 1.23eV for manganese and -3.44eV for cobalt respectively, which is significantly lower for the case of cobalt and slightly lower for manganese than the previously calculated defect creation energies. The segregation behavior of cobalt is expected to be altered significantly (probably segregation is no longer observed) due to this change whereas the one for manganese

Table 5.9: ZnO Mn and Co substitutional defect potential parameters fitted to be incorporated into the potential set published by Whitmore [62].

New Potential							
Species	Charge (e)						
Mn core	2.000000						
Co core	2.000000						
Buckingham	Range (Å)	A (eV)	ρ (Å)	C (eVÅ^6)			
Mn core - O shell	0.0 - 2.2	720.191718	0.366840	22.117849			
Mn core - O shell	3.1 - 3.4	23.134845	0.679829	1.500381			
Mn core - O shell	3.6 - 12.0	912.517869	0.078935	0.043161			
Co core - O shell	0.0 - 2.2	1235.560866	0.352124	12.922781			
Co core - O shell	3.1 - 3.4	158.542147	0.439397	5.816665			
Co core - O shell	3.6 - 12.0	912.517869	0.078936	12.064733			
Polynomial	Range (Å)	C$_0$ (eV)	C$_1$ (eVÅ)	C$_2$ (eVÅ^2)	C$_3$ (eVÅ^3)	C$_4$ (eVÅ^4)	C$_5$ (eVÅ^5)
Zn core - O shell	2.2 - 3.1	82.745993	-35.869958	-56.847476	51.472478	-15.092742	1.520912
Zn core - O shell	3.4 - 3.6	54.875141	-44.306812	13.358705	-1.871543	0.123123	-0.003077
Co core - O shell	2.2 - 3.1	48.080029	-42.807102	13.672735	-1.951152	0.133065	-0.002815
Co core - O shell	3.4 - 3.6	55.216264	-45.003532	13.654713	-1.937851	0.130864	-0.002882

Table 5.10: ZnO potential parameters of the basis potential set published by Whitmore [62].

Whitmore Potential							
Species	Charge (e)						
Zn core	2.000000						
O core	1.754415						
O shell	-3.754415						
Spring	k^2 (eVÅ^{-2})	k^4 (eVÅ^{-4})					
O core - O shell	55.518883	2625.567362					
Buckingham	Range (Å)	A (eV)	ρ (Å)	C (eVÅ^6)			
Zn core - O shell	0.0 - 2.2	592.342818	0.352159	12.896893			
Zn core - O shell	3.1 - 3.3	157.297013	0.429673	5.815914			
Zn core - O shell	3.6 - 12.0	912.517869	0.078935	11.723055			
O shell - O shell	0.0 - 12.0	23674.698081	0.226404	33.476469			
Lennard-Jones	Range (Å)	A (eVÅ^{12})	C (eVÅ^6)				
Zn core - O shell	0.0 - 2.2	316.435204	0.000000				
Polynomial	Range (Å)	C_0 (eV)	C_1 (eVÅ)	C_2 (eVÅ^2)	C_3 (eVÅ^3)	C_4 (eVÅ^4)	C_5 (eVÅ^5)
Zn core - O shell	2.2 - 3.1	111.901725	-158.72704	89.657363	-24.98635	3.399631	-0.177932
Zn core - O shell	3.3 - 3.6	64102.354057	-93216.170229	54188.8077	-15741.070904	2284.873362	-132.581025

should only be slightly affected. These defect potentials need however to be further tested in bulk and interface calculations.

5.4 Conclusions

In this chapter it was shown that dopant segregation calculations can give important indications on dopant locations in the structure, their role, and also possible risks for second phase precipitation linked with high dopant concentrations. More specifically it was shown that magnesium does homogenize the interfacial energies as often proposed from a pragmatic interpretation of experimental results, which will lead to equiaxed grains as preferential growth directions are less likely. Yttrium was shown not to have this effect. It was shown that grain boundaries can accommodate a lot less dopants than free surfaces and thus care has to be taken to avoid precipitation when highly doped powder surfaces join to form a grain boundary. It was found that in general high energy interfaces accommodate more dopants, which in turn lowers their interfacial energy.

For lanthanide dopants it was found that the segregation behavior is governed by the ionic size whereas dissolution behavior depends on the energy of the dopant mineral phase. It was seen that for lanthanum, gadolinium and ytterbium strongly segregate to interfaces and that accommodation in the grain boundary is less favorable than in second phase precipitates. This suggests a high risk of precipitate formation for these dopants. For the case of gadolinium doping it was shown that the interfacial energy between a second phase and alumina is comparable to the interfacial energy and does not present an energy barrier for nucleation of precipitates. Energy decreases at high dopant concentrations also suggest formation of second phase like regions, which can act as nucleation centers.

It was found that ZnO is a rather difficult material in which to model grain boundaries. For the two cases that were actually physically stable, the segregation of substitutational dopants (Mn and Co) was found to be favorable only in the less ordered grain boundary. This same trend was also observed for aluminum doping, where the more ordered grain boundary can accommodate little or no dopants depending on the way the dopants is charge balanced. The more open structures grain boundary could accommodate dopants either way. To overcome difficulties with existing potentials, defect potentials for further studies can be derived from first principle calculations. ZnO is however due to its semi conducting property difficult to model using empirical potentials. Charge transfers as well as conversion into metallic zinc are known to occur, which can not be modeled using the present potential models. Also for the determination of the very important electron density of states in the grain boundary, ab-initio calculations are indispensable.

Bibliography

[1] S. Baik. Segregation of Mg to the (0001) surface of single-crystal alumina - quantification of AES results. *Journal of the American Ceramic Society*, 69(5):C101–C103, 1986.

[2] K. L. Gavrilov, S. J. Bennison, K. R. Mikeska, and R. Levi-Setti. Grain boundary chemistry of alumina by high-resolution imaging SIMS. *Acta Materialia*, 47(15-16):4031–4039, 1999.

[3] A. M. Thompson, K. K. Soni, H. M. Chan, M. P. Harmer, D. B. Williams, J. M. Chabala, and R. Levi-Setti. Dopant distributions in rare-earth-doped alumina. *Journal of the American Ceramic Society*, 80(2):373–376, 1997.

[4] J. Bruley, J. Cho, H. M. Chan, M. P. Harmer, and J. M. Rickman. Scanning transmission electron microscopy analysis of grain boundaries in creep-resistant yttrium- and lanthanum-doped alumina microstructures. *Journal of the American Ceramic Society*, 82(10):2865–2870, 1999.

[5] T. Gemming, S. Nufer, W. Kurtz, and M. Rühle. Structure and chemistry of symmetrical tilt grain boundaries in α-Al_2O_3: II. bicrystals with Y at the interface. *Journal of the American Ceramic Society*, 86(4):590–594, 2003.

[6] G. D. West, J. M. Perkins, and M. H. Lewis. Characterisation of fine-grained oxide ceramics. *Journal of Materials Science*, 39(22):6687–6704, 2004.

[7] D. Bouchet, S. Lartigue-Korinek, R. Molins, and J. Thibault. Yttrium segregation and intergranular defects in alumina. *Philosophical Magazine*, 86(10):1401–1413, 2006.

[8] K. A. Berry and M. P. Harmer. Effect of MgO solute on microstructure development in Al_2O_3. *Journal of the American Ceramic Society*, 69(2):143–149, 1986.

[9] S. I. Bae and S. Baik. Critical concentration of MgO for the prevention of abnormal grain-growth in alumina. *Journal of the American Ceramic Society*, 77(10):2499–2504, 1994.

[10] S. J. Bennison and M. P. Harmer. Grain-growth kinetics for alumina in the absence of a liquid-phase. *Journal of the American Ceramic Society*, 68(1):C22–C24, 1985.

[11] C. W. Park and D. Y. Yoon. Effects of SiO_2, CaO_2, and MgO additions on the grain growth of alumina. *Journal of the American Ceramic Society*, 83(10):2605–2609, 2000.

[12] W. Jo, D. Y. Kim, and N. M. Hwang. Reply to the comment on “effect of interface structure on the microstructural evolution of ceramics”. *Journal of the American Ceramic Society*, 90(7):2293–2295, 2007.

[13] K. K. Soni, A. M. Thompson, M. P. Harmer, D. B. Williams, J. M. Chabala, and R. Levisetti. Solute segregation to grain-boundaries in MgO-doped alumina. *Applied Physics Letters*, 66(21):2795–2797, 1995.

[14] L. Miller, A. Avishai, and W. D. Kaplan. Solubility limit of MgO in Al_2O_3 at 1600 °c. *Journal of the American Ceramic Society*, 89(1):350–353, 2006.

[15] S. M. Mukhopadhyay, a. P. Jardine, J. M. Blakely, and S. Baik. Segregation of magnesium and calcium to the (1010) prismatic surface of magnesium-implanted sapphire. *Journal of the American Ceramic Society*, 71(5):358–362, 1988.

[16] J. Cho, C. M. Wang, H. M. Chan, J. M. Rickman, and M. P. Harmer. Role of segregating dopants on the improved creep resistance of aluminum oxide. *Acta Materialia*, 47(15-16):4197–4207, 1999.

[17] W. Y. Ching and Y. N. Xu. Nonscalability and nontransferability in the electronic properties of the Y-Al-O system. *Physical Review B*, 59(20):12815–12821, 1999.

[18] C. M. Wang, G. S. Cargill, M. P. Harmer, H. M. Chan, and J. Cho. Atomic structural environment of grain boundary segregated Y and Zr in creep resistant alumina from EXAFS. *Acta Materialia*, 47(12):3411–3422, 1999.

[19] C. M. Wang, G. S. Cargill, H. M. Chan, and M. P. Harmer. X-ray absorption near-edge structure of grain-boundary-segregated Y and Zr in creep-resistant alumina. *Journal of the American Ceramic Society*, 85(10):2492–2498, 2002.

[20] J. P. Buban, K. Matsunaga, J. Chen, N. Shibata, W. Y. Ching, T. Yamamoto, and Y. Ikuhara. Grain boundary strengthening in alumina by rare earth impurities. *Science*, 311(5758):212–215, 2006.

[21] M. Exner and M. W. Finnis. Atomistic simulation of grain boundaries in alumina. *Intergranular and Interphase Boundaries in Materials*, 207:225–228, 1996.

[22] J. Chen, L. Z. Ouyang, and W. Y. Ching. Molecular dynamics simulation of Y-doped $\Sigma 37$ grain boundary in alumina. *Acta Materialia*, 53(15):4111–4120, 2005.

[23] J. Chen, Y. N. Xu, P. Rulis, L. Z. Ouyang, and W. Y. Ching. Ab initio theoretical tensile test on Y-doped Σ=3 grain boundary in α-al_2o_3. *Acta Materialia*, 53(2):403–410, 2005.

[24] C. Elsässer and A. G. Marinopoulos. Substitutional cation impurities in α-Al_2O_3: Ab-initio case study of segregation to the rhombohedral twin boundary. *Acta Materialia*, 49(15):2951–2959, 2001.

[25] S. Fabris and C. Elsässer. First-principles analysis of cation segregation at grain boundaries in α-Al_2O_3. *Acta Materialia*, 51(1):71–86, 2003.

[26] C. Elsässer and T. Elsässer. Codoping and grain-boundary cosegregation of substitutional cations in α-Al_2O_3: A density-functional-theory study. *Journal of the American Ceramic Society*, 88(1):1–14, 2005.

[27] W. Y. Ching, J. Chen, P. Rulis, L. Ouyang, and A. Misra. Ab initio modeling of clean and Y-doped grain boundaries in alumina and intergranular glassy films (IGF) in β-Si_3N_4. *Journal of Materials Science*, 41(16):5061–5067, 2006.

[28] J. H. Cho, M. P. Harmer, H. M. Chan, J. M. Rickman, and A. M. Thompson. Effect of yttrium and lanthanum on the tensile creep behavior of aluminum oxide. *Journal of the American Ceramic Society*, 80(4):1013–1017, 1997.

[29] Q. H. Yang, Z. J. Zeng, J. Xu, H. W. Zhang, and J. Ding. Effect of La_2O_3 on microstructure and transmittance of transparent alumina ceramics. *Journal of Rare Earths*, 24(1):72–75, 2006.

[30] J. X. Fang, A. M. Thompson, M. P. Harmer, and H. M. Chan. Effect of yttrium and lanthanum on the final-stage sintering behavior of ultrahigh-purity alumina. *Journal of the American Ceramic Society*, 80(8):2005–2012, 1997.

[31] A. G. Marinopoulos and C. Elsässer. Density-functional and shell-model calculations of the energetics of basal-plane stacking faults in sapphire. *Philosophical Magazine Letters*, 81(5):329–338, 2001.

[32] M. Matsuoka, T. Masuyama, and Y. Iida. Voltage nonlinearity of zinc oxide ceramics doped with alkali earth metal oxide. *Japanese Journal of Applied Physics*, 8(10):1275–1276, 1969.

[33] M. Matsuoka. Nonohmic properties of zinc oxide ceramics. *Japanese Journal of Applied Physics*, 10(6):736–746, 1971.

[34] D. R. Clarke. Varistor ceramics. *Journal of the American Ceramic Society*, 82(3):485–502, 1999.

[35] W. C. Mackrodt, R. F. Stewart, J. C. Campbell, and I. H. Hillier. The calculated defect structure of ZnO. *Journal de Physique*, 41(7-C6):64–67, 1980.

[36] D. J. Binks and R. W. Grimes. Incorporation of monovalent ions in ZnO and their influence on varistor degradation. *Journal of the American Ceramic Society*, 76(9):2370–2372, 1993.

[37] Y. Sato, T. Yamamoto, and Y. Ikuhara. Atomic structures and electrical properties of ZnO grain boundaries. *Journal of the American Ceramic Society*, 90(2):337–357, 2007.

[38] H. S. Domingos and P. D. Bristowe. Atomistic simulation of grain boundary segregation in zinc oxide. *Scripta Materialia*, 41(12):1347–1352, 1999.

[39] J. M. Carlsson, H. S. Domingos, B. Hellsing, and P. D. Bristowe. Electronic structure of a Bi-doped Σ=13 tilt grain boundary in ZnO. *Interface Science*, 9(3-4):143–148, 2001.

[40] H. S. Domingos, J. M. Carlsson, P. D. Bristowe, and B. Hellsing. Charge accumulation and barrier formation at grain boundaries in ZnO decorated with bismuth. *Journal of Physics-Condensed Matter*, 14(48):12717–12724, 2002.

[41] J. M. Carlsson, B. Hellsing, H. S. Domingos, and P. D. Bristowe. The effects of doping a grain boundary in ZnO with various concentrations of Bi. *Surface Science*, 532:351–358, 2003.

[42] H. S. Domingos, J. M. Carlsson, P. D. Bristowe, and B. Hellsing. The formation of defect complexes in a ZnO grain boundary. *Interface Science*, 12(2-3):227–234, 2004.

[43] J. M. Carlsson, B. Hellsing, H. S. Domingos, and P. D. Bristowe. Electronic properties of a grain boundary in Sb-doped ZnO. *Journal of Physics-Condensed Matter*, 13(44):9937–9943, 2001.

[44] H. S. Domingos and P. D. Bristowe. Electronic structure of twist grain-boundaries in ZnO and the effect of Sb doping. *Computational Materials Science*, 22(1-2):38–43, 2001.

[45] H. S. Domingos, P. D. Bristowe, J. Carlsson, and B. Hellsing. Segregation effects at a high-angle twist boundary in ZnO. *Interface Science*, 9(3-4):231–235, 2001.

[46] J. R. Lee, Y. M. Chiang, and G. Ceder. Pressure-thermodynamic study of grain boundaries: Bi segregation in ZnO. *Acta Materialia*, 45(3):1247–1257, 1997.

[47] G. W. Watson, E. T. Kelsey, N. H. de Leeuw, D. J. Harris, and S. C. Parker. Atomistic simulation of dislocations, surfaces and interfaces in MgO. *Journal of the Chemical Society-Faraday Transactions*, 92(3):433–438, 1996.

[48] P. W. Tasker. Stability of ionic-crystal surfaces. *Journal of Physics C-Solid State Physics*, 12(22):4977–4984, 1979.

[49] G. V. Lewis and C. R. A. Catlow. Potential models for ionic oxides. *Journal of Physics C-Solid State Physics*, 18(6):1149–1161, 1985.

[50] M. Wilson, M. Exner, Y. M. Huang, and M. W. Finnis. Transferable model for the atomistic simulation of Al_2O_3. *Physical Review B*, 54(22):15683–15689, 1996.

[51] J. D. Gale and A. L. Rohl. The general utility lattice program (GULP). *Molecular Simulation*, 29(5):291–341, 2003.

[52] M. Blanchard, K. Wright, and J. D. Gale. Atomistic simulation of Mg_2SiO_4 and Mg_2GeO_4 spinels: a new model. *Physics and Chemistry of Minerals*, 32(5-6):332–338, 2005.

[53] R. S. Liu, W. C. Shi, Y. C. Cheng, and C. Y. Huang. Crystal structures and peculiar magnetic properties of α- and γ-Al_2O_3 powders. *Modern Physics Letters B*, 11(26-27):1169–1174, 1997.

[54] M. F. Mott and M. J. Littleton. Conduction in polar crystals: I. electrolytic conduction in solid salts. *Transactions of the Faraday Society*, 34(1):485–499, 1938.

[55] W. C. Mackrodt and P. W. Tasker. Segregation isotherms at the surfaces of oxides. *Journal of the American Ceramic Society*, 72(9):1576–1583, 1989.

[56] R. C. McCune, W. T. Donlon, and R. C. Ku. Yttrium segregation and YAG precipitation at surfaces of yttrium-doped α-Al_2O_3. *Journal of the American Ceramic Society*, 69(8):C196–C199, 1986.

[57] S. Galmarini. Atomistic simulation study of yttrium and magnesium at α-alumina interfaces. Technical report, EPFL, 2006.

[58] G. Achutaramayya and W. D. Scott. Interfacial energies of coherent twin boundaries in alumina. *Acta Metallurgica*, 23(12):1469–1472, 1975.

[59] K. Kihara and G. Donnay. Anharmonic thermal vibrations in ZnO. *Canadian Mineralogist*, 23:647–654, 1985.

[60] Ch. Monachon. Simulating segregation of iso- and aliovalent dopants in zinc oxide. Technical report, EPFL, 2007.

[61] A. A. Sokol, S. A. French, S. T. Bromley, C. R. A. Catlow, H. J. J. van Dam, and P. Sherwood. Point defects in ZnO. *Faraday Discussions*, 134:267–282, 2007.

[62] L. Whitmore, A. A. Sokol, and C. R. A. Catlow. Surface structure of zinc oxide (1010), using an atomistic, semi-infinite treatment. *Surface Science*, 498(1-2):135–146, 2002.

[63] X. Gonze, J. M. Beuken, R. Caracas, F. Detraux, M. Fuchs, G. M. Rignanese, L. Sindic, M. Verstraete, G. Zerah, F. Jollet, M. Torrent, A. Roy, M. Mikami, P. Ghosez, J. Y. Raty, and D. C. Allan. First-principles computation of material properties: the ABINIT software project. *Computational Materials Science*, 25(3):478–492, 2002.

[64] X. Gonze, G. M. Rignanese, M. Verstraete, J. M. Beuken, Y. Pouillon, R. Caracas, F. Jollet, M. Torrent, G. Zerah, M. Mikami, P. Ghosez, M. Veithen, J. Y. Raty, V. Olevanov, F. Bruneval, L. Reining, R. Godby, G. Onida, D. R. Hamann, and D. C. Allan. A brief introduction to the ABINIT software package. *Zeitschrift für Kristallographie*, 220(5-6):558–562, 2005.

[65] W. Humphrey, A. Dalke, and K. Schulten. Vmd: Visual molecular dynamics. *Journal of Molecular Graphics*, 14(1):33–38, 1996.

[66] Y. Aman. Modelisation atomistique de la segregation des dopants lanthanides (La, Gd, Yb) dans α-Al_2O_3. Technical report, EPFL, 2007.

[67] W. C. Mackrodt, R. J. Davey, S. N. Black, and R. Docherty. The morphology of α-Al_2O_3 and α-Fe_2O_3 - the importance of surface relaxation. *Journal of Crystal Growth*, 80(2):441–446, 1987.

[68] P. Hartman. The effect of surface relaxation on crystal habit - cases of corundum (α-Al_2O_3) and hematite (α-Fe_2O_3). *Journal of Crystal Growth*, 96(3):667–672, 1989.

[69] A. Marmier and S. C. Parker. Ab initio morphology and surface thermodynamics of α-Al_2O_3. *Physical Review B*, 69(11):115409, 2004.

[70] M. Kitayama and A. M. Glaeser. The Wulff shape of alumina: III. undoped alumina. *Journal of the American Ceramic Society*, 85(3):611–622, 2002.

[71] J. H. Choi, D. Y. Kim, B. J. Hockey, S. M. Wiederhorn, C. A. Handwerker, J. E. Blendell, W. C. Carter, and A. R. Roosen. Equilibrium shape of internal cavities in sapphire. *Journal of the American Ceramic Society*, 80(1):62–68, 1997.

[72] A. G. Marinopoulos, S. Nufer, and C. Elsässer. Interfacial structures and energetics of basal twins in α-Al_2O_3: First-principles density-functional and empirical calculations. *Physical Review B*, 63(16):165112, 2001.

[73] S. Fabris, S. Nufer, C. Elsässer, and T. Gemming. Prismatic $\Sigma3$ $(10\bar{1}0)$ twin boundary in α-Al_2O_3 investigated by density functional theory and transmission electron microscopy. *Physical Review B*, 66(15):155415, 2002.

[74] P. Bowen, C. Carry, D. Luxembourg, and H. Hofmann. Colloidal processing and sintering of nanosized transition aluminas. *Powder Technology*, 157(1-3):100–107, 2005.

[75] Z. J. Shen, M. Johnsson, Z. Zhao, and M. Nygren. Spark plasma sintering of alumina. *Journal of the American Ceramic Society*, 85(8):1921–1927, 2002.

[76] F. Claeyssens, C. L. Freeman, N. L. Allan, Y. Sun, M. N. R. Ashfold, and J. H. Harding. Growth of ZnO thin films - experiment and theory. *Journal of Materials Chemistry*, 15(1):139–148, 2005.

[77] M. Nyberg, M. A. Nygren, L. G. M. Pettersson, D. H. Gay, and A. L. Rohl. Hydrogen dissociation on reconstructed ZnO surfaces. *Journal of Physical Chemistry*, 100(21):9054–9063, 1996.

[78] A. Hausmann and B. Schallenberger. Interstitial oxygen in zinc-oxide single-crystals. *Zeitschrift für Physik B-Condensed Matter*, 31(3):269–273, 1978.

Chapter 6

Nd:YAG laser ceramics

Ceramic lasers have advantages such as better optical homogeneity, cheaper production and more freedom in shape compared to their monocrystalline counterparts. However equal or better laser performances are required. Interface segregation is important as ceramics contain a high number of interfaces, segregation to which may locally alter the concentration of luminescent dopants, which in turn may influence laser performance. Atomistic simulation techniques in combination with larger mesoscale models were used to investigate the segregation of Nd dopants to surfaces and mirror twin grain boundaries in YAG and the effects on optical and laser performance of this new class of lasers. These results allow a better understanding of interfacial segregation and its influence on laser performance of Nd:YAG ceramics and should show laser physicists routes to explore in the optimization of Nd:YAG ceramic lasers.

6.1 Introduction

Neodymium doped yttrium aluminum garnet (Nd:YAG, Nd:$Y_3Al_5O_{12}$) has become since it's discovery by Geusic and coworkers [1] a well known high performance laser material. It is generally used in the form of single crystals grown by the Czochralski method. However as this method of growth is extremely slow and as it is difficult to homogeneously dope YAG with more than 1.4 at. % of Nd, recent advances towards the use of polycrystalline Nd:YAG ceramics have been made, notably by Ikesue [2, 3, 4] and coworkers. Significant contributions on synthesis and processing have also been made by Ueda [5, 6, 7] and coworkers and Lupei [8, 9] and coworkers. Besides a higher optical homogeneity, the major advantages of the ceramic route would be a lower cost and higher production rate as well as much more freedom in shape - even samarium cladded composite structures can be produced as shown by Ikesue [4] which lead to significant improvements in laser performance and quality due to absorption of the amplified spontaneous emissions (ASE), which present one of the major problems in lasers as will be discussed in the next paragraphs dealing with the functioning of lasers as well as the nomenclature used by this community.

A laser consists of a so called gain medium, which can be a solid, liquid or gas. The gain medium is surrounded by the optical cavity which can in its simplest form consist of two mirrors, one being partially transparent to let the laser beam escape. This setup is shown schematically in figure 6.1. For a laser to work the gain medium is pumped with energy in form of light or electricity, which will promote electrons to higher energy levels [10]. The critical step in achieving lasing is the production of a so called population inversion, which means that more electrons are found in high energy states than in low energy states contrary to the partitioning predicted by the Boltzmann distribution. This is achieved by a sufficiently high pumping input power above the so called lasing threshold. Compared to the normal distribution of electrons on energy states this situation inverses the population, hence the name. An electron in a high energy state may loose its energy in either of two ways. The first being spontaneous emission, where light is emitted according to Bohr's frequency relation $E_2 - E_1 = h\nu_{21}$. In this case a photon will be emitted in any direction and at any phase. The other mode is by stimulated emission. Here the excited electron interacts with a photon and the resulting photon is emitted in the same direction and with the same phase as the incident photon. This will give a very monochromatic light, the out of phase contributions coming from spontaneous emissions. The optical cavity has the role of letting photons travel trough the gain medium many times, thus creating more stimulated emissions and further amplifying the beam. Spontaneous

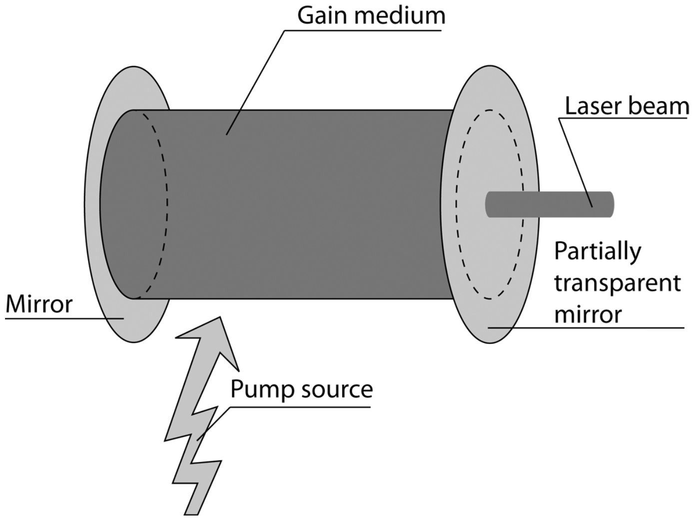

Figure 6.1: Schematic view of a laser cavity.

emissions may also get amplified which creates the problem of amplified spontaneous emissions (ASE) mentioned above. The laser medium is continuously pumped in order to maintain the population inversion and have enough electrons in high energy states. Lasers can be operated either in continuous wave, where the output power is constant over time or pulsed, where techniques such as Q-switching or mode locking [10] are used to modulate the beam.

In solid state lasers the electrons are usually promoted from their ground state into a series of high energy states located in the so called absorption or pump band, which is a wide collection of high energy states. From there they will by fast radiationless transition return to a sharp lower level followed by relaxation via stimulated emission either towards the ground state (three level systems) or towards an energy level slightly above the ground state (four level systems) as shown in figure 6.2.

The gain medium or host material for solid state lasers has to be mechanically resistant, a good thermal conductor and ideally optically isotropic. These requirements have made YAG a predominant material for this class of lasers. For laser operation a relatively narrow electron band distribution is required, which is normally not present in the host crystals and is achieved by insertion of luminescent dopants. The electronic structure of rare earth ions has the particularity of having a complete rare gas shell as the outermost shell (xenon shell with two $5s$ electrons and six $5p$ electrons), which means that the internal electron levels are only weakly affected by the surrounding crystal. A certain number the so called $4f$ levels inside this xenon shell are unoccupied and electrons from lower $4f$ levels can be excited to these empty levels, resulting in the required sharp laser transitions.

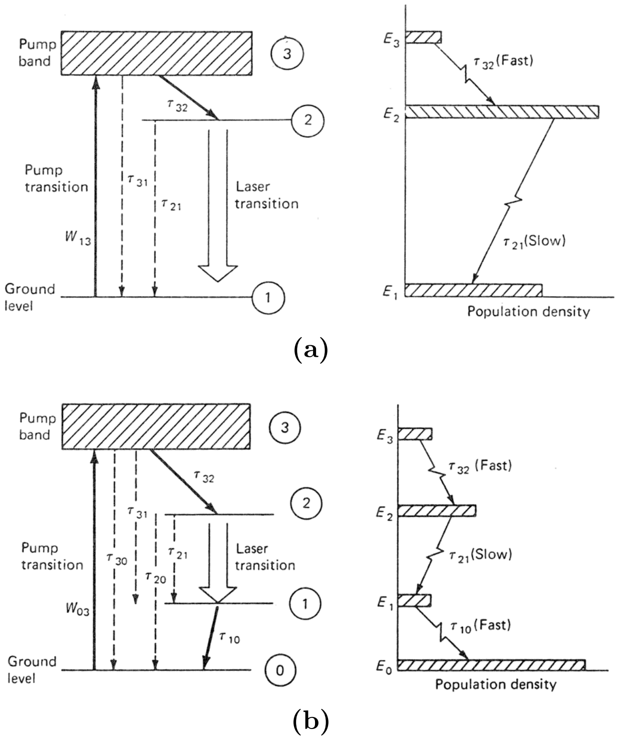

Figure 6.2: Schematic view of the different laser systems: (a) Three level laser and (b) four level laser. Extracted from [10]

Neodymium, being one of the rare earth ions, has 3 electrons in the $4f$ shell, which are in energy levels designated as $^4I_{9/2}$, $^4I_{11/2}$, $^4I_{13/2}$ and $^4I_{15/2}$, where the subscript is the total angular momentum. The electrons are promoted from the ground state ($^4I_{9/2}$) into the high energy pump band from which they relax to the excited $^4F_{3/2}$ state. The laser transition then takes place to the $^4I_{11/2}$ level with emission at a wavelength of 1.0641μm as shown on the left side of figure 6.3. As mentioned above the xenon shell leaves the electron structure of the Nd^{3+} ion almost unchanged when in a YAG crystal. The crystal field will however still result in small changes, which can be seen as a splitting of the electron levels into sublevels as shown on the right side of figure 6.3. The laser transition in Nd:YAG originates from the R$_2$ sublevel of the $^4F_{3/2}$ level. Normally at room temperature 60% of the electrons are found in the lower energy R$_1$ sublevel according to the Boltzmann distribution. As lasing takes place the electrons in the R$_2$ sublevel are replenished by thermal transition from the lower R1 sublevel.

L'huillier et al. [11] have shown that it is possible to grow monocrystalline Nd:YAG containing 2 at. % of neodymium and even higher concentrations of 2.5 at. % have been reported by the use of special growth techniques such as thermal-gradient growth [9]. Ceramic materials on the other hand can be doped with up to

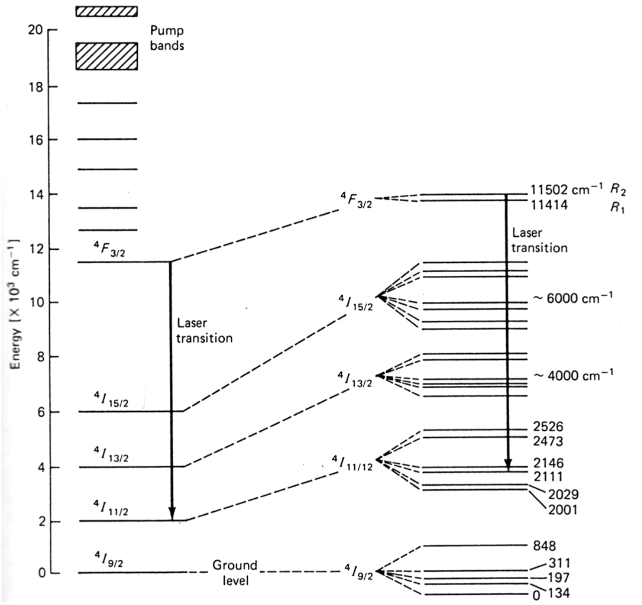

Figure 6.3: Energy bands of the Nd ion showing the pump band, the excited states $(^4F_{3/2} \rightarrow^4 I_{11/2})$ between which the laser transition takes place as well as the ground level $(^4I_{9/2})$. The left side of the figure shows the energy levels of the isolated ion whereas the right side shows the effect of the crystal field, which results in splitting of the energy levels in sublevels with slightly different energy. Figure extracted from [10].

8 at. % of Nd (Konoshima Chemicals Co. Ltd., Osaka, Japan), however the exact location of these dopants is not fully known as the resolution of measurement by fluorescence life-time as reported by L'huillier [12] is limited to 50μm. Segregation from the bulk towards the interfaces is likely to occur due to the difference in ionic size between Nd (0.995 Å) and Y (0.900 Å), the Nd being substituted on Y sites in the YAG structure.

An important phenomenon occurring in Nd:YAG lasers is concentration quenching, which means that with increasing Nd concentration the spacing between neodymium ions decreases and interaction between dopant ions, the so called cross-relaxation, reduces the emission life-time of the luminescent neodymium ions. This effect decreases the laser power and has been measured by Deb et al. [13] Merkle et al. [14] and Dong et al. [15] and modeled by Huang [16]. As there may be local variations in concentration due to segregation in polycrystalline ceramic lasers, localized concentration quenching may occur.

The laser performance of single crystals and ceramics has been compared by Lupei et al. [8] and it has been found that ceramic lasers can under carefully chosen pumping conditions yield the same performances as single crystals. Further advances in the field of polycrystalline Nd:YAG lasers may be achieved by knowledge-based microstructure control, the target values of grain size and dopant concentration with predicted degree of segregation may be provided by simulations.

Atomic scale simulations of garnet type crystals [17, 18, 19, 20, 21, 22] and more specifically YAG [23, 24, 25, 26, 27, 28, 29] are still very few, which may be due to the rather large unit-cell of the material (192 atoms for the full cubic cell and 96 for the primitive cell), making it a rather expensive material to study in terms of computer resources required. The studies so far have solely looked at the bulk lattice [17, 22, 26], defects therein [23] as well as melting [29] and electron excitations of the crystal ions [28] as well as selected dopants such as Cr [27] using a variety of empirical or first-principle methods. YAG interfaces and segregation have to our knowledge not been attempted in calculations so far.

The present chapter will look at segregation of neodymium dopant ions towards surfaces and grain boundaries in YAG. Based on this atomistic simulation information meso-scale models will be constructed in order to predict laser performances in presence of segregated dopants. This information is extremely important for the optimization of this novel class of lasers as the role of interfaces on optical and transport properties is still largely unknown. Preliminary electron structure calculations have been undertaken however the results are not presented here.

6.2 Atomistic calculations

6.2.1 Approach

The computer code METADISE [30] was used for the structure generation and subsequent energy minimization of all YAG surfaces and grain boundaries. The basic data for the simulation is the crystallographic unit cell of YAG, which was taken from the Rietveld refined neutron diffraction data recorded at 10 K published by Rodic et al. [31] and an interatomic potential set published by Lewis and Catlow [32], previously applied with success to a large range of garnets [17]. This potential describes the interatomic forces between a pair of ions by a combination of long-range coulombic forces (section 2.1.1) as well as a Buckingham potential (section 2.1.2) for the short-range interaction. In order to model the polarizability of the oxygen ion, the core-shell model (section 2.1.4) has been used.

A comparison of experimental bulk properties [31, 33, 34, 35] with those predicted by the potential model is given in table 6.1. As it can be seen the structural parameters of the lattice are very well reproduced, whereas the mechanical and di-

Table 6.1: Comparison of experimental bulk properties of YAG with those calculated. The lattice constants are the ones determined by Rodic et al. [31] at 10K, the elastic constants have been measured at 300K by Stoddart et al. [33], the dielectric constant is the one reported by Tomiki et al. [34] for room temperature and the refractive index was measured by Bond [35] at room temperature for a wavelength of 1μm.

Property	**Lattice constant** [Å]	**Elastic constants** $\mathbf{C_{11}}$ [GPa]	$\mathbf{C_{12}}$ [GPa]	$\mathbf{C_{44}}$ [GPa]	**Dielectric constant** [-]	**Refractive index** [-]
Experiment	11.9927	339	114	116	3.28	1.82
Simulation	11.9287	399.25	128.69	126.13	2.55	1.60

electric properties show higher deviations. This means that the current potentials are well suited to investigate atomic structures. However dielectric properties calculated based on the current potentials should be interpreted with care, the potentials should be refined or first principle methods applied for optical property calculations. A very important property of the employed potential set is that it describes undercoordinated environments reasonably well, without leading to unphysical relaxations [36]. Many authors [37, 38, 39, 40, 41] have applied it to bulk, surfaces and interfaces of different materials and found it to qualitatively reproduce the structures as well as quantitative properties such as interfacial energies, illustrating its suitability for the study of surfaces and grain boundaries.

Experimental data published by Cherepanova et al. [42] and Roberts and Elwell [43] suggests the (110) and (112) surfaces are dominant in the morphology of YAG crystals. In addition the (100) and (111) surfaces were studied, as low index surfaces are likely to have low interfacial energies as mentioned in the introduction (section 1.2.1). Surfaces can be cleaved at different depths perpendicular to a direction defining the surface normal. Depending on the position of this cleaving plane, different atoms will be exposed at the surface. Some of these so called surface terminations or cuts will present a dipole moment perpendicular to the surface, which makes them physically unstable as discussed in the previous chapter (section 5.3.4). For the four aforementioned surface planes all surface terminations without a dipole moment were constructed resulting in 5, 6, 7 and 3 possible terminations for the 4 directions respectively. In the following the terminations will be designated by consecutive numbers "(111) cut 4" meaning for example to the 4th cut perpendicular to the [111] surface normal direction. All interfaces were described using the two-region model as introduced in section 2.3.5.

Grain boundary structures were constructed as described in the previous chapter for alumina grain boundaries (section 5.2.1). It should be noted that this method of grain boundary construction introduces certain simplifications. Firstly only mirror images of the exact same surface are joined to form a grain boundary, whereas two different surfaces or even terminations with a dipole could result in a lower energy. Secondly grain boundary faceting is not explicitly taken into account in this method of construction. During relaxation of the structures the position and shape of boundary plane may freely change, however the energy barriers associated with an important structural change such as grain boundary faceting are most likely too high to be overcome. Despite these points, the choice is considered reasonable with respect to the grain boundary types looked at as otherwise the computational effort and the complexity of the problem would be overwhelming.

The interfacial energies for surfaces and grain boundaries were calculated as defined in the the methods chapter (equation 2.35). Dopants incorporation energies have been calculated using the probability based approach described for lanthanide dopants in alumina (section 5.2.1) since the YAG unit-cell and thus also it's surfaces present a lot of dopant incorporation sites. The enthalpy of segregation $\Delta \mathrm{H}_{\mathrm{seg}}$, enthalpy of dissolution $\Delta \mathrm{H}_{\mathrm{sol}}$ of YAG in contact with $\mathrm{Nd_2O_3}$ particles (equation 6.1) and the change in interfacial energy associated with this dissolution have been evaluated for the lowest energy configuration for each dopant concentration. The dissolution approach is most realistic here since doping is usually carried using a solid state mixing route [2] however the direct precipitation route is used as well [7].

$$\mathrm{undoped} + n \cdot \mathrm{NdO_{1.5}} \Longrightarrow \mathrm{doped} + n \cdot \mathrm{YO_{1.5}} \tag{6.1}$$

The required bulk dopants incorporation energies were calculated using the Mott-Littleton approach [44] (section 2.3.6) implemented in the GULP [45] code.

6.2.2 Results & Discussion

Interfacial Energies

We have calculated the undoped as well as the Nd doped structure for surfaces and mirror twin grain boundaries in YAG. The respective interfacial energies are given in table 6.2. First off all these results show that the (100) surface is the most stable followed by the (111), (110) and (112) surfaces, the latter two having similar surface energies. The equilibrium morphology of such a crystal as determined by a Wulff construction is given in figure 6.4a. This sequence of stable surfaces is retained for the doped case, the resulting equilibrium shape is given in figure 6.4b. The surfaces

Table 6.2: Surface and grain boundary energies for the undoped and the doped case. For the doped case the equilibrium concentration (as reported in table 6.3) at minimum interfacial energy has been considered.

		Surface energy [Jm^{-2}]		**Grain boundary energy** [Jm^{-2}]	
Surface	**Cut**	**Undoped**	**Doped**	**Undoped**	**Doped**
(100)	1	2.32	2.24	2.09	1.97
	2	1.81	1.77	1.93	1.73
	3	2.31	2.26	3.26	2.81
	4	2.40	1.94	2.95	2.52
	5	1.91	1.86	2.84	2.82
	Mean	2.15	2.01	2.61	2.37
(110)	1	2.43	2.23	1.41	1.31
	2	2.36	2.33	1.79	1.61
	3	2.75	2.25	0.82	0.82
	4	2.61	2.49	2.52	2.52
	5	2.67	2.47	2.31	2.31
	6	3.05	2.28	1.23	1.10
	Mean	2.65	2.34	1.68	1.61
(111)	1	2.33	2.33	1.90	1.78
	2	2.25	2.11	1.78	1.73
	3	2.92	2.59	2.38	2.28
	4	2.48	2.21	3.49	3.43
	5	2.39	2.18	3.08	2.94
	6	2.76	2.68	3.36	3.32
	7	2.95	2.83	3.13	2.93
	Mean	2.58	2.42	2.73	2.63
(112)	1	2.36	2.22	1.65	1.65
	2	2.61	2.52	2.70	2.54
	3	2.50	2.36	2.86	2.80
	Mean	2.49	2.37	2.40	2.33

areas change only slightly as a result of doping (100): 66.8 % to 61.2 %, (110): 5.0 % to 6.8 %, (111): 28.2 % to 32.0 %. It has to be noted that for the (110) surface a different cut becomes the lowest energy surface termination when doped, which would mean a shift of the surface plane. Another finding is that all surfaces can lower their surface energies by incorporating dopants.

For the undoped grain boundaries, the (110) mirror twin boundary has by far the lowest interfacial energy, followed by the (112), (111) and (100) mirror twins. When doped, the same cuts stay stable, the sequence of interfacial energy also being conserved. However the (100) mirror twin approaches the interfacial energy of the (111) mirror twin. It can be seen that of the most stable grain boundaries only the

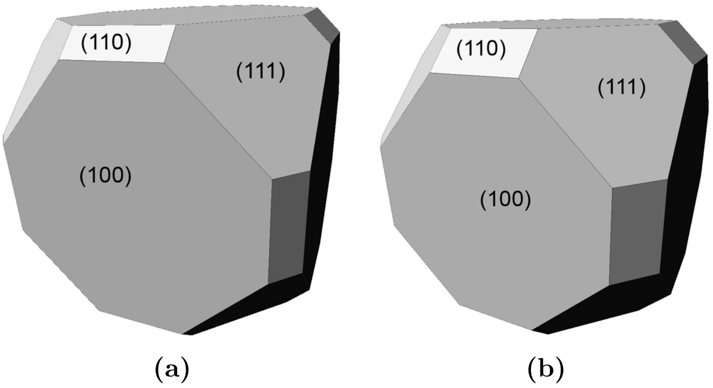

(a) (b)

Figure 6.4: Morphologies calculated from (a) the undoped surface energies and (b) the doped surface energies

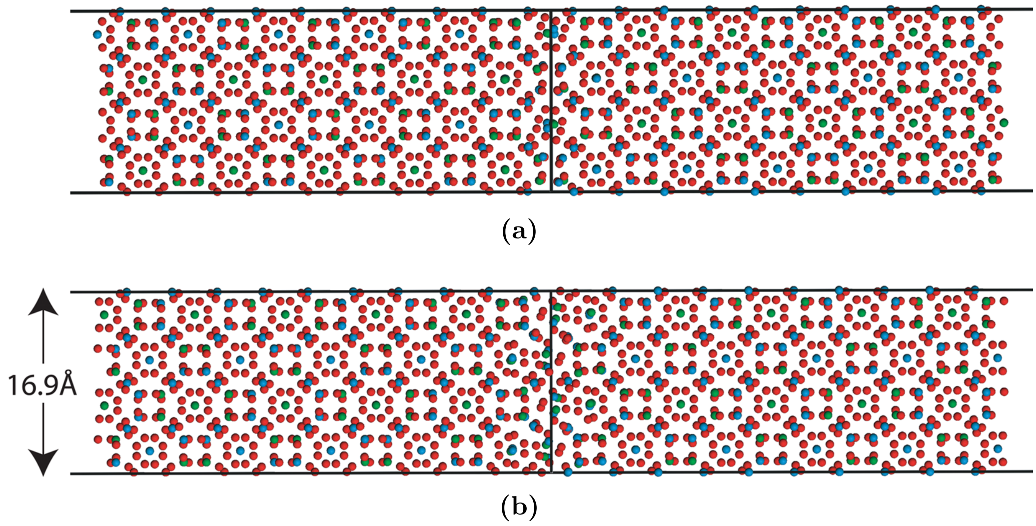

(a)

(b)

Figure 6.5: (110) mirror twin grain boundary structures viewed along the [010] direction: (a) the most stable boundary (Cut 3) and (b) the least stable boundary (Cut 4). Neither accepts any dopants at the interface. Color code: Red = Oxygen, Blue = Aluminum, Green = Yttrium.

(100) and (111) mirror twins reduce their interfacial energy by taking up dopants. Grain boundary structures for the most and least stable (110) mirror twins, neither of which accepts dopants, are shown in figure 6.5. Figure 6.6 shows the structures of the most and least stable (112) mirror twins, where only the least stable accept dopants.

Enthalpies of Segregation

The coverage dependent values for the enthalpy of segregation are reported in figure 6.7 for the four investigated surfaces and their mirror twin boundaries, for clarity of presentation only the most and least stable cut of each face is shown, the rest

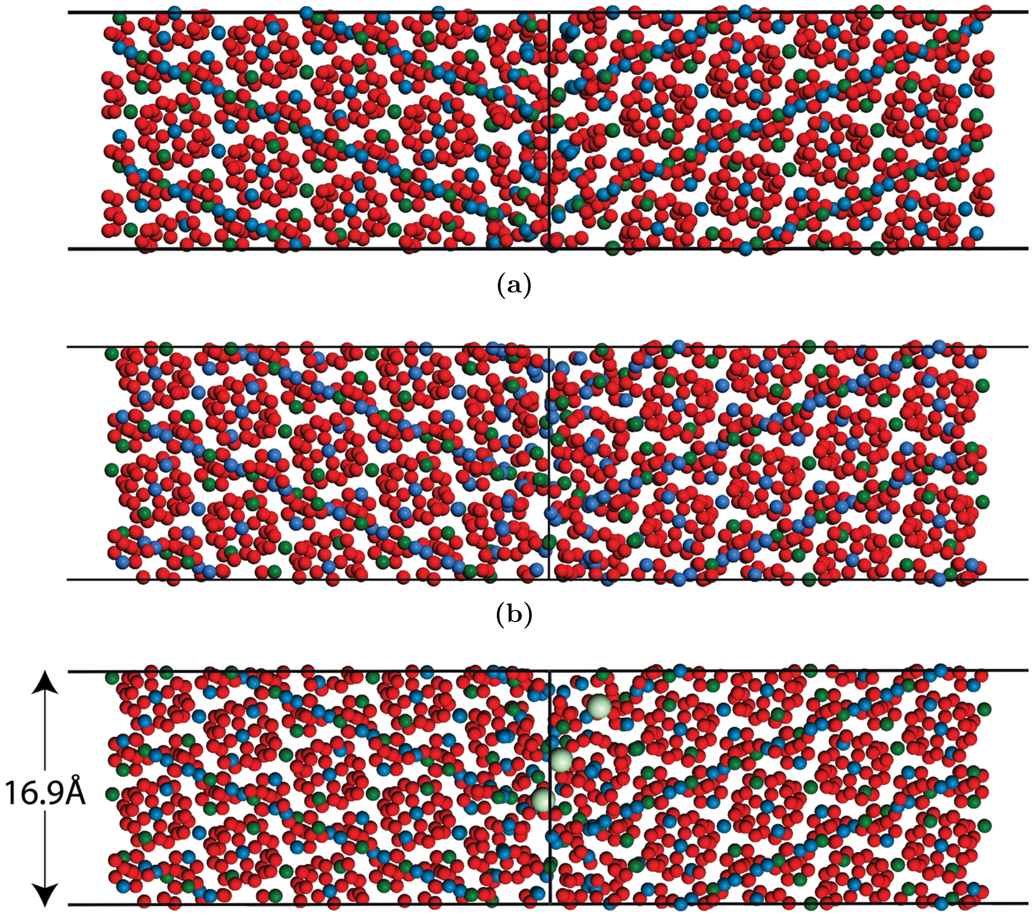

(a)

(b)

(c)

Figure 6.6: (112) mirror twin grain boundary structures viewed along the [0-21] direction: (a) the most stable boundary (Cut 1) and the least stable boundary (Cut 3) (b) undoped and (c) doped at its equilibrium concentration respectively. Only the least stable boundary accepts dopants. The dopants are shown oversized. Color code: Red = Oxygen, Blue = Aluminum, Dark Green = Yttrium, Light Green = Neodymium.

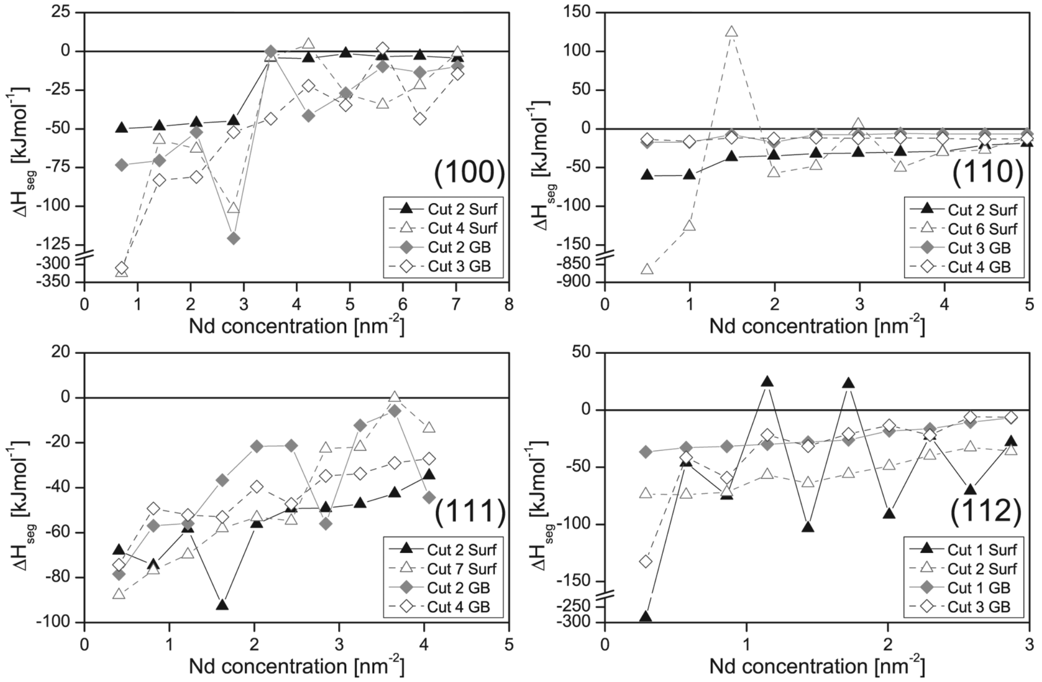

Figure 6.7: Coverage dependent enthalpy of segregation of the four surfaces (different scales are used on different graphs). For clarity only the most and least stable cut of each surface and grain boundary is shown, the rest being in between these two extremes. Surfaces have triangular markers whereas grain boundaries have rhombic ones. Stable cuts are drawn in solid, whereas unstable ones are dashed.

being situated in between these two extremes. For the higher index surfaces, the concentrations investigated are lower, due to the higher surface area, however even for the case of the (112) surface, the highest concentrations will never be attained in experiment, as will be illustrated later during the discussion of the equilibrium interfacial energy. It can be seen that some surfaces and grain boundaries have extremely high enthalpies of segregation for the first dopant ion, however for the second dopant ion the enthalpies of segregation lie in the same range as for the other terminations. The incorporation of the first dopant is thus extremely favorable at these interfaces. Another important result seen in figure 6.7 is the oscillatory nature of some of the curves. This indicates that the incorporation of a single dopant is less favorable than the incorporation of a pair, suggesting the formation of patterns or clusters at the interfaces. For some cases, the value of the curve becomes positive, before falling back into the negative range. This means that a certain configuration is highly unfavorable, supporting the idea of formation of patterns. This behavior indicates some sort of interaction between the dopant ions.

Enthalpies of Solution and Interfacial Concentration

In figure 6.8 the enthalpy of solution per dopant ion as a function of the interfacial concentration is shown, the resulting interfacial energies are shown in figure 6.9. For clarity, again only the most and least stable cuts are shown, the rest being in between these two extreme cases. For the [100] direction, the least stable surface and grain boundary have a high affinity for the dopants as can be seen from the very exothermic enthalpy of solution at low coverages. This results in an important lowering of the surface energies as can be seen from the initial decrease of the curves. This effect is a lot less important for the most stable (100) surfaces and grain boundaries. However it does occur to some extent for all cuts resulting in a minimum of interfacial energy around 3 to 4 dopant ions per nm^2. For the [110] direction, where the very exothermic solution behavior is observed only for the least stable surface, however very marked, resulting in a stabilization which brings the surface energy to a level comparable to the most stable termination for coverages of 1 Nd/nm^2. It can be seen that the (110) grain boundaries are very stable in the undoped state, the incorporation of dopants increases the surface energy in every case, meaning that these grain boundaries should not accept any dopant ions. As seen for the enthalpy of segregation, the (111) surfaces and grain boundaries exhibit a very different behavior from the others. The surfaces and grain boundaries perpendicular to the [111] direction do not show an extreme exothermic enthalpy of solution for low coverages as all the others do. The most stable surface along this direction shows a very high capacity for dopant accommodation going up to 4 Nd/nm^2.

The (112) surface breaks with the systematic behavior of the highest energy surfaces or grain boundaries exhibiting the extremely exothermic enthalpy of solution. For the [112] direction it is the most stable surface and the least stable grain boundary which show this behavior. No definitive explanation for the segregation behavior of this surface could be found from the atomic structure. Eventually the size of the surface cell could have an influence as increasing the size reduces dopant-dopant interactions which will be present even for low coverages for the smaller surface cells. The most stable (112) grain boundary does, like the (110) boundary, not accept any dopants at all. This illustrates that extremely low energy boundaries, which have a very regular atomic structure do not easily accommodate dopants which would lead to a disruption of this regularity and thus an increase in energy. Despite these irregularities it can be stated that generally low energy interfaces show limited or even no trend towards segregation as already seen for alumina in the previous chapter. Since the enthalpy of dissolution does not take into account the energy of the bulk/interface system, but the one associated with the exchange between the pure

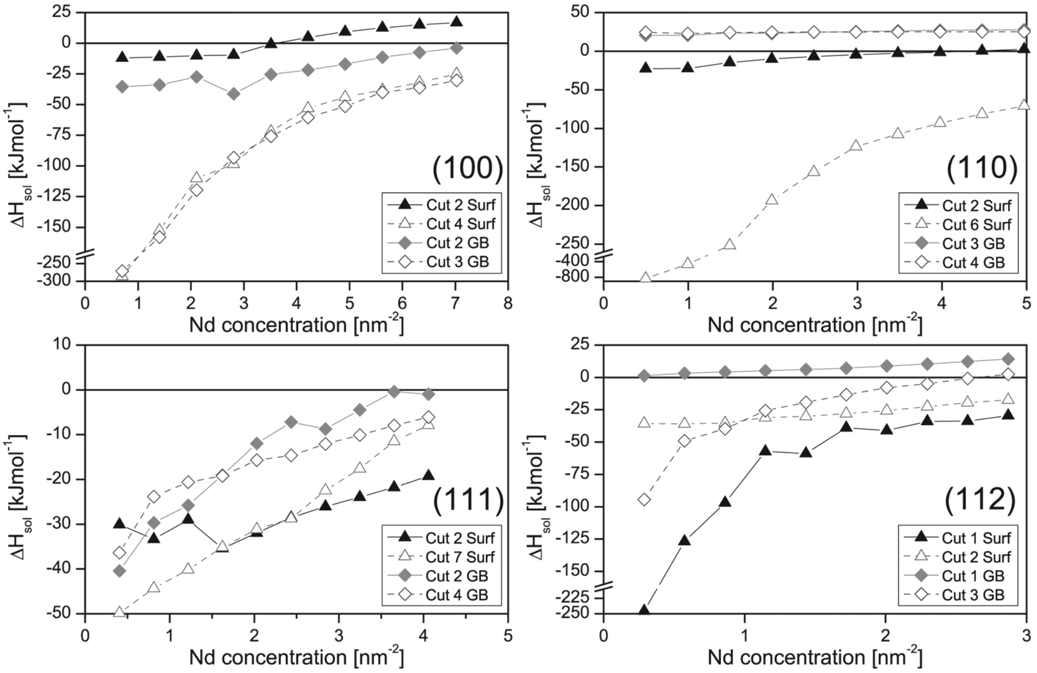

Figure 6.8: The coverage dependent enthalpy of solution per dopant ion (different scales are used on different graphs). Only the most stable and unstable cut of each surface and grain boundary are shown, the rest being in between these two extremes. Surfaces have triangular markers whereas grain boundaries have rhombic ones. Stable cuts are drawn in solid, whereas unstable ones are dashed.

dopant oxide and the interface it is reasonable to assume that segregation is governed by the minimization of the interfacial energy, which will also minimize the one of the bulk/interface system. When the dopant concentration in the system is sufficient to provide dopant ions to all interfaces, it would be expected that the surfaces and grain boundaries show a dopant concentration equal to that of the minimum on the interfacial energy curve. At lower dopant concentration in the system, the interfacial concentration will be lower and the minimization of the system's energy incomplete. It can be seen that in every case this equilibrium concentration is well below the maximum concentration calculated, showing that even for the large surfaces the calculated range of the dopant concentration is sufficient. For these equilibrium dopant concentrations the atomic structure has been analyzed and characteristics of the enriched zone extracted which can be found in table 6.3. It can be seen that the enriched depth varies from 0Å to 5Å depending on the surface and cut. All surfaces are covered to a certain degree, the fraction of yttrium sites occupied by the dopant ranging from 0.15 to a complete coverage of 1.0 in the enriched zone. There are some grain boundaries that do not accept any dopant ions and thus have coverage of 0.0 others accept again full coverage in the enriched zone. Attempts at correlating the density of the enriched zone and the interfacial energy with the dopant accommo-

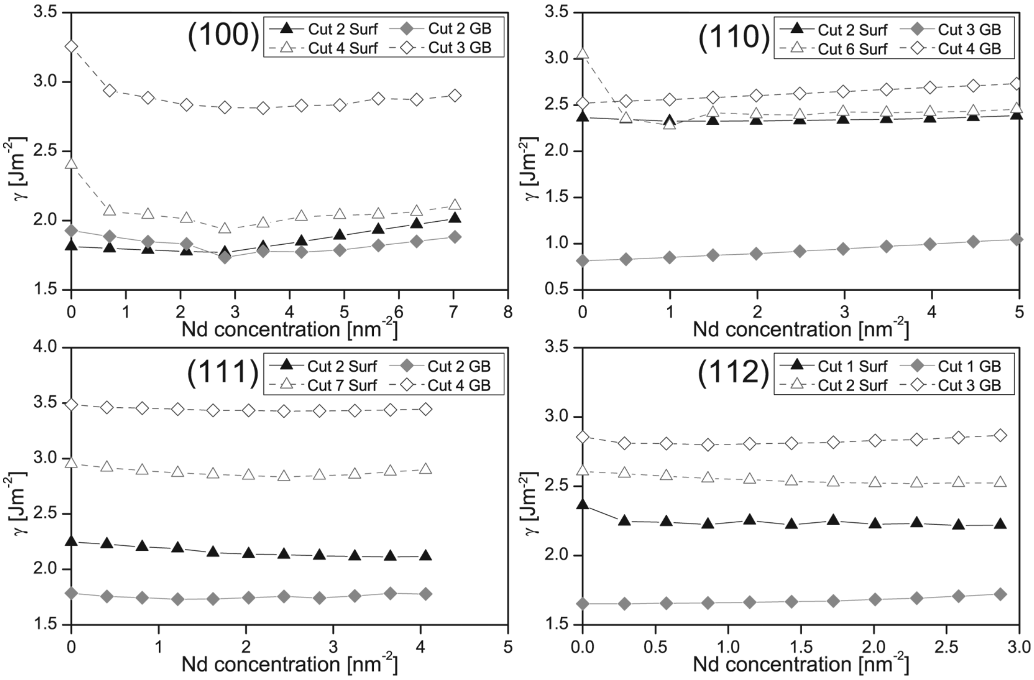

Figure 6.9: The coverage dependent interfacial energy (different scales are used on different graphs). Only the most stable and unstable cut of each surface and grain boundary are shown, the rest being in between these two extremes. Surfaces have triangular markers whereas grain boundaries have rhombic ones. Stable cuts are drawn in solid, whereas unstable ones are dashed.

dation capacity have not shown any clear trends as the scattering of values is too large. It can however be stated that it does not solely depend on these two factors but also on the bonding environment, which plays a critical role in determining the equilibrium concentration of Nd in YAG grain boundaries.

Estimated Influence on Lasing Properties

The quenching effect due to segregation can be estimated by the following method. Dong et al. [15] have found a reduction of 49% in laser performance at 3 at.% Nd in single crystals due to concentration quenching. Considering a homogeneous dopant distribution in a perfect crystal the nearest neighbor spacing at 3 at.% Nd can be calculated to be 1.3nm as shown on the graph in figure 6.10. In the simulated surfaces the nearest neighbor spacing lies between 0.2 and 0.75nm and between 0.39 and 0.73nm for the grain boundaries, which corresponds to a local doping level of 18 at.% Nd and above. These values suggest a quenching significantly higher than the 49% reported by Dong for 3% Nd in single crystals. Therefore the assumption can be made that much of the dopant ions segregated at interfaces will not contribute to the lasing effect.

Table 6.3: Characteristics of the enriched zone for all surfaces and grain boundaries at their lowest interfacial energy (equilibrium dopant concentration). As the grain boundary segregation profiles are not symmetric, the depth in each of the two half crystals is given separated by slashes.

		Surface			**Grain boundary**		
Surface	**Cut**	**[Nd]** [nm^{-2}]	**Depth** [nm]	**Coverage** [-]	**[Nd]** [nm^{-2}]	**Depth** [nm]	**Coverage** [-]
(100)	1	2.11	0.30	0.375	4.93	0.39/0.12	0.500
1.42nm^2	2	2.82	0.13	1.000	2.82	0.23/0.28	0.400
	3	3.52	0.22	0.833	3.52	0.57/0.36	0.250
	4	2.82	0.43	0.571	5.63	0.52/0.41	0.467
	5	2.11	0.14	0.600	1.41	0.14/0.00	1.000
(110)	1	2.49	0.22	0.417	1.99	0.26/0.20	0.200
2.01nm^2	2	1.00	0.12	0.333	2.99	0.18/0.14	0.375
	3	2.49	0.31	0.500	0.00	0.00/0.00	0.000
	4	1.00	0.11	0.600	0.00	0.00/0.00	0.000
	5	1.99	0.12	1.000	0.50	0.00/0.13	0.250
	6	1.00	0.26	0.167	0.50	0.00/0.19	0.125
(111)	1	1.22	0.01	0.500	4.07	0.32/0.21	0.417
2.46nm^2	2	3.66	0.49	0.474	1.22	0.16/0.14	0.188
	3	2.03	0.41	0.278	2.44	0.30/0.11	0.350
	4	2.85	0.41	0.389	2.44	0.30/0.23	0.273
	5	1.22	0.51	0.150	4.07	0.36/0.33	0.370
	6	2.03	0.14	0.500	2.03	0.21/0.14	0.278
	7	2.44	0.15	0.545	3.66	0.22/0.17	0.409
(112)	1	2.58	3.28	0.409	0.00	0.00/0.00	0.000
3.49nm^2	2	2.29	0.20	0.500	0.86	0.25/0.24	0.094
	3	2.87	0.45	0.400	0.86	0.04/0.28	0.167

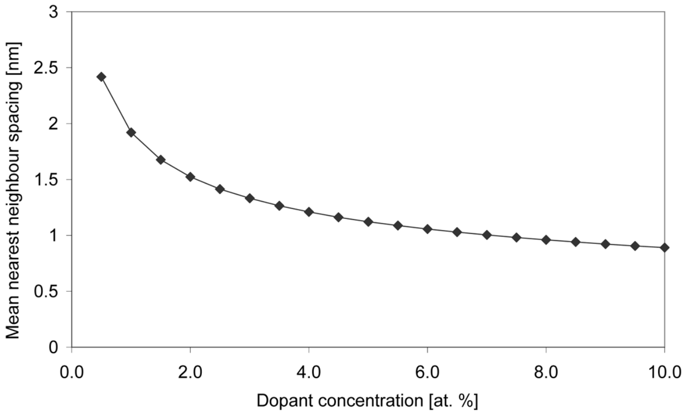

Figure 6.10: Nearest neighbor spacing in Nd doped YAG as a function of dopant concentration, assuming a homogeneous dopant distribution.

With the data presented here only the estimations of segregation to isolated grain boundaries is possible. The interfacial energy and concentration data will however enable the construction of microstructural models, allowing the investigation of segregation in microstructures containing a population of interfaces and as a function of grain size. One problem which needs to be addressed is to estimate how representative special grain boundaries are for the ones found in real ceramic microstructures. Mirror twin boundaries are an easy to study model system in experimental bicrystal studies as well as simulations, approaching general grain boundaries as the interfacial area of the periodic cell and thus their Σ value increases. However even the larger (111) and (112) grain boundaries investigated here can probably not be considered as close to general. The relatively high number of calculated grain boundaries showing a large dispersion in interfacial energies should result in a certain degree generality when they all appear in the interface population of the microstructural model.

Another aspect which will need to be investigated is the effect of codoping with silicon, which is very often used as a sintering agent during experimental production of YAG ceramics. The tetravalent silicon ion will introduce charge compensating defects in the structure, which if silicon is also preferentially found at interfaces could considerably influence the incorporation of Nd dopant ions at the interfaces.

6.2.3 Conclusions of atomistic calculations

The (100) surface was found to have the lowest surface energy, followed by the (111), (110) and (112) surfaces for both doped and undoped cases. For the grain boundaries the sequence of increasing interfacial energy is different with the (110) mirror twin having an extremely low interfacial energy followed by the (112), (111) and (100) mirror twin boundaries. It is shown that generally interfaces with a high interfacial energy show a higher trend for segregation. However the (112) mirror twin boundary does not completely comply with this rule. Also an open and less dense atomic structure does not seem to be the only factor governing dopant incorporation at the surfaces. The bonding environment and thus the atomic structure are likely to play a crucial role as well, which needs further investigation using ab-initio methods. It is shown that interfacial doping concentrations due to segregation are high enough to result in considerable local concentration quenching. Due to this fact, not all the segregated dopants are expected to contribute to the lasing effect.

The data developed will enable the construction of microstructural models allowing the study of segregation within a microstructure of variable grain size, which will be addressed in the next section.

6.3 Meso-scale optical and performance modeling

In order to evaluate segregation effect in a microstructure as well as the optical behavior of such a granular medium with segregated dopants, two models have been used. The two models will be presented separately followed by a conclusion on the results obtained by them.

6.3.1 Segregation in microstructures

In the atomistic simulations only flat and infinite interfaces have been modeled. The results obtained so far in their current form allow the prediction of the results as they could be observed in single crystal surface studies or diffusion-bonded bicrystal experiments. However in order to predict segregation in a real powder or polycrystalline ceramic it would be desirable to extrapolate the results found atomistically to the ensemble of surfaces of a powder particle or the grain boundaries found in a microstructure. The method developed here starts from the classical Wulff construction [46] for particles and extends the ideas to interfaces in microstructures.

Method

The Wulff construction (section 1.2.1) allows us to predict the relative fraction each crystallographic surface will occupy of the total powder surface at equilibrium. This can directly be applied to the calculated undoped and doped surfaces, as their surface energies are known. Since the Wulff construction considers the equilibrium case, only the lowest energy terminations along each direction will be used. The GEM module in the METADISE code [30] was used to calculate the proportion of each surface, which is independent of the particle size.

In order to calculate the surface area and the volume of a particle of given size, an approach based on polyhedra would be desirable due to the simple analytical determination of surface and volume. The polyhedron-approximation will not have the exact same shape as a particle predicted by the Wulff construction but a regular polyhedron should present a good approximation for reasonably equiaxed grains. In this work the rhombic dodecahedron [47] shown in figure 6.11 is used, the equations for the volume and the surface area of which are given by equations 6.2 and 6.3 respectively. This polyhedron has the advantage of being space filling, which will be

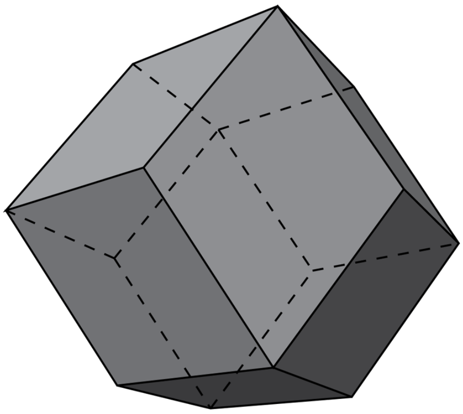

Figure 6.11: Sketch of a rhombic dodecahedron

important later when the method is extended to ceramic microstructures.

$$V = \frac{16}{9}\sqrt{3}a^3 \tag{6.2}$$

$$A = 8\sqrt{2}a^2 \tag{6.3}$$

Here a is the edge length of one of the rhomboeders making up the polyeder. The grain size can be defined based on the circumradius of the rhombic dodecahedron, which is $2a$.

If one now considers that the surfaces of the particles get enriched by segregation according to the atomistically calculated data above (table 6.3) the fraction of dopants found at the surface can be calculated as a function of the particle size. First the number of dopant ions N_{Nd} in the particle is calculated based on the total number of yttrium host ions in the particle N_{Y} (evaluated via the volume of the particle V and the number of yttrium ions $N_{\mathrm{Y,\ UC}}$ in the unit-cell volume V_{UC}) and the nominal ratio of Nd to yttrium ions $x_{\mathrm{b,\ nominal}}$ as given by equation 6.5.

$$N_{\mathrm{Y}} = V\frac{N_{\mathrm{Y,\ UC}}}{V_{\mathrm{UC}}} \tag{6.4}$$

$$N_{\mathrm{Nd}} = x_{\mathrm{b,\ nominal}} \cdot N_{\mathrm{Y}} \tag{6.5}$$

The number of dopant ions at the surface is obtained from the relative surface area A_i of each surface and it's corresponding surface concentration $[\mathrm{Nd}]_i$ as given by equation 6.6, where A_{total} is the sum over all surface areas ($\sum_i A_i$).

$$N_{\mathrm{Nd,surf}} = \sum_i \frac{A_i}{A_{\mathrm{total}}}[\mathrm{Nd}]_i \tag{6.6}$$

The fraction of dopants at the surface is then obtained as the ratio of $N_{\mathrm{Nd,\ surf}}$ to

Table 6.4: Summary of the YAG powder and microstructure models for equilibrium and non equilibrium.

Model	Interface set	Proportion
Powder equilibrium	Lowest energy surface termination for each crystallographic direction.	Wulff shape
Powder non-equilibrium	All surface terminations.	$\frac{\gamma_i^{-1}}{\sum_j \gamma_j^{-1}}$
Ceramic equilibrium	Lowest energy grain boundary plane for each direction.	
Ceramic non-equilibrium	All grain boundary planes.	

N_{Nd} (equation 6.7) and the remaining bulk dopant concentration can be calculated as given by equation 6.8. Another interesting property is the bulk depletion as defined by equation 6.9.

$$x_{\mathrm{segregated}} = \frac{N_{\mathrm{Nd,surf}}}{N_{\mathrm{Nd}}} \tag{6.7}$$

$$x_{\mathrm{b}} = \frac{N_{\mathrm{Nd}} - N_{\mathrm{Nd,surf}}}{N_{\mathrm{Y}}} \tag{6.8}$$

$$x_{\mathrm{depletion}} = x_{\mathrm{b,\ nominal}} - x_{\mathrm{b}} \tag{6.9}$$

Usual Nd:YAG dopant concentrations are expressed in % rather than fractions, which will therefore be adopted in the results to be presented in order to facilitate comparision with experiments.

So far only segregation in an equilibrium powder having the Wulff shape has been discussed. The above model can however be extended to non-equilibrium powders and equilibrium as well as non-equilibrium microstructures by changing the set of interfaces contained in the sum of equation 6.6. Table 6.4 list the set of interfaces as well as the way their proportion in the total interface population is calculated.

It has to be noted that all models not based on the Wulff shape do not assume the presence of well defined faces but are rather based on the assumption that the grain contour is somehow made up of interfaces in the given proportion. Even if the model does not make an assumption on how this occurs, it may be seen to take place by grain boundary faceting, which is often observed in ceramics [48, 49].

Results & Discussion

Table 6.5 gives the fractions of each interface in the equilibrium case, whereas table 6.6 contains the ones for the non equilibrium case.

Table 6.5: The different interfaces as they appear in the equilibrium model. For surfaces the Wulff shape is used, whereas for boundaries the inverse of the interfacial energy is used for weighting.

		Surfaces		**Grain boundaries**	
Direction	**Cut**	γ [Jm^{-2}]	**Fraction** [%]	γ [Jm^{-2}]	**Fraction** [%]
(100)	2	1.77	52.16	1.73	19.32
(110)	1	2.23	3.88	0.82	41.07
(111)	2	2.11	6.73	1.73	19.34
(112)	1	2.22	37.24	1.65	20.27

Table 6.6: The different interfaces as they appear in the non-equilibrium model, the inverse of the interfacial energy being used for weighting.

		Surface		**Grain boundary**	
Direction	**Cut**	γ [Jm^{-2}]	**Fraction** [%]	γ [Jm^{-2}]	**Fraction** [%]
(100)	1	2.24	4.82	1.97	4.73
	2	1.77	6.09	1.73	5.37
	3	2.26	4.77	2.81	3.31
	4	1.94	5.57	2.52	3.69
	5	1.86	5.80	2.82	3.30
(110)	1	2.23	4.82	1.31	7.11
	2	2.33	4.64	1.61	5.78
	3	2.25	4.79	0.82	11.41
	4	2.49	4.34	2.52	3.69
	5	2.47	4.36	2.61	4.03
	6	2.28	4.73	1.10	8.43
(111)	1	2.33	4.62	1.78	5.24
	2	2.11	5.10	1.73	5.37
	3	2.59	4.17	2.28	4.08
	4	2.21	4.88	3.43	2.71
	5	2.18	4.94	2.94	3.16
	6	2.68	4.03	3.32	2.80
	7	2.83	3.81	2.93	3.18
(112)	1	2.22	4.87	1.65	5.63
	2	2.52	4.28	2.54	3.66
	3	2.36	4.57	2.33	3.32

As discussed above the dopant ions segregated to grain boundaries will be at a higher local concentration than in the bulk. This will affect their luminescent properties by concentration quenching, which reduces the luminescent lifetime and thus the laser power. It was discussed above that the dopants in the grain boundary can be assumed not to contribute to the lasing effect. The amount of dopants at interfaces as a function of grain size is presented in figure 6.12 for the four different models discussed above.

It can be seen from these figures that in general with decreasing grain size an increasing number of dopants will be located at the interfaces, which are considered as saturated in these models. The quantity of dopants at the grain boundary can go up to 100% at very small grain sizes around 50nm. As a consequence the depletion of the bulk is also higher at small grain sizes and can reach up to 1.4 at.%. For low nominal doping rates (1 at.%) the proportion of segregated dopants is always the highest and laser performance will thus be more severly affected.

Comparing the two models for surfaces it is interesting to note that the percentage of segregated dopants is always slightly higher for the equilibrium case. When doing the same comparison for the grain boundary case it can be seen that the exact opposite is the case. This comes from the fact that the low energy boundaries do not accommodate any dopants, whereas the surfaces in the Wulff shape still accommodate a fair amount. For powders the depletion is as a result more marked for the equilibrium case where the bulk doping level can be reduced by more than 1 at.%., which will go along with a reduction in luminescence lifetime and thus laser power. For the non equilibrium case this reduction is less marked and luminescence experiments carried out on differently prepared powders should thus give different results, which was also seen in experiments [50]. It is further interesting to note that whereas the difference between the two surface models is small, it is very marked for the grain boundary case. In the equilibrium case almost no dopants will be segregated at the grain boundaries (less than 10% at 500nm grain size even at low dopant levels). This means that a large amount of dopants is found in the bulk and will contribute to the lasing properties of the material. For the non-equilibrium ceramic case a significantly larger proportion of dopants will be found at the grain boundaries and thus not contribute to the lasing. The degree of equilibrium reached during sintering should thus influence the laser performance of a ceramic laser.

Powders for YAG ceramic are produced by two main routes as mentioned in the introduction to this chapter: Solid state mixing of the powder and dopant oxides by milling [2, 4] or powder synthesis in presence of the dopants [6, 51, 52, 53, 54]. In the first case it can be assumed that the powder will exhibit a number of high

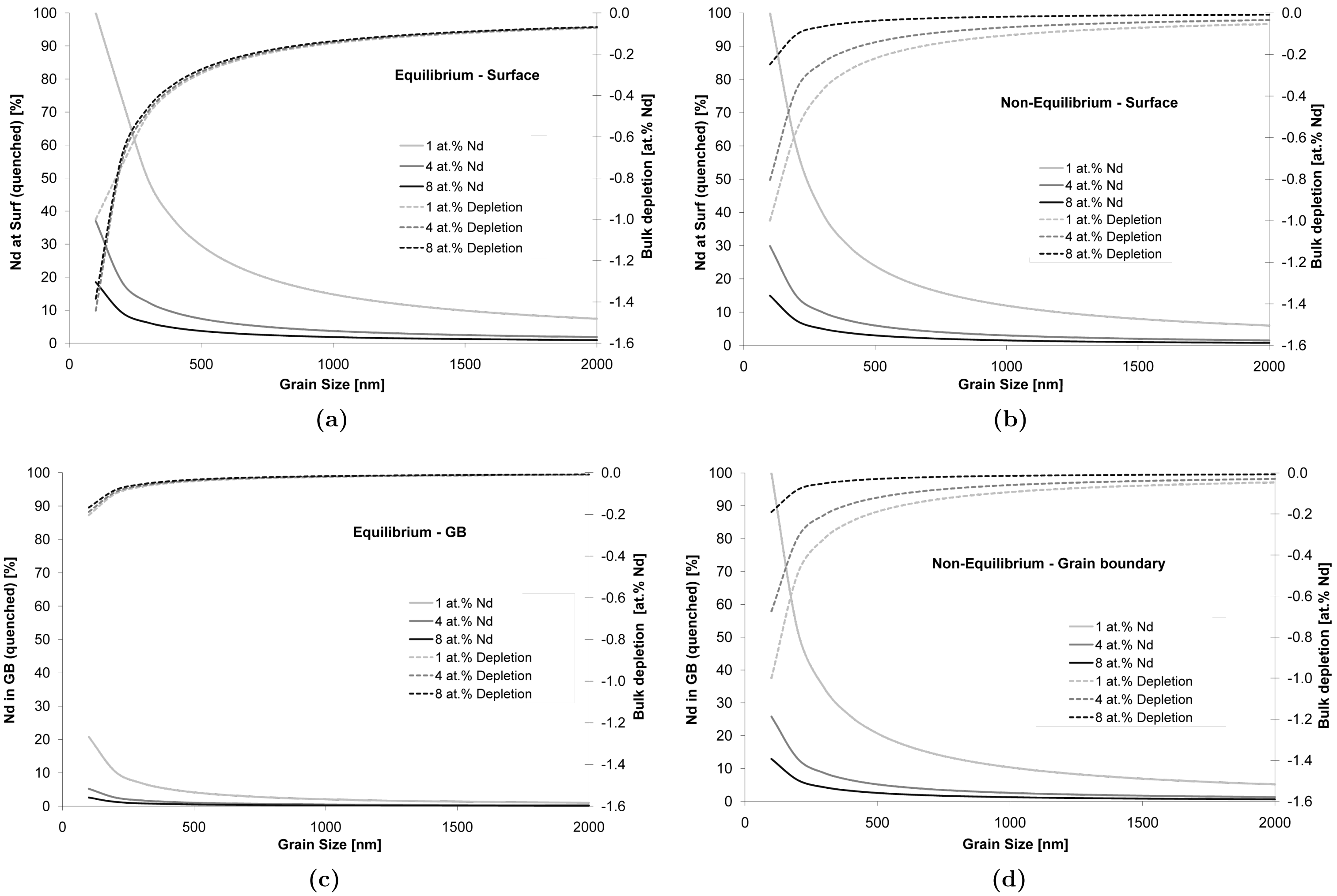

(a) (b) (c) (d)

Figure 6.12: Segregation in YAG powders and ceramic microstructures as predicted by the four models: (a) The equilibrium powder model based on the Wulff shape, (b) the non equilibrium powder model, (c) the equilibrium ceramic model and (d) the non equilibrium ceramic model

energy surfaces which result from breaking the particles during milling whereas in the second case the particles should have more or less the equilibrium morphology. It can thus be assumed that these two powder preparation routes are close to the two extreme cases of an equilibrium and a non-equilibrium powder.

These powders are then sintered either by conventional methods, possibly under vacuum [6, 2, 7], by fast sintering methods such as spark plasma sintering (SPS) [55, 56] or also by high-pressure-low-temperature methods [57, 58, 50], which conserve nano-sizes of the powder particles. The conventional method can be assumed to give microstructures which are closest to equilibrium, the high-pressure-low-temperature methods will be situated in between the two extremes, whereas the fast sintering methods are likely to result in out of equilibrium microstructures.

In view of these consideration the different combinations of powder production and sintering methods can be discussed and estimations on the resulting laser performance can be drawn. It is easiest to present these consideration in form of a matrix (table 6.7) listing all combinations of the two powder preparation and sintering routes.

The estimations have been based on the following aspects:

- For the dopant reject the amount of dopants at the surface and the grain boundary have been compared. If the surface can accommodate significantly more dopants than the grain boundary, these dopants have to diffuse into the bulk during sintering. For both powders a dopant accumulation at the surface is assumed. Even if the majority of the dopants is located in the bulk for precipitated powders, the surface should see an enrichment when diffusional processes are activated during the early stages of sintering. This enrichment is supposed more important for slow than for fast sintering methods.

- The risk for precipitate formation is a function of the amount of dopants to be rejected from the interface as well as the time available for this diffusion process.

- The bulk doping level is estimated from the depletion as presented above.

- The dopant accumulation at grain boundaries is estimated from the percentage of segregated dopants.

- The risk for grain growth is determined by the energy of the surfaces present. An equilibrium powder will present in general low energy faces, which have a low tendency for grain growth. Also fast sintering will suppress grain growth by limiting the kinetics.

By looking at the data in table 6.7 it can be seen that from a laser performance point of view it would be interesting to sinter Nd:YAG ceramics by conventional slow sintering routes in order to obtain microstructures as close to equilibrium as possible. In these microstructures the majority of dopants should be found in sites active for lasing. However since the surfaces of powders will always carry more dopants than the grain boundaries can accommodate, care has to be taken as to avoid second phase precipitation along the grain boundaries during conventional sintering. The only combination for which the risk for precipitation is low is fast sintering of a non-equilibrium powder, however at the cost of loosing in laser performance. There are thus advantages and drawbacks for each combination and most likely a middle course would give the best ceramic. The present extreme cases serve however as illustrative examples for the understanding of these phenomena in laser ceramics.

To resume the results here it can be said that at smaller grain sizes a larger amount of dopants is segregated. It was also seen that this could be compensated by higher nominal doping levels, scarifying the segregated dopants. However this dopant accumulation at the grain boundaries could affect the transparency which will be investigated in the next section.

6.3.2 Scattering in inhomogeneous microstructures

In order to evaluate light scattering by the regions close to grain boundaries, having a higher neodymium content and thus a slightly different refractive index light scattering models can be used. In the present case two models of different complexity will be applied. The first one being a mean-field model based on the Mie scattering theory and the second one a purely numerical approach called the discrete dipole approximation (DDA). For both methods the change in refractive index with the dopant concentration was evaluated via atomistic calculations by gradually substituting the yttrium ions in a bulk unit-cell always retaining the energetically most favorable configuration. Of these cells the refractive indices were calculated in the GULP [45] code using the pair potentials also employed in the atomistic calculations. It is clear that this is only a first approximation and that refractive index changes in grain boundaries should be calculated from first principles. This change in refractive index is shown in figure 6.13.

It can be seen that the total change even at full coverage is quite small. Using the two models for equilibrium and non equilibrium outlined above the mean coverages

Table 6.7: The different combinations of starting powders and sintering methods and the expected effects on ceramic processing and laser performance.

	Equilibrium Microstructure (Conventional Sintering)	**Non-Equilibrium Microstructure** (Fast Sintering)
Equilibrium Powder (precipitated)	Important dopant reject from GB Risk for second phase formation High bulk doping level Small dopant accumulation at GB Moderate risk of grain growth	Moderate dopant reject from GB Risk for second phase formation Significant dopant level change Dopant accumulation at GB Small grains
Non-Equilibrium Powder (solid state)	Moderate dopant reject from GB Risk for second phase formation High bulk doping level Small dopant accumulation at GB High risk of grain growth	No dopant reject No second phase formation Significant dopant level change Dopant accumulation at GB Moderate risk of grain growth

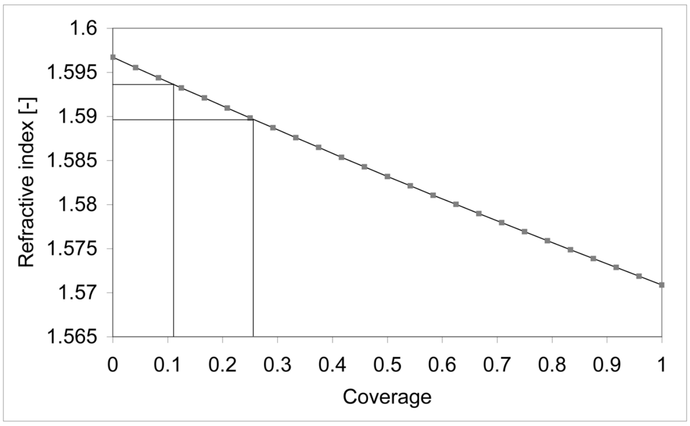

Figure 6.13: Refractive index of Nd:YAG as a function of the dopant concentration.

for the two cases can be evaluated as 0.11 for the equilibrium and 0.26 for the non-equilibrium case respectively. This will correspond to a refractive index change of maximum 0.007. This value will be used as a homogeneous grain boundary refractive index in the mean field model. It can be seen from the coverages that regions with a local refractive index change higher than this mean value can exist. In the following the mean field and DDA method used will be described along with the results obtained by each method.

Mean field model

The optical mean field model is derived from the one published by Apetz and van Bruggen [59], where the influence of the optical anisotropy in alumina ($n_{\text{ordinary}} = 1.768$, $n_{\text{extraordinary}} = 1.760$) on the transparency is modeled by considering 50% vol. of grains ($x_{\text{grain}} = 0.5$) of a refractive index slightly different by Δn to be embedded in a matrix having the alumina mean refractive index n. They then model the scattering by the grain boundaries within the Rayleigh-Gans-Debye approximation where the scattering cross section (C_{sca}) of a grain in the matrix is given by equation 6.10 at a certain wavelength $\lambda_m = \lambda_0/n$ in the medium, λ_0 being the incident wavelength. The validity range for this approximation is given by equation 6.11.

$$C_{\text{sca}} = \frac{8\pi^3 r^4}{\lambda_m^2}\left(\frac{\Delta n}{n}\right)^2 \tag{6.10}$$

$$2r\Delta n \ll 2\pi\lambda_m \tag{6.11}$$

The scattering coefficient γ is then given via the density (number/volume) of

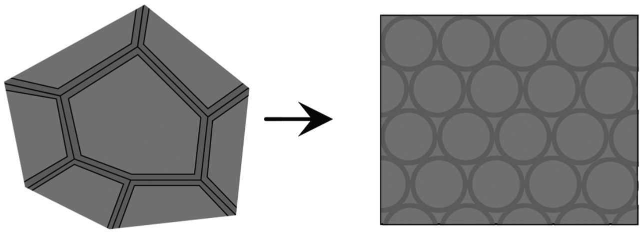

Figure 6.14: The approximation of the YAG microstructure with segregated dopants by the hexagonal close packed array of coated spheres.

grains in the matrix times the scattering cross section (equation 6.12).

$$\gamma = x_{\text{grain}} \frac{1}{V_{\text{grain}}} C_{\text{sca}} = \frac{1}{2} \frac{1}{\frac{4}{3}\pi r^3} \frac{8\pi^3 r^4}{\lambda_m^2} \left(\frac{\Delta n}{n}\right)^2 = 3\frac{\pi^2 r}{\lambda_0^2}\Delta n^2 \tag{6.12}$$

The real inline transmittance (RIT) of a sample is defined as given in equation 6.13 where R_s is the surface reflectance (perpendicular total Fresnel reflectance coefficient as given by equations 6.14 and 6.15) and d the thickness of the sample.

$$RIT = (1 - R_s) exp\left(-\gamma d\right) = (1 - R_s) exp\left(-\frac{3\pi^2 r \Delta n^2 d}{\lambda_0^2}\right) \tag{6.13}$$

$$R_s = \frac{2R'}{1 + R'} \tag{6.14}$$

$$R' = \left(\frac{n-1}{n+1}\right)^2 \tag{6.15}$$

In the present case the scattering will not come from the anisotropy but from a layer of different refractive index at the grain boundary. The model can therefore be adapted in the following way. The microstructure is simulated as a hexagonal close packed array of spheres ($x_{\text{grain}} = 0.74$) of YAG refractive index (1.597) in the center and coated by a small layer of different refractive index (1.594 for equilibrium and 1.590 for non-equilibrium). This setup is shown in figure 6.14 and the RIT relation for this case is given by equation 6.16.

$$RIT = (1 - R_s) exp\left(-0.74\frac{3Q_{\text{sca}}}{4r} d\right) = (1 - R_s) exp\left(-0.74\frac{3C_{\text{sca}}}{4\pi r^3} d\right) \tag{6.16}$$

The scattering cross section of such a coated sphere can be calculated from the Mie theory using for example the publicly available BHCOAT code from Bohren and

Huffman [60]. This model has been programmed in the GBOptics2 code developed during this thesis, which has been used for all calculations presented below.

The graphs presenting the loss in transmittance in the visible (640nm) and lasing wavelength (1064nm) for a grain boundary thickness of 1nm=2·0.5nm are shown in figure 6.15 for different grain sizes. The sample thickness d was taken to be 0.8mm. It can be seen that the influence of equilibrium is negligible, the graphs for the two cases being almost equivalent. The change from laser to visible is more marked, however even at the visible wavelength the changes in RIT are well below 1%. It is however interesting to note that with increasing grain size there is first a decrease in RIT followed by an increase. The grain size for which the transmittance is minimal being located around 200nm for the lasing frequency and around 100nm for the visible one. The influence of the grain boundary thickness was also found to be small - even layers of 10nm only resulting in RIT changes of the order of 1%.

This model has however the drawback that it does not consider a percolation of the grain boundaries and thus light scattering defects are always considered isolated even if the spheres should touch as predicted by the volume fraction for hexagonal close packing. Another similar model can be constructed as shown in figure 6.16 where the matrix has the same refractive index as the grain boundary layer. This will result in an overestimation of the grain boundary volume fraction but gives indications on the effect of percolation.

The results are shown in figure 6.17 where it can be seen that the percolation changes the results considerably, the defect now scattering like an extended network of grain boundaries, the effect of the grain size being more important than the effect of the grain boundary phase refractive index. The results on the RIT at a grain size of one micron are quite severe ranging at lasing wavelengths from a 10% loss for the equilibrium model to a 45% loss for the non equilibrium model. In the visible range the losses are even more marked being at 30% and 80% respectively.

These results show that if grain boundary phase percolation occurs, sub-micron sizes ceramics are of a big importance in order to reduce the effects of scattering. Since these results overestimate the volume fraction of the grain boundary phase and thus the light scattering the so called discrete dipole approximation (DDA) was considered in order to further evaluate the importance of percolation.

Discrete Dipole Approximation - DDA

The discrete dipole approximation was initially developed by Purcell and Pennypacker [61] and is based on the idea of replacing the scattering body by a set of

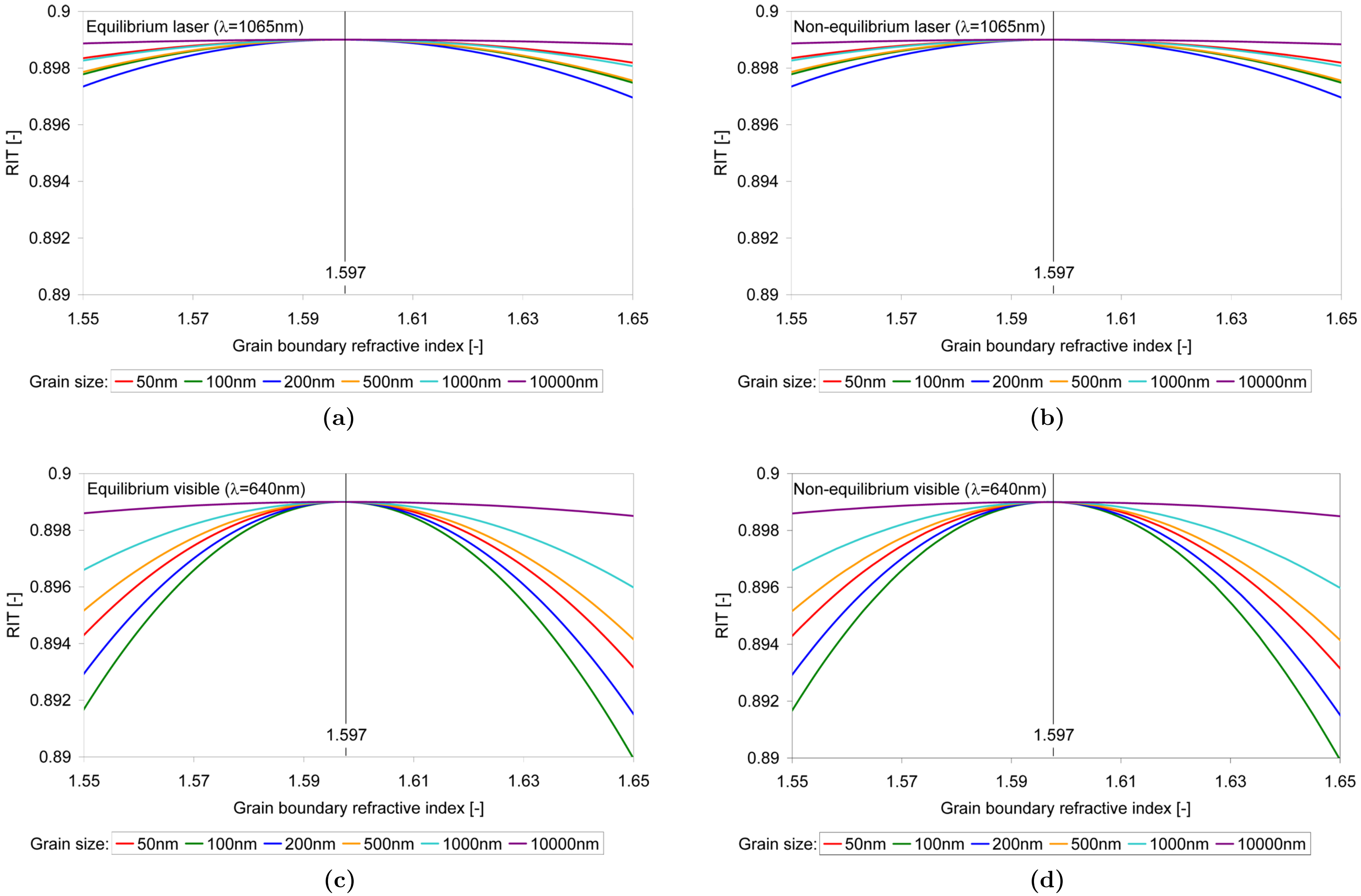

Figure 6.15: Real inline transmittance (RIT) changes as a function of the grain boundary refractive index at a grain boundary thickness of 1nm: (a) The equilibrium model at the laser wavelength, (b) the non-equilibrium model at the laser wavelength, (c) the equilibrium model in the visible range and (d) the non-equilibrium model in the visible range.

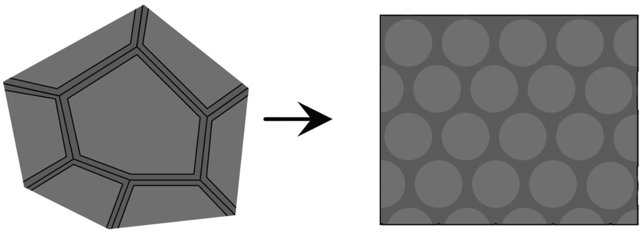

Figure 6.16: The approximation of the YAG microstructure with segregated dopants by the hexagonal close packed array of coated spheres embedded in a matrix of the coating refractive index to simulate percolation of the grain boundary phase.

interacting dipoles, which are subject to an incident electromagnetic wave. The polarization at each point is then obtained by solving a set of linear equations. The exact method will not be described here details on the implementation in the DDSCAT code used in this work [62] can be found by Draine and Flatau [63] and Yurkin and Hoekstra [64].

For the present application a microstructural element based on a space filling arrangement of rhombic dodecahedrons has been defined within a cubic cell as shown in figure 6.18. The number of dipoles in this element was taken as 50 in each direction and the boundary width was assumed as 1nm. An element is considered part of the boundary if it's center is closer to the boundary plane than the GB width. The bulk elements in the grains were considered to have a refractive index of 1 by dividing both the refractive indices of the the boundary (1.59) and the incident wavelength (80nm-2400nm) by the bulk refractive index. This resulted in a refractive index of 1.01 and wavelengths in the range 50nm-1500nm. The dipole arrays created by a small software (MSBuilder developed during this thesis) contained thus only the boundary elements. These grain boundary elements were populated randomly with the grain boundary refractive index at different proportions below and above the percolation threshold in order to check for the effect of an extended defect. In order to have a sufficiently large target to be seen as bulk by the incident wave, the microstructural element was repeated 5 times in the direction of the beam and 2 times in the direction of the polarization, the number of repetitions being limited by the amount of RAM available (the 5x2x1 configurations taking already about 1GB of RAM and the calculation time also being considerable).

Figure 6.19 shows the evolution of the scattering efficiency parameter as a function of the wavelength for grain sizes of 500nm and 1000nm. An analytical model [60]

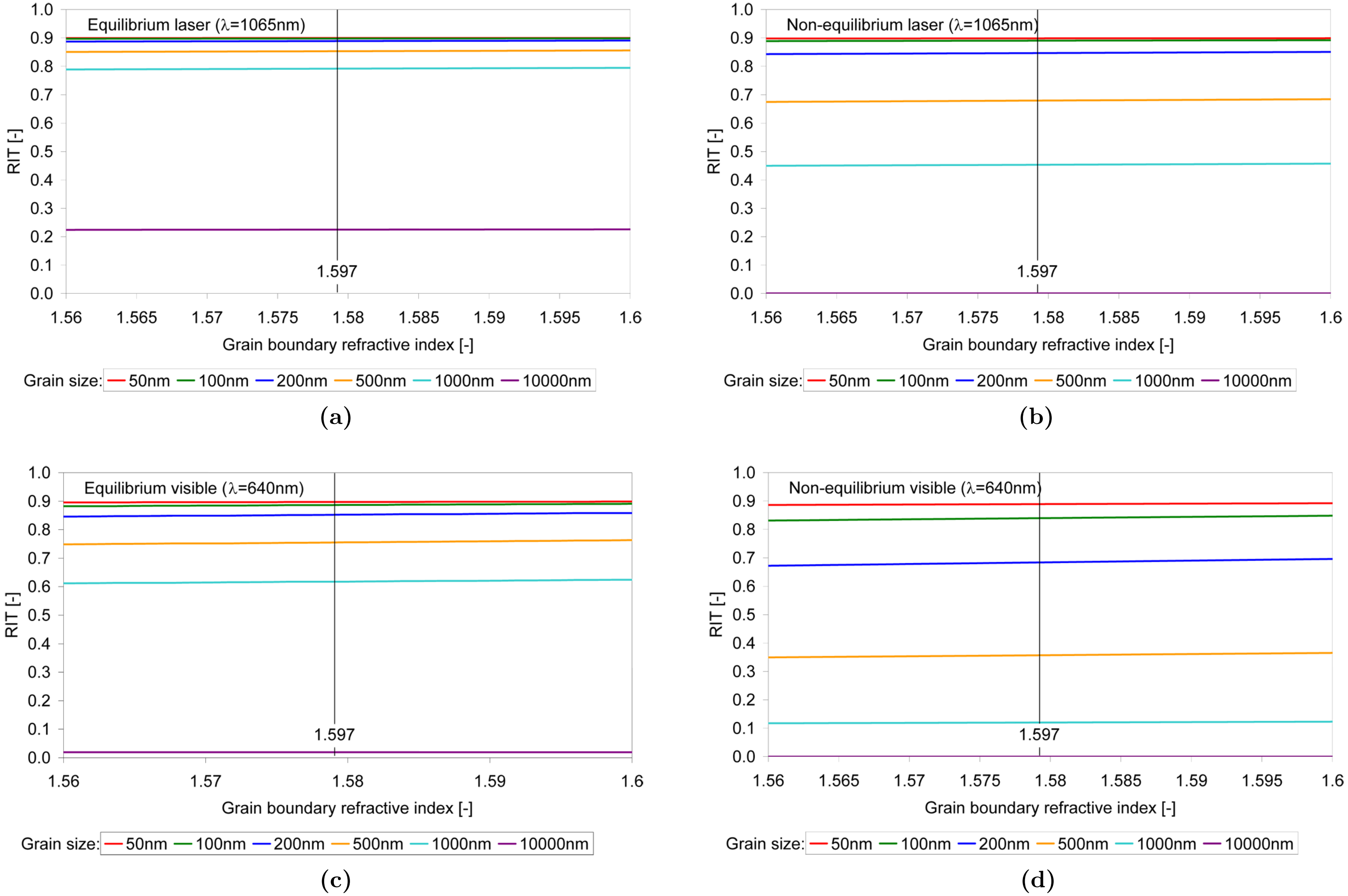

Figure 6.17: Real inline transmittance (RIT) changes as a function of the grain boundary refractive index at a grain boundary thickness of 1nm using the percolated model: (a) The equilibrium model at the laser wavelength, (b) the non-equilibrium model at the laser wavelength, (c) the equilibrium model in the visible range and (d) the non-equilibrium model in the visible range.

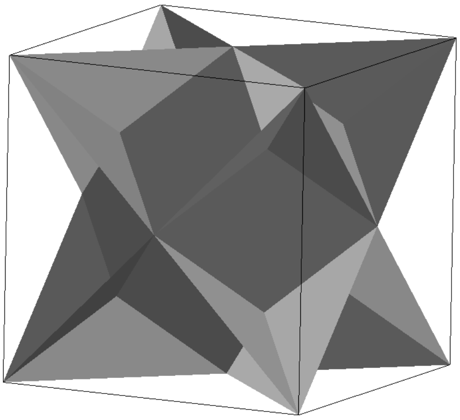

Figure 6.18: Microstructural element used for the DDSCAT calculations.

for touching but filled spheres predicts a Rayleigh like scattering ($\propto \lambda^{-4}$) at high wavelengths and a Rayleigh-Gans-Debye like scattering ($\propto \lambda^{-2}$) at low wavelengths, the transition occurring at a point proportional to d/λ, d being the grain size. In the present results this change of slope is also to be observed for all population fractions except 0.1 and varies approximately from 250nm to 400nm for grains of 500nm and from 270nm to 700nm for grains of 1000nm. It should however be noted that even if changes in the slope can be seen, the transition is gradual and that the Rayleigh scattering limit is never attained, the slope always being lower than -4. The case of 0.1 population fraction is below the percolation threshold (0.19) and the scatterers are thus isolated, which explains the sudden drop in scattering efficiency as well as the break-down of the analytical model. This means that as scattering by this microstructural element follows a law similar to the analytical one for touching spheres with the exception that the transition point is not constant for a given grain size and that below a certain population threshold, the microstructural element can no longer be considered to scatter like a sphere.

Figure 6.20 shows the scattering efficiency parameter as a function of the grain size for a visible (yellow) and a lasing (IR) wavelength. As for the mean field model it can be seen that the scattering is more severe for visible wave lengths than for the lasing ones.

In order to compare the scattering results obtained here to the ones obtained with the mean field models, the scattering efficiencies for different population fractions between 1.0 and 0.1 were taken and the RIT calculated according to equation 6.17, where r is the grain radius and d the sample thickness (0.8mm).

$$RIT = (1 - R_s)exp\left(-\frac{Q_{\text{sca}}}{\frac{4}{3}r}d\right) \tag{6.17}$$

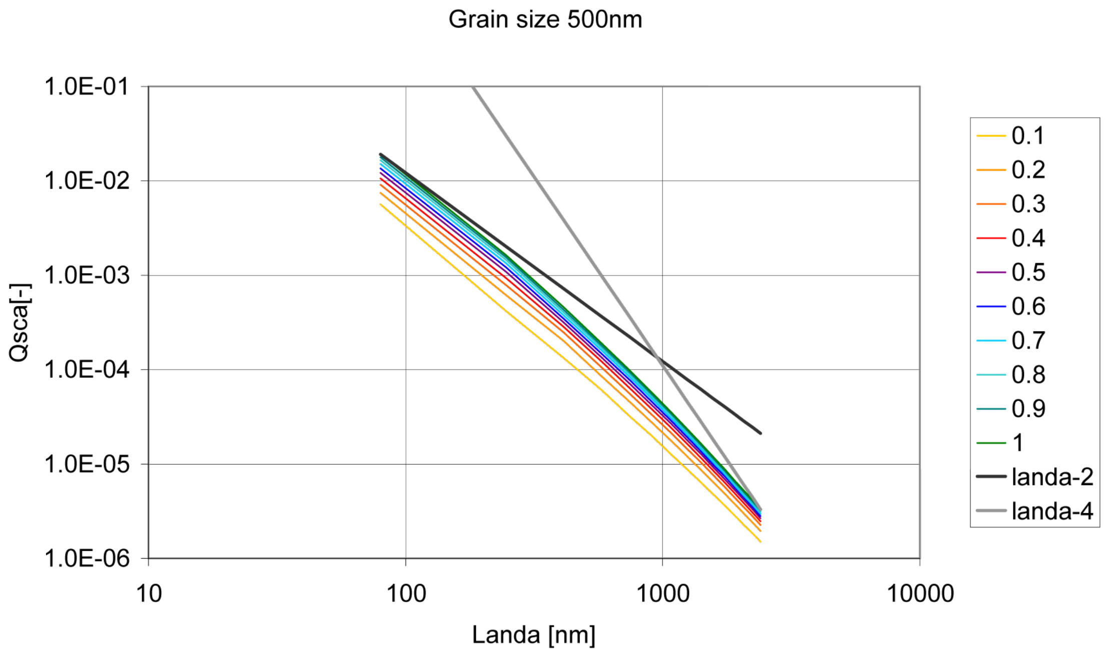

(a)

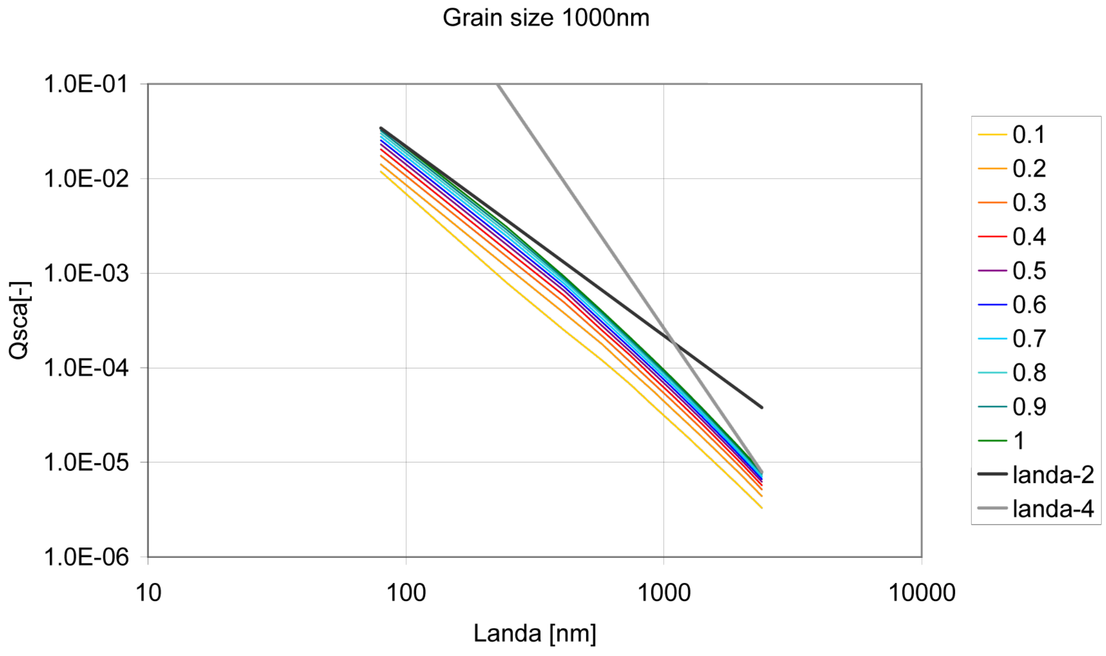

(b)

Figure 6.19: Model parameters λ^{-2} (Rayleigh-Gans-Debye scattering) and λ^{-4} (Rayleigh scattering) and calculated scattering efficiency parameter (Q_{sca}) as a function of the wavelength for grain sizes of: (a) 500nm and (b) 1000nm.

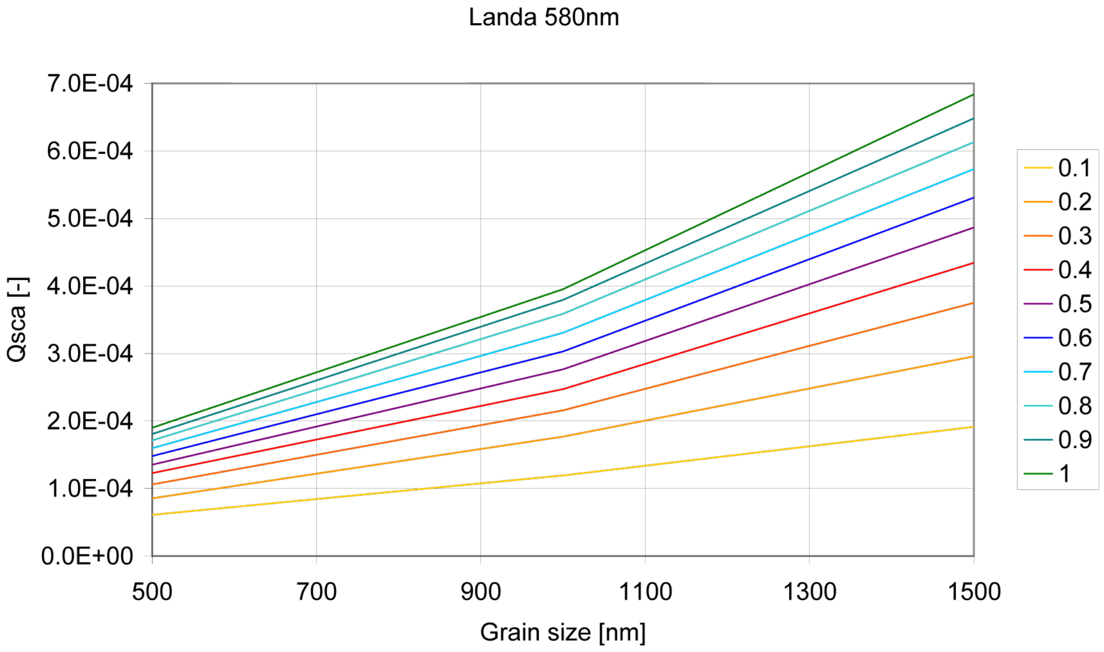

(a)

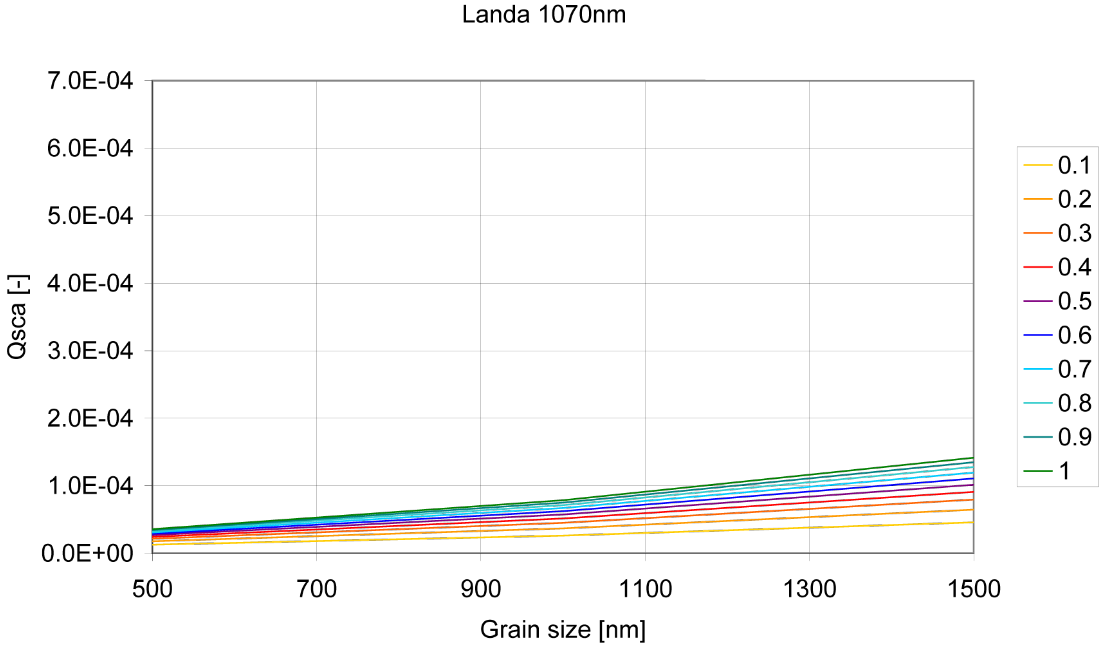

(b)

Figure 6.20: Scattering efficiency parameter (Q_{sca}) as a function of grain size (a) for visible (580nm, yellow) and (b) lasing (1070nm, IR) wavelengths.

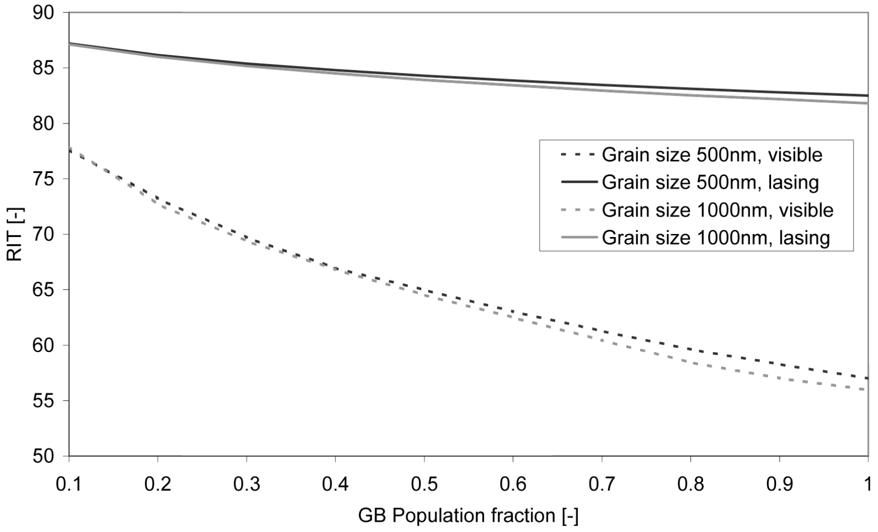

Figure 6.21: The real inline transmittance as a function of the fraction of scattering grain boundary elements as predicted by the DDA.

The results obtained are plotted in figure 6.21. As it could already be estimated from the scattering efficiencies the transparency reduction is a lot more marked for the visible than the lasing wave length. A drastic decrease in RIT can be observed when the percolation threshold is passed (around 20% of the grain boundary elements having a different refractive index than the bulk) followed by a more or less linear decrease with increasing number of scatterers at the grain boundary. It can be seen that the extended defect modeled by the DDA scatters a lot more effectively than non-interconnected defects modeled by the mean field model, resulting in RIT reductions of about 5% in the infrared lasing wavelengths and even 20% in the visible range. The scattering is slightly higher for larger grain sizes than for smaller ones.

It is not easy to directly link the fraction of scatters in the grain boundary to the coverage. In fact the local coverage would determine the efficiency of each scattering dipole element. For an element to be considered as scattering it has to contain a certain number of dopant ions, which for the present case is set at 20% of Y being replaced by Nd. A local coverage above that value will result in a scattering element, whereas below it will be considered as bulk-like. The population fraction is thus the fraction of grain boundary volume elements having a coverage higher than 20%.

By considering again the equilibrium and non equilibrium model for grain boundaries and summing up the proportions given in tables 6.5 and 6.6 for the boundaries having a coverage higher than 20% in table 6.3 it can be seen that this is true for 39% of the boundaries in the equilibrium case and 79% in the nonequilibrium case. These values can approximately be used as the population fractions. The result will be maximimally 5% loss of transparency in the lasing regime but a considerable 20% in the visible range for non equilibrium ceramics. The fact that equilibrium ceramics are less prone to scattering is supported by the fact that extremely high sintering temperatures close to the melting point were required to sinter transparent YAG [6, 2, 4].

It has been confirmed using the DDA that extended defects scatter differently from isolated defects and that grain boundaries, which are fully covered by dopants and form a continuous network will scatter light significantly even if the difference in refractive index is relatively small. The grain boundary coverage will be higher in the non equilibrium case, where lower light transmission is obtained. The effect attached to equilibrium (transparencies at 0.4 and 0.8 fraction GB population for the equilibrium and non-equilibrium case respectively) is larger than the effect of the grain size (difference between the 500nm and 1000nm curves).

6.4 Conclusions

It was seen that the combination of atomistic with larger scale microstructural and optical simulation approaches provides a powerful combination for the investigation of segregation related optical phenomena in ceramics. The microstructural model suggests that at smaller grain sizes a higher proportion of dopants is segregated and that the lasing performance will decrease for a given nominal doping level. This is especially true for the sub-micron sized regime where due to the high proportion of interface volume a significant proportion of dopants can be found at grain boundaries. In practice this depletion in actively lasing dopants could be counterbalanced by increasing the doping level. The accumulation of dopants will however lead to refractive index changes at the grain boundaries, which when forming continuous networks of extended defects can severely scatter light. This scattering is more marked in non equilibrium ceramics and at large grain sizes. Whereas for the lasing wavelength the reduction transparency may be acceptable, it is clearly not in the visible range. This results in the schematic behavior shown in figure 6.22.

This data suggests that on one hand in order to obtain high power lasers even at low doping, one would like to keep the grain size large. The scattering of light by segregated dopants is however more marked at large grain sizes than at small ones. This suggests that there is an optimal grain size for which laser power is still high and scattering is already low as shown in figure 6.22. It was also seen that equilibrium microstructures show a lot less scattering than non-equilibrium ones. This means

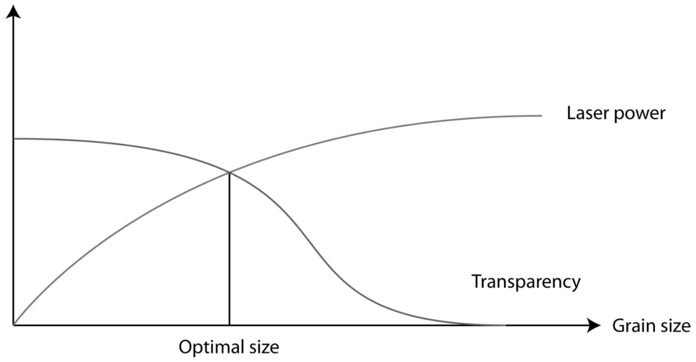

Figure 6.22: Schematic view of the evolution of transparency and laser power for YAG ceramics. Also shown is the resulting optimal grain size.

that slow conventional sintering methods will give higher quality ceramics, however in that case again care has to be taken to limit grain growth as otherwise scattering will increase. The present predictions however place a higher importance on the degree of equilibrium than on the grain size.

Bibliography

[1] J. E. Geusic, H. M. Marcos, and L. G. Vanuitert. Laser oscillations in Nd-doped yttrium aluminum, yttrium gallium and gadolinium garnets. *Applied Physics Letters*, 4(10):182–184, 1964.

[2] A. Ikesue, K. Kamata, and K. Yoshida. Synthesis of Nd^{3+}, Cr^{3+}-codoped YAG ceramics for high-efficiency solid-state lasers. *Journal of the American Ceramic Society*, 78(9):2545–2547, 1995.

[3] A. Ikesue, K. Kamata, and K. Yoshida. Effects of neodymium concentration on optical characteristics of polycrystalline Nd:YAG laser materials. *Journal of the American Ceramic Society*, 79(7):1921–1926, 1996.

[4] A. Ikesue and Y. L. Aung. Synthesis and performance of advanced ceramic lasers. *Journal of the American Ceramic Society*, 89(6):1936–1944, 2006.

[5] J. Lu, M. Prabhu, J. Song, C. Li, J. Xu, K. Ueda, A. A. Kaminskii, H. Yagi, and T. Yanagitani. Optical properties and highly efficient laser oscillation of Nd:YAG ceramics. *Applied Physics B-Lasers and Optics*, 71(4):469–473, 2000.

[6] J. R. Lu, K. Ueda, H. Yagi, T. Yanagitani, Y. Akiyama, and A. A. Kaminskii. Neodymium doped yttrium aluminum garnet ($Y_3Al_5O_{12}$) nanocrystalline ceramics - a new generation of solid state laser and optical materials. *Journal of Alloys and Compounds*, 341(1-2):220–225, 2002.

[7] J. Lu, H. Yagi, K. Takaichi, T. Uematsu, J. F. Bisson, Y. Feng, A. Shirakawa, K. I. Ueda, T. Yanagitani, and A. A. Kaminskii. 110 W ceramic Nd^{3+}:$Y_3Al_5O_{12}$ laser. *Applied Physics B-Lasers and Optics*, 79(1):25–28, 2004.

[8] V. Lupei, A. Lupei, N. Pavel, T. Taira, and A. Ikesue. Comparative investigation of spectroscopic and laser emission characteristics under direct 885-nm pump of concentrated Nd:YAG ceramics and crystals. *Applied Physics B-Lasers and Optics*, 73(7):757–762, 2001.

[9] N. Pavel, V. Lupei, J. Saikawa, T. Taira, and H. Kan. Neodymium concentration dependence of 0.94-, 1.06- and 1.34-mm laser emission and of heating effects under 809- and 885-nm diode laser pumping of Nd:YAG. *Applied Physics B-Lasers and Optics*, 82(4):599–605, 2006.

[10] W. Koechner. *Solid-State Laser Engineering*, volume 1 of *Springer Series in Optical Sciences*. Springer-Verlag, Berlin, second edition edition, 1988.

[11] J. A. L'huillier, G. Bitz, V. Wesemann, P. von Loewis, R. Wallenstein, A. Borsutzky, L. Ackermann, K. Dupre, D. Rytz, and S. Vernay. Characterization and laser performance of a new material: 2 at. Nd:YAG grown by the Czochralski method. *Applied Optics*, 41(21):4377–4384, 2002.

[12] J. A. L'huillier, G. Bitz, V. Wesemann, A. Borsutzky, and R. Wallenstein. A sensitive non-destructive method for measuring the Nd doping concentration in Nd:YAG with high spatial resolution. *Applied Physics B-Lasers and Optics*, 77(6-7):601–606, 2003.

[13] K. K. Deb, R. G. Buser, and J. Paul. Decay kinetics of $^4F_{3/2}$ fluorescence of Nd^{+3} in YAG at room temperature. *Applied Optics*, 20(7):1203–1206, 1981.

[14] L. D. Merkle, M. Dubinskii, K. L. Schepler, and S. M. Hegde. Concentration quenching in fine-grained ceramic Nd:YAG. *Optics Express*, 14(9):3893–3905, 2006.

[15] J. Dong, A. Rapaport, M. Bass, F. Szipocs, and K. Ueda. Temperature-dependent stimulated emission cross section and concentration quenching in highly doped Nd^{3+}:YAG crystals. *Physica Status Solidi A-Applications and Materials Science*, 202(13):2565–2573, 2005.

[16] Z. Y. Huang, Y. D. Huang, Y. J. Chen, and Z. D. Luo. Theoretical study on the laser performances of Nd^{3+}:YAG and Nd^{3+}:YVO_4 under indirect and direct pumping. *Journal of the Optical Society of America B-Optical Physics*, 22(12):2564–2569, 2005.

[17] G. A. Saunders, S. C. Parker, N. Benbattouche, and H. L. Alberts. Elastic and nonlinear acoustic properties of the terbium iron garnet $Tb_3Fe_5O_{12}$ in relation to those of other garnets. *Physical Review B*, 46(14):8756–8767, 1992.

[18] H. Donnerberg and C. R. A. Catlow. Atomistic computer-simulations of yttrium-iron-garnet (YIG) as an approach to materials defect chemistry: I. intrinsic defects. *Journal of Physics-Condensed Matter*, 5(18):2947–2960, 1993.

[19] H. Donnerberg and C. R. A. Catlow. Atomistic computer-simulations of yttrium-iron-garnet as an approach to studying its defect chemistry - extrinsic defects. *Physical Review B*, 50(2):744–750, 1994.

[20] K. Wright, R. Freer, and C. R. A. Catlow. The energetics and structure of the hydrogarnet defect in grossular - a computer-simulation study. *Physics and Chemistry of Minerals*, 20(7):500–503, 1994.

[21] K. Wright, R. Freer, and C. R. A. Catlow. Oxygen diffusion in grossular and some geological implications. *American Mineralogist*, 80(9-10):1020–1025, 1995.

[22] A. Beltran, J. Andres, J. A. Igualada, and J. Carda. Garnet crystal-structures - an ab-initio perturbed ion study. *Journal of Physical Chemistry*, 99(17):6493–6501, 1995.

[23] M. M. Kuklja and R. Pandey. Atomistic modeling of native point defects in yttrium aluminum garnet crystals. *Journal of the American Ceramic Society*, 82(10):2881–2886, 1999.

[24] W. Y. Ching, Y. N. Xu, and B. K. Brickeen. Ab-initio calculation of excited state absorption of Cr^{4+} in $Y_3Al_5O_{12}$. *Applied Physics Letters*, 74(25):3755–3757, 1999.

[25] M. A. Gülgün, W. Y. Ching, Y. N. Xu, and M. Rühle. Electron states of YAG probed by energy-loss near-edge spectrometry and ab initio calculations. *Philosophical Magazine B-Physics of Condensed Matter Statistical Mechanics Electronic Optical and Magnetic Properties*, 79(6):921–940, 1999.

[26] Y. N. Xu and W. Y. Ching. Electronic structure of yttrium aluminum garnet ($Y_3Al_5O_{12}$). *Physical Review B*, 59(16):10530–10535, 1999.

[27] Y. N. Xu, W. Y. Ching, and B. K. Brickeen. Electronic structure and bonding in garnet crystals $Gd_3Sc_2Ga_3O_{12}$, $Gd_3Sc_2Al_3O_{12}$, and $Gd_3Ga_3O_{12}$ compared to $Y_3Al_3O_{12}$. *Physical Review B*, 61(3):1817–1824, 2000.

[28] Y. N. Xu, Y. Chen, S. D. Mo, and W. Y. Ching. Core exciton, valence exciton, and optical properties of yttrium aluminum garnet ($Y_3Al_5O_{12}$). *Physical Review B*, 65(23):235105, 2002.

[29] J. Chen, D. Q. Chen, and J. L. Zhang. Molecular dynamics simulation of thermodynamic properties of YAG. *Chinese Physics*, 16(9):2779–2785, 2007.

[30] G. W. Watson, E. T. Kelsey, N. H. de Leeuw, D. J. Harris, and S. C. Parker. Atomistic simulation of dislocations, surfaces and interfaces in MgO. *Journal of the Chemical Society-Faraday Transactions*, 92(3):433–438, 1996.

[31] D. Rodic, M. Mitric, R. Tellgren, and H. Rundlof. The cation distribution and magnetic structure of $Y_3Fe_{(5-x)}Al_xO_{12}$. *Journal of Magnetism and Magnetic Materials*, 232(1-2):1–8, 2001.

[32] G. V. Lewis and C. R. A. Catlow. Potential models for ionic oxides. *Journal of Physics C-Solid State Physics*, 18(6):1149–1161, 1985.

[33] P. R. Stoddart, P. E. Ngoepe, P. M. Mjwara, J. D. Comins, and G. A. Saunders. High-temperature elastic-constants of yttrium-aluminum-garnet. *Journal of Applied Physics*, 73(11):7298–7301, 1993.

[34] T. Tomiki, Y. Ganaha, T. Shikenbaru, T. Futemma, M. Yuri, Y. Aiura, H. Fukutani, H. Kato, J. Tamashiro, T. Miyahara, and A. Yonesu. Optical-spectra of $Y_3Al_5O_{12}$ (YAG) single-crystals in the vacuum ultraviolet region: II. *Journal of the Physical Society of Japan*, 62(4):1388–1400, 1993.

[35] W. L. Bond. Measurement of refractive indices of several crystals. *Journal of Applied Physics*, 36(5):1674–1677, 1965.

[36] M. J. Davies, P. R. Kenway, P. J. Lawrence, S. C. Parker, W. C. Mackrodt, and P. W. Tasker. Impurity segregation to the surfaces of corundum-structured oxides. *Journal of the Chemical Society-Faraday Transactions II*, 85(5):555–563, 1989.

[37] O. Robach, G. Renaud, and A. Barbier. Very-high-quality MgO(001) surfaces: roughness, rumpling and relaxation. *Surface Science*, 401(2):227–235, 1998.

[38] D. J. Harris, J. H. Harding, and S. C. Parker. Simulations of surfaces and interfaces in MgO. *Radiation Effects and Defects in Solids*, 151(1-4):299–304, 1999.

[39] C. M. Fang, S. C. Parker, and G. de With. Atomistic simulation of the surface energy of spinel $MgAl_2O_4$. *Journal of the American Ceramic Society*, 83(8):2082–2084, 2000.

[40] S. Kerisit, D. J. Cooke, A. Marmier, and S. C. Parker. Atomistic simulation of charged iron oxyhydroxide surfaces in contact with aqueous solution. *Chemical Communications*, (24):3027–3029, 2005.

[41] M. Y. Lavrentiev, N. L. Allan, J. H. Harding, D. J. Harris, and J. A. Purton. Atomistic simulations of surface diffusion and segregation in ceramics. *Computational Materials Science*, 36(1-2):54–59, 2006.

[42] T. A. Cherepanova, P. Bennema, Y. A. Yanson, and L. J. P. Vogels. Morphology of synthetic and natural garnets - theory and observations. *Journal of Crystal Growth*, 121(1-2):17–32, 1992.

[43] K. J. Roberts and D. Elwell. Crystal habit and surface-morphology of flux-grown yttrium aluminum garnet. *Journal of Crystal Growth*, 53(2):249–260, 1981.

[44] M. F. Mott and M. J. Littleton. Conduction in polar crystals: I. electrolytic conduction in solid salts. *Transactions of the Faraday Society*, 34(1):485–499, 1938.

[45] J. D. Gale and A. L. Rohl. The general utility lattice program (GULP). *Molecular Simulation*, 29(5):291–341, 2003.

[46] G. Wulff. On the question of speed of growth and dissolution of crystal surfaces. *Zeitschrift für Krystallographie und Mineralogie*, 34(5-6):449–530, 1901.

[47] R. Williams. *The Geometrical Foundation of Natural Structure: A Source Book of Design.* Dover Publications, Inc., Dover, 1979.

[48] K. J. Morrissey and C. B. Carter. Faceted grain-boundaries in Al_2O_3. *Journal of the American Ceramic Society*, 67(4):292–301, 1984.

[49] N. Shibata, F. Oba, T. Yamamoto, T. Sakuma, and Y. Ikuhara. Grain-boundary faceting at a Σ=3, [110]/112 grain boundary in a cubic zirconia bicrystal. *Philosophical Magazine*, 83(19):2221–2246, 2003.

[50] D. Hreniak, W. Strek, P. Gluchowski, R. Fedyk, and W. Lojkowski. The concentration dependence of luminescence of $Nd : Y_3Al_5O_{12}$ nanoceramics. *Journal of Alloys and Compounds*, 451(1-2):549–552, 2008.

[51] X. Li, H. Liu, J. Y. Wang, H. M. Cui, and F. Han. Production of nanosized YAG powders with spherical morphology and nonaggregation via a solvothermal method. *Journal of the American Ceramic Society*, 87(12):2288–2290, 2004.

[52] L. P. Lu, J. H. Liu, F. M. Zeng, Y. C. Wan, and M. Yang. Nd:YAG ultrafine powder for transparent ceramics. *American Ceramic Society Bulletin*, 84(12):9401–9404, 2005.

[53] Y. Wang, L. G. Zhang, Y. Fan, J. S. Lu, D. E. McCready, C. Wang, and L. N. An. Synthesis, characterization, and optical properties of pristine and doped yttrium aluminum garnet nanopowders. *Journal of the American Ceramic Society*, 88(2):284–286, 2005.

[54] A. L. Costa, L. Esposito, V. Medri, and A. Bellosi. Synthesis of Nd:YAG material by citrate-nitrate sol-gel combustion route. *Advanced Engineering Materials*, 9(4):307–312, 2007.

[55] R. Chaim, R. Marder-Jaeckel, and J. Z. Shen. Transparent YAG ceramics by surface softening of nanoparticles in spark plasma sintering. *Materials Science and Engineering a-Structural Materials Properties Microstructure and Processing*, 429(1-2):74–78, 2006.

[56] R. Chaim, M. Kalina, and J. Z. Shen. Transparent yttrium aluminum garnet (YAG) ceramics by spark plasma sintering. *Journal of the European Ceramic Society*, 27(11):3331–3337, 2007.

[57] W. Strek, A. Bednarkiewcz, D. Hreniak, P. Mazur, and W. Lojkowski. Fabrication and optical properties of transparent Nd^{3+}:YAG nanoceramics. *Journal of Luminescence*, 122:70–73, 2007.

[58] R. Pazik, P. Gluchowski, D. Hreniak, W. Strek, M. Ros, R. Fedyk, and W. Lojkowski. Fabrication and luminescence studies of $Ce:Y_3Al_5O_{12}$ transparent nanoceramic. *Optical Materials*, 30(5):714–718, 2008.

[59] R. Apetz and M. P. B. van Bruggen. Transparent alumina: A light-scattering model. *Journal of the American Ceramic Society*, 86(3):480–486, 2003.

[60] C.F. Bohren and D.R. Huffman. *Absorption and scattering of light by small particles.* Wiley, New York, 1998.

[61] E. M. Purcell and Pennypac.Cr. Scattering and absorption of light by nonspherical dielectric grains. *Astrophysical Journal*, 186(2):705–714, 1973.

[62] B. T. Draine and P. J. Flatau. *User Guide for the Discrete Dipole Approximation Code DDSCAT (Version 6.1)*, 2004.

[63] B. T. Draine and P. J. Flatau. Discrete-dipole approximation for scattering calculations. *Journal of the Optical Society of America A - Optics Image Science and Vision*, 11(4):1491–1499, 1994.

[64] M. A. Yurkin and A. G. Hoekstra. The discrete dipole approximation: An overview and recent developments. *Journal of Quantitative Spectroscopy & Radiative Transfer*, 106(1-3):558–589, 2007.

Chapter 7

Oxygen self-diffusion in α-alumina

In this chapter the first results on oxygen diffusion by the vacancy mechanism using a combination of Metadynamics and kinetic Monte Carlo simulations are presented. This method is very versatile and may be used to investigate many of the unresolved diffusion problems in alumina and other ceramics. The results presented here suggest that previously reported vacancy migration energies may have been too low and that only higher energy jumps can contribute to the macroscopic diffusion coefficient, the low energy jumps allowing only local diffusion within groups of three atoms. The validity of this hypothesis is confirmed by a relatively good reproduction of experimentally observed diffusion coefficients.

This method can in the future be used to calculate diffusion of oxygen and aluminum in the doped bulk and doped and undoped grain boundaries. It can also be used to investigate the possibility of interstitial diffusion as well as of dopant ion migration, which is important to understand mechanisms such the grain growth limiting solute drag effect.

7.1 Introduction

As seen in the introduction diffusion is a very important phenomenon for the majority of processes in material science as transport of matter be it in gas, liquid or solid phase is required for many important mechanisms to function. In the present chapter diffusion in solids, which has the lowest diffusion coefficient amongst the aforementioned phases will be looked at. Although the fact that α-alumina is one of the most common ceramic materials diffusion processes are still not understood to date [1]. In his recent review Heuer [2] points out that “not a great deal” is understood and identifies the following main questions:

1. What is the nature of the “buffering” that appears to control $\mathrm{D_{oxy}}$?
2. What process(es) are occurring during annealing that eliminate non-Fickian behavior when measuring $\mathrm{D_{oxy}}$?
3. How should the magnitude of the measured activation energies of $\mathrm{D_{oxy}}$ be interpreted?
4. Have all defect types involved in oxygen diffusion been identified?
5. Does oxygen diffusion occur by an interstitial mechanism?
6. What is the order of magnitude of $\mathrm{D_{Al}/D_{oxy}}$?
7. What is the order of magnitude of $\mathrm{D_{b\text{-}Al}/D_{b\text{-}oxy}}$?
8. It appears that the activation energy for $\mathrm{D_{b\text{-}oxy}}$ is greater than for $\mathrm{D_{oxy}}$. How should this be understood?

In this list $\mathrm{D_{oxy}}$ and $\mathrm{D_{Al}}$ stand for the self-diffusion coefficients of oxygen and aluminum ions in α-alumina respectively and the diffusion coefficients prefixed with “b” stand for grain boundary diffusion coefficients.

It can be seen from this list that most problems are related to oxygen diffusion, which will also be investigated in this work and for which previous simulation results will be resumed in the following paragraphs.

Catlow [3] calculated defect energies in undoped and doped alumina, which give access to the defect equilibrium concentration. Such calculations were also carried out by Grimes [4] and Atkinson [5]. Migration energies of cation and anion vacancies in bulk α-alumina was only looked at by James [6] and Jacobs and Kotomin [7, 8], who calculated the migration energies to lie between 0.34 and 5.10eV and postulated a diffusion mechanism for which an intermediate jump of 1.85eV is rate limiting. Their approach is however based on linear transition paths. Harding and coworkers [9, 10] looked at migration energies in alumina grain boundaries using a “drag technique”, where an additional force in the desired direction is applied to the ion in question and used these in kinetic Monte Carlo methods to access the diffusion constants. They state in the introduction that the calculated [6, 8] migration activation energies are of the order of 1.5-2.0eV whereas the ones derived from experiment are of the order of 5eV [1], which seems too high for an oxide. This discrepancy could according to the authors be related to the presence of impurities or to deficiencies of the methods which can not deal with the complicated migration paths in alumina.

The present approach is on one hand inspired by Krishnamurthy [11, 12] who used density functional theory methods to calculate the activation energies for oxygen diffusion in yttrium stabilized cubic zirconia (YSZ) then using these in kinetic Monte Carlo simulations and on the other hand by the Metadynamics method [13, 14, 15] which allows the determination of the free energy associated with processes, while allowing for arbitrarily complicated transition paths without any restriction.

The present chapter will be substructured in a Metadynamics part and a kinetic Monte Carlo part since the results of the former are required to understand the approach of the latter.

7.2 Metadynamics

7.2.1 Approach

In the present work the calculation of the defect migration energies using ab-initio methods would not have been possible due to the large number of calculations required. It was therefore decided to implement the (direct) Metadynamics (MTD) method into the classical empirical potential molecular dynamics code DL_POLY 2.0 [16] and to write a small kinetic Monte Carlo (kMC) code to carry out the diffusion calculations within the bulk-alumina oxygen sublattice.

The DL_POLY MTD calculations were carried out on a 6x6x2 supercell of the hexagonal unitcell of alumina [17] using the Lewis and Catlow pair potentials [18]. The supercell approach is required since the simulation cell has to be twice as large as the short range cutoff of 10Å due to the implementation of the code. The supercell has been equilibrated in the NPT ensemble by heating in steps of 100K for 100ps using a timestep of 0.0001ps in the velocity-verlet integrator due to the presence of the shells. A Nose-Hoover thermostat and a Hoover barostat with 0.5ps relaxation times were used during these equilibration runs. Heating was carried out from 1K up to 2600K.

For MTD calculations the vacancy was subsequently created on all sites within the first unit-cell of the supercell and the charge compensated by smearing the -2.00 charge over the aluminum sublattice which consequently carried a charge of 2.997685 per aluminum ion. This should not affect the interactions considerably due to the very small variation in charge and isotropic nature of this charge distribution. Charge balancing by incorporation aliovalent dopant ions would have been more problematic in this respect. All oxygen ions surrounding this vacancy (nearest neighbor cutoff radius of 3.1Å) were then allowed to jump into the vacancy by setting up a collective variable (CV) (section 2.6) being the distance between the position at which the vacancy was created and the jumping atom. This setup compared to a coordination number definition has the advantage that it can be controlled using a single CV which oxygen ion will jump into the vacancy. Projected into real space, each point on this CV would corresponds to a spherical shell centered on the vacancy and hills added on one point on the shell will affect all other points on the same shell. Since however the simulation starts far from the center of the sphere and there will be one transition path towards the center, the jumping atoms will traverse the spherical shells in one well defined location and this CV definition will still describe the migration correctly. If however the jumping atom is close to the center of the sphere, as will be the case once the transition occurred, this is not valid anymore, which is why the backward reaction can not be calculated in the same run. The calculations were for this reason stopped once the jumping atom reached the vacancy position. The parameters used for Metadynamics were the number of MD steps between hill insertions n_h=20, the height of the hills h_h=80Jmol^{-1} and their width h_w=0.3Å. The relaxation of the structure after vacancy creation was determined to be accomplished after 500 MD steps and metadynamics were started at this point, inserting hills of energy every n_h MD steps. The hill height used here is a lot smaller than the ones used in ab-initio methods for similar calculations [19] (5kJmol^{-1}) but is was found that such large hills result in a too coarse filling of the underlying free energy surface, the only reason these are used in ab-initio methods probably being the limitation in the number of timesteps available in these methods.

Metadynamics calculations were carried out at 1K, 300K, 1100K and 1700K in the NVT ensemble using a Nose-Hoover thermostat with a 0.5ps relaxation time. In order to prevent crystal warping (the simulation cell's total momentum is non-null and the system starts to translate in space) during the 1K simulations, the atoms outside a sphere of radius 12Å centered on the vacancy had to be frozen, which does however not affect the system as vibrational motion is small at this temperature. For the higher temperatures the momentum carried by the atoms is sufficient to prevent this problem. For the high temperature cases (300K, 1100K and 1700K) three samples of the trajectory were taken at intervals of 1ps in order to account for thermal fluctuations around the vacancy and Metadynamics calculations run on all of these samples. Per sample 134 runs were performed, which together with the multiple samples at higher temperatures should result in a good statistical average of the jump energies. This requirement of a high number of jumps due to thermal fluctuation also highlights that using the rhombohedral unitcell would not have presented an advantage since the supercell size would have been the same and a higher number of samples would have had to be calculated in order to get the same statistical accuracy.

The activation free energies for vacancy migration were extracted from the Metadynamics hill history by summing up the contributions of all hills in 1000 points $\vec{r}$ along the collective variable as given by equation 2.59 and then locating the peak of this distribution, which represents the activation energy as it will be the saddle point on the transition path. Transition rates for the kinetic Monte Carlo method were calculated from the the activation energies using equation 2.63.

7.2.2 Results & Discussion

Figure 7.1 shows the distribution of the jump energies as a function of the jump distance for the 1K runs. As it can be seen there exist three clearly distinct groups of transitions, the one with the shortest jump distance having a very low activation energy, the middle one having the highest transition energy and the furthest one an intermediate jump energy. In the following the three classes will be named class 1, class 2 and class 3 ordered according to increasing jump distance.

The transition rates calculated using these activation free energies at 1800K are 2eV$\rightarrow 9.44\cdot 10^{7}\mathrm{s}^{-1}$, 5.4eV$\rightarrow 2.86\cdot 10^{-2}\mathrm{s}^{-1}$ and 7.7eV$\rightarrow 1.04\cdot 10^{-8}\mathrm{s}^{-1}$. This shows that there are 9 orders of magnitude in the frequency of occurrence of the lowest energy jump and the middle energy jump.

It is therefore very interesting to see which are these low energy jumps. Figure 7.2 shows these jumps displayed by bonds in the α-alumina structure.

As it can be seen the low energy jumps are always in triangles which are located in the midplane between two aluminum ions. This is what Jacobs and Kotomin [7] call the “small triangles”. These jumps do thus not form a continuous diffusion path but

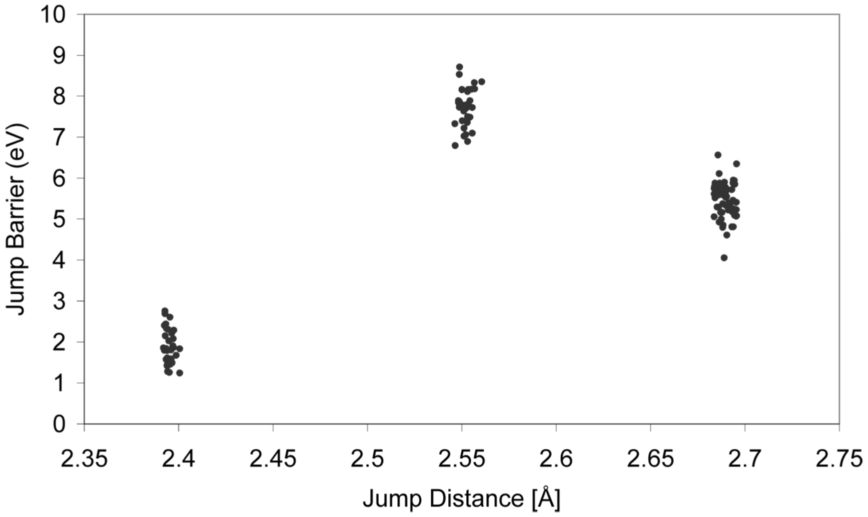

Figure 7.1: Distribution of jump energies as a function of the jump distance determined using Metadynamics at 1K.

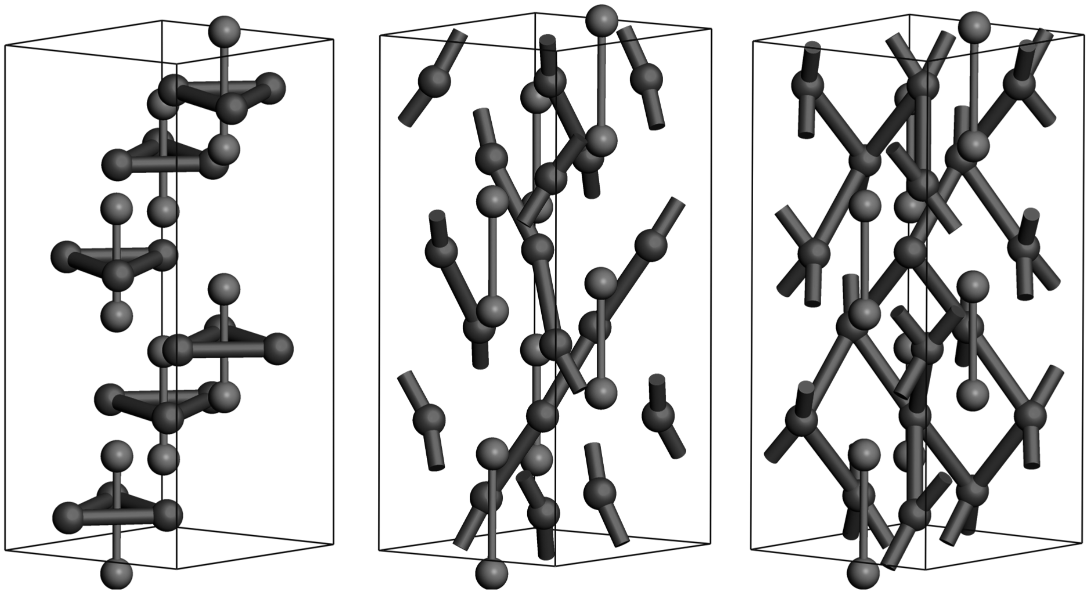

(a) (b) (c)

Figure 7.2: The distribution of jumps in the alumina unitcell: (a) class 1 jumps, (b) class 2 jumps and (c) class 3 jumps. The red bonds designate the jumps of the specific class and the thin green bonds link the aluminum ions on top and bottom of the small triangles. Color code: light=aluminum, dark=oxygen

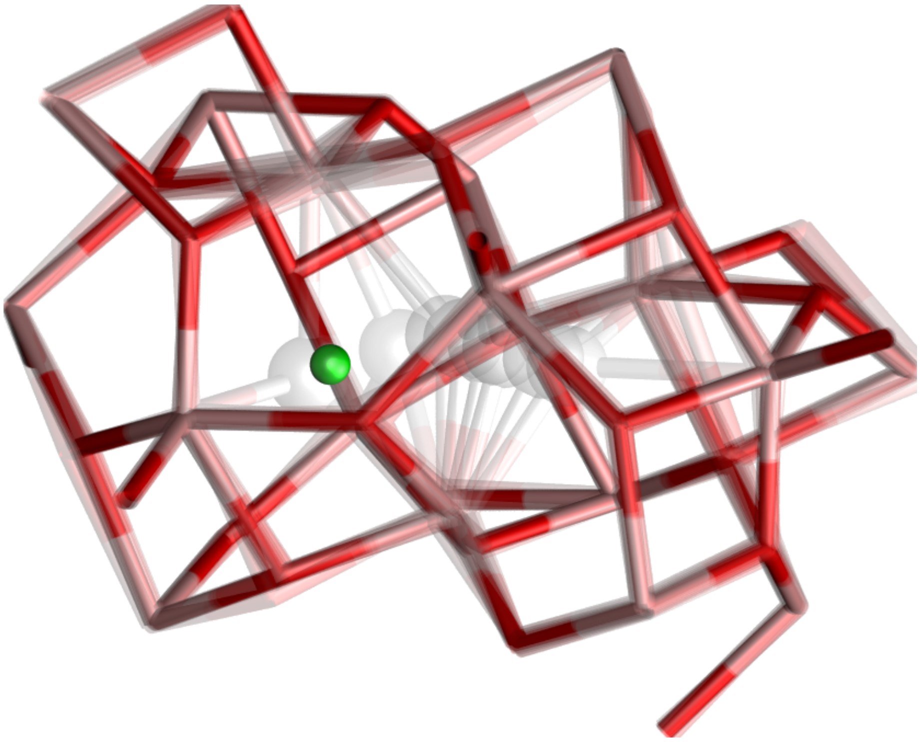

Figure 7.3: Transition path of a class 3 jump. The small green sphere denotes the vacancy position and the semi-transparent sequence of gray spheres shows the jumping oxygen moving from right to left, finally ending up on the vacancy position. The curved shape of the path as well as breaking and reforming the tetrahedral coordination can be seen. Color code: Red=oxygen, rose=aluminum.

will only allow the oxygen ions to jump within the triangles, which is as a matter of fact observed if this data is input into a kinetic Monte Carlo code. The second class of jumps forms 3 non-interconnected diffusion pipes running in the crystallographic c direction, whereas the third class of jumps form a network of jumps, which are interconnected along the c-axis but not in the a-b plane.

This jump energy distribution in the alumina unit-cell is a very interesting result since it shows for the first time that the low energy jumps which were reported so far do not form a continuous network and will thus not allow macroscopic diffusion. This possibility was mentioned by Harding [10] and is proved correct by the present results. The present work does not show as many different classes of jumps as reported by Jacobs and Kotomin [7], which suggest that their linear path method oversimplified the real transition paths and sampled incorrect saddle points. This is supported by the fact that the transition paths found in the present work (figure 7.3) are in fact curved, the oxygen ions "swinging" around the closest aluminum ions.

Figure 7.4 shows the same jump energy distribution for the remaining calculated temperatures. The lowest energy for each jump across all samples performed at

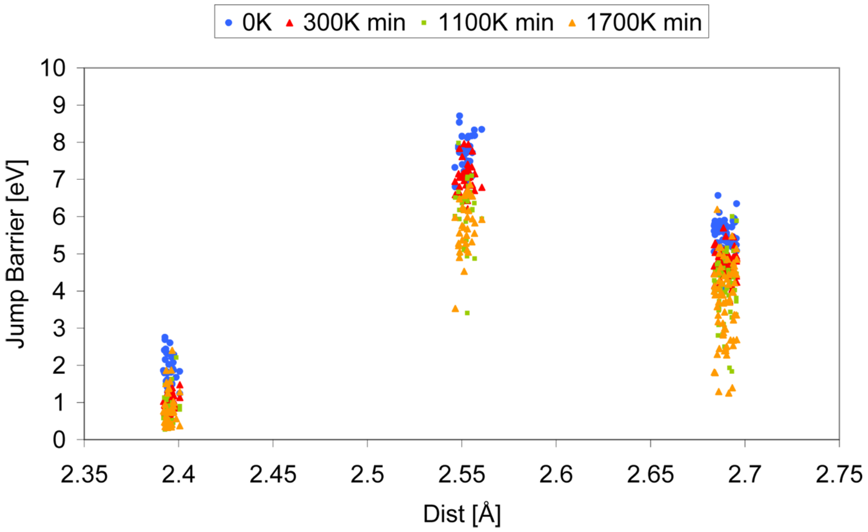

Figure 7.4: Jump free energies as a function of the distance for 1K, 300K, 1100K and 1700K.

a certain temperature is given. Since in nature the transition will occur at the lowest possible energy, this seems a reasonable choice. It can be seen that the mean energy and spread of the three jump classes changes but the three classes still remain distinct.

By plotting the average of the jump energies in each jump energy "cloud" as a function of temperature, the plot shown in figure 7.5 is obtained. It can be seen that the evolution is not strictly linear and the enthalpy and entropy component of the free energy of migration can not easily be extracted using a linear trendline ($\Delta G(T) = \Delta H + T\Delta S$). It was therefore decided to use these jump energy functions in the kinetic Monte Carlo code and to apply linear interpolation between the points as well as an linear extrapolation at higher temperatures

7.3 Kinetic Monte Carlo

7.3.1 Approach

The kinetic Monte Carlo code reads the oxygen sublattice within the first unit-cell of the 1K equilibrated alumina 6x6x2 supercell, which corresponds to 18 atoms. The code then places the vacancy randomly on one of these 18 atoms. In order to have a good memory and speed efficiency, the code does not treat a large but finite volume by replicating this cell but shifts the unit-cell around in space together with its 26 periodic neighbors. This reduces the number of atoms to be searched for possible

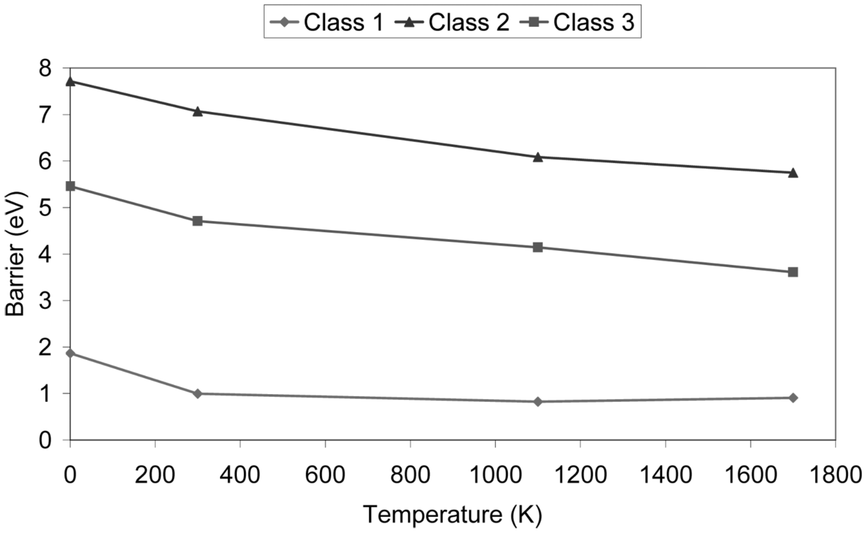

Figure 7.5: Jump energies for the three classes as a function of temperature.

transitions as well as the memory requirements.

Within this block of 27 unit-cells (3x3x3 supercell) the code then locates the atoms which are closer to the vacancy than the nearest neighbor cutoff and associates them with a jump class via their jump distance. As it was seen above, the jump rate of the lowest energy jump is by orders of magnitude higher than the ones of other classes. Further this class does not contribute to the macroscopic diffusion in the material. By carrying out a kinetic Monte Carlo simulation in the usual way one would observe around 10^7 low energy jumps within the triangles followed by one jump contributing to macroscopic diffusion. This method would thus take a lot of iterations to get a statistically reliable diffusion coefficient. For the present case it was thus decided to adapt the method as outlined in the following paragraph.

The jump classes are further split into “normal” jumps and jumps which are of low energy and thus high rate, the second type being called “random transitions”. In the present case class 1 would be of the random transition type, the other two being normal. These random transitions are then implicitly included in the kMC scheme as follows. Each time the code creates its list of possible transitions it will carry out one normal transition which would be followed by a high number of random transitions. As these random transitions will not affect the macroscopic diffusion but only change the position of the vacancy in the triangle, they will have the same effect as placing the vacancy randomly on one of the the sites in the triangle. The simulation time has however to be advanced by the time this number of low energy transitions would have taken. This timestep is determined as given by equation 7.1 where r_{random} is the rate of the random transition, Δt_{last} is the timestep by which the last normal transition advanced the simulation time and u is a random number between 0 and 1.

$$\Delta t = r_{\text{random}} \Delta t_{\text{last}} \cdot \frac{1}{r_{\text{random}}} \cdot 2u = \Delta t_{\text{last}} \cdot 2u \tag{7.1}$$

The first term in this equation expresses the number of random transitions occurring during the last normal time step, which is multiplied by the second term representing the timestep associated with a single random transition. This number is then multiplied with $2u$, which represents a random number centered on 1, in order to account for the stochastic nature of the process. It can be seen that the rate of the random transition does not appear if the equation is simplified and that conceptually this approach is equivalent to placing the vacancy randomly somewhere in it's triangle and advancing the time by a random step centered on the timestep of the last normal transition.

The mean squared displacement (MSD) has been calculated according to equation 7.2.

$$\text{MSD}(t) = \left\langle |\vec{r_i}(t) - \vec{r_i}(t_0)|^2 \right\rangle \tag{7.2}$$

Where $\vec{r_i}(t)$ is the vacancy position in run i at the time t, $\vec{r_i}(t_0)$ is the starting position of the vacancy and $\langle \ldots \rangle$ denotes an average over all runs. The MSD is then related to the diffusion coefficient via Einsteins formula (equation 7.3).

$$D = \lim_{t \to \infty} \frac{\text{MSD}(t)}{6t} \tag{7.3}$$

This shows that the MSD should ideally follow a straight line if the number of repetitions per temperature of the kinetic Monte Carlo simulations is sufficient to give a statistical average, the slope of the line being the diffusion coefficient multiplied by 6.

kMC simulations were carried out in a way that each trajectory consisted of at least 500'000 “normal” jumps and in order to obtain a good average a total of 100 runs per temperature were carried out. The temperatures simulated were 1400K, 1600K, 1800K, 2000K and 2200K.

7.3.2 Results & Discussion

Figure 7.6 shows a typical trajectory of a vacancy at 1800K projected in each of the three cartesian planes with figure 7.7 showing the square displacement of the same

Table 7.1: Jump proportions observed at different temperatures. Only the proportion of the minority normal class (class 2) is given, the rest being class 3 jumps.

Temperature [K]	**Class 2 Jumps** [%]
1400K	$3.079 \cdot 10^{-6}$
1600K	$1.418 \cdot 10^{-5}$
1800K	$3.906 \cdot 10^{-5}$
2000K	$1.336 \cdot 10^{-4}$
2200K	$2.832 \cdot 10^{-4}$

run together with the mean square displacement produced by the 100 runs carried out at this temperature.

It can be seen from this figure that the method places no restriction on the diffusion, the vacancy being able to move randomly in all directions. It can also be seen from the square displacement plot that this particular run has at the beginning a tendency to be below average with respect to the square displacement, whereas towards the end it overestimates the average. This behavior requires the summing over many runs to get a reliable average. This is shown in figure 7.8 where the (mean) square displacements for 1, 10, 100 and 1000 runs respectively carried out at 1600K is shown. It can be seen that whereas the single runs shows large fluctuations, these become smaller and smaller with increasing number of runs to form an almost straight line at 1000 runs. In order to have a reasonable computational time 100 runs were chosen as the give a relatively smooth and straight curve, the slope of a linear fit to which will represent the 1000 runs curve very well.

In figure 7.9 the mean square displacement slopes are reported for the five temperatures. Because of the large dispersion in time and to keep the lines linear a log-log scale is used. The curves are reasonably linear for all temperatures and well approximated by the linear trendlines, the fitting coefficient being larger than 0.99 in all cases.

It will be interesting to know which jumps are activated. In order to do this, the number of jumps of each normal class was tracked during the simulations and their percentage is given in table 7.1. It can be seen that the number of high energy class 2 jumps continuously increases with increasing temperature, however remaining negligible even at high temperatures.

Diffusion coefficients are usually plotted on a logarithmic scale as a function of the inverse temperature. This is shown in figure 7.10a. In order to compare the values found here to existing experimental values, they have been added on top of a

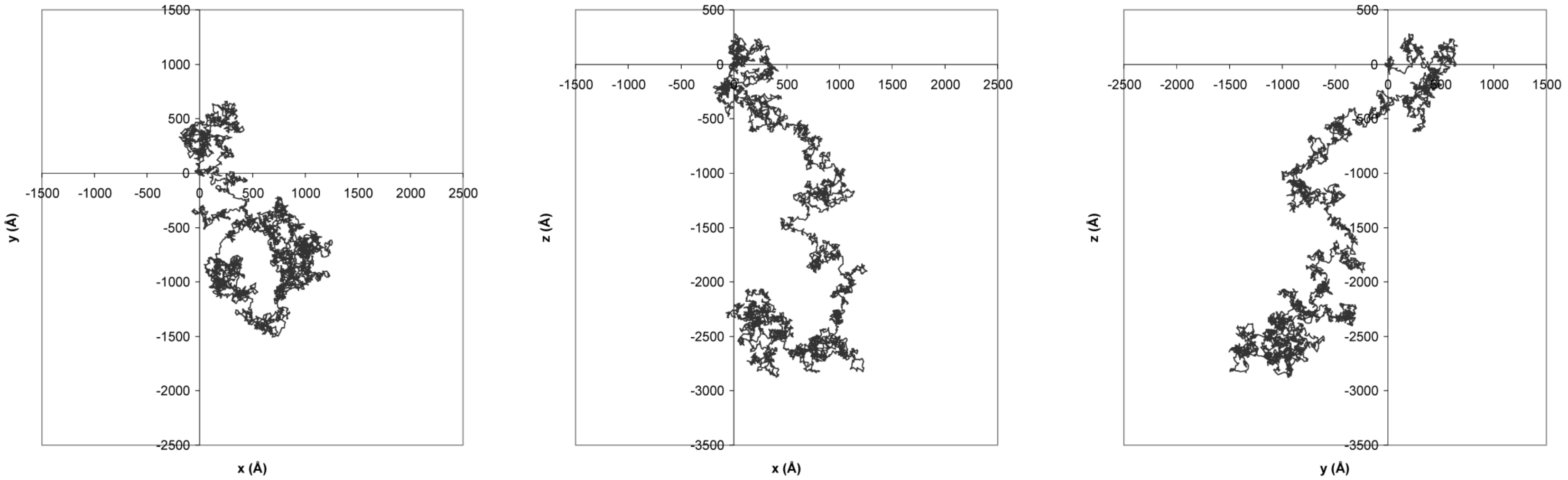

(a) (b) (c)

Figure 7.6: The trajectories of the vacancy of a typical run at 1800K projected in (a) the xy = ac plane, (b) the xz plane and (c) the yz plane.

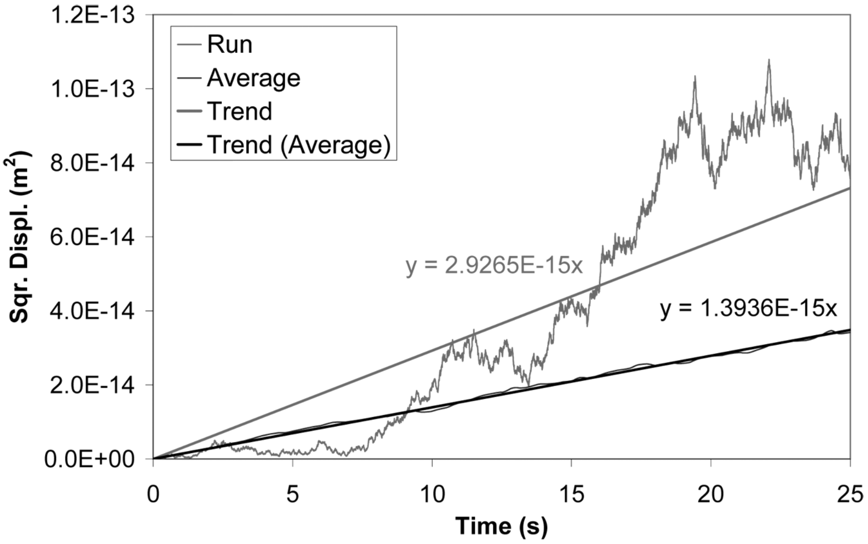

Figure 7.7: Square displacement of the diffusion run shown in figure 7.6 as well as the mean square displacement resulting from all 100 runs carried out at this temperature.

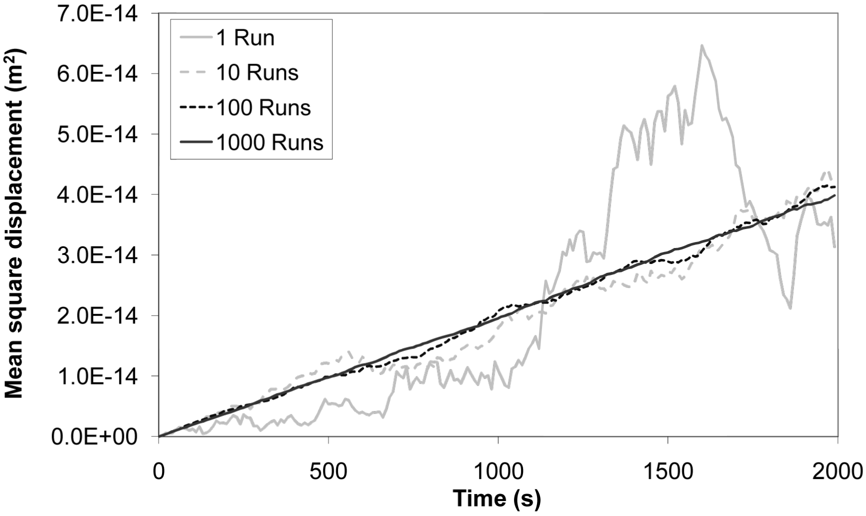

Figure 7.8: Comparison of the mean square displacements produced by 1, 10, 100 and 1000 runs.

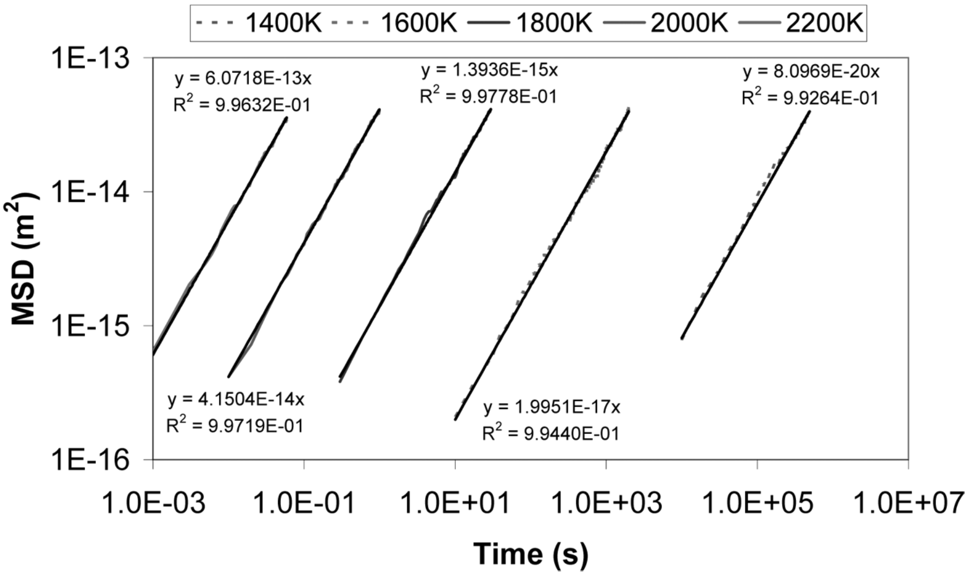

Figure 7.9: The mean square displacement as a function of time. The slope of the curves is the diffusion coefficient multiplied by 6.

graph extracted from [2] and presented in figure 7.10b.

It can be seen that the calculated values lie on an almost straight line, thus confirming that the number of runs used to calculate the MSD is sufficient to get a good average. By comparing the value to experimentally determined ones it can be seen that the diffusion coefficient is slightly larger than the experimental values, the slope as a function of T however being reproduced very well. This may be due to the fact that the jump energies are extrapolated beyond 1700K using the slope between 1100K and 1700K. As it can be seen in figure 7.5 the dominating class 3 jumps show a large slope in this region, which may lead to an underestimation of the jump energies. It would thus be interesting to confirm these energies by calculating jump energies at a higher temperature (2200K) in order to avoid the extrapolation. It could also be argued that taking the lowest value for the energy barrier leads to too low activation energies. In fact averaging over all calculated barriers will lead to a slightly higher energy barrier around 5.3eV for the dominant normal jump class. Ideally a large number of jumps would be fitted to a normal distribution and the actual jump energy extracted using the expectation value and an offset determined by the variance and a random multiplying factor. Alternatively one point within the jump cloud could be chosen at random. Another reason for the higher diffusion coefficient calculated here may be that in experiment diffusion modifying defects such as impurities are present.

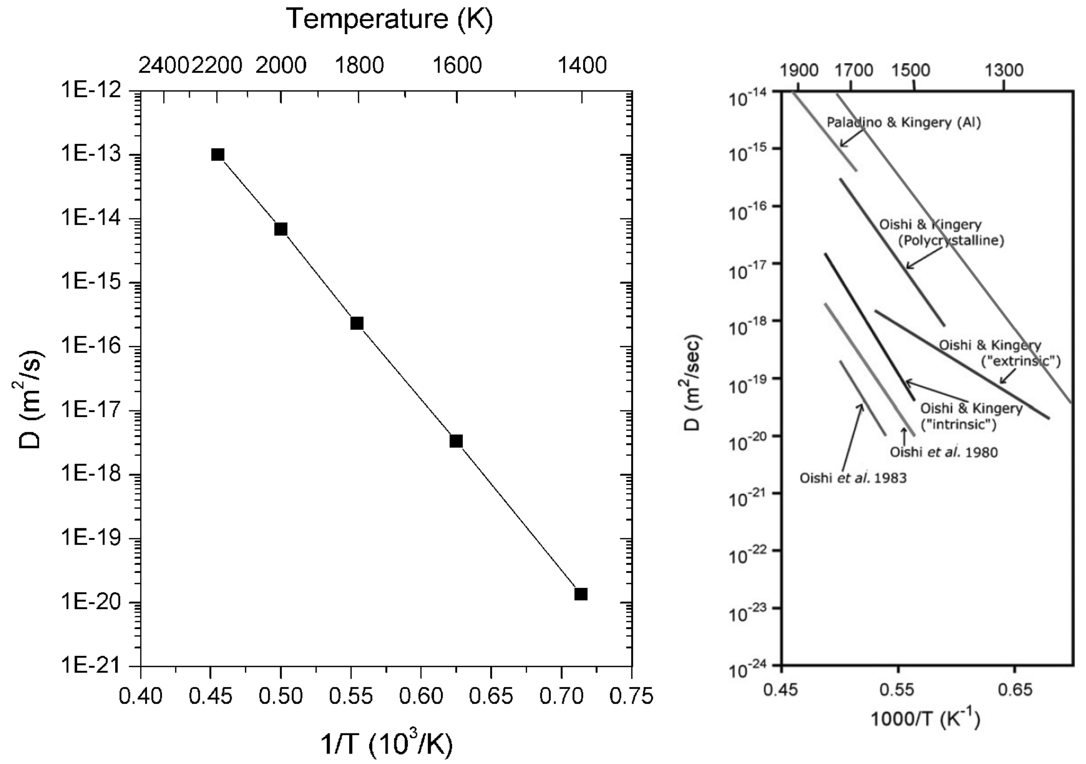

(a) (b)

Figure 7.10: Calculated diffusion coefficient as a function of the inverse temperature. The temperature is shown on the top scale: (a) The present results alone and (b) superposed (topmost line) on experimental results compiled by Heuer [2]. Please note that the temperature scale on top of the second figure is in °C and not Kelvin. Second figure adapted from [2]

7.4 Conclusions

The combination of Metadynamics and kinetic Monte Carlo was found to be a very powerful tool for the investigation of diffusive phenomena in ceramics. The Metadynamics technique was able to show the curved nature of diffusion paths in alumina and to evaluate the free energy barrier associated with these jumps. The Metadynamics calculation of the energy barriers was found to be computationally expensive part even if a more rigorous sampling at more temperatures with more runs per temperature would have been beneficial in order to get an even better statistical average. The relatively small hill height used here results in a slow filling of the free energy surface and thus a more precise determination of the activation energy, which is a clear advantage over ab-initio methods.

The jump map determined using the Metadynamics method is a lot simpler than the one previously published [7] being only dependent on the distance between the jumping atom and the vacancy. The jumps of the lowest energy (1eV) form a triangle between two aluminum ions and do not form a continuous diffusion network, the diffusion thus being limited by the next class of jumps, which has an energy barrier of around 4eV.

The Metadynamics derived data has been used in kinetic Monte Carlo simulations in order to calculate the macroscopic diffusion coefficient. The quality of the simulations was very good and the resulting diffusion coefficient is close to the experimentally observed one. A reason for the slight deviation may be the extrapolation used, an underestimation by including only the average jump energy or the absolutely defect free crystal used here whereas in experiments a certain degree of diffusion modifying defects will always be present.

The reasonably good match with the experimental data confirms however that the diffusion controlling mechanism has been correctly determined using the Metadynamics approach. The present chapter thus gives an answer to Heuer's questions 1 and 3 mentioned in the introduction. The buffering is due to the presence of high energy jumps which separate the low energy jumps reported before and the measured activation energies may not be too high since the rate determining transition found in this work has an activation energy very similar to the one determined experimentally.

The method developed here is very generic and can be applied to grain boundaries as well as doped environments be it in the bulk or at grain boundaries. It should be suited in order to find answers to Heuer's questions 5-8. In order to do this the diffusion by oxygen interstitials and aluminum ions should be looked at as well as diffusion in grain boundaries, where the Metadynamics method should have advantages over the previously used “drag” technique [20] as more complex transition paths can be realized. Another interesting aspect will be the interaction of dopants with the diffusing species. Also diffusion of dopant species will be an interesting topic to study as it will give kinetic informations on the segregation phenomena calculated in the previous chapters as well as being able to better understand the solute drag effect resulting from different ions.

Bibliography

[1] A. H. Heuer and K. P. D. Lagerlof. Oxygen self-diffusion in corundum (α-Al_2O_3): a conundrum. *Philosophical Magazine Letters*, 79(8):619–627, 1999.

[2] A. H. Heuer. Oxygen and aluminum diffusion in α-Al_2O_3: How much do we really understand? *Journal of the European Ceramic Society*, 28(7):1495–1507, 2008.

[3] C. R. A. Catlow, R. James, W. C. Mackrodt, and R. F. Stewart. Defect energetics in α-Al_2O_3 and rutile TiO_2. *Physical Review B*, 25(2):1006–1026, 1982.

[4] R. W. Grimes. Solution of MgO, CaO, and TiO_2, in α-Al_2O_3. *Journal of the American Ceramic Society*, 77(2):378–384, 1994.

[5] K. J. W. Atkinson, R. W. Grimes, M. R. Levy, Z. L. Coull, and T. English. Accommodation of impurities in α-Al_2O_3, α-Cr_2O_3 and α-Fe_2O_3. *Journal of the European Ceramic Society*, 23(16):3059–3070, 2003.

[6] R. James. PhD thesis, University of London, 1978.

[7] P. W. M. Jacobs and E. A. Kotomin. Defect energies for pure corundum and for corundum doped with transition-metal ions. *Philosophical Magazine A - Physics of Condensed Matter Structure Defects and Mechanical Properties*, 68(4):695–709, 1993.

[8] P. W. M. Jacobs and E. A. Kotomin. Theory of point-defects and vacancy motion in corundum crystals. *Journal of Solid State Chemistry*, 106(1):27–34, 1993.

[9] J. H. Harding and D. J. Harris. Simulation of grain-boundary diffusion in ceramics by kinetic Monte Carlo. *Physical Review B*, 6309(9):–, 2001.

[10] J. H. Harding, K. J. W. Atkinson, and R. W. Grimes. Experiment and theory of diffusion in alumina. *Journal of the American Ceramic Society*, 86(4):554–559, 2003.

[11] R. Krishnamurthy, Y. G. Yoon, D. J. Srolovitz, and R. Car. Oxygen diffusion in yttria-stabilized zirconia: A new simulation model. *Journal of the American Ceramic Society*, 87(10):1821–1830, 2004.

[12] R. Krishnamurthy, D. J. Srolovitz, K. N. Kudin, and R. Car. Effects of lanthanide dopants on oxygen diffusion in yttria-stabilized zirconia. *Journal of the American Ceramic Society*, 88(8):2143–2151, 2005.

[13] A. Laio and M. Parrinello. Escaping free-energy minima. *Proceedings of the National Academy of Sciences of the United States of America*, 99(20):12562–12566, 2002.

[14] M. Iannuzzi, A. Laio, and M. Parrinello. Efficient exploration of reactive potential energy surfaces using Car-Parrinello molecular dynamics. *Physical Review Letters*, 90(23):238302, 2003.

[15] A. Laio, A. Rodriguez-Fortea, F. L. Gervasio, M. Ceccarelli, and M. Parrinello. Assessing the accuracy of metadynamics. *Journal of Physical Chemistry B*, 109(14):6714–6721, 2005.

[16] W. Smith and T. R. Forester. DL_POLY 2.0: A general-purpose parallel molecular dynamics simulation package. *Journal of Molecular Graphics*, 14(3):136–141, 1996.

[17] R. S. Liu, W. C. Shi, Y. C. Cheng, and C. Y. Huang. Crystal structures and peculiar magnetic properties of α- and γ-Al_2O_3 powders. *Modern Physics Letters B*, 11(26-27):1169–1174, 1997.

[18] G. V. Lewis and C. R. A. Catlow. Potential models for ionic oxides. *Journal of Physics C-Solid State Physics*, 18(6):1149–1161, 1985.

[19] K. Jug, N. N. Nair, and T. Bredow. Molecular dynamics investigation of oxygen vacancy diffusion in rutile. *Physical Chemistry Chemical Physics*, 7(13):2616–2621, 2005.

[20] J. H. Harding. Short-circuit diffusion in ceramics. *Interface Science*, 11(1):81–90, 2003.

Chapter 8

Summary, Outlook & General Conclusions

In this thesis a number of key steps in the production cycle of a ceramic have been looked at by simulation techniques at the atomic scale. Since the the majority of unresolved problems in ceramic production are linked to interfacial phenomena, the focus of this work has been put on the investigation of the role of surfaces and grain boundaries in the production of ceramics.

In the following the main results will be resumed for each of the investigated topics, followed by a general conclusion on the prospects of atomistic simulation techniques applied to problems in powder and ceramic technology. Possible ways to carry on this work will be given along with the summary of the results and then resumed at the end of this chapter.

8.1 Growth modification

During the synthesis of a ceramic powder, which is often carried out by precipitation from aequous solution, the morphology of the powder particles can be influenced in a variety of ways, one being the use of extrinsic species, the so called additives. In the present work, the attachment of small phosphonic acid molecules as well as larger polycarboxylic acid and polyamino acid oligomeres have been looked at for two crystal systems (hematite α-Fe_2O_3 and calcite $CaCO_3$) where they are experimentally relevant. The methods used where energy minimization for the hematite and molecular dynamics for the calcite simulations.

It was found that phosphonic acid molecules can bind with very different energies to different hematite surfaces. As a result the equilibrium morphology will be modified with changes in the fraction of appearance of certain surfaces as well as the appearance of new surfaces. The simulations were made in vacuum but the effect of water was implicitly included via the solvation energies of the additives as well as species removed from the surface during the anticipated condensation reaction leading to binding on hydroxylated surfaces. The predicted changes were also seen in experiment thus validating the approach and making it useful as a predictive tool when looking at the binding of other phosphonate additives. A main drawback of the energy minimization technique used lies in the number of configurations which has to be sampled in order to find the global minimum energy configuration with a reasonably high probability. This is due to the fact that the rotation and translation the additive may undergo during the simulation are rather limited. Nevertheless this approach presents most likely the computationally cheapest way of studying additive interaction with surfaces. In the future it would be interesting to carry out these calculations for different phosphonic acids in order to make use of this predictive tool.

For calcite modified by polycarboxylic acids and polyamino acids molecular dynamics simulations were undertaken in presence of water, which requires a lot more computational resources than the previous method. It takes however the effect of water explicitly into account and also samples the configurational space much better. Whereas for a small molecule such a phosphonic acid the possible configurations at the surface may still be guessed, this is clearly impossible for a polymer, which thus requires a more sophisticated approach. The simulations were undertaken in order to elucidate experimentally observed differences between the two additives polyacrylic acid (PAA) and polyaspartic acid (p-ASP), p-ASP resulting in nanostructured calcite particles with a lot higher specific surface area than obtained in presence of PAA, which means that the primary particles formed in presence of p-ASP have to be smaller than those with PAA.

The results showed that the differences between the two additives start with the way they complex ions in solution. Whereas PAA forms extremely stable inner sphere complexes with calcium ions, p-ASP only form the weaker outer-sphere complexes, which continuously break and reform even on the simulation time-scale, whereas PAA complexes remain stable once formed for the whole simulation. Also PAA seems to complex more calcium ions with the same number of functional groups than p-ASP. This results in a decrease of the supersaturation of $CaCO_3$ in presence of PAA and thus modifies nucleation and growth kinetics. This is supported by the fact that PAA can at high concentration completely inhibit calcite nucleation. A reason for the lower complexation strength of p-ASP may be it's lower flexibility due to the high double-bond character of it's peptide backbone, the molecule thus not being able to complex calcium ions with two functional groups as easily as PAA. An additive forming complexes in solution will be less reactive with surfaces, which will perhaps result in less PAA actually binding to the surfaces when calcium ions are in a high enough concentration in solution.

The next difference between the two additives is their approach speed to the surface, which is higher for p-ASP than for PAA. This may be linked two two aspects, the first being the more linear shape of p-ASP, which has thus a smaller hydrodynamic radius than the more spherical shaped PAA. It was found that the additives do not bind to flat surfaces but even desorb when put onto such a surface. Binding was only observed to charged defects, surface steps being the likeliest site for surface vacancies and thus charges during growth. The increased attractive strength of p-ASP with charged surface steps due to the interaction of the quite negatively charged nitrogen atoms of the backbone with calcium ions at the surface as well as the van der Waals interaction of the nitrogen with the carbonate oxygen atoms may be another explanation. This higher attractive strength is confirmed by the binding energies, where p-ASP shows a highly negative value whereas PAA has a positive binding energy. The fact that PAA still binds suggests that binding is entropy driven for this additive. This is supported by calorimetric measurements of carboxylic acids adsorbing on calcite which report an endothermic adsorption behavior. The faster and stronger binding of p-ASP to the surface will result in a more marked growth modifying effect due to it's longer residence time on steps, which are often the main growth sites on a surface. Due to this and the fact that more p-ASP than PAA is expected to actually bind to surfaces as mentioned above, p-ASP will result in a higher growth inhibiting effect thus resulting in smaller particles.

A last possible reason for the differences is due to the adsorption conformation on the surface, which was found to be different for the two additives but also to depend on the presence of counterions in solution. This is an aspect which still has to be studied in more detail. The present results however suggest that p-ASP forms a more long ranged steric barrier than PAA which can adsorb flat on a step. This would prevent particle agglomeration in presence of p-ASP but not PAA, being a possible explanation why p-ASP can better conserve the nanostructure of the particles.

All three mentioned effects can explain the higher growth inhibiting effect of p-ASP and in practice most likely all will play a role.

In the future it would be interesting to look at the adsorption on different steps (obtuse vs. acute) and on different surfaces. This could then explain possible changes in the particle morphology.

8.2 Segregation

Surface and mirror twin grain boundary segregation in α-Al_2O_3 and ZnO ceramics was investigated using energy minimization. The pristine interfaces were constructed looking at their interfacial energy and predicting the equilibrium shape of powder particles resulting from the surface energies. Dopant ions were then inserted at increasing concentrations and the enthalpies of segregation and solution calculated as well as the change in interfacial energy going along with the incorporation of the dopant ions. Microstructural models were constructed based on the atomistic simulation results in order to predict segregation in powders and microstructures as a function of particle and grain size.

It was found that oversized ions (Mg, Y, La, Gd and Yb) strongly segregate to surfaces and grain boundaries in alumina, decreasing the interfacial energies for all dopants, the magnitude of this decrease however varying a lot from interface to interface and being less marked for grain boundaries than for surfaces. The latter is not surprising as surfaces can accommodate a higher amount of dopants due to the more flexible atomic environment. The variability for different interfaces can be explained with their atomic structures. On interfaces showing faceting dopant incorporation is a lot easier as the interface structure is more open for accommodation of misfit strains, whereas on highly symmetric interfaces, the whole surface has to undergo significant changes.

Comparing magnesium and yttrium doping it was seen that both dopants on average decrease surface energies quite significantly, however leading to a slight inhomogenization, which is more severe for yttrium than for magnesium. This effect can also be seen on the equilibrium shapes, where less faces appear due to the significant lowering of certain surface energies. Yttrium doping result in a less regular shape than magnesium doping, which can be attributed to the inhomogenizing effect. For the case of grain boundaries yttrium and magnesium were found to not be accommodated by all interfaces, the dopant ions being located preferentially at high energy interfaces, the interfacial energy of which is reduced as a result. The lowering of the average interfacial energy is considerable and higher for magnesium than for yttrium. This could be one aspect of the grain growth suppressing effect of magnesium in alumina amongst others such as the solute drag effect. Magnesium also has the effect of making the interfacial energies more homogeneous resulting in more equiaxed grains, which is also an experimentally observed difference between undoped or yttrium doped alumina and magnesium doped alumina.

Using the microstructural model it was found that the percentage of magnesium at surfaces and grain boundaries will be higher than yttrium for all grain sizes. The amount of dopants at interfaces increases markedly with decreasing grain size. Further the amount of dopants at grain boundaries is a lot smaller than at surfaces, which means when surfaces join to form a grain boundary, dopants have to move away from the grain boundary if second phase precipitation is to be avoided. This is even more marked if grain growth occurs during sintering, which will further decrease the amount of dopants able to be accommodated at grain boundaries.

The dissolution behavior of La, Gd and Yb was found to be governed by the relative stability of their minerals rather than by the misfit strain, the large lanthanum in general showing the highest tendency to be incorporated in surfaces at concentrations of up to $10\mathrm{nm}^{-2}$. Interestingly these rare earth ions can not be dissolved in most grain boundaries, only the very open structured grain boundaries showing an exothermic dissolution of dopants up to maximally $5\mathrm{nm}^{-2}$. The segregation behavior however was found to be governed by the misfit strain resulting in the large lanthanum ion to segregate most markedly from the bulk to interfaces, resulting in an enriched layer of about 7Å for surfaces and 4Å on both sided of grain boundaries. These rare earth ions will thus show a high tendency to be located at interfaces due to their very exothermal segregation behavior, while dissolution of the dopants is favorable only for a small number of the grain boundaries calculated in this study. This will result in a high risk of precipitate formation when dopants are found at grain boundaries but would be more thermodynamically stable in their mineral form. Secondary minima observed on the dissolution curves can be linked to the formation of second phase like regions, which would facilitate nucleation of these phases. The interfacial energy has further been shown not to present an energy barrier for nucleation. It has to be noted that the boundaries which did not accommodate dopants were of the more special type with low Σ values, whereas the ones where dopants can be accommodated are more general. The risk of precipitate formation is thus linked to the proportion of special boundaries in a microstructure. The current findings are however supported by the experimentally observed severe precipitate formation in Gd doped alumina.

Segregation of cobalt and manganese dopants in zinc oxide was found to be highly different for the two grain boundaries investigated, the highly regular one not showing any trend for segregation whereas the more open structured one showed a slight trend for segregation for both dopants, the slightly larger manganese segregating stronger than cobalt. Cobalt and manganese are normally assumed to be in solid solution in the bulk acting as electron donors. If they segregate to some of the grain boundaries this role may become less marked in nano ZnO ceramics where the number of grain boundaries and thus segregated dopants is higher than for common micron sized ceramics.

For aluminum segregation in zinc oxide two defect cluster types with either oxygen interstitial or zinc vacancy creation have been investigated. It was found that the oxygen interstitial type segregated to both grain boundaries calculated, whereas the zinc vacancy type segregates only to the open structured boundary. The oxygen interstitial cluster has a lower formation energy and is thus expected to be the dominant species, which would predict an aluminum accumulation at grain boundaries. Since oxygen excess at grain boundaries is experimentally known but not the presence of aluminum, the dissociation of the defect cluster during segregation should be investigated. It would also be interesting to calculate the segregation of bismuth, which together with excess oxygen at the grain boundaries is thought to be responsible for the varistor effect in these ceramics.

ZnO is a material which presents due to its semiconducting nature certain problems in empirical potential calculations since charge transfers and conversion to metallic character of the zinc ions can not be taken into account. Also potentials for many important dopants do not exist. It was shown that these potentials may be obtained by fitting to potential energy surfaces calculated by ab-initio methods. Another and probably more promising approach would be to carry out all calculations using these first-principle methods, which would furthermore give access to the electronic structure being responsible for the varistor effect and allow for charge transfers within the structure.

8.3 Ceramic Nd:YAG lasers

As for rare earth ions in alumina, neodymium was also found to strongly segregate to interfaces in YAG when substituting the slightly smaller yttrium ion. For the calculated surfaces and grain boundaries it was found that in general high energy interfaces can accommodate a higher number of dopants at concentrations around 3nm^{-2}. Some of the low energy interfaces can accommodate almost as many dopant ions whereas others do not accommodate any. There was no clear correlation between the density of an interface and the amount of dopants that can be accommodated, which makes it likely that the bonding environment plays an important role. It was found that segregation can result in very high local dopant concentrations at interfaces. This dopant accumulation can render the dopant inactive with respect to lasing due to a reduction of their fluorescence lifetime by the so called concentration quenching effect.

The estimated effect of segregation on laser performance was evaluated by using a microstructural model to predict the percentage of dopant ions at grain boundaries as a function of particle or grain size. Different models describing powder and microstructures at different degrees of equilibrium are used, which can be linked to typical Nd:YAG synthesis routes. It is shown that at smaller grain sizes more dopants are segregated to grain boundaries. These models further show that in order to obtain the highest number of active luminescent dopant ions conventional sintering is desirable to achieve a high degree of equilibrium. During sintering dopant transport from the grain boundary under formation has to take place which makes it necessary to take care about second phase precipitation. The proportion of actively lasing dopant could be kept at a high level by increasing the dopant concentration, however the accumulated dopants at the grain boundary can also lead to a scattering of light and thus loss of transparency due to the slightly different local refractive index. It was shown using mean field and discrete dipole approximation models that this scattering is important when a percolated grain boundary phase exists. This scattering is less important for small grain sizes, which is why it could be interesting to decrease the grain size.

These results suggest that the laser power decreases with decreasing grain size due to the higher number of quenched dopants, whereas the loss in transparency is more important for large grain sizes. This would mean that an optimal grain size exists, where the luminescence and transparency of the material lead to an optimal laser performance.

For the present case the estimation of the refractive index with increasing Nd concentration as well as the quenching have been estimated from empirical calculations as well as experimental results. It would be desirable in the future to do these calculations using ab-inito methods as both phenomena are governed by electron excitations, which can be taken into account by these methods.

8.4 Diffusion

There still exists a number of problems linked with diffusion in alumina, most of them related to the self-diffusion of oxygen ions. A combination of the two simulation techniques Metadynamics and kinetic Monte Carlo was used in order to investigate the self-diffusion of oxygen in α-alumina. Metadynamics were used to extract the activation free energies of diffusive jumps whereas the kinetic Monte Carlo method was used to calculate the macroscopic diffusion coefficient from these activation energies.

It was found that previous simulation work may have resulted in a too complicated picture of oxygen diffusion due to the use of linear diffusion paths. In the present work it was found that diffusion of oxygen vacancies in alumina is possible by three distinct classes of jumps to nearest neighbors. The low energy jumps of the order of 1eV which were often reported do in fact not form a continuous diffusive network, diffusion being controlled by the rate of the next highest jump barriers.

The standard kinetic Monte Carlo method was adapted in order to take into account that around 10^7 of these low energy jumps take place before each jump actually contributing to diffusion. The obtained diffusion coefficient is slightly higher than those determined experimentally. This may be related to an extrapolation of the jump energies to higher temperatures, taking into account only the average jump energy or the complete absence of diffusion hindering defects in the simulations, whereas these will always be present in experiments. It will be interesting to include all calculated jump barriers in the kinetic Monte Carlo calculations either by choosing one at random or by using a fitted continuous function.

Nevertheless the present method gave answers to two of the remaining questions of oxygen self-diffusion in alumina, which is limited by high energy jumps of the order of 5eV. This same reason is also responsible for the buffering effect since the vacancies spend the majority of their time with diffusive jumps, which do not actually contribute to macroscopic diffusion as they allow only transitions within groups of three oxygen ions in a closed triangular geometry.

The method is however generic and may in the future be applied to investigate many of the remaining questions linked to whether oxygen diffusion occurs by a vacancy or interstitial mechanism, the diffusion of aluminum as well as dopant cations and diffusion of all these species in grain boundaries.

8.5 General Conclusions

During this thesis atomistic simulation techniques have been applied to interfacial phenomena in ceramic materials. Surface adsorption of organic species was investigated as well as the segregation of dopant species to surfaces and grain boundaries.

Finally oxygen self diffusion in alumina was looked at using a novel simulation approach.

While atomistic simulations give access to precise atom geometries and energy related information, for applications in powder and ceramic technology this information is often too localized and larger scale models have to be used to gain insights useful to understand experiment. Throughout this thesis these large scale models have been used, be it Wulff's equilibrium shape construction for morphology prediction, it's extension to non-equilibrium powders and microstructures as well as the optical models and the kinetic Monte Carlo method. All these methods allow a gain in understanding of a system at the experimental scale by using information derived at the atomic scale.

In a general philosophy atomistic simulations should be used in order to understand experiments and to help design next key experiments, which will allow faster scientific progress than by a traditional trial and error approach. The empirical methods used throughout this thesis still have a merit compared to the more modern first principle methods since they allow the calculation of a higher number of cases required to approximate the experimental scale. Even if the energies and atomic positions may not be as precise as they could be with higher level methods, the results will allow a better understanding of experimental processes and to adapt experiments in a knowledge based fashion, which will save resources in the development of novel materials for high-tech applications.

It has however been seen throughout this thesis that there are fields in which the use of ab-initio methods is indispensable, these being the cases where electron related phenomena occur such as during covalent bond formation, when dopants change the band structure of the material as well as optical phenomena. The combination of all methods in a so called "multi-scale-modeling" approach, where information impossible to obtain at one scale are obtained from simulations at the next smaller scale, will thus allow the investigation of many aspects of problems encountered in powder and ceramic technology and even more generally in material science.

8.6 Outlook

This thesis has lead to many new ground-breaking insights into problems related to all investigated aspects. However there is still a lot of work to be done in order to completely resolve these problems. These have been mentioned above during the summary and will be resumed here.

It will be interesting to use the simulation approach developed for phosphonate modified hematite as a predictive tool for other phosphonate additives, trying to tune the morphology into particular shapes, which could then be experimentally verified.

In the case of calcite further work looking at more types of surfaces and the effect of the surface charge and counterion concentration on the adsorption behavior should be looked at. For p-ASP the differences between the α and the β form would be an interesting study as well as the adsorption of co-polymers based on both forms at the experimental 30/70 proportion. Another aspect could be the conformation of the adsorbed layer as a function of the polymer length as well as additives with slightly different functional groups. Also by gradually reducing the gap between the slabs the steric repulsion potential could be calculated and the phenomenological models replaced with atomistically derived data.

For segregation calculation in ZnO more defect potentials should be fitted using ab-initio methods or the calculations carried out directly using the higher level methods in order to account for electron transfer as well as looking at the change of the band structure in doped grain boundaries. It will also be necessary to increase the number of grain boundaries looked at and to include reconstructed boundaries in order to get a good idea of segregation towards many different types of boundaries.

The luminescence of Nd ions in YAG as a function of their concentration as well as the refractive index change of YAG grain boundaries with segregated dopants will be very interesting problems to be looked at using first principle methods. This will allow to better understand the nature of concentration quenching and the limiting concentration of dopants.

Finally the diffusion calculations should be extended to oxygen interstitials, aluminum vacancies and interstitials as well as dopant cations both in the bulk and grain boundaries. Also other models for the jump barrier energy distribution should be looked at. This will answer many of the remaining questions linked to diffusion in alumina.

Curriculum Vitae

Ulrich Johannes Aschauer

Date of Birth: May 22nd 1979
Nationality: German

Education

2005-2008	PhD "Atomistic Simulation in Powder Technology: from growth control and dispersion stabilization to segregation at doped interfaces" at the Powder Technology Laboratory of EPFL in Lausanne, Switzerland.
1999-2005	Bachelor and Masters Degrees in Material Science and Engineering at EPFL in Lausanne, Switzerland **Master Thesis** "Growth Control of Hematite using Phosphonate Additives: a combined Laboratory and Atomistic Simulation Study" undertaken in the Group of Julian Gale at the Curtin University of Technology in Perth (Australia). **Semester Projects** 2004: "Geometric simulation of Dendrite Growth in Al-Zn-Si coatings" 2003: "Optimization of the deposition of pyroelectric PMN ceramic thin films on sapphire substrates" 2003: "Precipitation hardening of Al-4.5%Cu metallic foams" 2001: "Novel luminescent materials based on Strontium Silicates"
1998	Swiss Federal High School Diploma Mathematical/Scientific Type in Laufen, Switzerland.

Work experience

Course Teaching

2006-2008: Two-hour segment “Introduction to atomistic simulation in Powder Technology” in the Powder Technology master level course

Lab work

2005-2008: “Sintering and microstructures”
2005-2008: “Particle size measurement”
2003: “Jominy test” as a student assistant
2002: “Metallography” as a student assistant

Supervision or co-supervision(*) of Master projects

2008: “Effect of Doping and Grain Boundary Composition on Polycrystalline Alumina for Transparent Ceramic Applications”, Michael Stuer
2007: “Atomistic Simulation of Lanthanide (La, Gd, Yb) Dopant Segregation in α-Al_2O_3”, Yann Aman
2006: “Precipitation of Nanostructured Calcium Carbonate, Effect of additive type” (*), Johannes Ebert
2006: “Atomistic Simulation Study of Yttrium and Magnesium at α-Alumina Interfaces”, Sandra Galmarini

Supervision or co-supervision(*) of Semester projects

2008: “Monte Carlo Methods for the determination of the entropic contribution in interfacial segregation of dopants in alumina”, Sandra Galmarini
2007: “Simulating segregation of iso- and aliovalent dopants in zinc oxide”, Christian Monachon
2006: “Precipitation of Nanostructured Calcite: Effect of additive weight” (*), Simone Pedrazzini
2006: “Synthesis of Cerium Oxide Nanoparticles”, Julie O’Keane
2006: “Transparent polycrystalline Alumina”, Fréderic de Borman
2006: “Evaluation of production methods for transparent polycrystalline alumina” (*), Caroline Rodriguez, Nadège Caillet-Bois, Lucien Germond, John Peter Loughman
2006: “Development of luminescent materials”, Pierre Burdet

Doctoral school courses

2008: Introduction to parallel programming with MPI
2007: Tutoring Skills
2006: High performance computing methods
2006: Quantum Simulation of Solids and Liquids (CECAM, Lyon/France)
2006: Modeling as a complementary technique to experiments
2005: Experimental optimization of materials

Internships

2003: “Development of hard non-stick coatings” at Hort Coating Center in Sierre/Switzerland

1998: “Computer modeling of geologic structures” at Cantonal Geologic Service, Basel/Switzerland

Programming

2001-2006: Development and deployment multiple websites and web-based database membership tracking and billing systems for sport-clubs in Switzerland

2006: Development of a web-based Chemical Product Database and Device Reservation tool for the Powder Technology Laboratory at EPFL Lausanne/Switzerland

2000-2001: Development of a Driver/GUI for geologic feature acquisition from maps using a digitizing table

Miscellaneous

2004: Responsible for Human Resources at the Swiss-Ski-Festival in Basel (100th anniversary celebration of the Swiss Ski Federation). Planning, organization and scheduling of about 500 voluntaries.

1998: Work as a cycle messenger in Basel/Switzerland

Skills

Languages

German (mother tongue), English (fluent), French (fluent)

Computers Skills

Good knowledge of Linux, Mac and Windows systems

14 years of programming experience in BASIC, Pascal, C, C++, Objective-C/C++, Perl, PHP, FORTRAN 77/90 and Java

Interests

Long distance running, Mountain biking, Skiing, Video Game Programming

Publication List

Articles

1. Aschauer U., Bowen P., Parker S.C., “Atomistic Simulation of Surface Segregation in Nd:YAG”, Journal of the American Ceramic Society, 89(12), 2006
2. Aschauer U., Jones F., Richmond W.R., Bowen P., Rohl A.L., Parkinson G.M., Hofmann H., “Growth modification of hematite by phosphonate additives”, Journal of Crystal Growth, 310(3), 2008
3. Aschauer U., Bowen P., Parker S.C., “Surface and mirror twin grain boundary segregation in Nd:YAG: An atomistic simulation study”, Journal of the American Ceramic Society, 91(8), 2008
4. Galmarini S., Aschauer U., Bowen P, Parker S.C., “Atomistic Simulation of Y doped α-Alumina Interfaces”, Journal of the American Ceramic Society, in Press
5. Aschauer U., Ebert S., Pedrazzini S., Bowen P., “Growth Modification of Calcite using Carboxylic Acids”, in preparation
6. Aschauer U., Spagnoli D., Bowen P., Parker S.C., “Molecular Dynamics Simulation of PAA and p-ASP Adsorption on Calcite”, in preparation
7. Aschauer U., Aman Y., Bowen P., “Dopant Segregation in Lanthanide doped α-Alumina Ceramics: An atomistic modeling study”, in preparation

Conference Talks

1. Aschauer U., Galmarini S., Bowen P, Parker S.C., “Segregation in Y and Mg Doped α-Alumina: New Insights from Atomistic Simulations”, Science et Technologie des Poudres 2007, Albi, France
2. Aschauer U., Ebert J., Peddrazini S., Spagnoli D., Bowen P., Parker S.C., “Atomistic simulation of calcite growth modification by organic additives”, Euromat 2007, Nürnberg, Germany

3. Aschauer U., Bowen P., Parker S.C., “Surface and Grain Boundary Segregation in Nd:YAG”, 3rd Laser Ceramics Symposium, Paris, France

Conference Posters

1. Aschauer U., Jones F., Richmond W., Bowen P., Rohl A.L., Hofmann H., Parkinson G., “Growth Modification of Hematite by Phosponate Molecules”, MM 2006, Perth, Australia
2. Aschauer U., Bowen P., Parker S.C., Hofmann H., “Atomistic Simulation of surface segregation in Nd:YAG”, Swiss Material Science Association Assembly 2006, Colombier, Switzerland

Conference Abstracts / Proceedings

1. Aschauer U., Hockridge J.G., Jones F., Loan M., Parkinson G.M., Richmond W.R., “Morphology Control in the Sythesis of Iron Oxide and Oxyhydroxide Nanoparticles”, International Conference on Nanotechnology 2006, Brisbane, Australia
2. Bowen P., Aschauer U., Galmarini S., Parker S.C., “Grain Growth in Doped Oxide Ceramics: From Nanosized Powders and Atomistic Simulations to Tailored Interfaces”, 10th European Interregional Conference on Ceramics, Swansea, UK
3. Bowen P., O’Keane J., Aschauer U., “Nanostructured Ceria: Sythesis of Rods and Cubes – Towards Tubes?”, Science et Technologie des Poudres 2007, Albi, France
4. Aschauer U., Galmarini S., Bowen P., Parker S.C., “Segregation in Y and Mg Doped α-Alumina: New Insights from Atomistic Simulations”, Science et Technologie des Poudres 2007, Albi, France

Acknowledgments

First of all I'd like to thank Dr. Paul Bowen for accepting me as a PhD student, for his great scientific coaching and stimulating discussions, his constant guidance trough this project and for introducing me to many very interesting researchers.

I'd also like to thank the European sixth Framework Programme Integrated Project "IP Nanoker" (Contract N°NMP3-CT-2005-515784) for funding this work. Amongst the partners in the project a special thank goes to Dr. Carlos Pecharromán for his support and discussions related to light scattering models.

A very special thank goes to Professor Stephen C. Parker of the University of Bath (UK) for his constant availability for all questions related to atomistic simulations. Without his help this work would have been a lot less rich.

I'd also like to thank Prof. Heinrich Hofmann for welcoming me in his group and for providing a very friendly work environment.

A big thanks also goes to all the colleagues from the powder technology laboratory of the EPFL for many nice moments during these years.

I'd like to thank the students I had the pleasure to work with and especially Sandra Galmarini, Yann Aman, Christian Monachon, Johannes Ebert and Simone Pedrazzini whose contributions can be found in this thesis.

I'd further like to thank Dr. Dino Spagnoli for getting me started with the calcite simulations and Prof. Gordon Parkinson, Asoc. Prof. Andrew Rohl, Dr. Franka Jones and Dr. Bill Richmond from the Curtin University in Perth, Australia for their support with the Hematite work.

I'm grateful to Dr. Helmut Cölfen from the Max Planck Institute for Colloids and Interfaces, (Golm, Germany) for insights on the polymer chemistry of the additives used for calcite.

I acknowledge the computer resources provided by EPFL through the mizar cluster and greedy grid as well as those made available to me on the faculty's pleiades cluster and the SGI Altix machine of the material science department.

I'd also like to thank my family for their support and encouragement throughout my life, for having guided my desire to get into computer programming at a young age and for having given me the opportunity to undertake my studies which finally led to this thesis.

And last but not least I'd like to thank Eik Szee for being very understanding during these years and especially during the last months of this work, supporting me in undertaking my thesis despite it being the reason for this awfully long distance and very limited time together.

Appendix A

Fe_2O_3 Potential Parameters

The following gives the complete potential parameters used for the hematite chapter. An electronic version is available as supplementary electronic material to the article published in the Journal of Crystal Growth 310(3), 688-698, (2008). The following file is the potential section of a GULP input file.

Atom types:	
Fe	Hematite iron (core + shell)
O1	Hematite oxygen (core + shell)
O2	Hydroxyl oxygen (core + shell)
H2	Hydroxyl oxygen
O3	Phosphonate functional oxygen
P	Phosphonate functional phosphorous
C1	Phosphonate backbone carbon
N	Phosphonate backbone nitrogen
H1	Phosphonate backbone hydrogen
C2	Phosphonate sidegroup carbon

```
molmec fix

species
Fe    core  -1.76540
Fe    shel   4.76540
O1    core   0.86902
O1    shel  -2.86902
O2    core   0.69187
O2    shel  -2.11787
H2    core   0.42600
O3    core  -1.19300
P     core   2.10500
C1    core  -0.62500
```

```
N         core  -0.35000
H1        core  0.07000
C2        core  0.07000
end

elements
cova        Fe  0.1
ends
nobond           Fe   core            Fe          shel
nobond           O1   core            O1          shel
nobond           O2   core            O2          shel

buck
O1        shel  O1   shel  22764.3000   0.149000    27.879      0.0   12.0
buck
O1        shel   Fe  shel  1102.40000   0.329900     0.000      0.0   12.0
spring
Fe     173.192
spring
O1      26.499

buck inter
O2        shel  O2   shel    22764.30    0.14900     7.840      0.0   12.0
buck
H2        core  O2   shel    109.0888    0.25547     0.000      0.0   12.0
morse intra bond
H2        core  O2   shel      7.0525     2.1986    0.9485   0.0000
spring
O2      40.385

buck
O2        shel   Fe  shel    965.0067    0.32990      0.00      0.0   12.0
buck inter
H2        core  O1   shel    701.0801    0.22278      0.00      0.0   12.0

lennard 12 6 x13
C1        core  C1   core   77689.066  22.932654       0.0     15.0
lennard 12 6 x13
H1        core  C1   core   4895.3078  5.7193170       0.0     15.0
lennard 12 6 x13
C1        core    P  core   142528.86  46.742924       0.0     15.0
lennard 12 6 x13
C1        core    N  core   87418.951  34.993722       0.0     15.0
lennard 12 6 x13
C1        core  O3   core   30331.206  22.281108       0.0     15.0
lennard 12 6 x13
```

```
C2   core C2  core  77689.066  22.932654       0.0   15.0
lennard 12 6 x13
H1   core C2  core  4895.3078  5.7193170       0.0   15.0
lennard 12 6 x13
C2   core  P  core  142528.86  46.742924       0.0   15.0
lennard 12 6 x13
C2   core  N  core  87418.951  34.993722       0.0   15.0
lennard 12 6 x13
C2   core O3  core  30331.206  22.281108       0.0   15.0
lennard 12 6 x13
C1   core C2  core  77689.066  22.932654       0.0   15.0
lennard 12 6 x13
H1   core O3  core  1911.2160  5.5568240       0.0   15.0
lennard 12 6 x13
H1   core  P  core  8980.9628  11.657507       0.0   15.0
lennard 12 6 x13
H1   core  N  core  5508.4028  8.7273010       0.0   15.0
lennard 12 6 x13
H1   core H1  core  308.46089  1.4263760       0.0   15.0
lennard 12 6 x13
O3   core O3  core  11841.847  21.648074       0.0   15.0
lennard 12 6 x13
O3   core  P  core  55645.823  45.414898       0.0   15.0
lennard 12 6 x13
N    core O3  core  34129.927  33.999506       0.0   15.0
lennard 12 6 x13
P    core  P  core  261484.35  95.274665       0.0   15.0
lennard 12 6 x13
N    core  P  core  160379.37  71.326627       0.0   15.0
lennard 12 6 x13
N    core  N  core  98367.421  53.398117       0.0   15.0
harmonic intra bond
C1   core  P  core    21.6186    1.75000  0.000000
harmonic intra bond
O3   core  P  core    41.6577    1.53000  0.000000
harmonic intra bond
H1   core C1  core    29.5611    1.10500  0.000000
harmonic intra bond
H1   core C2  core    29.5611    1.10500  0.000000
harmonic intra bond
C1   core  N  core    30.9481    1.47000  0.000000
harmonic intra bond
C2   core  N  core    30.9481    1.47000  0.000000
harmonic intra bond
C2   core C2  core    28.0075    1.52600  0.000000
three bond intra
```

```
C1     core  H1  core      P        core  3.8186    109.50
three bond intra
C1     core  N   core      P        core  4.3393    109.50
three bond intra
P      core  C1  core      O3       core  9.5466    120.00
three bond intra
P      core  O3  core      O3       core  9.5466    109.50
three bond intra
C1     core  H1  core      N        core  4.9729    109.50
three bond intra
C2     core  H1  core      N        core  4.9729    109.50
three bond intra
N      core  C1  core      C1       core  7.4897    110.25
three bond intra
N      core  C1  core      C2       core  7.4897    110.25
three bond intra
C2     core  C2  core      N        core  4.3393    109.50
three bond intra
C2     core  H1  core      C2       core  3.8533    110.00
three bond intra
C2     core  H1  core      H1       core  3.4281    106.40
three bond intra
C1     core  H1  core      H1       core  3.4281    106.40
torsion bond intra
P      core  C1  core   N core   C1 core  0.005784       3  0.00
torsion bond intra
P      core  C1  core   N core   C2 core  0.005784       3  0.00
torsion bond intra
C1     core  N   core  C1 core   H1 core  0.005784       3  0.00
torsion bond intra
C1     core  N   core  C2 core   H1 core  0.005784       3  0.00
torsion bond intra
C2     core  N   core  C1 core   H1 core  0.005784       3  0.00

lennard 9 6 inter
N      core  Fe  shel    546.00    24.300       0.0    15.0
lennard 9 6 inter
C1     core  Fe  shel    676.00    25.900       0.0    15.0
lennard 9 6 inter
C2     core  Fe  shel    646.00    25.300       0.0    15.0
lennard 9 6 inter
P      core  Fe  shel   2430.00    67.300       0.0    15.0
lennard 9 6 inter
O3     core  Fe  shel    440.00    20.600       0.0    15.0
lennard 9 6 inter
H1     core  Fe  shel     81.30     6.460       0.0    15.0
```

```
lennard 9 6 inter
N       core   O1   shel     858.00     24.800      0.0    15.0
lennard 9 6 inter
C1      core   O1   shel    1010.00     26.400      0.0    15.0
lennard 9 6 inter
C2      core   O1   shel     972.00     25.700      0.0    15.0
lennard 9 6 inter
P       core   O1   shel    3320.00     68.500      0.0    15.0
lennard 9 6 inter
O3      core   O1   shel     705.00     21.000      0.0    15.0
lennard 9 6 inter
H1      core   O1   shel     163.00      6.580      0.0    15.0

lennard 9 6 inter
N       core   O2   shel     871.00     22.400      0.0    15.0
lennard 9 6 inter
C1      core   O2   shel    1020.00     23.800      0.0    15.0
lennard 9 6 inter
C2      core   O2   shel     978.00     23.300      0.0    15.0
lennard 9 6 inter
P       core   O2   shel    3260.00     61.900      0.0    15.0
lennard 9 6 inter
O3      core   O2   shel     718.00     19.000      0.0    15.0
lennard 9 6 inter
H1      core   O2   shel     172.00      5.950      0.0    15.0
lennard 9 6 inter
H2      core    N   core      35.40      1.650      0.0    15.0
lennard 9 6 inter
H2      core   C1   core      44.20      1.760      0.0    15.0
lennard 9 6 inter
H2      core   C2   core      42.20      1.710      0.0    15.0
lennard 9 6 inter
H2      core    P   core     161.00      4.560      0.0    15.0
lennard 9 6 inter
H2      core   O3   core      28.50      1.400      0.0    15.0
lennard 9 6 inter
H1      core   H2   core       5.09      0.438      0.0    15.0
```

Appendix B

$CaCO_3$ Forcefield Parameters

The following gives the complete potential parameters (DL_POLY FIELD files) used for PAA and p-ASP systems simulated the calcite chapter.

PAA

Atom types:	
CA	Calcium ion
C	Carbonate carbon atom
O, O(S)	Carbonate oxygen atoms (core + shell)
T	PAA terminal carbon
X	PAA backbone carbon
C1	PAA carboxy carbon
A	PAA carboxy oxygen
OW, OW(S)	Water oxygen (core + shell)
HW	Water hydrogen

```
calcium + carbonate + PAA + water
UNITS eV
molecules 4
CALCIUM
nummols 180
atoms 1
CA                          40.00        2.00
finish
CARBONATE
nummols 175
atoms 7
C                           12.00      1.1350
O                           15.80      0.5870
O(S)                         0.20     -1.6320
```

```
O                                15.80      0.5870
O(S)                              0.20     -1.6320
O                                15.80      0.5870
O(S)                              0.20     -1.6320
shell 3
           2    3                507.4
           4    5                507.4
           6    7                507.4
bonds 24
mors       1    3                 4.71        1.18       3.80       1.50
mors       1    5                 4.71        1.18       3.80       1.50
mors       1    7                 4.71        1.18       3.80       1.50
coul       1    2                 1.00
coul       1    4                 1.00
coul       1    6                 1.00
coul       1    3                 1.00
coul       1    5                 1.00
coul       1    7                 1.00
coul       2    4                 1.00
coul       2    6                 1.00
coul       4    6                 1.00
coul       3    5                 1.00
coul       3    7                 1.00
coul       5    7                 1.00
coul       2    5                 1.00
coul       2    7                 1.00
coul       4    3                 1.00
coul       4    7                 1.00
coul       6    3                 1.00
coul       6    5                 1.00
buck       3    5              16372.0       0.213       3.47
buck       3    7              16372.0       0.213       3.47
buck       5    7              16372.0       0.213       3.47
angles 3
harm       3    1    5            1.69      120.00
harm       3    1    7            1.69      120.00
harm       5    1    7            1.69      120.00
dihedrals 3
cos        1    3    5    7     0.1129      180.00       2.00
cos        1    5    3    7     0.1129      180.00       2.00
cos        1    7    3    5     0.1129      180.00       2.00
finish
PAA
NUMMOLS 1
ATOMS 50
T                              15.0350       0.000
```

X	14.0270	-0.030
C1	12.0110	0.370
A	15.9999	-0.670
A	15.9999	-0.670
X	14.0270	-0.000
X	14.0270	-0.030
C1	12.0110	0.370
A	15.9999	-0.670
A	15.9999	-0.670
X	14.0270	-0.000
X	14.0270	-0.030
C1	12.0110	0.370
A	15.9999	-0.670
A	15.9999	-0.670
X	14.0270	-0.000
X	14.0270	-0.030
C1	12.0110	0.370
A	15.9999	-0.670
A	15.9999	-0.670
X	14.0270	-0.000
X	14.0270	-0.030
C1	12.0110	0.370
A	15.9999	-0.670
A	15.9999	-0.670
X	14.0270	-0.000
X	14.0270	-0.030
C1	12.0110	0.370
A	15.9999	-0.670
A	15.9999	-0.670
X	14.0270	-0.000
X	14.0270	-0.030
C1	12.0110	0.370
A	15.9999	-0.670
A	15.9999	-0.670
X	14.0270	-0.000
X	14.0270	-0.030
C1	12.0110	0.370
A	15.9999	-0.670
A	15.9999	-0.670
X	14.0270	-0.000
X	14.0270	-0.030
C1	12.0110	0.370
A	15.9999	-0.670
A	15.9999	-0.670
X	14.0270	-0.000
X	14.0270	-0.030

```
C1                  12.0110     0.370
A                   15.9999    -0.670
A                   15.9999    -0.670
CONSTRAINTS 19
1       2            1.530
2       6            1.530
6       7            1.530
7      11            1.530
11     12            1.530
12     16            1.530
16     17            1.530
17     21            1.530
21     22            1.530
22     26            1.530
26     27            1.530
27     31            1.530
31     32            1.530
32     36            1.530
36     37            1.530
37     41            1.530
41     42            1.530
42     46            1.530
46     47            1.530
BONDS 30
harm    3    4      65.0899     1.220
harm    3    5      65.0899     1.220
harm    8    9      65.0899     1.220
harm    8   10      65.0899     1.220
harm   13   14      65.0899     1.220
harm   13   15      65.0899     1.220
harm   18   19      65.0899     1.220
harm   18   20      65.0899     1.220
harm   23   24      65.0899     1.220
harm   23   25      65.0899     1.220
harm   28   29      65.0899     1.220
harm   28   30      65.0899     1.220
harm   33   34      65.0899     1.220
harm   33   35      65.0899     1.220
harm   38   39      65.0899     1.220
harm   38   40      65.0899     1.220
harm   43   44      65.0899     1.220
harm   43   45      65.0899     1.220
harm   48   49      65.0899     1.220
harm   48   50      65.0899     1.220
harm    2    3      27.4385     1.522
harm    7    8      27.4385     1.522
```

```
harm     12  13            27.4384     1.522
harm     17  18            27.4384     1.522
harm     22  23            27.4384     1.522
harm     27  28            27.4384     1.522
harm     32  33            27.4384     1.522
harm     37  38            27.4384     1.522
harm     42  43            27.4384     1.522
harm     47  48            27.4384     1.522
ANGLES 48
harm      4   3   5         4.3395    123.00
harm      9   8  10         4.3395    123.00
harm     14  13  15         4.3395    123.00
harm     19  18  20         4.3395    123.00
harm     24  23  25         4.3395    123.00
harm     29  28  30         4.3395    123.00
harm     34  33  35         4.3395    123.00
harm     39  38  40         4.3395    123.00
harm     44  43  45         4.3395    123.00
harm     49  48  50         4.3395    123.00
harm      4   3   2         6.0755    125.00
harm      9   8   7         6.0755    125.00
harm     14  13  12         6.0755    125.00
harm     19  18  17         6.0755    125.00
harm     24  23  22         6.0755    125.00
harm     29  28  27         6.0755    125.00
harm     34  33  32         6.0755    125.00
harm     39  38  37         6.0755    125.00
harm     44  43  42         6.0755    125.00
harm     49  48  47         6.0755    125.00
harm      2   3   5         6.0755    125.00
harm      7   8  10         6.0755    125.00
harm     12  13  15         6.0755    125.00
harm     17  18  20         6.0755    125.00
harm     22  23  25         6.0755    125.00
harm     27  28  30         6.0755    125.00
harm     32  33  35         6.0755    125.00
harm     37  38  40         6.0755    125.00
harm     42  43  45         6.0755    125.00
harm     47  48  50         6.0755    125.00
harm      1   2   6         5.3894    109.28
harm      2   6   7         5.3894    109.28
harm      6   7  11         5.3894    109.28
harm      7  11  12         5.3894    109.28
harm     11  12  16         5.3894    109.28
harm     12  16  17         5.3894    109.28
harm     16  17  21         5.3894    109.28
```

```
harm     17   21   22          5.3894      109.28
harm     21   22   26          5.3894      109.28
harm     22   26   27          5.3894      109.28
harm     26   27   31          5.3894      109.28
harm     27   31   32          5.3894      109.28
harm     31   32   36          5.3894      109.28
harm     32   36   37          5.3894      109.28
harm     36   37   41          5.3894      109.28
harm     37   41   42          5.3894      109.28
harm     41   42   46          5.3894      109.28
harm     42   46   47          5.3894      109.28
DIHEDRALS 118
cos       1    2    3    4     0.0054      -180.0     6.0     1.0   1.00
cos       1    2    3    5     0.0054      -180.0     6.0     1.0   1.00
cos       6    2    3    4     0.0054      -180.0     6.0     1.0   1.00
cos       6    2    3    5     0.0054      -180.0     6.0     1.0   1.00
cos       2    6    7    8     0.0217         0.0     3.0     1.0   1.00
cos       2    6    7   11     0.0217         0.0     3.0     1.0   1.00
cos       6    7    8    9     0.0054      -180.0     6.0     1.0   1.00
cos       6    7    8   10     0.0054      -180.0     6.0    1.00   1.00
cos      11    7    8    9     0.0054      -180.0     6.0    1.00   1.00
cos      11    7    8   10     0.0054      -180.0     6.0    1.00   1.00
cos       7    8    9    5     0.0217       180.0     2.0    1.00   1.00
cos      10    8    9    5     0.0217       180.0     2.0    1.00   1.00
cos       7   11   12   13     0.0217         0.0     3.0    1.00   1.00
cos       7   11   12   16     0.0217         0.0     3.0    1.00   1.00
cos      11   12   13   14     0.0054      -180.0     6.0    1.00   1.00
cos      11   12   13   15     0.0054      -180.0     6.0    1.00   1.00
cos      16   12   13   14     0.0054      -180.0     6.0    1.00   1.00
cos      16   12   13   15     0.0054      -180.0     6.0    1.00   1.00
cos      12   13   14   10     0.0217       180.0     2.0    1.00   1.00
cos      15   13   14   10     0.0217       180.0     2.0    1.00   1.00
cos      12   16   17   18     0.0217         0.0     3.0    1.00   1.00
cos      12   16   17   21     0.0217         0.0     3.0    1.00   1.00
cos      16   17   18   19     0.0054      -180.0     6.0    1.00   1.00
cos      16   17   18   20     0.0054      -180.0     6.0    1.00   1.00
cos      21   17   18   19     0.0054      -180.0     6.0    1.00   1.00
cos      21   17   18   20     0.0054      -180.0     6.0    1.00   1.00
cos      17   18   19   15     0.0217       180.0     2.0    1.00   1.00
cos      20   18   19   15     0.0217       180.0     2.0    1.00   1.00
cos      17   21   22   23     0.0217         0.0     3.0    1.00   1.00
cos      17   21   22   26     0.0217         0.0     3.0    1.00   1.00
cos      21   22   23   24     0.0054      -180.0     6.0    1.00   1.00
cos      21   22   23   25     0.0054      -180.0     6.0    1.00   1.00
cos      26   22   23   24     0.0054      -180.0     6.0    1.00   1.00
cos      26   22   23   25     0.0054      -180.0     6.0    1.00   1.00
```

cos	22	23	24	20	0.0217	180.0	2.0	1.00	1.00
cos	25	23	24	20	0.0217	180.0	2.0	1.00	1.00
cos	22	26	27	28	0.0217	0.0	3.0	1.00	1.00
cos	22	26	27	31	0.0217	0.0	3.0	1.00	1.00
cos	26	27	28	29	0.0054	-180.0	6.0	1.00	1.00
cos	26	27	28	30	0.0054	-180.0	6.0	1.00	1.00
cos	31	27	28	29	0.0054	-180.0	6.0	1.00	1.00
cos	31	27	28	30	0.0054	-180.0	6.0	1.00	1.00
cos	27	28	29	25	0.0217	180.0	2.0	1.00	1.00
cos	30	28	29	25	0.0217	180.0	2.0	1.00	1.00
cos	27	31	32	33	0.0217	0.0	3.0	1.00	1.00
cos	27	31	32	36	0.0217	0.0	3.0	1.00	1.00
cos	31	32	33	34	0.0054	-180.0	6.0	1.00	1.00
cos	31	32	33	35	0.0054	-180.0	6.0	1.00	1.00
cos	36	32	33	34	0.0054	-180.0	6.0	1.00	1.00
cos	36	32	33	35	0.0054	-180.0	6.0	1.00	1.00
cos	32	33	34	30	0.0217	180.0	2.0	1.00	1.00
cos	35	33	34	30	0.0217	180.0	2.0	1.00	1.00
cos	32	36	37	38	0.0217	0.0	3.0	1.00	1.00
cos	32	36	37	41	0.0217	0.0	3.0	1.00	1.00
cos	36	37	38	39	0.0054	-180.0	6.0	1.00	1.00
cos	36	37	38	40	0.0054	-180.0	6.0	1.00	1.00
cos	41	37	38	39	0.0054	-180.0	6.0	1.00	1.00
cos	41	37	38	40	0.0054	-180.0	6.0	1.00	1.00
cos	37	38	39	35	0.0217	180.0	2.0	1.00	1.00
cos	40	38	39	35	0.0217	180.0	2.0	1.00	1.00
cos	37	41	42	43	0.0217	0.0	3.0	1.00	1.00
cos	37	41	42	46	0.0217	0.0	3.0	1.00	1.00
cos	41	42	43	44	0.0054	-180.0	6.0	1.00	1.00
cos	41	42	43	45	0.0054	-180.0	6.0	1.00	1.00
cos	46	42	43	44	0.0054	-180.0	6.0	1.00	1.00
cos	46	42	43	45	0.0054	-180.0	6.0	1.00	1.00
cos	42	43	44	40	0.0217	180.0	2.0	1.00	1.00
cos	45	43	44	40	0.0217	180.0	2.0	1.00	1.00
cos	42	46	47	48	0.0434	0.0	3.0	1.00	1.00
cos	46	47	48	49	0.0217	-180.0	6.0	1.00	1.00
cos	46	47	48	50	0.0217	-180.0	6.0	1.00	1.00
cos	47	48	49	45	0.0217	180.0	2.0	1.00	1.00
cos	50	48	49	45	0.0217	180.0	2.0	1.00	1.00
cos	2	3	5	9	0.0217	180.0	2.0	1.00	1.00
cos	4	3	5	9	0.0217	180.0	2.0	1.00	1.00
cos	7	8	10	14	0.0217	180.0	2.0	1.00	1.00
cos	9	8	10	14	0.0217	180.0	2.0	1.00	1.00
cos	12	13	15	19	0.0217	180.0	2.0	1.00	1.00
cos	14	13	15	19	0.0217	180.0	2.0	1.00	1.00
cos	17	18	20	24	0.0217	180.0	2.0	1.00	1.00

```
cos    19  18  20  24    0.0217     180.0    2.0    1.00  1.00
cos    22  23  25  29    0.0217     180.0    2.0    1.00  1.00
cos    24  23  25  29    0.0217     180.0    2.0    1.00  1.00
cos    27  28  30  34    0.0217     180.0    2.0    1.00  1.00
cos    29  28  30  34    0.0217     180.0    2.0    1.00  1.00
cos    32  33  35  39    0.0217     180.0    2.0    1.00  1.00
cos    34  33  35  39    0.0217     180.0    2.0    1.00  1.00
cos    37  38  40  44    0.0217     180.0    2.0    1.00  1.00
cos    39  38  40  44    0.0217     180.0    2.0    1.00  1.00
cos    42  43  45  49    0.0217     180.0    2.0    1.00  1.00
cos    44  43  45  49    0.0217     180.0    2.0    1.00  1.00
cos     1   2   6   7    0.0217       0.0    3.0    1.00  1.00
cos     3   2   6   7    0.0217       0.0    3.0    1.00  1.00
cos     3   5   9   8    0.2168     180.0    2.0    1.00  1.00
cos     6   7  11  12    0.0217       0.0    3.0    1.00  1.00
cos     8   7  11  12    0.0217       0.0    3.0    1.00  1.00
cos     8  10  14  13    0.2168     180.0    2.0    1.00  1.00
cos    11  12  16  17    0.0217       0.0    3.0    1.00  1.00
cos    13  12  16  17    0.0217       0.0    3.0    1.00  1.00
cos    13  15  19  18    0.2168     180.0    2.0    1.00  1.00
cos    16  17  21  22    0.0217       0.0    3.0    1.00  1.00
cos    18  17  21  22    0.0217       0.0    3.0    1.00  1.00
cos    18  20  24  23    0.2168     180.0    2.0    1.00  1.00
cos    21  22  26  27    0.0217       0.0    3.0    1.00  1.00
cos    23  22  26  27    0.0217       0.0    3.0    1.00  1.00
cos    23  25  29  28    0.2168     180.0    2.0    1.00  1.00
cos    26  27  31  32    0.0217       0.0    3.0    1.00  1.00
cos    28  27  31  32    0.0217       0.0    3.0    1.00  1.00
cos    28  30  34  33    0.2168     180.0    2.0    1.00  1.00
cos    31  32  36  37    0.0217       0.0    3.0    1.00  1.00
cos    33  32  36  37    0.0217       0.0    3.0    1.00  1.00
cos    33  35  39  38    0.2168     180.0    2.0    1.00  1.00
cos    36  37  41  42    0.0217       0.0    3.0    1.00  1.00
cos    38  37  41  42    0.0217       0.0    3.0    1.00  1.00
cos    38  40  44  43    0.2168     180.0    2.0    1.00  1.00
cos    41  42  46  47    0.0217       0.0    3.0    1.00  1.00
cos    43  42  46  47    0.0217       0.0    3.0    1.00  1.00
cos    43  45  49  48    0.2168     180.0    2.0    1.00  1.00
INVERSIONS 10
plan    3   2   4   5    1.7346       0.0
plan    8   7   9  10    1.7346       0.0
plan   13  12  14  15    1.7346       0.0
plan   18  17  19  20    1.7346       0.0
plan   23  22  24  25    1.7346       0.0
plan   28  27  29  30    1.7346       0.0
plan   33  32  34  35    1.7346       0.0
```

```
plan     38     37     39     40          1.7346          0.0
plan     43     42     44     45          1.7346          0.0
plan     48     47     49     50          1.7346          0.0
finish
WATER
nummols 1410
atoms 4
OW                                       15.8000       1.2500
OW(S)                                     0.2000      -2.0500
HW                                        1.0080       0.4000
HW                                        1.0080       0.4000
shell 1
          1      2                      209.4496
bonds 8
mors      2      3                        6.2037       0.9237    2.2200
mors      2      4                        6.2037       0.9237    2.2200
mors      3      4                        0.0000       1.5000    2.8405
coul      2      3                           0.5
coul      2      4                           0.5
coul      3      4                           0.5
coul      1      3                           1.0
coul      1      4                           1.0
angles 1
harm      3      2      4                4.19978   108.693195
finish
vdw 30
CA       O(S)        buck                 1550.0       0.2970         0.0
CA       OW(S)       buck                 1186.6       0.2970         0.0
CA       C1          lj                   0.0040       2.9998
CA       A           buck               815.8069       0.2970         0.0
C        OW(S)       buck                  435.0       0.3400
O(S)     O(S)        buck                16372.0       0.2130        3.47
O(S)     OW(S)       buck                12533.6       0.2130       12.09
O(S)     HW          hbnd                   26.0       1.8000
O(S)     C1          lj                   0.0040       3.2963
O(S)     A           buck              9557.0586       0.2130        7.47
OW(S)    OW(S)       12-6               39344.98        42.15
OW(S)    HW          nm                   0.0556            9           6   1.8171
OW(S)    T           lj                   0.0057       3.4760
OW(S)    X           lj                  0.00567       3.4760
OW(S)    C1          lj                   0.0040       3.2963
OW(S)    A           lj                   0.0052       3.0290
HW       A           lj                   0.0032       1.7145
HW       C1          lj                   0.0025       1.9818
HW       X           lj                   0.0035       2.1615
HW       T           lj                   0.0036       2.0700
```

```
T      T      lj          0.0066      3.7400
T      X      lj          0.0064      3.8230
T      A      lj          0.0059      3.3845
T      C1     lj          0.0050      3.6518
X      X      lj          0.0062      3.9230
X      A      lj          0.0057      3.4760
X      C1     lj          0.0043      3.7433
C1     C1     lj          0.0030      3.5636
C1     A      lj          0.0040      3.2963
A      A      lj          0.0052      3.0290
close
```

p-ASP

Atom types:	
CA	Calcium ion
C	Carbonate carbon atom
O, O(S)	Carbonate oxygen atoms (core + shell)
N	p-ASP backbone nitrogen
Y	p-ASP backbone carbon
X	p-ASP carboxy sidechain carbon
C1	p-ASP carboxy carbon
A	p-ASP carboxy oxygen
B	p-ASP sidechain oxygen
TY	p-ASP terminal carbon
OW, OW(S)	Water oxygen (core + shell)
HW	Water hydrogen

```
calcium + carbonate + p-ASP + water
UNITS eV
molecules 4
CALCIUM
nummols 180
atoms 1
CA                            40.0000      2.0000
finish
CARBONATE
nummols 175
atoms 7
C                             12.0000      1.1350
O                             15.8000      0.5870
O(S)                           0.2000     -1.6320
O                             15.8000      0.5870
O(S)                           0.2000     -1.6320
O                             15.8000      0.5870
```

```
O(S)                             0.2000      -1.6320
shell 3
         2    3                507.4000
         4    5                507.4000
         6    7                507.4000
bonds 24
mors     1    3                  4.7100       1.1800    3.80    1.50
mors     1    5                  4.7100       1.1800    3.80    1.50
mors     1    7                  4.7100       1.1800    3.80    1.50
coul     1    2                  1.0000
coul     1    4                  1.0000
coul     1    6                  1.0000
coul     1    3                  1.0000
coul     1    5                  1.0000
coul     1    7                  1.0000
coul     2    4                  1.0000
coul     2    6                  1.0000
coul     4    6                  1.0000
coul     3    5                  1.0000
coul     3    7                  1.0000
coul     5    7                  1.0000
coul     2    5                  1.0000
coul     2    7                  1.0000
coul     4    3                  1.0000
coul     4    7                  1.0000
coul     6    3                  1.0000
coul     6    5                  1.0000
buck     3    5              16372.0000       0.2130    3.47
buck     3    7              16372.0000       0.2130    3.47
buck     5    7              16372.0000       0.2130    3.47
angles 3
harm     3    1    5             1.6900     120.0000
harm     3    1    7             1.6900     120.0000
harm     5    1    7             1.6900     120.0000
dihedrals 3
cos      1    3    5    7        0.1129     180.0000    2.00
cos      1    5    3    7        0.1129     180.0000    2.00
cos      1    7    3    5        0.1129     180.0000    2.00
finish
PASPA
NUMMOLS 1
ATOMS 73
N                               15.0000      -0.1700
Y                               13.0000       0.2263
C1                              12.0000       0.4000
A                               15.9994      -0.6700
```

A	15.9994	-0.6700
X	14.0000	0.0000
C1	12.0000	0.4000
A	15.9994	-0.6700
A	15.9994	-0.6700
N	15.0000	-0.1700
Y	13.0000	0.2263
C1	12.0000	0.4000
B	15.9994	-0.5200
X	14.0000	0.0000
C1	12.0000	0.4000
A	15.9994	-0.6700
A	15.9994	-0.6700
N	15.0000	-0.1700
Y	13.0000	0.2263
C1	12.0000	0.4000
B	15.9994	-0.5200
X	14.0000	0.0000
C1	12.0000	0.4000
A	15.9994	-0.6700
A	15.9994	-0.6700
N	15.0000	-0.1700
Y	13.0000	0.2263
C1	12.0000	0.4000
B	15.9994	-0.5200
X	14.0000	0.0000
C1	12.0000	0.4000
A	15.9994	-0.6700
A	15.9994	-0.6700
N	15.0000	-0.1700
Y	13.0000	0.2263
C1	12.0000	0.4000
B	15.9994	-0.5200
X	14.0000	0.0000
C1	12.0000	0.4000
A	15.9994	-0.6700
A	15.9994	-0.6700
N	15.0000	-0.1700
Y	13.0000	0.2263
C1	12.0000	0.4000
B	15.9994	-0.5200
X	14.0000	0.0000
C1	12.0000	0.4000
A	15.9994	-0.6700
A	15.9994	-0.6700
N	15.0000	-0.1700

```
Y                          13.0000   0.2263
C1                         12.0000   0.4000
B                          15.9994  -0.5200
X                          14.0000   0.0000
C1                         12.0000   0.4000
A                          15.9994  -0.6700
A                          15.9994  -0.6700
N                          15.0000  -0.1700
Y                          13.0000   0.2263
C1                         12.0000   0.4000
B                          15.9994  -0.5200
X                          14.0000   0.0000
C1                         12.0000   0.4000
A                          15.9994  -0.6700
A                          15.9994  -0.6700
N                          15.0000  -0.1700
TY                         15.0350   0.0800
C1                         12.0000   0.4000
B                          15.9994  -0.5200
X                          14.0000   0.0000
C1                         12.0000   0.4000
A                          15.9994  -0.6700
A                          15.9994  -0.6700
BONDS 72
harm     1   2             30.3623   1.4620   0.00
harm     2   3             30.3623   1.4300   0.00
harm     3   4             45.5435   1.2200   0.00
harm     6   7             30.3623   1.4300   0.00
harm     7   8             45.5435   1.2200   0.00
harm    10  11             30.3623   1.4620   0.00
harm    11  12             30.3623   1.5300   0.00
harm    12  13             30.3623   1.3200   0.00
harm    14  15             30.3623   1.4300   0.00
harm    15  16             45.5435   1.2200   0.00
harm    18  19             30.3623   1.4620   0.00
harm    19  20             30.3623   1.5300   0.00
harm    20  21             30.3623   1.3200   0.00
harm    22  23             30.3623   1.4300   0.00
harm    23  24             45.5435   1.2200   0.00
harm    26  27             30.3623   1.4620   0.00
harm    27  28             30.3623   1.5300   0.00
harm    28  29             30.3623   1.3200   0.00
harm    30  31             30.3623   1.4300   0.00
harm    31  32             45.5435   1.2200   0.00
harm    34  35             30.3623   1.4620   0.00
harm    35  36             30.3623   1.5300   0.00
```

harm	36	37	30.3623	1.3200	0.00
harm	38	39	30.3623	1.4300	0.00
harm	39	40	45.5435	1.2200	0.00
harm	42	43	30.3623	1.4620	0.00
harm	43	44	30.3623	1.5300	0.00
harm	44	45	30.3623	1.3200	0.00
harm	46	47	30.3623	1.4300	0.00
harm	47	48	45.5435	1.2200	0.00
harm	50	51	30.3623	1.4620	0.00
harm	51	52	30.3623	1.5300	0.00
harm	52	53	30.3623	1.3200	0.00
harm	54	55	30.3623	1.4300	0.00
harm	55	56	45.5435	1.2200	0.00
harm	58	59	30.3623	1.4620	0.00
harm	59	60	30.3623	1.5300	0.00
harm	60	61	30.3623	1.3200	0.00
harm	62	63	30.3623	1.4300	0.00
harm	63	64	45.5435	1.2200	0.00
harm	66	67	30.3623	1.4620	0.00
harm	67	68	30.3623	1.5300	0.00
harm	68	69	30.3623	1.3200	0.00
harm	70	71	30.3623	1.4300	0.00
harm	71	72	45.5435	1.2200	0.00
harm	3	5	45.5435	1.2200	0.00
harm	7	9	45.5435	1.2200	0.00
harm	15	17	45.5435	1.2200	0.00
harm	23	25	45.5435	1.2200	0.00
harm	31	33	45.5435	1.2200	0.00
harm	39	41	45.5435	1.2200	0.00
harm	47	49	45.5435	1.2200	0.00
harm	55	57	45.5435	1.2200	0.00
harm	63	65	45.5435	1.2200	0.00
harm	71	73	45.5435	1.2200	0.00
harm	11	14	30.3623	1.5300	0.00
harm	19	22	30.3623	1.5300	0.00
harm	27	30	30.3623	1.5300	0.00
harm	35	38	30.3623	1.5300	0.00
harm	43	46	30.3623	1.5300	0.00
harm	51	54	30.3623	1.5300	0.00
harm	59	62	30.3623	1.5300	0.00
harm	67	70	30.3623	1.5300	0.00
harm	2	6	30.3623	1.5300	0.00
harm	10	20	30.3623	1.4620	0.00
harm	18	28	30.3623	1.4620	0.00
harm	26	36	30.3623	1.4620	0.00
harm	34	44	30.3623	1.4620	0.00

```
harm    42  52           30.3623     1.4620    0.00
harm    50  60           30.3623     1.4620    0.00
harm    58  68           30.3623     1.4620    0.00
harm     1  12           30.3623     1.4620    0.00
ANGLES 98
hcos     2   1  12        4.7279   106.7000    0.00
hcos     1   2   3        4.8796   109.4710    0.00
hcos     1   2   6        4.8796   109.4710    0.00
hcos     3   2   6        4.8796   109.4710    0.00
hcos     2   3   4        5.7833   120.0000    0.00
hcos     2   3   5        5.7833   120.0000    0.00
hcos     4   3   5        5.7833   120.0000    0.00
hcos     2   6   7        4.8796   109.4710    0.00
hcos     6   7   8        5.7833   120.0000    0.00
hcos     6   7   9        5.7833   120.0000    0.00
hcos     8   7   9        5.7833   120.0000    0.00
hcos    11  10  20        4.7279   106.7000    0.00
hcos    10  11  12        4.8796   109.4710    0.00
hcos    10  11  14        4.8796   109.4710    0.00
hcos    12  11  14        4.8796   109.4710    0.00
hcos    11  12  13        4.8796   109.4710    0.00
hcos     1  12  11        4.8796   109.4710    0.00
hcos     1  12  13        4.8796   109.4710    0.00
hcos    11  14  15        4.8796   109.4710    0.00
hcos    14  15  16        5.7833   120.0000    0.00
hcos    14  15  17        5.7833   120.0000    0.00
hcos    16  15  17        5.7833   120.0000    0.00
hcos    19  18  28        4.7279   106.7000    0.00
hcos    18  19  20        4.8796   109.4710    0.00
hcos    18  19  22        4.8796   109.4710    0.00
hcos    20  19  22        4.8796   109.4710    0.00
hcos    19  20  21        4.8796   109.4710    0.00
hcos    10  20  19        4.8796   109.4710    0.00
hcos    10  20  21        4.8796   109.4710    0.00
hcos    19  22  23        4.8796   109.4710    0.00
hcos    22  23  24        5.7833   120.0000    0.00
hcos    22  23  25        5.7833   120.0000    0.00
hcos    24  23  25        5.7833   120.0000    0.00
hcos    27  26  36        4.7279   106.7000    0.00
hcos    26  27  28        4.8796   109.4710    0.00
hcos    26  27  30        4.8796   109.4710    0.00
hcos    28  27  30        4.8796   109.4710    0.00
hcos    27  28  29        4.8796   109.4710    0.00
hcos    18  28  27        4.8796   109.4710    0.00
hcos    18  28  29        4.8796   109.4710    0.00
hcos    27  30  31        4.8796   109.4710    0.00
```

hcos	30	31	32	5.7833	120.0000	0.00
hcos	30	31	33	5.7833	120.0000	0.00
hcos	32	31	33	5.7833	120.0000	0.00
hcos	35	34	44	4.7279	106.7000	0.00
hcos	34	35	36	4.8796	109.4710	0.00
hcos	34	35	38	4.8796	109.4710	0.00
hcos	36	35	38	4.8796	109.4710	0.00
hcos	35	36	37	4.8796	109.4710	0.00
hcos	26	36	35	4.8796	109.4710	0.00
hcos	26	36	37	4.8796	109.4710	0.00
hcos	35	38	39	4.8796	109.4710	0.00
hcos	38	39	40	5.7833	120.0000	0.00
hcos	38	39	41	5.7833	120.0000	0.00
hcos	40	39	41	5.7833	120.0000	0.00
hcos	43	42	52	4.7279	106.7000	0.00
hcos	42	43	44	4.8796	109.4710	0.00
hcos	42	43	46	4.8796	109.4710	0.00
hcos	44	43	46	4.8796	109.4710	0.00
hcos	43	44	45	4.8796	109.4710	0.00
hcos	34	44	43	4.8796	109.4710	0.00
hcos	34	44	45	4.8796	109.4710	0.00
hcos	43	46	47	4.8796	109.4710	0.00
hcos	46	47	48	5.7833	120.0000	0.00
hcos	46	47	49	5.7833	120.0000	0.00
hcos	48	47	49	5.7833	120.0000	0.00
hcos	51	50	60	4.7279	106.7000	0.00
hcos	50	51	52	4.8796	109.4710	0.00
hcos	50	51	54	4.8796	109.4710	0.00
hcos	52	51	54	4.8796	109.4710	0.00
hcos	51	52	53	4.8796	109.4710	0.00
hcos	42	52	51	4.8796	109.4710	0.00
hcos	42	52	53	4.8796	109.4710	0.00
hcos	51	54	55	4.8796	109.4710	0.00
hcos	54	55	56	5.7833	120.0000	0.00
hcos	54	55	57	5.7833	120.0000	0.00
hcos	56	55	57	5.7833	120.0000	0.00
hcos	59	58	68	4.7279	106.7000	0.00
hcos	58	59	60	4.8796	109.4710	0.00
hcos	58	59	62	4.8796	109.4710	0.00
hcos	60	59	62	4.8796	109.4710	0.00
hcos	59	60	61	4.8796	109.4710	0.00
hcos	50	60	59	4.8796	109.4710	0.00
hcos	50	60	61	4.8796	109.4710	0.00
hcos	59	62	63	4.8796	109.4710	0.00
hcos	62	63	64	5.7833	120.0000	0.00
hcos	62	63	65	5.7833	120.0000	0.00

```
hcos    64  63  65          5.7833   120.0000   0.00
hcos    66  67  68          4.8796   109.4710   0.00
hcos    66  67  70          4.8796   109.4710   0.00
hcos    68  67  70          4.8796   109.4710   0.00
hcos    67  68  69          4.8796   109.4710   0.00
hcos    58  68  67          4.8796   109.4710   0.00
hcos    58  68  69          4.8796   109.4710   0.00
hcos    67  70  71          4.8796   109.4710   0.00
hcos    70  71  72          5.7833   120.0000   0.00
hcos    70  71  73          5.7833   120.0000   0.00
hcos    72  71  73          5.7833   120.0000   0.00
DIHEDRALS 104
cos     12   1   2   3      0.0217     0.0000   3.00   1.00   1.00
cos     12   1   2   6      0.0217     0.0000   3.00   1.00   1.00
cos      1   2   3   4      0.0054  -180.0000   6.00   1.00   1.00
cos      1   2   3   5      0.0054  -180.0000   6.00   1.00   1.00
cos      6   2   3   4      0.0054  -180.0000   6.00   1.00   1.00
cos      6   2   3   5      0.0054  -180.0000   6.00   1.00   1.00
cos      2   6   7   8      0.0108  -180.0000   6.00   1.00   1.00
cos      2   6   7   9      0.0108  -180.0000   6.00   1.00   1.00
cos     20  10  11  12      0.0217     0.0000   3.00   1.00   1.00
cos     20  10  11  14      0.0217     0.0000   3.00   1.00   1.00
cos     10  11  12  13      0.0108     0.0000   3.00   1.00   1.00
cos     10  11  12   1      0.0108     0.0000   3.00   1.00   1.00
cos     14  11  12  13      0.0108     0.0000   3.00   1.00   1.00
cos     14  11  12   1      0.0108     0.0000   3.00   1.00   1.00
cos     11  14  15  16      0.0108  -180.0000   6.00   1.00   1.00
cos     11  14  15  17      0.0108  -180.0000   6.00   1.00   1.00
cos     28  18  19  20      0.0217     0.0000   3.00   1.00   1.00
cos     28  18  19  22      0.0217     0.0000   3.00   1.00   1.00
cos     18  19  20  21      0.0108     0.0000   3.00   1.00   1.00
cos     18  19  20  10      0.0108     0.0000   3.00   1.00   1.00
cos     22  19  20  21      0.0108     0.0000   3.00   1.00   1.00
cos     22  19  20  10      0.0108     0.0000   3.00   1.00   1.00
cos     19  22  23  24      0.0108  -180.0000   6.00   1.00   1.00
cos     19  22  23  25      0.0108  -180.0000   6.00   1.00   1.00
cos     36  26  27  28      0.0217     0.0000   3.00   1.00   1.00
cos     36  26  27  30      0.0217     0.0000   3.00   1.00   1.00
cos     26  27  28  29      0.0108     0.0000   3.00   1.00   1.00
cos     26  27  28  18      0.0108     0.0000   3.00   1.00   1.00
cos     30  27  28  29      0.0108     0.0000   3.00   1.00   1.00
cos     30  27  28  18      0.0108     0.0000   3.00   1.00   1.00
cos     27  30  31  32      0.0108  -180.0000   6.00   1.00   1.00
cos     27  30  31  33      0.0108  -180.0000   6.00   1.00   1.00
cos     44  34  35  36      0.0217     0.0000   3.00   1.00   1.00
cos     44  34  35  38      0.0217     0.0000   3.00   1.00   1.00
```

cos	34	35	36	37	0.0108	0.0000	3.00	1.00	1.00
cos	34	35	36	26	0.0108	0.0000	3.00	1.00	1.00
cos	38	35	36	37	0.0108	0.0000	3.00	1.00	1.00
cos	38	35	36	26	0.0108	0.0000	3.00	1.00	1.00
cos	35	38	39	40	0.0108	-180.0000	6.00	1.00	1.00
cos	35	38	39	41	0.0108	-180.0000	6.00	1.00	1.00
cos	52	42	43	44	0.0217	0.0000	3.00	1.00	1.00
cos	52	42	43	46	0.0217	0.0000	3.00	1.00	1.00
cos	42	43	44	45	0.0108	0.0000	3.00	1.00	1.00
cos	42	43	44	34	0.0108	0.0000	3.00	1.00	1.00
cos	46	43	44	45	0.0108	0.0000	3.00	1.00	1.00
cos	46	43	44	34	0.0108	0.0000	3.00	1.00	1.00
cos	43	46	47	48	0.0108	-180.0000	6.00	1.00	1.00
cos	43	46	47	49	0.0108	-180.0000	6.00	1.00	1.00
cos	60	50	51	52	0.0217	0.0000	3.00	1.00	1.00
cos	60	50	51	54	0.0217	0.0000	3.00	1.00	1.00
cos	50	51	52	53	0.0108	0.0000	3.00	1.00	1.00
cos	50	51	52	42	0.0108	0.0000	3.00	1.00	1.00
cos	54	51	52	53	0.0108	0.0000	3.00	1.00	1.00
cos	54	51	52	42	0.0108	0.0000	3.00	1.00	1.00
cos	51	54	55	56	0.0108	-180.0000	6.00	1.00	1.00
cos	51	54	55	57	0.0108	-180.0000	6.00	1.00	1.00
cos	68	58	59	60	0.0217	0.0000	3.00	1.00	1.00
cos	68	58	59	62	0.0217	0.0000	3.00	1.00	1.00
cos	58	59	60	61	0.0108	0.0000	3.00	1.00	1.00
cos	58	59	60	50	0.0108	0.0000	3.00	1.00	1.00
cos	62	59	60	61	0.0108	0.0000	3.00	1.00	1.00
cos	62	59	60	50	0.0108	0.0000	3.00	1.00	1.00
cos	59	62	63	64	0.0108	-180.0000	6.00	1.00	1.00
cos	59	62	63	65	0.0108	-180.0000	6.00	1.00	1.00
cos	66	67	68	69	0.0108	0.0000	3.00	1.00	1.00
cos	66	67	68	58	0.0108	0.0000	3.00	1.00	1.00
cos	70	67	68	69	0.0108	0.0000	3.00	1.00	1.00
cos	70	67	68	58	0.0108	0.0000	3.00	1.00	1.00
cos	67	70	71	72	0.0108	-180.0000	6.00	1.00	1.00
cos	67	70	71	73	0.0108	-180.0000	6.00	1.00	1.00
cos	10	11	14	15	0.0217	0.0000	3.00	1.00	1.00
cos	12	11	14	15	0.0217	0.0000	3.00	1.00	1.00
cos	18	19	22	23	0.0217	0.0000	3.00	1.00	1.00
cos	20	19	22	23	0.0217	0.0000	3.00	1.00	1.00
cos	26	27	30	31	0.0217	0.0000	3.00	1.00	1.00
cos	28	27	30	31	0.0217	0.0000	3.00	1.00	1.00
cos	34	35	38	39	0.0217	0.0000	3.00	1.00	1.00
cos	36	35	38	39	0.0217	0.0000	3.00	1.00	1.00
cos	42	43	46	47	0.0217	0.0000	3.00	1.00	1.00
cos	44	43	46	47	0.0217	0.0000	3.00	1.00	1.00

```
cos      50   51   54   55        0.0217      0.0000      3.00     1.00   1.00
cos      52   51   54   55        0.0217      0.0000      3.00     1.00   1.00
cos      58   59   62   63        0.0217      0.0000      3.00     1.00   1.00
cos      60   59   62   63        0.0217      0.0000      3.00     1.00   1.00
cos      66   67   70   71        0.0217      0.0000      3.00     1.00   1.00
cos      68   67   70   71        0.0217      0.0000      3.00     1.00   1.00
cos       1    2    6    7        0.0217      0.0000      3.00     1.00   1.00
cos       3    2    6    7        0.0217      0.0000      3.00     1.00   1.00
cos      11   10   20   19        0.0217      0.0000      3.00     1.00   1.00
cos      11   10   20   21        0.0217      0.0000      3.00     1.00   1.00
cos      19   18   28   27        0.0217      0.0000      3.00     1.00   1.00
cos      19   18   28   29        0.0217      0.0000      3.00     1.00   1.00
cos      27   26   36   35        0.0217      0.0000      3.00     1.00   1.00
cos      27   26   36   37        0.0217      0.0000      3.00     1.00   1.00
cos      35   34   44   43        0.0217      0.0000      3.00     1.00   1.00
cos      35   34   44   45        0.0217      0.0000      3.00     1.00   1.00
cos      43   42   52   51        0.0217      0.0000      3.00     1.00   1.00
cos      43   42   52   53        0.0217      0.0000      3.00     1.00   1.00
cos      51   50   60   59        0.0217      0.0000      3.00     1.00   1.00
cos      51   50   60   61        0.0217      0.0000      3.00     1.00   1.00
cos      59   58   68   67        0.0217      0.0000      3.00     1.00   1.00
cos      59   58   68   69        0.0217      0.0000      3.00     1.00   1.00
cos       2    1   12   11        0.0217      0.0000      3.00     1.00   1.00
cos       2    1   12   13        0.0217      0.0000      3.00     1.00   1.00
INVERSIONS 10
plan      3    2    4    5        1.7350      0.0000
plan      7    6    8    9        1.7350      0.0000
plan     15   14   16   17        1.7350      0.0000
plan     23   22   24   25        1.7350      0.0000
plan     31   30   32   33        1.7350      0.0000
plan     39   38   40   41        1.7350      0.0000
plan     47   46   48   49        1.7350      0.0000
plan     55   54   56   57        1.7350      0.0000
plan     63   62   64   65        1.7350      0.0000
plan     71   70   72   73        1.7350      0.0000
finish
WATER
nummols 1389
atoms 4
OW                               15.8000      1.2500
OW(S)                             0.2000     -2.0500
HW                                1.0080      0.4000
HW                                1.0080      0.4000
shell 1
          1    2                209.4496
bonds 8
```

```
mors     2   3                 6.2037     0.9237   2.2200
mors     2   4                 6.2037     0.9237   2.2200
mors     3   4                 0.0000     1.5000   2.8405
coul     2   3                 0.5000
coul     2   4                 0.5000
coul     3   4                 0.5000
coul     1   3                 1.0000
coul     1   4                 1.0000
angles 1
harm     3   2   4             4.1998   108.6932
finish
vdw 58
N        N        12-6     98206.5000    53.3100
N        Y        12-6    112386.8000    55.3100
N        C1       12-6    112386.8000    55.3100
N        X        12-6    112386.8000    55.3100
N        A        12-6     36653.7900    25.2250
N        B        12-6     36653.7900    25.2250
N        TY       12-6    112386.8000    55.3100
Y        Y        lj           0.0062     3.9230
C1       Y        lj           0.0043     3.7433
X        Y        lj           0.0062     3.9230
Y        A        lj           0.0057     3.4760
Y        B        lj           0.0057     3.4760
TY       Y        lj           0.0062     3.9230
C1       C1       lj           0.0030     3.5636
C1       X        lj           0.0043     3.7433
C1       A        lj           0.0040     3.2963
C1       B        lj           0.0040     3.2963
C1       TY       lj           0.0043     3.7433
X        X        lj           0.0062     3.9230
X        A        lj           0.0057     3.4760
X        B        lj           0.0057     3.4760
X        TY       lj           0.0062     3.9230
A        A        lj           0.0052     3.0290
B        A        lj           0.0052     3.0290
TY       A        lj           0.0057     3.4760
B        B        lj           0.0052     3.0290
TY       TY       lj           0.0062     3.9230
TY       B        lj           0.0057     3.4760
O(S)     O(S)     buck     16372.0000     0.2130     3.47
CA       O(S)     buck      1550.0000     0.2970     0.00
OW(S)    OW(S)    12-6     39344.9800    42.1500
HW       OW(S)    nm           0.0556     9.0000     6.00   1.8171
C1       CA       lj           0.0040     2.9998
A        CA       buck       859.3900     0.3372     0.00
```

```
B      CA     buck     859.3900   0.3372   0.00
CA     N      buck     663.2600   0.3372   0.00
X      OW(S)  lj         0.0057   3.4760
C1     OW(S)  lj         0.0040   3.2963
A      OW(S)  lj         0.0052   3.0290
Y      OW(S)  lj         0.0057   3.4760
TY     OW(S)  lj         0.0057   3.4760
B      OW(S)  lj         0.0052   3.0290
N      OW(S)  12-6   62314.5800  62.0100
N      HW     12-6    5482.1000   8.7200
HW     A      lj         0.0032   1.7145
HW     B      lj         0.0032   1.7145
HW     C1     lj         0.0025   1.9818
HW     X      lj         0.0035   2.1615
HW     Y      lj         0.0035   2.1615
HW     TY     lj         0.0035   2.1615
O(S)   OW(S)  buck   12533.6000   0.2130  12.09
CA     OW(S)  buck    1186.6000   0.2970   0.00
HW     O(S)   hbnd      26.0000   1.8000
C      OW(S)  buck     435.0000   0.3400
O(S)   C1     lj         0.0040   3.2963
O(S)   A      buck    9557.0586   0.2130   7.47
N      O(S)   12-6   36653.7900  25.2250
O(S)   B      buck    9557.0586   0.2130   7.47
close
```